Modification of polymeric carbon nitride based photocatalysts for enhanced photocatalytic NO removal performance

	Gu Zhanyong
	Tohoku University
	11301　19963
URL	http://hdl.handle.net/10097/00134369

Modification of polymeric carbon nitride based photocatalysts for enhanced photocatalytic NO removal performance

NO 除去光触媒性能を向上させるためのカーボンナイトライドベース光触媒修飾

A Thesis

Submitted for the Degree of

DOCTOR OF PHILOSOPHY (Ph.D.)

By:

Zhanyong Gu (B8GD3001)

Supervisor: Prof. Shu Yin

Graduate School of Environmental Studies
TOHOKU UNIVERSITY
Aoba-ku, Sendai, 980-8577, JAPAN
January 2021

Table of content

Acknowledgement

First of all, I would like to express my sincere thanks to Professor Shu Yin. During my doctoral studies, Professor Yin not only guides my scientific research work but also helps me in my life.   Moreover, Professor Yin is very kind and tolerable to my careless mistakes. When I make careless mistakes, he always helps me to find the reasons and correct the errors instead of simply giving a bad name to me. Thanks to the help and guidance of Professor Yin, I can enjoy my life in Japan even though the research work is very tiring. At same time, I would like to express my sincere thanks to Professor Itaru Honma and Prof. Daisuke Nagao for reviewing my doctoral dissertation to improve my research work.

Secondly, I would like to express the gratitude to Assistant Professors Yusuke Asakura and Takuya Hasegawa. They give me useful suggestions for the doctoral dissertation and help me do the experimental characterization.

Thirdly, I would like to express the gratitude to all the members of Yin lab for their kindness and cooperation. They are Dr. Anung Riapanitra, Dr. Angga Hermawan, Dr. Biao Zhang, Mr. Peng Sun, Ms. Zijing Wang, Mr. Ardiansyah Taufik, Mr. Tingru Chen, Ms. Jinweng Wang, Ms. Shio Komatsuda, Ms. Chiaki Noda, Ms. Misuzu, Nakamura, Ms. Yukiho Nishimura, Ms. Jingdi Cao, Ms. Tomoyo Akahira, Ms. Nonoko Suzuki, Mr. Namiki Uchiyama, Ms. Tetsuhiro Onodera, Mr. Hanyu Liu, Mr. Iimura and Mr. Yasuo Hangai.

Also, I would like to express the gratitude to Professor Kenta Hongo, Professor Ryo Maezono, Mr. Ken Sinkou Qin, Mr. Dawei Wen, Mr. Zhitao Cui, Mr. Jia wei Xue and Ms. Xuan Zhou for their useful help for the DFT calculations. I would like to express the gratitude to Professors Satoshi Tsukuda, Hideki Kato, Masato Kakihana for the useful experimental characterization.

At the same time, I would like to express the gratitude to my strong motherland. It provides the CSC scholarship to cover the living expense and encourages me to work hard.

Lastly, I would like to express the gratitude to my family. Thank you for your love,

understanding and encouraging. When I meet with difficulties, you always tell me not to give up. And I would like to express my gratitude and love to my wife Yingxia Wang. Meeting you is the greatest luck of my life.

Chapter 1 General Introduction

1.1 Air pollution

With the fast development of industrialization and human activities, environmental pollution and energy crisis have become the two major challenges in the world [1, 2]. Air pollution is one of the serious problems [3, 4]. There are a great deal of air pollutants including carbon dioxide (CO_2), sulfur trioxide (SO_3), sulfur dioxide (SO_2), nitrogen dioxide (NO_2), nitric oxide (NO) and so on (**Table1.1**). Air pollution would bring about a variety of environmental issues: it can damage and corrode the buildings and equipment; it is harmful to humans, animals and vegetables; it can lead to climate change. NO is especially serious among the air pollutants [5-8]. To more specific, as shown in **Fig.1.1**, NO pollutants result in ground level ozone, acid rain, global warming and so on. Moreover, it could cause damage to human health and increase the risk of diseases such as emphysema, bronchitis, respiratory disease. If the human beings want to realize sustainable development and have a bright future, we must solve the air pollution as soon as possible.

Table1.1 Summary of the atmospheric pollutants and the corresponding to the major sources (https://www.encyclopedie-environnement.org/en/air-en/air-pollution/)

Pollutant/Pollutant category	Examples	Physical state	Major sources
Photochemical oxidants	Ozone	Gas	Pollutant in the troposphere produced from NOx, volatile organic compounds such as methane or CO, stratospheric origin. In the stratosphere, protection from UV but destroyed by chlorine or bromine compounds (ozone hole)
Sulphur dioxide	SO_2	Gas	Combustion of fossil fuels, volcanos, transformation of natural sulphur compounds
Carbon monoxide	CO	Gas	Incomplete combustion of carbon compounds, oxidation of volatile organic compounds (VOCs)
Nitrogen oxides (NOx)	NO, NO_2	Gas	Nitrogen oxidation during combustions, thunderstorms
Polycyclic hydrocarbons	Benzene 1, 3-butadiene, formaldehyde, acids	Gas	Incomplete combustion, Atmospheric chemistry, use of solvents
Mercury (Hg)	HgO, mercury methyl	Gas and particles	Combustion of carbon, ores refining, incinerators, natural
Lead (Pb)	Pb	Particles	Combustion of gas with lead (now removed), incinerators, foundries and lead transformation
PM, including PM10 & PM2.5, inhalable particles, suspended particles, black carbon	Inorganic ions (ex. sulphate; metallic oxides; carbon materials including inorganic carbon & elementary carbon)	Particles	Wind erosion, marine sprays, combustion of fossil fuels or biomass, agriculture, pollens, spores, viruses, bacteria, gas-particles conversion
Organic carbon	Hopanes, Steranes, hydrocarbons, levoglucosanes, terpenes, isoprenes	Gas and particles	Incomplete combustion of fossil combustibles or biomass, emissions by plants, oxidation of gaseous organic compounds
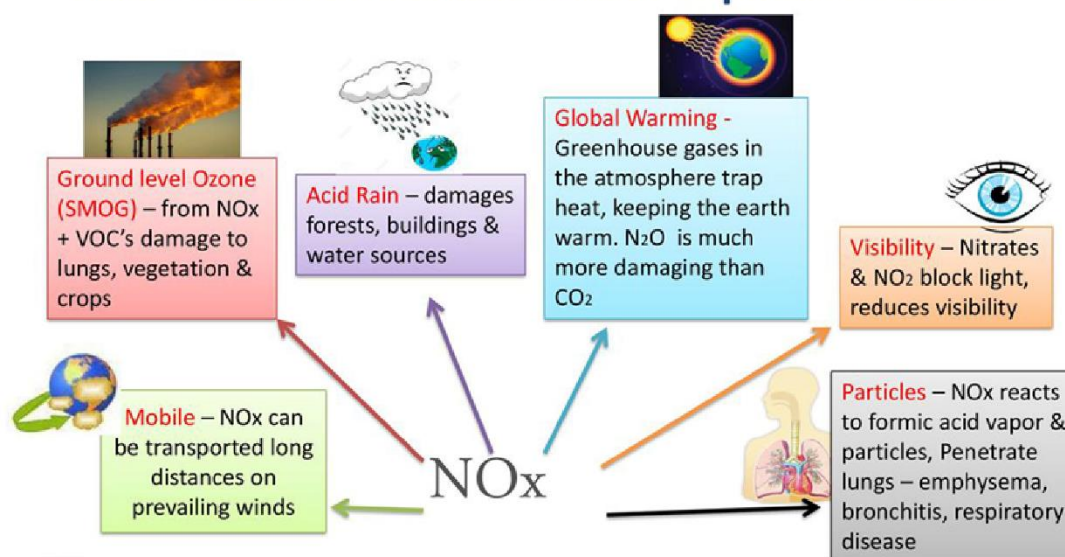
Fig.1.1 The different environmental problems caused by the NO_x (https://slideplayer.com/slide/15907376/)

1.2 Photocatalysis

Much work has been done to deal with the NO pollutant [9]. Recently, photocatalysis as a green technology has attracted a substantial amount of attention [3]. The research articles related to photocatalytic NO_x removal increase significantly in the last decades, demonstrating the hot topics of the photocatalytic NO_x removal using semiconductor materials irradiated by the solar light (**Fig.1.2**). Since Fujishima and Honda reported the photoelectrochemical water splitting in 1972[10], great progress has been made to unravel the photocatalysis mechanism [11-13]. Normally, as shown in **Fig.1.3**, the typical photocatalysis process including five consecutive steps [14]: (1) light harvesting; (2) charge excitation; (3) charge separation; (4) surface reduction (5) surface oxidation. It should be pointed out that a large number of charge carriers recombine during the charge separation process. Only the effective charge carriers, i.e., remained charge carriers, can attend the surface reduction and surface oxidation. Therefore, if we want to improve the photocatalytic performance of the photocatalysts, we can improve the light harvesting capability by reducing the bandgap, promote the

charge separation by constructing heterostructure, enhancing the surface reaction by increasing the specific surface areas and active sites.
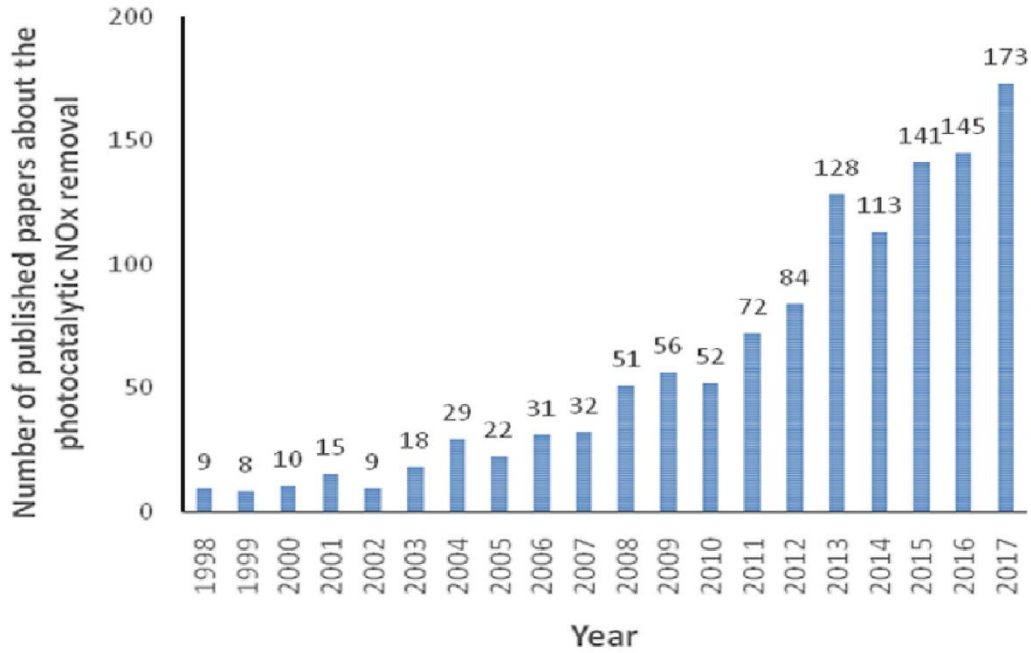
Fig.1.2 The number of the published papers per year related to the photocatalytic NO_x removal [3]
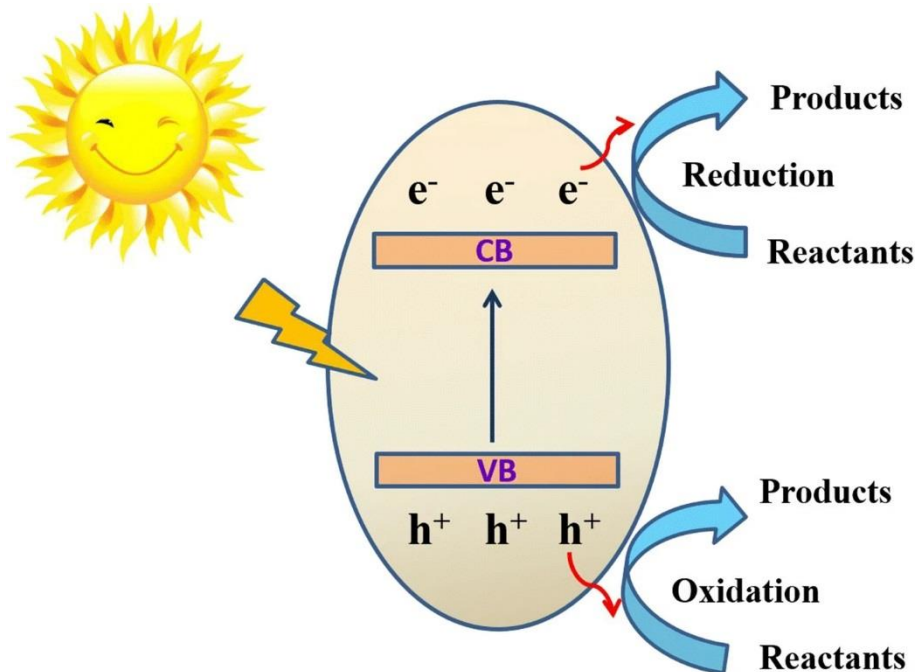
Fig.1.3 The typical process of photocatalytic process using the semiconductor material irradiated by the solar light [14]

1.3 The reaction mechanism of the photocatalytic NO removal

As one of the typical photocatalytic processes, the reaction mechanism of photocatalytic NO removal is carefully discussed about. When the photocatalyst is irradiated by the light with equal or greater energy than the bandgap energy of the photocatalyst, the electrons (e^-) can be excited from the valence band to the conduction band, resulting in positive holes (h^+) in the valance band [3, 15, 16]. It is well-understood that oxygen is the second most abundant gas, consisting of 21% of the atmosphere. The oxygen molecules absorbed on the surface would be reduced, which brought about the s superoxide radicals ($O_2 \cdot -$). At the same time, holes (h^+) in the valance band can oxide the water molecules and OH^- to obtain hydroxyl radicals ($OH \cdot$). In addition, the superoxide radicals ($O_2 \cdot -$) can react with electrons (e^-) and H^+ to get hydrogen peroxide (H_2O_2). Subsequently, the hydrogen peroxide ($H_2O_{2)}$ can react with the electrons (e^-) to obtain hydroxyl radicals ($OH \cdot$). It should be noted that these radicals played significant roles during the photocatalytic NO removal process. To be more specific, the NO absorbed on the surface of photocatalyst would be oxidized by superoxide radicals ($O_2 \cdot -$) and/ or hydroxyl radicals ($OH \cdot$) and/or positive holes to become the final products of nitrate ion (NO^{3-}), through the formation of intermediates related to NO_2 and HNO_2. These series reactions are illustrated as follows:

$$\text{Photocatalyst} + h\nu \rightarrow e^- + h^+ \tag{1.1-1}$$

$$O_2 + e^- \rightarrow O_2 \cdot - \tag{1.1-2}$$

$$h^+ + H_2O/OH^- \rightarrow OH \cdot \tag{1.1-3}$$

$$O_2 \cdot - + H^+ + e^- \rightarrow H_2O_2 \tag{1.1-4}$$

$$H_2O_2 + e^- \rightarrow OH \cdot \tag{1.1-5}$$

$$NO + O_2 \cdot - \rightarrow NO_3^- \tag{1.1-6}$$

$$NO + OH \cdot \rightarrow NO_3^- \tag{1.1-7}$$

$$NO + h^+ \rightarrow NO_3^- \tag{1.1-3}$$
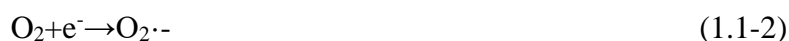
1.4 The photocatalysts

It is universally acknowledged that the key point of photocatalysis is to develop effective and stable photocatalysts. Since the pioneering work of Fujishima and Honda in 1972[10], a great number of photocatalysts have developed to be used in energy conversion and environmental remediation. The reported photocatalysts include metal oxides such as ZnO[17], metal sulfides such as CuS [18], and many more. Among these semiconductor photocatalysts, TiO_2 is considered as the most classical photocatalyst owing to its plenty of advantages such as non-toxicity, low-cost, long-term stability and so on[19-21]. However, the wide bandgap of TiO_2 (3.0-3.2 eV) constrains the photocatalytic response to only ultraviolet (UV) light [22, 23]. As we know, the full solar spectrum consists of near-infrared region (52 %), visible-light region (43%) and UV region (5%)[24]. Therefore, metal and non-metal doping are performed to reduce the bandgap to make the best use of solar energy [24, 25].

1.5 2D materials
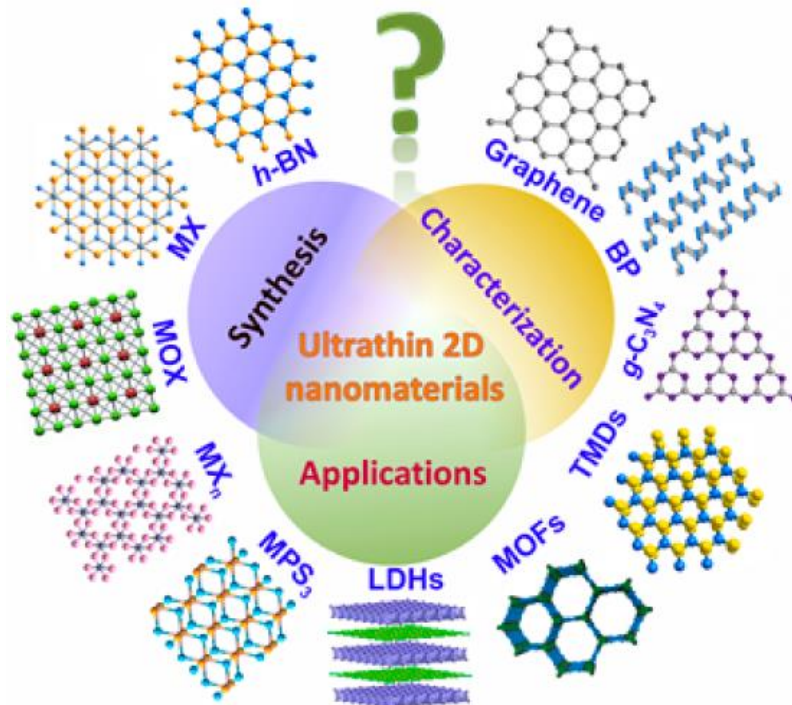
Fig.1.4 The recently developed different kinds of 2D materials [26]

Very recently, the two-dimensional (2D) materials have become the hot research topics in different fields including chemistry, physics, material science and so on [26-29]. The research of 2D materials is inspired by the successful preparation of graphene through mechanic exfoliation of graphite in 2004[26, 28]. The 2D materials exhibited outstanding optical, electrical and structural properties. In addition, the 2D materials display nanoscale thickness and high surface-to-volume ratio, which is beneficial for improving the photocatalytic performance. What is more, the electronic structures of the 2D materials could be modulated by controlling the thickness or doping strategy [26]. For instance, the band gap of MoS_2 can be changed from 1.29 eV to 1.9 eV, corresponding to bulk MoS_2 and monolayer MoS_2, respectively [27]. Up to the present, different kinds of 2D materials have been reported such as transition metal dichalcogenides (TMDs, including MoS_2, WS_2, $MoSe_2$ and WSe_2), metal hydroxides, carbon nitride, boron nitride, graphene, phosphene, MXene (**Fig.1.4**).

1.6 Polymeric carbon nitride
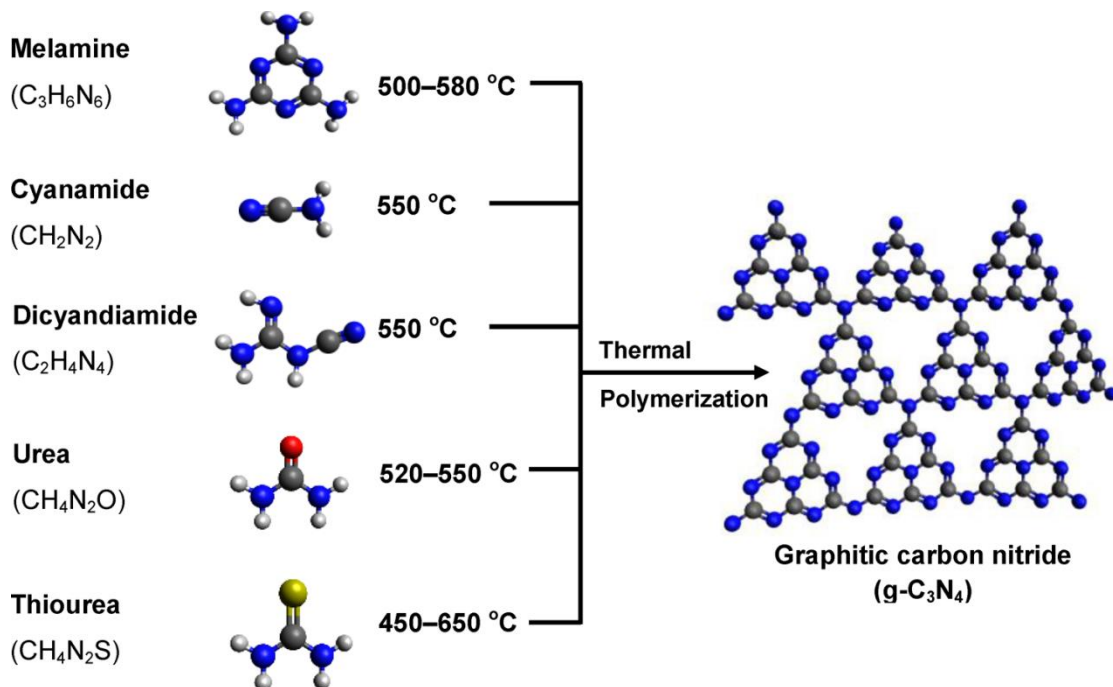
Fig.1.5 Synthesis of CN by thermal polymerization via different precursors [30]

Among the 2D materials, polymeric carbon nitride (CN), i.e., graphitic carbon nitride (g-C$_3$N$_4$) as metal-free photocatalyst has attracted much attention since Wang reported it could be used for H$_2$ production in 2009[31]. The CN not only shows the typical advantages of 2D materials, but also possesses visible-light response due to the suitable bandgap (2.7 eV), facile synthesis with cheap precursor such as melamine, dicyandiamide, urea and thiourea (**Fig.1.5** and **Fig.1.6**), high thermal and chemical stability and nontoxic nature [32-34]. Thanks to the excellent advantages, the CN has been performed in different fields including energy issues and environmental remediation. To be more specific, it has been reported in supercapacitors, electrocatalysis, photo-electro catalytic reactions, N$_2$ fixation, pollutant degradation, CO$_2$ reduction, water splitting, organic catalysis, and sensing [35-39]. To some extent, CN is the most promising material in the 2D material group.
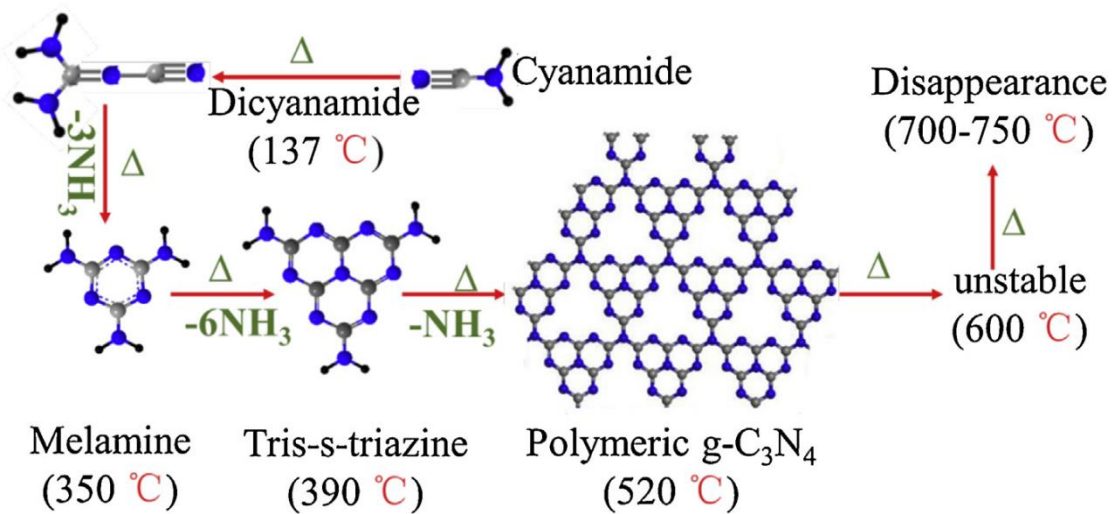
Fig.1.6 Reaction pathway of CN using cyanamide as the precursors [16]

The long history of CN can trace back to 1834, when Berzelius and Liebig prepared it by igniting mercuric thiocyanate [40]. The CN is normally considered as three basic structures: triazine-based CN, heptazine-based CN and triazine and heptazine mixed CN. However, it should be noted that the heptazine-based CN is the most stable phase at ambient conditions according to the first-principles density functional theory (DFT) calculations carried out by Kroke et. Therefore, more and more

researchers and scientists tend to recognize the heptazine as the building block for the formation of CN. **Fig.1.6** shows the typical structures of triazine-based CN, heptazine-based CN, respectively.
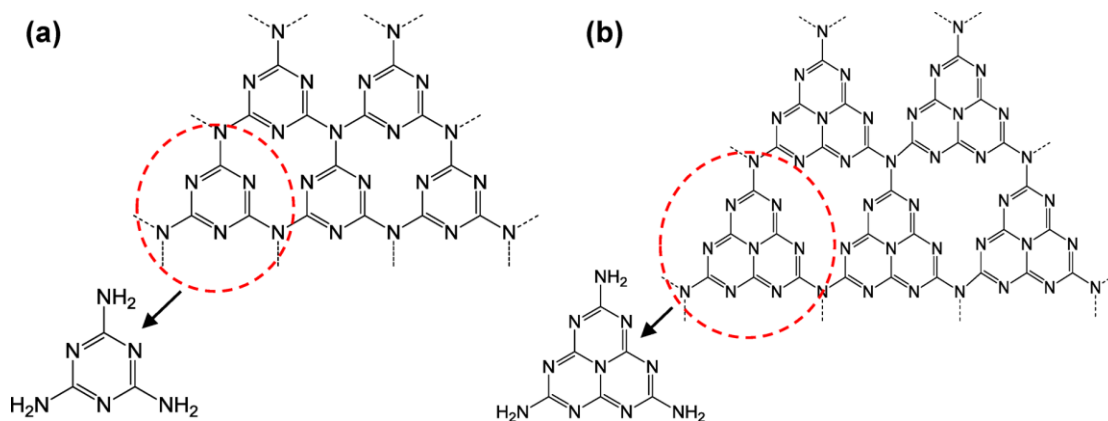
Fig.1.7 (a) Triazine and (b) tris-s-triazine (heptazine) structures of CN [30]

1.7 Synthesis of CN with different precursors

Since Wang et reported the CN as metal-free and visible-light response photocatalyst for H_2 production in 2009[31], CN-based photocatalysis has attracted much interest and great progress has been made to prepare CN-based photocatalyst. Up to now, CN can be successfully synthesized by a great number of precursors such as cyanamide, dicyandiamide, melamine, thiourea and urea [41-43]. The synthesis process of CN is a facile high temperature solid reaction with a temperature ranging from 150 °C to 650°C. X-ray diffraction (XRD) patterns is a powerful technique to study the phase of the samples. As shown in **Fig.1.8**, the CN exhibited two typical peaks at 13.0°and 27.4°, corresponding to the (100) plane and (002) plane, respectively. The (100) plane is index as the in-plane repeat heptazine units in the CN polymeric network while the (002) plane is ascribed to the interlayer stacking [30, 38].
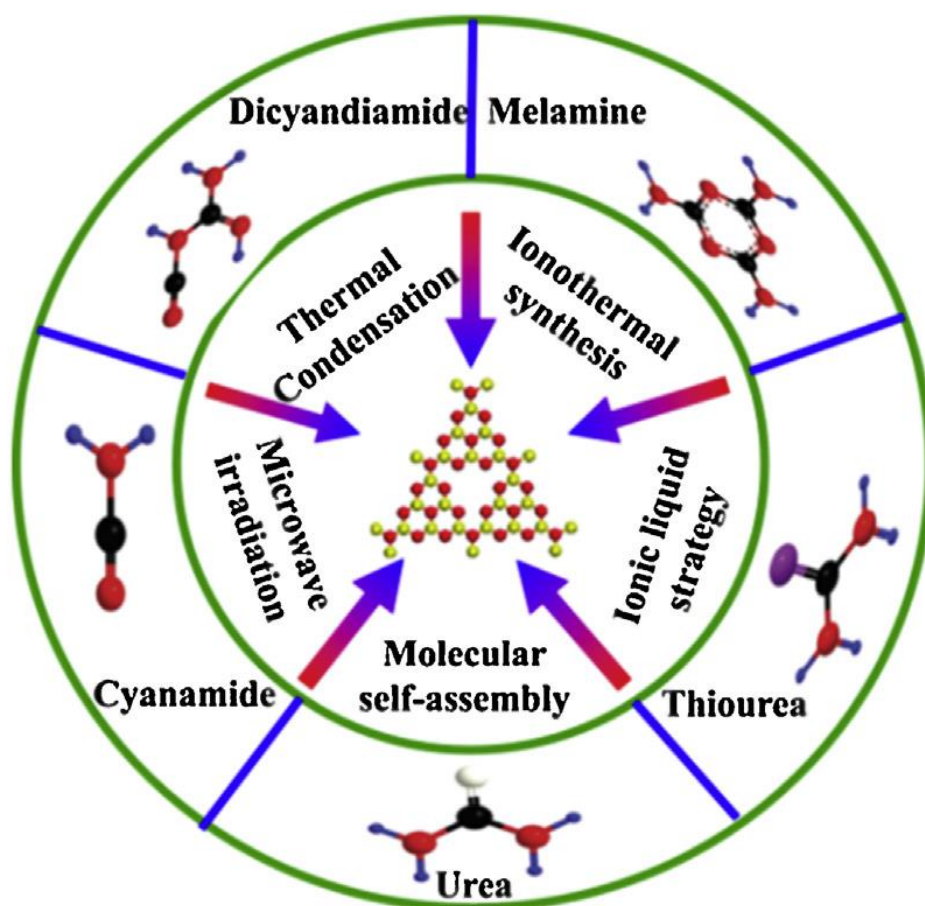
Fig.1.8 Summarized different strategies to synthesize CN [44]
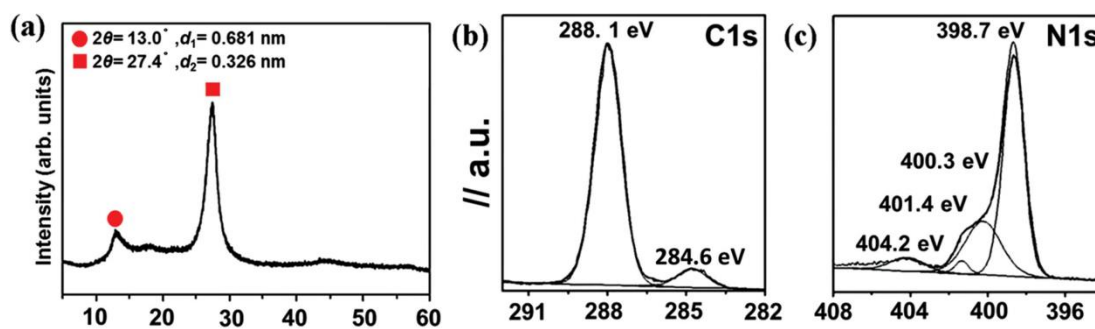
Fig.1.9 (a) XRD patterns (b) high-resolution XPS spectra of C1s, and high-resolution XPS spectra of C1s for CN [38]

X-ray photoelectron spectroscopy (XPS) spectra can give important information on carbon and nitrogen elements in CN. As shown in **Fig.1.9**, the high resolution XPS spectra of C 1s can be resolved into two peaks with binding energies at 288.1eV and 284.6 eV, which can be attributed to sp2-bonded carbon in C-C and N-C=N,

respectively. As for the high resolution XPS spectra of N 1s, it is deconvolved into four peaks centered at 404.2 eV, 401.4eV, 400.3eV and 398.7 eV, which correspond to charging effects, amino functional groups C-NH$_x$, nitrogen in tertiary N-(C)$_3$ groups, the sp2-bonded nitrogen C-N=C, respectively. In addition, the band gap of CN can be estimated by UV-vis diffuse reflectance spectra. Based on the equation E=1240/λ, the band gap is calculated around 2.7 eV. The suitable band of CN indicates the visible light response property, which is more promising than the classical TiO$_2$.
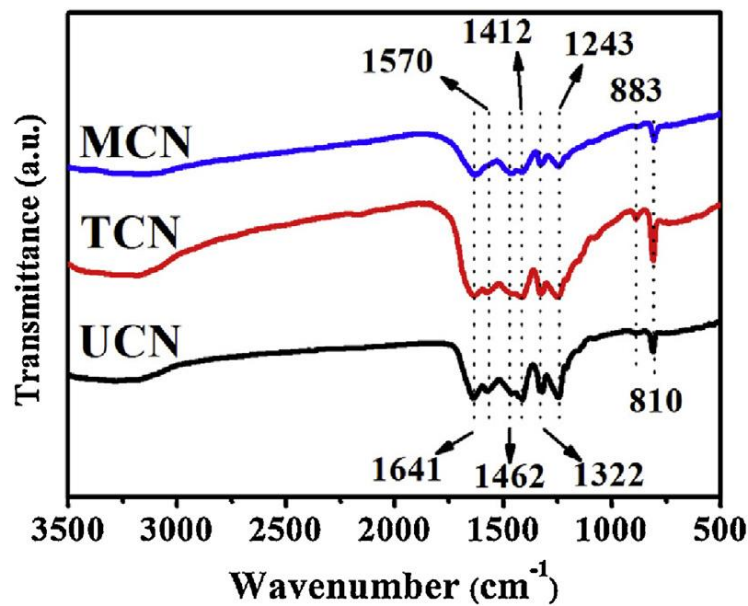
Fig.1.10. (a) FTIR spectra of CN samples using melamine, thiourea and urea [16]

The Fourier transform infrared (FTIR) spectrum is usually performed to investigate the functional groups. As shown in **Fig.1.10**, all the samples displayed similar peaks in the FTIR spectra, no matter what the precursors they are. Please note that MCN, TCN, and UCN are synthesized by melamine, thiourea and urea, respectively. The main characteristic peaks of CN are located in the region from 900 to 1700cm^{-1}[45, 46]. These peaks are related to the heptazine-derived repeating units. As for the distinct peaks located at 810 cm^{-1}, it is index as a characteristic breathing mode of heptazine cycles. At the same time, the peaks around at 883 cm^{-1} are attributed to the deformation mode of N-H. It should be noted that the broad peaks in the region of 3000-

3600 cm^{-1} were attributed to the N-H stretching and -OH absorbed on the surface of the samples [40, 47, 48].
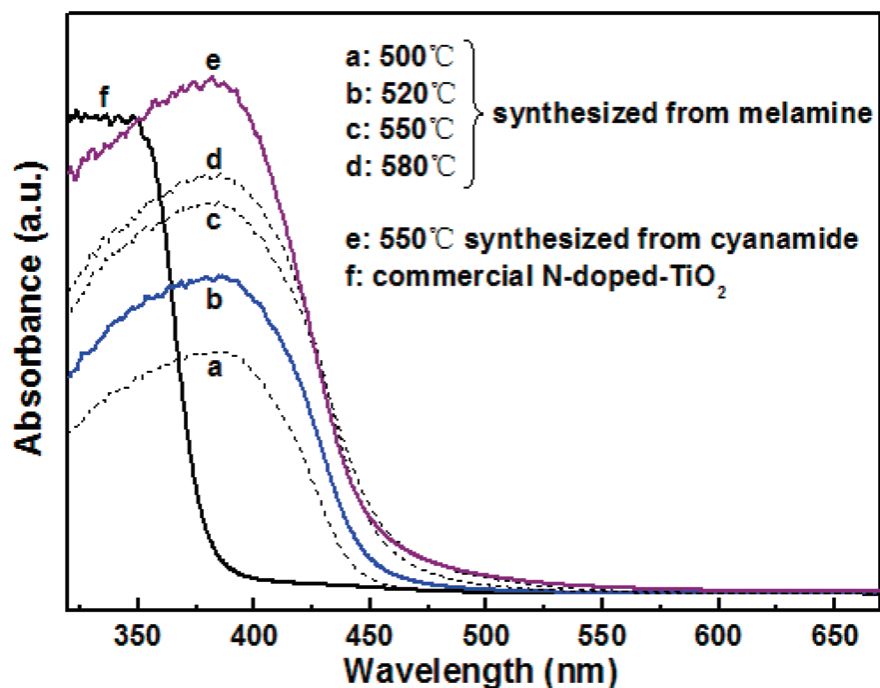
Fig.1.11 UV-VIS absorption spectra of the obtained samples including different CN and commercial N-doped-TiO$_2$[48]

It is universally accepted that the precursors and reaction parameters play crucial roles in the chemical and physical properties of CN samples. We can adjust the band gap, specific surface area, the C/N ratio and so on by controlling the reaction temperature, time and atmosphere and choosing different precursors. For example, Yan demonstrated that calcining melamine with different temperatures ranging from 500 °C to 580°C could result in the decreased band gap from 2.8 to 2.75 eV and increased C/N ratio from 0.721 to 0.742 (**Fig.1.11**) [48]. Similarly, Zhang reported that the band gap of CN can be tuned through different temperatures using thiourea as the precursor (**Fig.1.12**) [49]. With the increasing the heating temperature from 450 to 600°C, the band gap of CN samples was decreased gradually from 2.71 to 2.58 eV. It is interesting that when the heating temperature reached 650°C, the band gap of CN was increased to 2.76 eV. Based on the previously reported literatures, it is safe to conclude that the

parameter of heating temperature is very complex and we must optimize the calcination process to obtain the efficient photocatalyst.
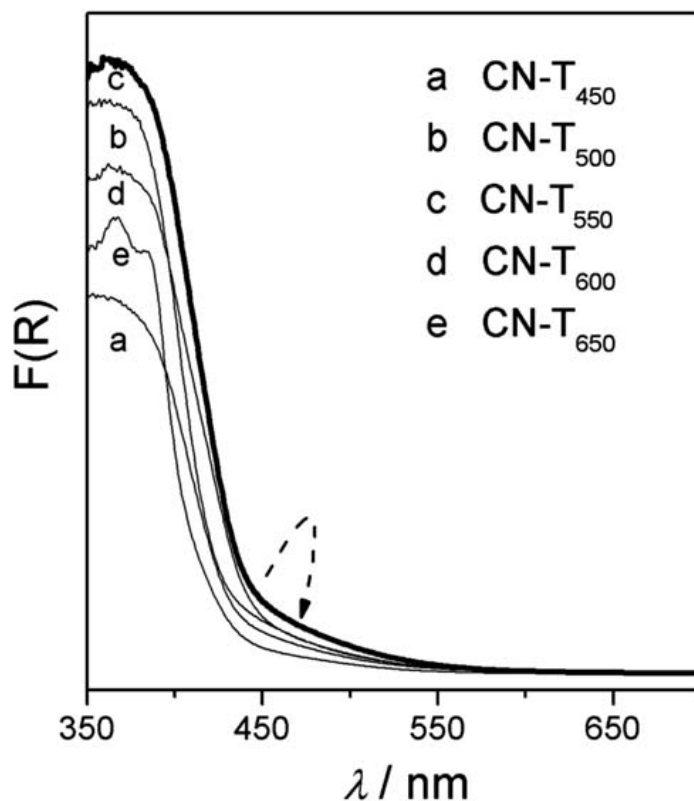
Fig.1.12 UV-VIS absorption spectra of the obtained samples from different calcination temperatures [49]

In addition, the different precursors bring about the different specific surface areas of the CN samples. For example, Yan showed that the specific surface area of CN synthesized from melamine was only 8 m^2g^{-1}, while the specific surface area of CN obtained from thiourea was improved to 52 m^2g^{-1} [48, 49]. Especially, the urea-derived CN displayed a higher specific surface area and it was about 228 m^2g^{-1}. Generally, the higher specific surface area means the more active sites and higher photocatalytic performance. As the band gaps and specific surface areas of CN samples depend on different calcination processes and precursors, we had better take full considerations of the effects of the precursors and reaction parameters when we prepare the CN based photocatalysts.

1.8 Band structure modification

The band structure of the photocatalysts plays crucial role in the photocatalysis process. The optimized band structure can absorb more solar energy to generate more electron-hole pairs; improve the charge carrier separation efficiency to obtain more effective electrons and holes for the surface reactions; modify the reaction sites and promote the adsorption of intermediates to improve the surface reactions. Up to now, tremendous efforts have been devoted to modulate the electronic structure of CN. The strategies of band-gap engineering can be roughly divided into three categories: metal doping, non-metal doping and copolymerization (**Fig.1.13 and 1.14**)[16].
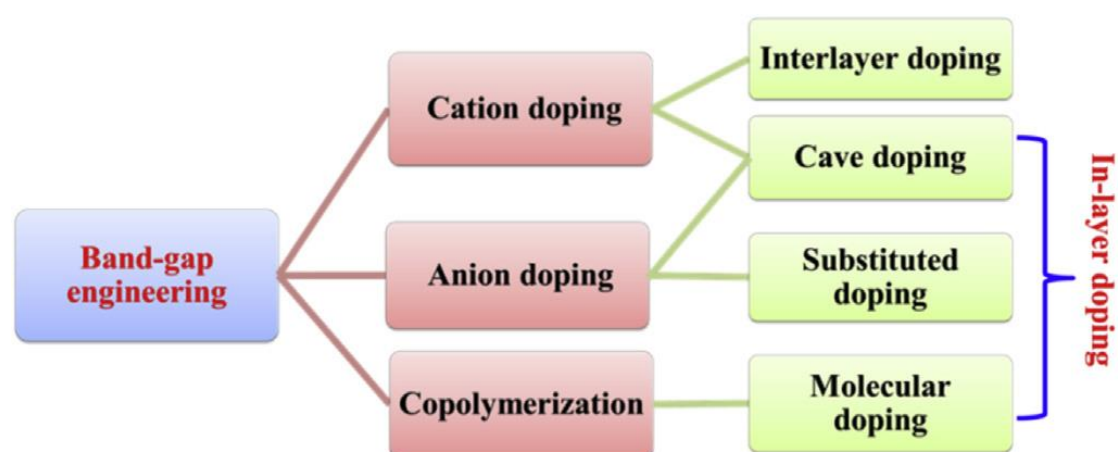
Fig.1.13 The strategies of band-gap engineering including metal doping, non-metal doping and copolymerization [16]
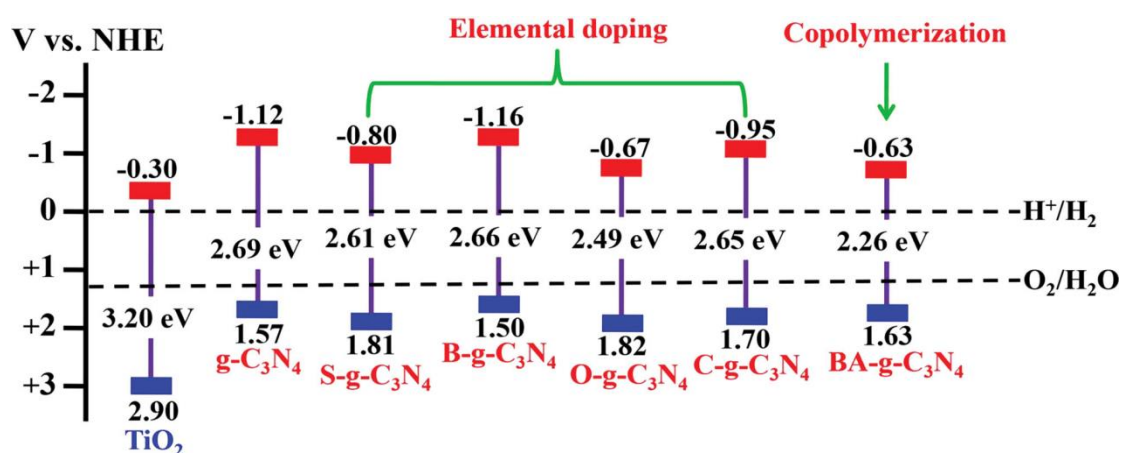
Fig.1.14 The band-gaps of CN-based photocatalystsmodified by element doping and copolymerization [16]

1.8.1 Metal element-doping

A series of metal cations have been used to modulate the band structure of pristine CN. There are two kinds of metal element-doping related to CN, which are cave doping and interlayer doping. As shown in **Fig.1.15**, the metal cations can be introduced into the triangular pores of CN between the heptazine structures. The strong coordination interaction between the metal cations and CN matrix and negatively charged nitrogen atoms enable to realize the cave doping [16]. According to the previously literatures, the transition metal elements including Fe, Mn, Co, Ni, Zn have been demonstrated to effective in optimizing the electronic structure [16, 30]. For example, Wang showed that the band gap could be reduced to enhance the visible-light harvesting capability through Fe and Zn doping into CN [50]. Ding also demonstrated that Fe, Mn, Co, Ni could be incorporated into CN framework to extend the visible-light absorption range and improve the separation efficiency of the photoinduced electrons and holes, which resulted in the enhanced photocatalytic performance [51].
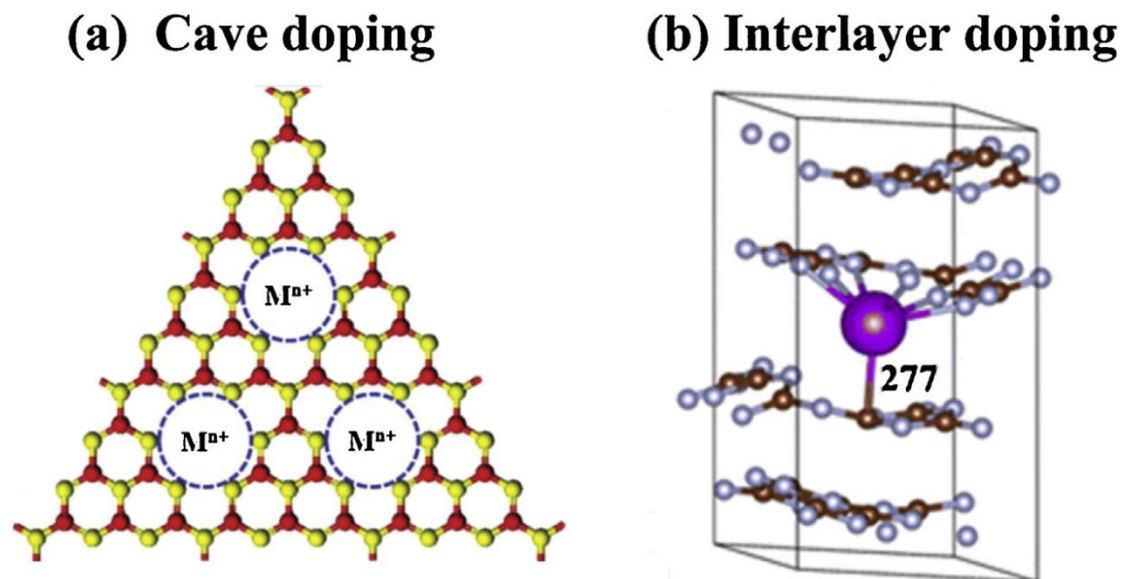
Fig.1.15 Schematic illustration of metal doping of CN framework: (a) cave doing through the coordination interactions, (b) interlayer doping [16]

In addition, according to the first-principle DFT calculation, Pan predicted that incorporation of Pt and Pd into the CN framework could promote the charge carrier

transport rate to improve the charge carrier separation efficiency and reduce the band gap to improve the light absorption, which played positive effects in improving the photocatalytic activity [52]. Recently, Dong found that K atoms could bring about an interlayer doping instead of caving doping in the CN matrix. It is claimed that K atoms connected the two adjacent CN layers to facilitate the charge carrier separation [53]. Also, Zhu revealed that K doping could decrease the VB level of CN, leading to the promoted separation and transportation of photo-induced electrons and holes under visible light irradiation [54].

1.8.2 Non-metal element doping

Compared with metal doping, the strategy of non-metal doping may be more popular because it not only tunes the electronic structure but also remains the metal-free property. So far, many non-metal elements such as S, P, B, O, C and I have demonstrated to be effective for the band-gap engineering by chemically substituting. As shown in **Fig.1.16**, the C atom self-doping can substitute the bridging N atoms while O, S and I atoms tend to replace the N atoms in the aromatic heptazine rings. Thanks to the no-metal doping, the delocalization of the π-conjugated electrons is enhanced to improve the conductivity, mobility and separation of the charge carriers, which is beneficial for improving the photocatalytic performance. As for the P and B atoms, they are inclined to substitute the C atoms.
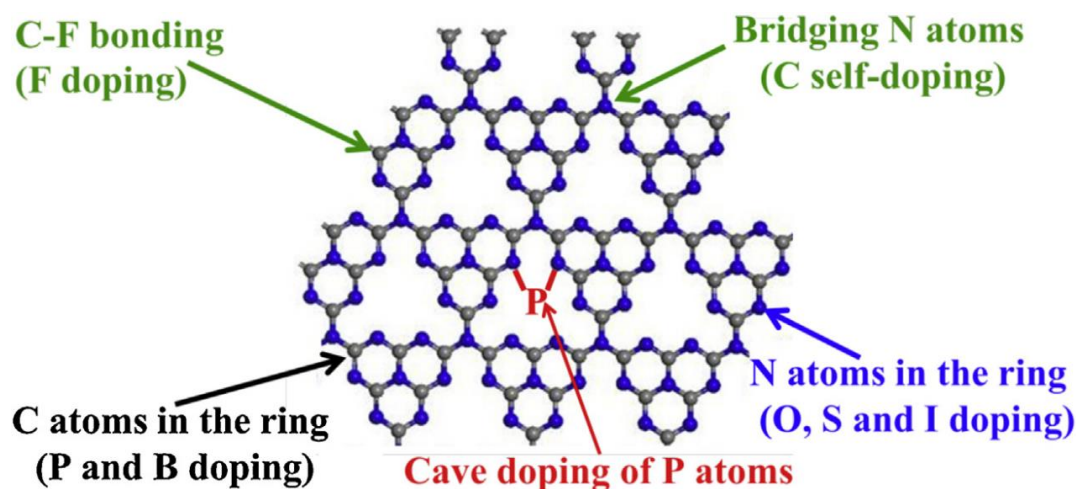
Fig.1.16 Schematic illustration of non-metal doping of CN framework [16]

1.9 Morphology control

Morphology control is considered as another promising strategy to improve the photocatalytic performance of bulk CN. Since the bulk CN is synthesized by high-temperature solid reaction, it suffers from low specific surface areas and few active sites, which is detrimental to the photocatalytic performance. In order to enlarge the specific surface areas and increase the active sites, much progress has been made such as: exfoliation of bulk CN, template strategy including hard-template and soft-template, and supramolecular preorganization method

1.9.1 Exfoliation of bulk CN

Inspired by the preparation of graphene sheets (**Fig.1.17**) [55-57], scientific researchers want to exfoliate the bulk CN into nanosheets. Compared with the bulk CN, CN nanosheets exhibited a great deal of distinct benefits owing to the morphology changing. It not only enlarges the specific surface areas and increases the active sites but also shortens the charge carriers transport distance, improves the solubility and modified the electronic structures owing to the famous quantum confine effect. More specifically, the photogenerated electrons and holes coming from the CN nanosheets can easily migrate to the surface of the photocatalysts to attend the surface reactions through the shorten paths. This phenomenon is instrumental in facilitating the charge carrier separation efficiency to improve the photocatalytic performance. In addition, the enlarged bandgap of CN nanosheets leads to the enhanced oxidation potential energy and reduction potential energy, which is useful for the surface reactions.
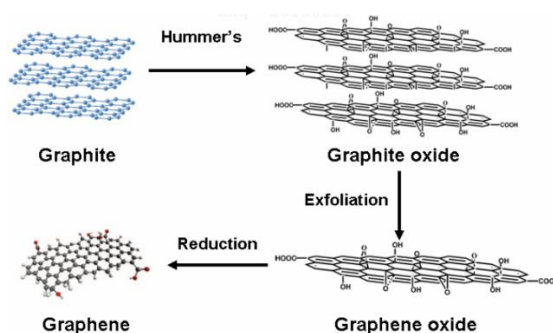
Fig.1.17 Iustration for preparation of graphene nanosheetS
(https://www.chemhui.com/16875.html)

1.9.1.1 Liquid exfoliation of bulk CN
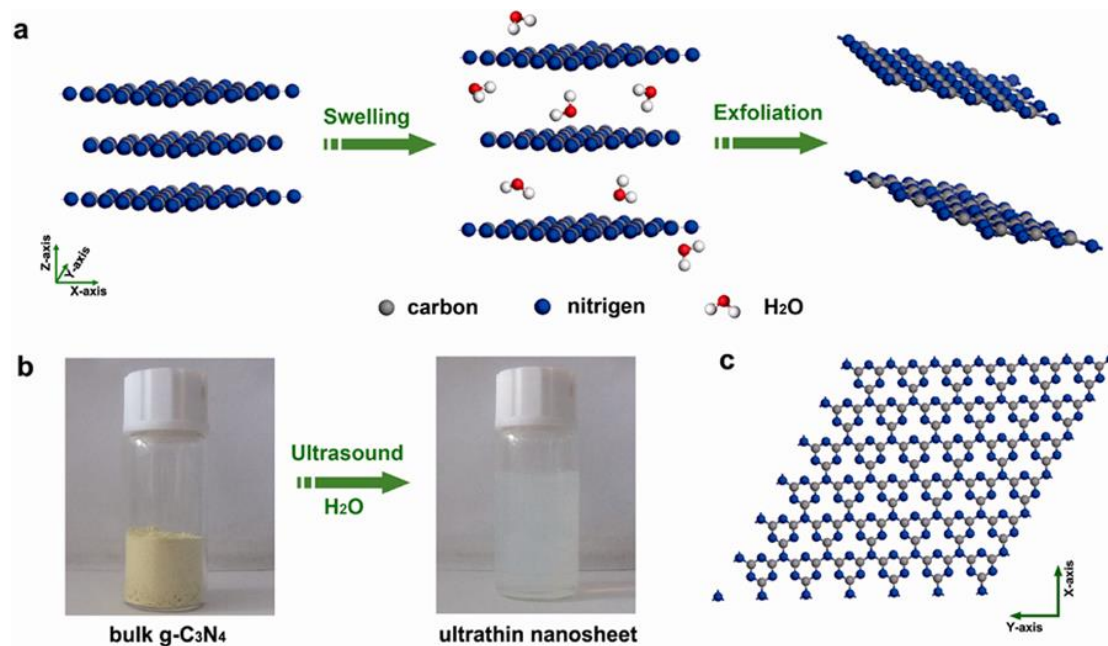
Fig.1.18 Schematic illustration for the liquid-exfoliation process of bulk CN [58].

Generally, the CN nanosheet structures could be achieved by three different strategies, i.e., liquid exfoliation of bulk CN, thermal exfoliation of bulk CN, and the combined approach of thermal exfoliation and liquid exfoliation. Various solvents with suitable surface energy, such as water, methanol, ethanol, N-methyl-pyrrolidone (NMP),1-isopropanol (IPA), acetone and their mixtures, have been used to overcome the weak van der Waals forces between the two adjacent layers of bulk CN by facile sonification. For example, Xie reported a green liquid exfoliation strategy to obtain ultrathin nanosheets by cheap and environmental water (**Fig.1.18**) [58]. The thickness of the exfoliated nanosheet is about 2.5 nm in height (around 7 layers) with the size distribution ranging from 70 nm to 160 nm. In addition, Zhu reported a concentrated H_2SO_4 (98%) assisted liquid exfoliation strategy to fabricate a single atomic layer of CN ultrathin nanosheet [59]. The intercalation of concentrated H_2SO_4 (98%) into the interplanar spacing of bulk CN resulted in the graphene-like single-layer CN structure with a small thickness of 0.4 nm and a large size of micrometers.

1.9.1.2 Thermal exfoliation of bulk CN
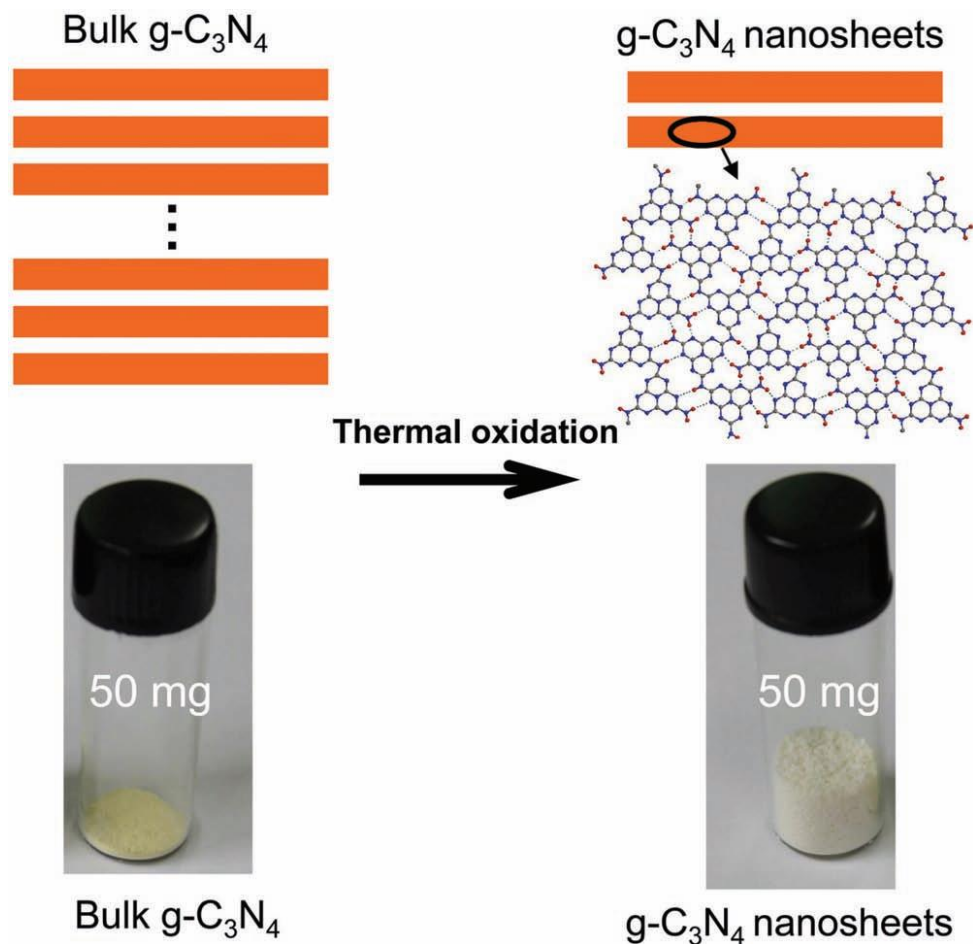
Fig.1.19 Schematic illustration of thermal oxidation of bulk CN to obtain nanosheets[60]

Compared with the liquid exfoliation strategy, thermal exfoliation is more facile and more environmentally friendly because it does not involve the toxic solutions such as aqueous ammonia, hydrochloric acid and concentrated H_2SO_4 (98%). The thermal exfoliation approach is fast, low-cost and low-pollution. However, the largest drawback of the thermal exfoliation strategy is the low-yield due to the thermal oxidation and thermal etching. For instance, Niu obtained CN nanosheets with a thickness of 2nm (about 6 to 7 layers) via the thermal exfoliation strategy (**Fig.1.19**) [60]. The synthesized CN nanosheets exhibited enhanced photocatalytic H_2 evolution under simulated solar light irradiation. The excellent photocatalytic H_2 production of the

obtained CN nanosheets was ascribed to the large specific surface area, low sheet thickness, enlarged band gap, increased electron-transport ability and prolonged lifetime of the charge carriers.

1.9.2 Template strategy
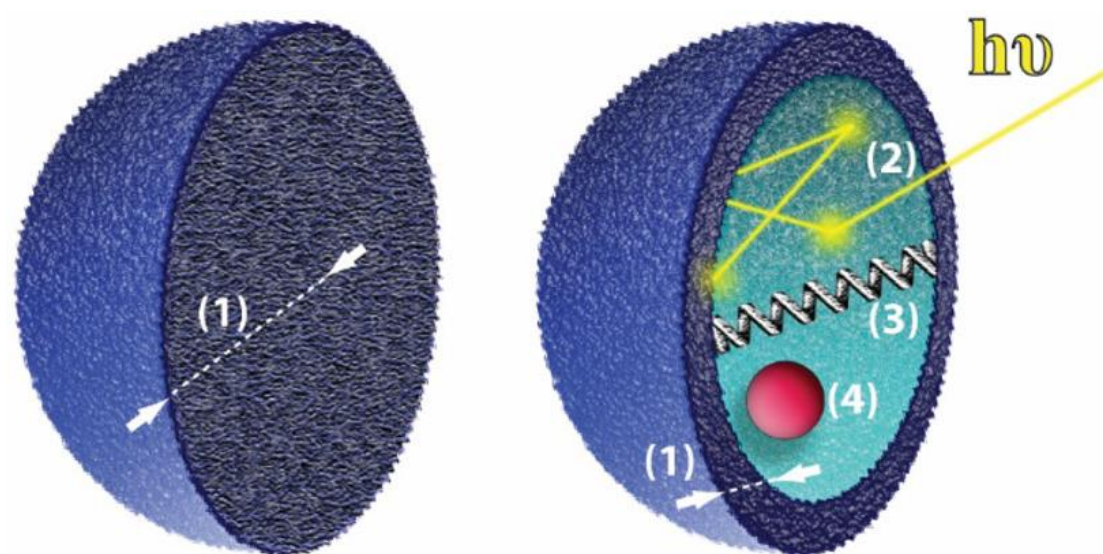
Fig.1.20 Schematic illustration for advantages of hollow nanostructured photocatalyst compared with bulk counterpart [44].

The template strategy is an effective approach to fabricate hollow or porous nanostructured CN, which can increase the specific surface areas and active sites of bulk CN [35, 44]. Moreover, the high porosity of nanostructured CN was beneficial for the mass and gas transport. Also, the voluminous void space in nanostructured CN can enhance the light absorption efficiency owing to the light trapping effect. These plentiful advantages can bring about outstanding photocatalytic performance in comparison with bulk counterpart [44]. In general, the template method is based on the use of inorganic or organic nanostructures as template，i.e., hard template and soft template (**Fig.1.20**). According to the individual situations, we can determine which one is suitable.
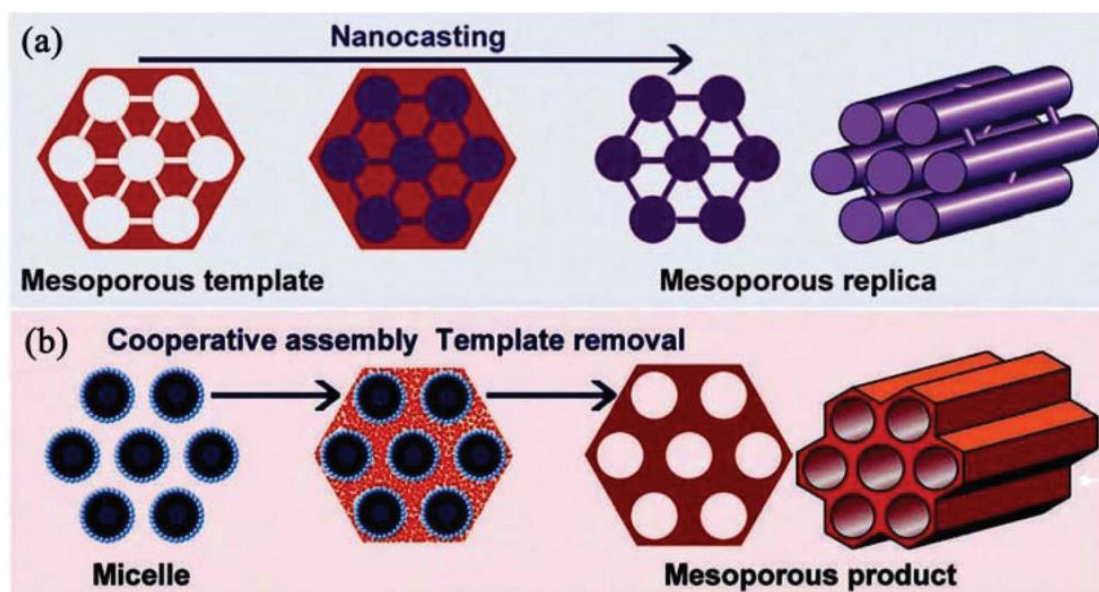
Fig.1.21 Schematic illustration for hard-template method (a) and soft-template method (b)[35].

1.9.2.1 Hard template

Hard template is a controllable and precious strategy to prepare nanostructured CN. Hard templates, in other words, solid material nano-casting, is performed as physical structure agent control the hollow or porous nanostructured CN. Up to now, a large number of hard templates have been studied. For example, Zhang et al. used the HCl treated SBA-15 silica as hard template to prepare ordered mesoporous CN (**Fig.1.21**) [61]. The obtained mesoporous CN displayed significantly enlarged specific surface area and pore volume, which were 517 m^2g^{-1} and 0.49 cm^3g^{-1}, respectively. Similarly, Sun et al reported hollow nanospheres of CN used silica based hard template (**Fig.1.23**) [62]. The hollow nanospheres of CN displayed excellent photocatalytic H_2 evolution performance due to the hollow sphere structure. However, the biggest drawback of the silica based hard template involves toxic reagent such as ammonium hydrogen difluoride (NH_4HF_2), when we remove the silica based hard templates. Recently, Zhang demonstrated that low-cost calcium carbonate ($CaCO_3$) is a promising environmentally friendly hard template (**Fig.1.24**) [63].
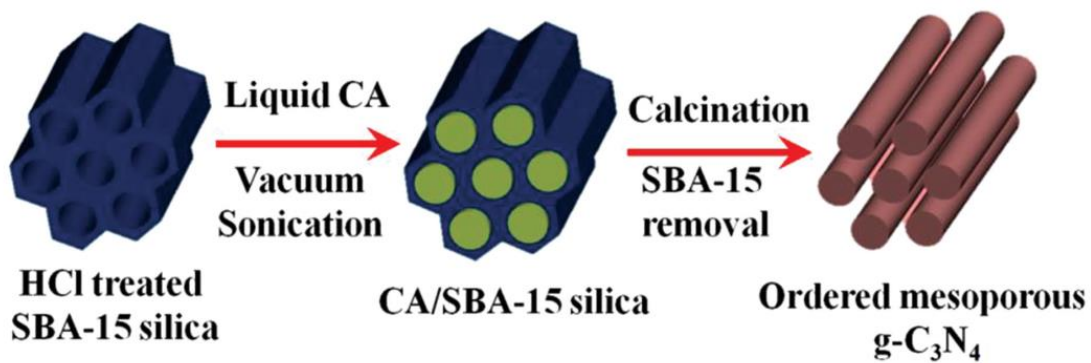
Fig.1.22 Schematic illustration for hard-template method to prepare ordered mesoporous CN using SBA-15 silica [61].
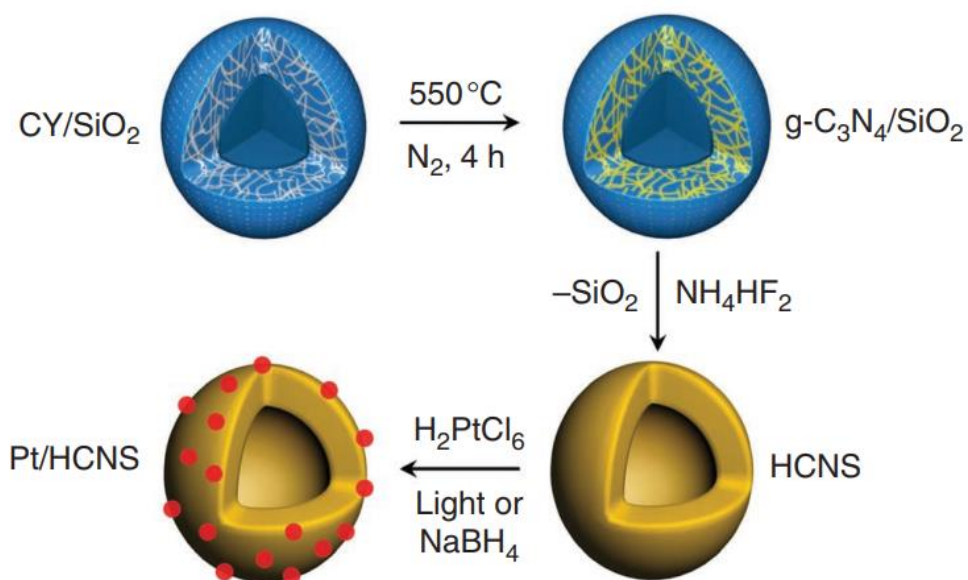
Fig.1.23 Schematic illustration for hard-template method to prepare hollow CN using SiO$_2$[62]
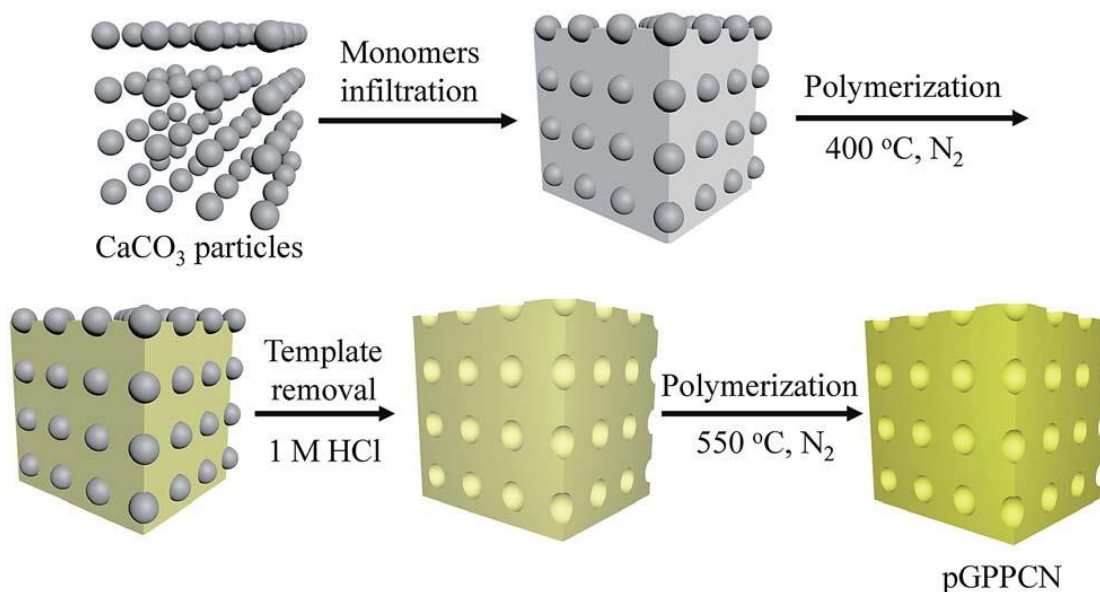
Fig.1.24 Schematic illustration for hard-template method to prepare hollow CN using SiO$_2$[63]

1.9.2.2 Soft template

Since the hard templates involve the hazardous fluoride-containing reagents, a tremendous amount of work has been done on soft template [64]. The key point of soft template is the molecular self-assembly process, which can chemically tailor the porosity and morphology of pristine CN. Wang showed that various templates, such as non-ionic surfactants and amphiphilic block polymers, could be chosen as soft templates. In addition, ionic liquids have demonstrated an effective soft template. The soft templates provide a facile and more environmentally friendly strategy to prepare nanostructured CN. It is important to point out that sulfur and NH$_4$CL also could be used to improve the specific surface areas of the bulk CN [65].

Very recently, the supramolecular preorganization has become an interesting topic to prepare the nanostructured CN. **Fig.1.25** and **Fig.1.26** showed the formation of the self-assembled structures to prepare the nanostructured CN. To some extent, the supramolecular preorganization strategy is similar to the soft template strategy. However, this strategy is based on the supramolecular interactions of CN monomers, including hydrogen bonds, Π-Π and so on.
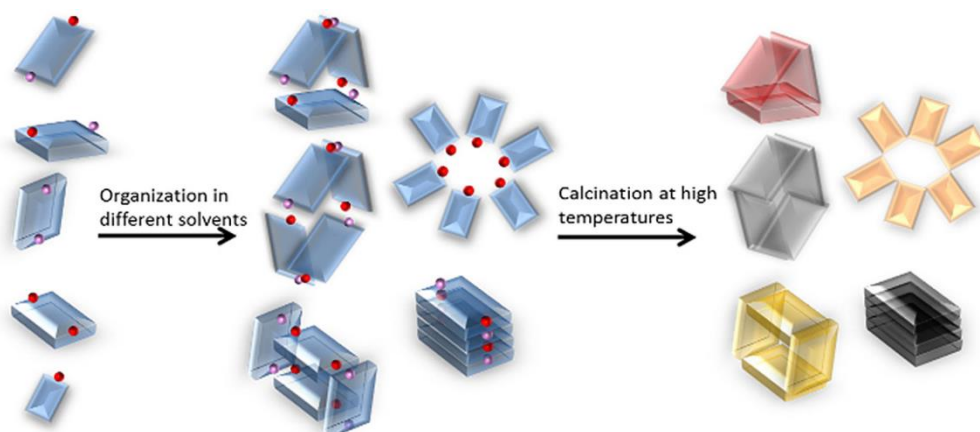
Fig.1.25 Schematic illustration for the self-assembled method to prepare different structures of CN [66].
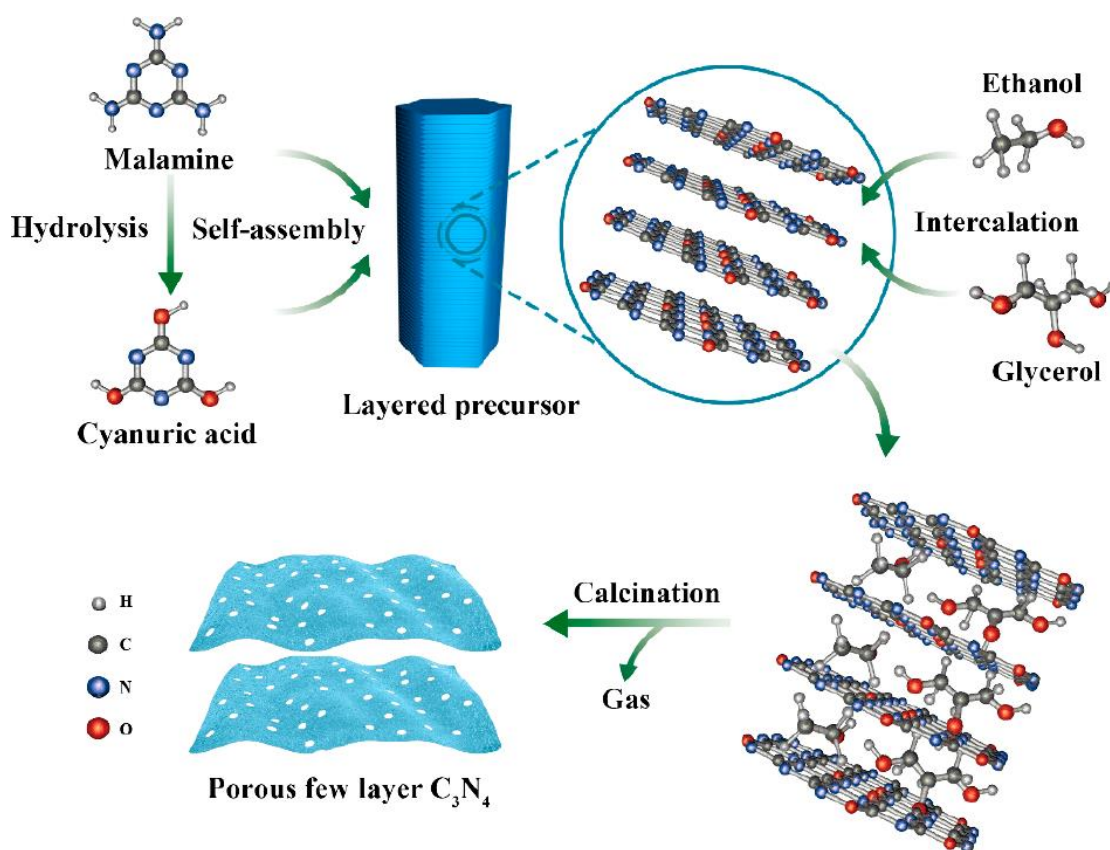
Fig.1.26 Schematic illustration for the self-assembled method to prepare few-layer structures of CN [67]

1.10 Heterostructures construction

Charge carrier transport and separation is decisive in the photocatalysis process. There are a large number of photogenerated electrons and holes suffered from the volume recombination and surface recombination (**Fig.1.27**), which result in unsatisfactory photocatalytic performance. Constructing CN-based heterostructure is an effective strategy to improve the photocatalytic performance. The spatial separation of photogenerated electron–hole pairs can be achieved through efficient charge transfer across the interface between the two semiconductors. At the same time, the CN based heterostructures can display advantages of the counterpart. In other words, the CN based heterostructures have both benefits of the two components. Up to present, two types of CN-based heterostructures have attracted much attention including traditional type-II heterostructure and all-solid-state Z-scheme heterostructures [2].
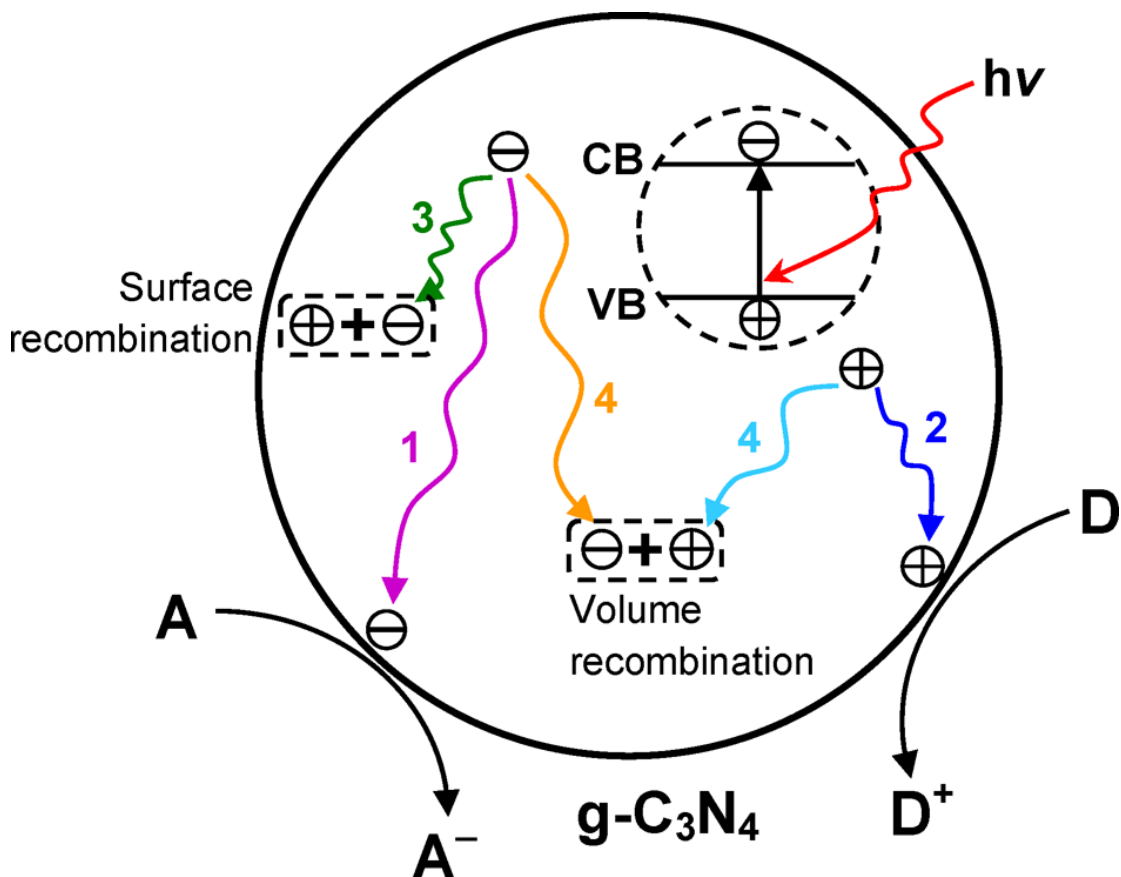
Fig.1.27 Schematic illustration for the volume recombination and surface recombination of photo-generated charge carriers in bulk CN [30].
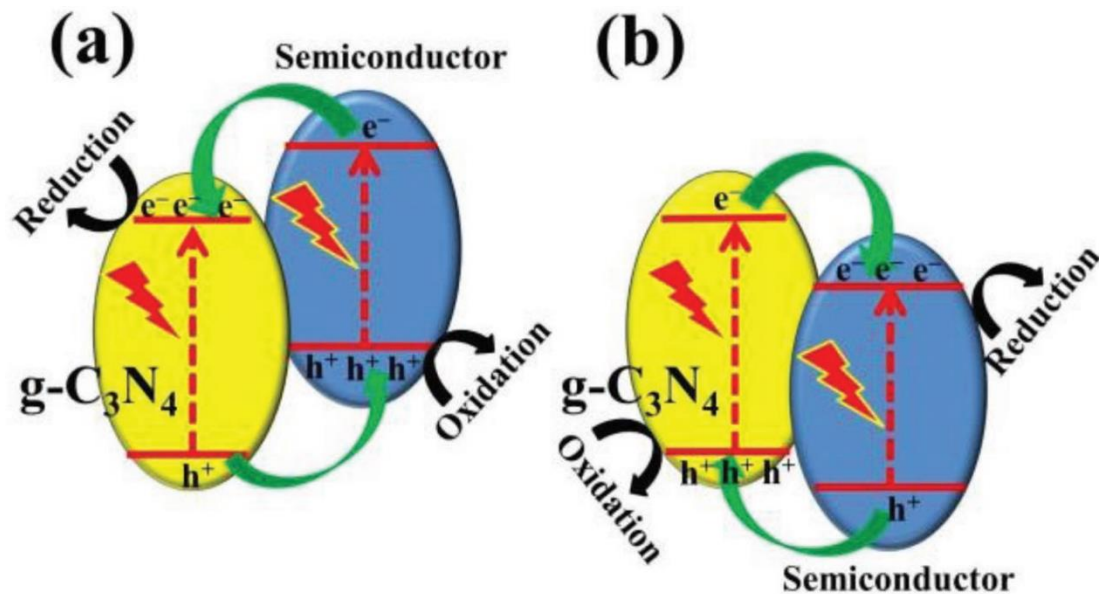
Fig.1.28 Schematic illustration for the charge transfer in the conventional type type-II heterostructure [2].

The traditional type-II heterostructure is facile construction and much progress has been made in this field (**Fig.1.28**). For example, Zhang reported that CdS/CN core-shell showed outstanding photocatalytic H_2 evolution performance (4152umol $h^{-1}g^{-1}$) (**Fig.1.29**), which was ascribed to the merits of well-matched type-II heterostructure. The obtained heterostructure could accelerate the separation of the charge carrier and reduce CdS corrosion [68]. Interestingly, Wang demonstrated that CN/S mediated CN exhibited a matched band gap and distinctly improved charge carrier separation efficiency, which resulted in the significantly enhanced photocatalytic H_2 production performance [69].
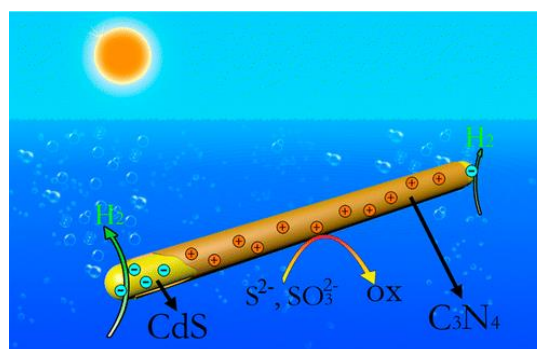
Fig.1.29 Schematic illustration for CdS/CN core-shell heterostructure [68]

Even though the traditional type-II heterostructure can improve the charge carrier separation efficiency to improve the photocatalytic performance, it sacrifices the oxidation potential energy and reduction potential energy. To overcome this drawback, the all-solid-state Z-scheme is developed inspired by the photosynthesis of plants [70]. The photosynthesis of plants consists of two isolated reactions of water oxidation and CO_2 reduction, which are linked together through the redox mediators. Thanks to the unique structure, it keeps the strong redox ability, improve the charge carrier separation efficiency and result in enhanced photocatalytic performance. **Fig.1.30 s**hows the typical all-solid-state Z-scheme heterostructure. For example, Yu made a great contribution to the preparation of all-solid-state Z-scheme heterostructure) (**Fig.1.31**) [71]. They, for the first time, reported the CN-TiO$_2$ Z-scheme heterostructure by facile calcination method. Moreover, they found that CN-TiO$_2$ Z-scheme heterostructure was largely dependent on the content of CN. To more specific, only the surface of TiO$_2$ is partially covered by the CN, and we can obtain the CN-TiO$_2$ Z-scheme heterostructure. If the content of CN was too much, we tend to fabricate the traditional type-II heterostructure.
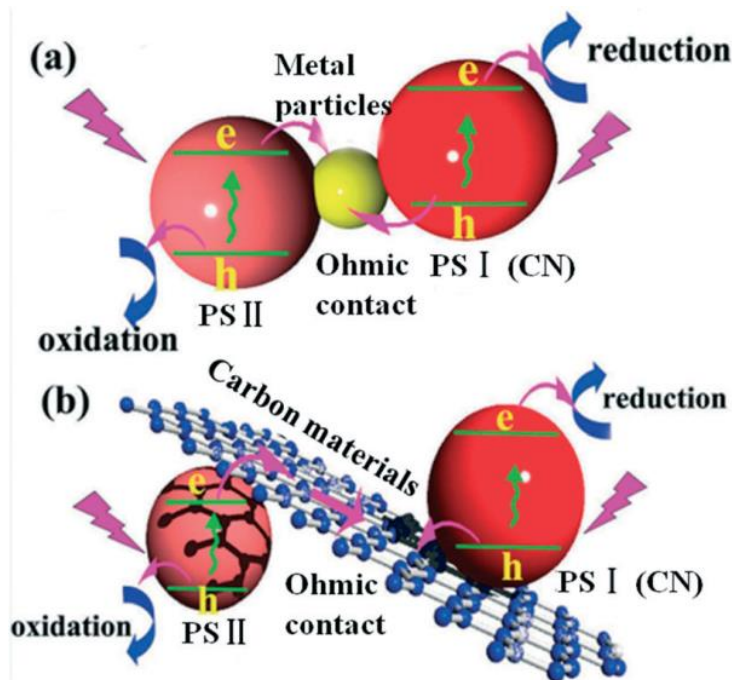
Fig.1.30 Schematic illustration for charge transfer in the all-solid-state Z-scheme heterostructure [70].
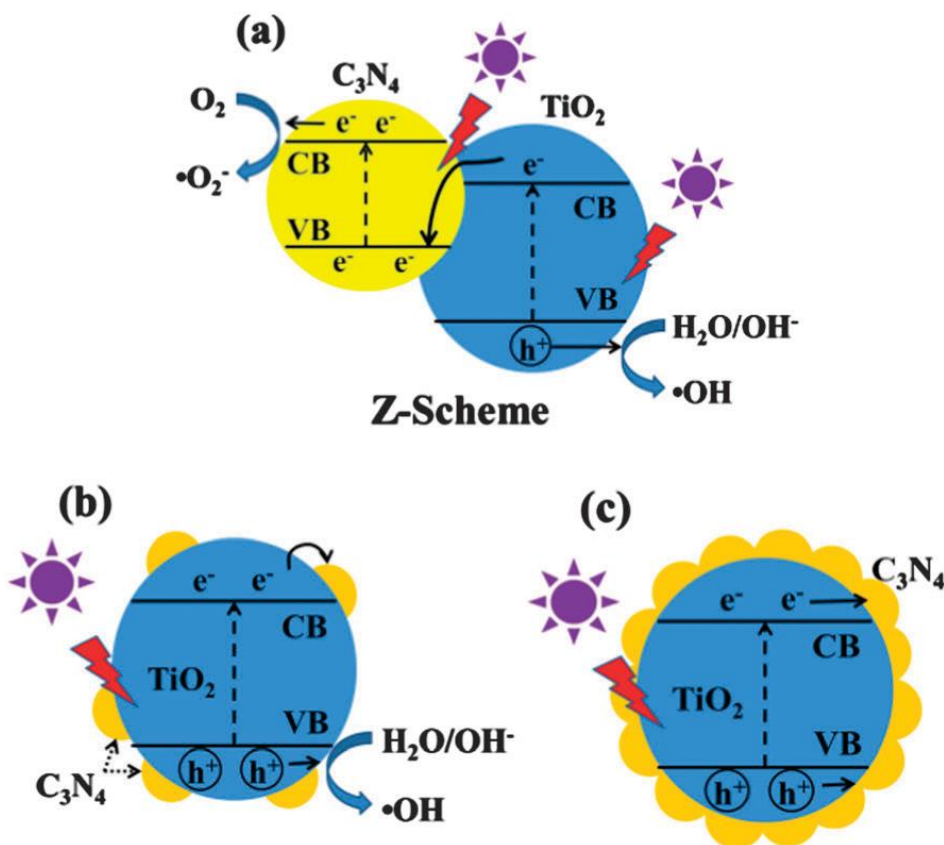
Fig.1.31 Schematic illustration for the charge and separation in the Z-scheme photocatalyts under UV light irradiation [71].

1.11 Noble metal deposition

Besides the heterostructure construction, noble metal deposition is also applied to improve the photocatalytic performance. The common noble metals are including Au, Pd，Pt and Au. Considering the high cost of the noble metals, the noble metal deposition method would increase the costs of CN based photocatalysts. Maye this is the largest shortcoming of the noble metal deposition. The noble metal deposition has some unique characteristics in comparison with other strategies. Recently, single-atom catalysts have become hot topics since Zhang reported single-atom catalysis of CO oxidation using Pt $1/FeO_x$[72]. Single atom (Au, Pd，Pt and Au) supported on CN as efficient photocatalysts for visible-light photocatalytic performance is promising to solve the energy problems and environment pollutions (**Fig.1.32**) [73-77].
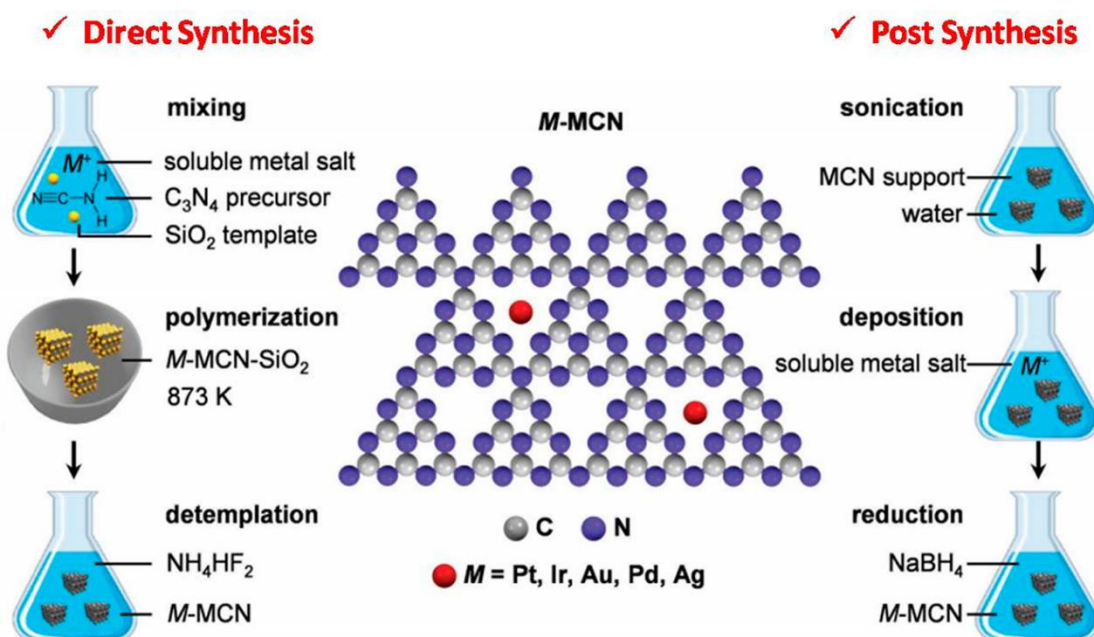
Fig.1.32 Schematic illustration for the preparation of single atom supported on CN photocatalyts [29]

1.12 Defect control

At the same time, defect control is also an effective strategy to improve the photocatalytic performance of pristine CN. Defect strategy is premature to modify the electronic structures of pristine TiO_2, which may due to the fact that the TiO_2 is the most classical and fully-studied photocatalyst [11, 78-80]. For example, the band structures and optical properties of pristine TiO_2 could be tuned by oxygen vancancies[81, 82]. The oxygen vacancies mediated TiO_2 can extend the visible-light range, enhance the charge carrier separation efficiency, improve the molecules to be adsorbed on the surface of the photocatalysts, which would result in the excellent photocatalytic performance. Inspired by the oxygen vacancies mediated TiO_2, defect strategy is used to improve the photocatalytic performance of pristine CN. For example, Wang reported the nitrogen vacancies mediated CN microtubes via a simple and green hydrothermal process [83]. The nitrogen vacancies mediated CN microtubes displayed significantly enhanced NO removal performance due to the enlarged specific surface areas and the curial roles of nitrogen vacancies. As shown in **Fig.1.33,** the nitrogen vacancies mediated CN was beneficial for the NO and O_2 adsorption, which contributed

to attending the surface reactions. The enhanced surface reactions resulted in the enhanced photocatalytic NO removal performance in comparison with pristine CN under visible-light irradiation.
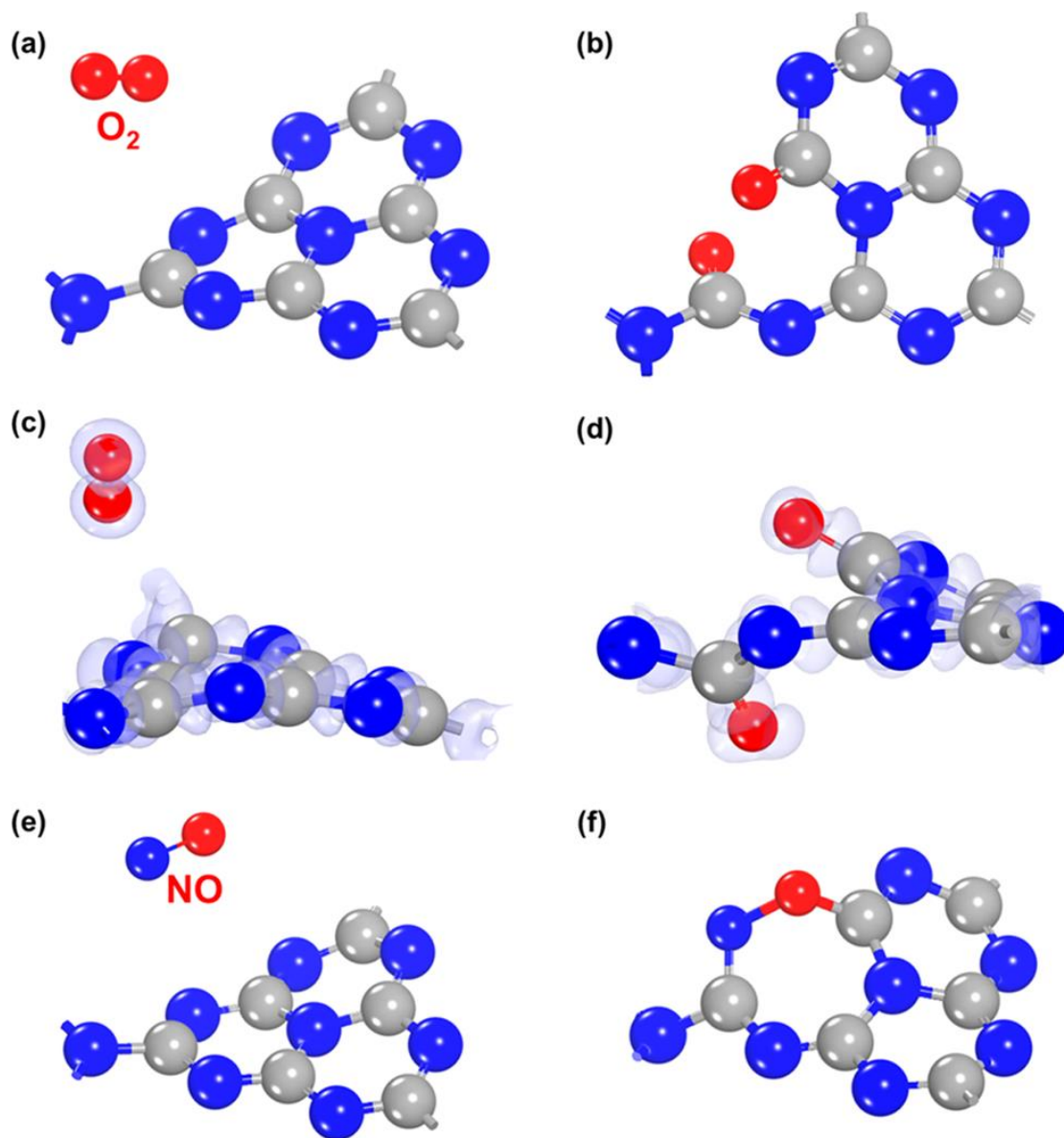
Fig.1.33 Schematic illustration for the nitrogen vacancies in CN photocatalysts for the enhanced adsorption behaviors [83]

1.13 Research objectives

As is mentioned above, photocatalysis is considering as a green technology to solve the NO pollution problem. We use a self-made instrument to measure the

photocatalytic performance of the CN-based photocatalysts. The self-made instrument is showed in **Fig.1.34.**

The NO removal percentage (%) was defined as follows:

$$NO(\%) = \frac{C_0 - C}{C_0} \times 100$$

Where C_0 and C were the concentrations of NO in the feed and outlet streams after 10 minutes of photocatalytic activity.
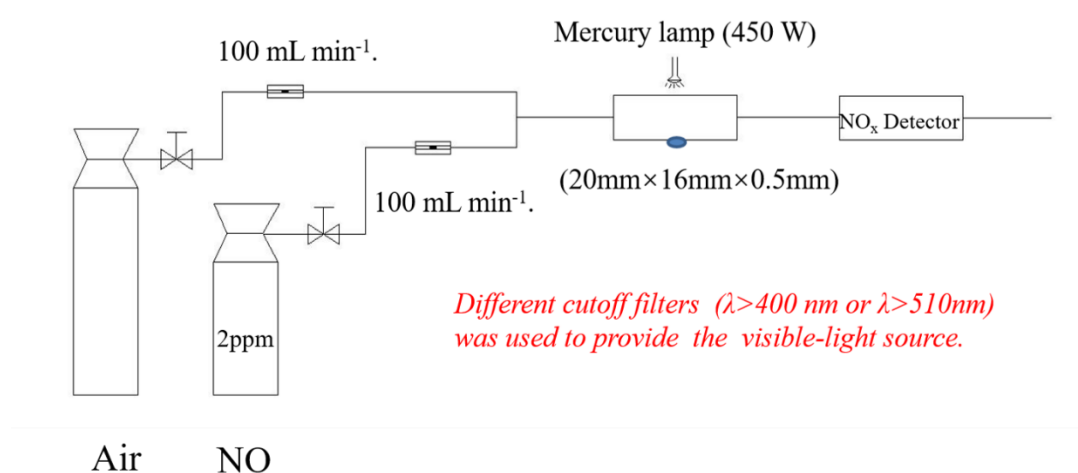
Fig.1.34 The instrument for the photocatalytic NO removal test in the dissertation.

The metal-free CN is believed to the most promising photocatalyst because of its advantages such as excellent electrical and optical properties, high surface-to-volume ratio, facile synthesis, low-cost and so on. However, the pristine CN, i.e., bulk CN suffers from a series if shortcomings are owing to high-temperature solid reactions. It displays low response to visible light, rapid charge carrier recombination, small specific surface area and few active sites, which results in deficient solar light efficiency and unsatisfactory photocatalytic performance. Therefore, inspired by the previous research, we propose some methods in the doctoral dissertation to improve the photocatalytic NO removal performance. The related strategies are as follows:

(I). Morphology control

Bulk CN was exfoliated into nanosheets to increase the specific surface area and active sites via facile post-thermal treatment. At the same time, the electronic structure

of bulk CN was optimized during the calcination process. The related research work is entitled "High yield post-thermal treatment of bulk graphitic carbon nitride with tunable band structure for enhanced deNOx photocatalysis" (Chapter 2).

(II). Defect engineering

The defect engineering involves two works. The first one is about the preparation of carbon vacancies and hydroxyls co-modified CN via the green hydrothermal method. The related research work is entitled "Carbon vacancies and hydroxyls in graphitic carbon nitride: promoted photocatalytic NO removal activity and mechanism" (Chapter 3.1).

The second one is about improving the crystallinity of pristine CN via a modified molten salt method. The related research work is entitled "Synthesis of crystalline carbon nitride with enhanced photocatalytic NO removal performance: an experimental and DFT theoretical study" (Chapter 3.2).

(III). Carbonaceous/CN hybrid

CN/rGO nanocomposites are fabricated via alkali-assisted hydrothermal process. The related research work is entitled "Alkali-assisted hydrothermal preparation of g-C_3N_4/rGO nanocomposites with highly enhanced photocatalytic NOx decomposition activity" (Chapter 4.1).

(IV). Heterostructure construction (oxygen vacancies mediated TiO_2)

Our target is to prepare CN/TiO_2 heterostructure via calcination assisted hydrothermal process to improve the photocatalytic NO removal performance. Interestingly, we find an intrinsic carbon-doping induced strategy to prepare oxygen vacancies mediated TiO_2. The first related research work is entitled "Intrinsic carbon-doping induced synthesis of oxygen vacancies-mediated TiO_2 nanocrystals: enhanced photocatalytic NO removal performance and mechanism" (Chapter 4.2.1). The second related research work is entitled "Reductant-free synthesis of oxygen vacancies-mediated TiO_2 nanocrystals with enhanced photocatalytic NO removal performance: an experimental and DFT study" (Chapter 4.2.2).

1.14 References

[1] H. Li, J. Li, Z. Ai, F. Jia, L. Zhang, Oxygen vacancy-mediated photocatalysis of BiOCl: reactivity, selectivity, and perspectives, Angewandte Chemie International Edition, 57 (2018) 122-138.

[2] J. Fu, J. Yu, C. Jiang, B. Cheng, g-C_3N_4-Based Heterostructured Photocatalysts, Advanced Energy Materials, 8 (2018) 1701503.

[3] A. Nikokavoura, C. Trapalis, Graphene and g-C_3N_4 based photocatalysts for NO_x removal: a review, Applied Surface Science, 430 (2018) 18-52.

[4] Y. Boyjoo, H. Sun, J. Liu, V.K. Pareek, S. Wang, A review on photocatalysis for air treatment: from catalyst development to reactor design, Chemical Engineering Journal, 310 (2017) 537-559.

[5] Y. Zou, Y. Xie, S. Yu, L. Chen, W. Cui, F. Dong, Y. Zhou, SnO_2 quantum dots anchored on g-C3N4 for enhanced visible-light photocatalytic removal of NO and toxic NO2 inhibition, Applied Surface Science, 496 (2019) 143630.

[6] G. Zhu, S. Li, J. Gao, F. Zhang, C. Liu, Q. Wang, M. Hojamberdiev, Constructing a 2D/2D $Bi_2O_2CO_3$/$Bi_4O_5Br_2$ heterostructure as a direct Z-scheme photocatalyst with enhanced photocatalytic activity for NOx removal, Applied Surface Science, 493 (2019) 913-925.

[7] L. Zhao, C. Li, S. Li, X. Du, J. Zhang, Y. Huang, Simultaneous removal of Hg0 and NO in simulated flue gas on transition metal oxide M'(M'= Fe_2O_3, MnO_2, and WO_3) doping on V_2O_5/ZrO_2-CeO_2 catalysts, Applied Surface Science, 483 (2019) 260-269.

[8] S. Shen, Y. Liu, D. Zhai, G. Qian, Electroplating sludge-derived spinel catalysts for NO removal via NH3 selective catalysis reduction, Applied Surface Science, 528 (2020) 146969.

[9] X. Wu, S. Yin, Q. Dong, C. Guo, H. Li, T. Kimura, T. Sato, Synthesis of high visible light active carbon doped TiO_2 photocatalyst by a facile calcination assisted solvothermal method, Applied Catalysis B: Environmental, 142 (2013) 450-457.

[10] A. Fujishima, K. Honda, Electrochemical photolysis of water at a semiconductor electrode, nature, 238 (1972) 37.

[11] Y. Huang, Y. Yu, Y. Yu, B. Zhang, Oxygen Vacancy Engineering in Photocatalysis, Solar RRL, (2020) 2000037.

[12] Y. Nam, J.H. Lim, K.C. Ko, J.Y. Lee, Photocatalytic activity of TiO_2 nanoparticles: a theoretical aspect, Journal of Materials Chemistry A, 7 (2019) 13833-13859.

[13] A. Jodlowski, D. Rodríguez-Padrón, R. Luque, G. de Miguel, Alternative perovskites for photovoltaics, Advanced Energy Materials, 8 (2018) 1703120.

[14] X. He, C. Zhang, Recent advances in structure design for enhancing photocatalysis, Journal of Materials Science, 54 (2019) 8831-8851.

[15] M. Pelaez, N.T. Nolan, S.C. Pillai, M.K. Seery, P. Falaras, A.G. Kontos, P.S.M. Dunlop, J.W.J. Hamilton, J.A. Byrne, K. O'Shea, A review on the visible light active titanium dioxide photocatalysts for environmental applications ☆, Applied Catalysis B Environmental, 125 (2012) 331-349.

[16] J. Wen, J. Xie, X. Chen, X. Li, A review on g-C_3N_4-based photocatalysts, Applied Surface Science, 391 (2017) 72-123.

[17] Y.P. Zhu, M. Li, Y.L. Liu, T.Z. Ren, Z.Y. Yuan, Carbon-Doped ZnO Hybridized Homogeneously with Graphitic Carbon Nitride Nanocomposites for Photocatalysis, Journal of Physical Chemistry C, 118 (2014) 10963-10971.

[18] J. Wu, B. Liu, Z. Ren, M. Ni, C. Li, Y. Gong, W. Qin, Y. Huang, C.Q. Sun, X. Liu, CuS/RGO hybrid photocatalyst for full solar spectrum photoreduction from UV/Vis to Near-Infrared light, Journal of Colloid and Interface Science, (2017).

[19] A. Tiwari, N. Vamsi Krishna, L. Giribabu, U. Pal, Hierarchical Porous TiO2 Embedded Unsymmetrical Zn-Phthalocyanine Sensitizer for Visible-Light-Induced Photocatalytic H2 Production, The Journal of Physical Chemistry C, (2017).

[20] M. Yan, G. Li, C. Guo, W. Guo, D. Ding, S. Zhang, S. Liu, WO $_{3-x}$ sensitized TiO $_2$ spheres with full-spectrum-driven photocatalytic activities from UV to near infrared, Nanoscale, 8 (2016) 17828-17835.

[21] S. Klosek, D. Raftery, Visible light driven V-doped TiO_2 photocatalyst and its photooxidation of ethanol, The Journal of Physical Chemistry B, 105 (2001) 2815-2819.

[22] S.M.A. Hossain, M.E. Ali, S.B. Abd Hamid, Synergizing TiO2 Surface to Enhance

Photocatalysis: A Green Technology for Clean and Safe Environment - A Review, Advanced Materials Research, 1109 (2015) 300-303.

[23] K. Nakata, A. Fujishima, TiO$_2$ photocatalysis: Design and applications, Journal of Photochemistry & Photobiology C Photochemistry Reviews, 13 (2012) 169-189.

[24] X. Chen, L. Liu, F. Huang, Black titanium dioxide (TiO$_2$) nanomaterials, Chemical Society Reviews, 44 (2015) 1861-1885.

[25] C. Di Valentin, G. Pacchioni, A. Selloni, Theory of carbon doping of titanium dioxide, Chemistry of Materials, 17 (2005) 6656-6665.

[26] C. Tan, X. Cao, X.J. Wu, Q. He, J. Yang, X. Zhang, J. Chen, W. Zhao, S. Han, G.H. Nam, Recent Advances in Ultrathin Two-Dimensional Nanomaterials, Chemical Reviews, 117 (2017) 6225.

[27] J.H. Han, M. Kwak, Y. Kim, J. Cheon, Recent advances in the solution-based preparation of two-dimensional layered transition metal chalcogenide nanostructures, Chemical reviews, 118 (2018) 6151-6188.

[28] H. Jin, C. Guo, X. Liu, J. Liu, A. Vasileff, Y. Jiao, Y. Zheng, S.-Z. Qiao, Emerging Two-Dimensional Nanomaterials for Electrocatalysis, Chemical Reviews, (2018).

[29] Y. Wang, J. Mao, X. Meng, L. Yu, D. Deng, X. Bao, Catalysis with two-dimensional materials confining single atoms: concept, design, and applications, Chemical reviews, 119 (2018) 1806-1854.

[30] W.J. Ong, L.L. Tan, H.N. Yun, S.T. Yong, S.P. Chai, Graphitic Carbon Nitride (g-C3N4)-Based Photocatalysts for Artificial Photosynthesis and Environmental Remediation: Are We a Step Closer To Achieving Sustainability?, Chemical Reviews, 116 (2016) 7159-7329.

[31] X. Wang, K. Maeda, A. Thomas, K. Takanabe, G. Xin, J.M. Carlsson, K. Domen, M. Antonietti, A metal-free polymeric photocatalyst for hydrogen production from water under visible light, Nature Materials, 8 (2009) 76-80.

[32] L. Lin, H. Ou, Y. Zhang, X. Wang, Tri-s-triazine-based crystalline graphitic carbon nitrides for highly efficient hydrogen evolution photocatalysis, ACS Catalysis, 6 (2016) 3921-3931.

[33] H. Ou, L. Lin, Y. Zheng, P. Yang, Y. Fang, X. Wang, Tri-s-triazine-based

crystalline carbon nitride nanosheets for an improved hydrogen evolution, Advanced Materials, 29 (2017) 1700008.

[34] G. Algara-Siller, N. Severin, S.Y. Chong, T. Björkman, R.G. Palgrave, A. Laybourn, M. Antonietti, Y.Z. Khimyak, A.V. Krasheninnikov, J.P. Rabe, Triazine-based graphitic carbon nitride: a two-dimensional semiconductor, Angewandte Chemie International Edition, 53 (2014) 7450-7455.

[35] S. Sun, S. Liang, Recent advances in functional mesoporous graphitic carbon nitride (mpg-C_3N_4) polymers, Nanoscale, 9 (2017) 10544-10578.

[36] M. Liu, S. Wageh, A.A. Al-Ghamdi, P. Xia, B. Cheng, L. Zhang, J. Yu, Quenching induced hierarchical 3D porous g-C_3N_4 with enhanced photocatalytic CO_2 reduction activity, Chemical Communications, 55 (2019) 14023-14026.

[37] Y.-J. Yuan, Y. Yang, Z. Li, D. Chen, S. Wu, G. Fang, W. Bai, M. Ding, L.-X. Yang, D.-P. Cao, Promoting Charge Separation in g-C_3N_4/Graphene/MoS_2 Photocatalysts by Two-Dimensional Nanojunction for Enhanced Photocatalytic H_2 Production, ACS Applied Energy Materials, (2018).

[38] S. Cao, J. Low, J. Yu, M. Jaroniec, Polymeric photocatalysts based on graphitic carbon nitride, Advanced Materials, 27 (2015) 2150-2176.

[39] Y. Wang, X. Wang, M. Antonietti, Polymeric graphitic carbon nitride as a heterogeneous organocatalyst: from photochemistry to multipurpose catalysis to sustainable chemistry, Angewandte Chemie International Edition, 51 (2012) 68-89.

[40] L. Lin, Z. Yu, X. Wang, Crystalline carbon nitride semiconductors for photocatalytic water splitting, Angewandte Chemie, 131 (2019) 6225-6236.

[41] A. Thomas, A. Fischer, F. Goettmann, M. Antonietti, J.-O. Müller, R. Schlögl, J.M. Carlsson, Graphitic carbon nitride materials: variation of structure and morphology and their use as metal-free catalysts, Journal of Materials Chemistry, 18 (2008) 4893-4908.

[42] J. Chen, S. Shen, P. Guo, P. Wu, L. Guo, Spatial engineering of photo-active sites on g-C_3N_4 for efficient solar hydrogen generation, Journal of Materials Chemistry A, 2 (2014) 4605-4612.

[43] Y. Li, R. Jin, X. Fang, Y. Yang, M. Yang, X. Liu, Y. Xing, S. Song, In situ loading of Ag_2WO_4 on ultrathin g-C_3N_4 nanosheets with highly enhanced photocatalytic

performance, Journal of Hazardous Materials, 313 (2016) 219-228.

[44] G. Prieto, H. Tüysüz, N. Duyckaerts, J. Knossalla, G.-H. Wang, F. Schüth, Hollow nano-and microstructures as catalysts, Chemical Reviews, 116 (2016) 14056-14119.

[45] D. Liu, D. Chen, N. Li, Q. Xu, H. Li, J. He, J.-M. Lu, Surface engineering of g-C3N4 by stacked oxygen vacancies-rich BiOBr sheets for boosting photocatalytic performance, Angewandte Chemie, (2019).

[46] G. Zhang, G. Li, T. Heil, S. Zafeiratos, F. Lai, A. Savateev, M. Antonietti, X. Wang, Tailoring the Grain Boundary Chemistry of Polymeric Carbon Nitride for Enhanced Solar Hydrogen Production and CO_2 Reduction, Angewandte Chemie, 131 (2019) 3471-3475.

[47] H. Yu, R. Shi, Y. Zhao, T. Bian, Y. Zhao, C. Zhou, G.I. Waterhouse, L.Z. Wu, C.H. Tung, T. Zhang, Alkali-Assisted Synthesis of Nitrogen Deficient Graphitic Carbon Nitride with Tunable Band Structures for Efficient Visible-Light-Driven Hydrogen Evolution, Advanced Materials, 29 (2017).

[48] S. Yan, Z. Li, Z. Zou, Photodegradation performance of g-C_3N_4 fabricated by directly heating melamine, Langmuir, 25 (2009) 10397-10401.

[49] G. Zhang, J. Zhang, M. Zhang, X. Wang, Polycondensation of thiourea into carbon nitride semiconductors as visible light photocatalysts, Journal of Materials Chemistry, 22 (2012) 8083-8091.

[50] X. Wang, X. Chen, A. Thomas, X. Fu, M. Antonietti, Metal-containing carbon nitride compounds: a new functional organic–metal hybrid material, Advanced Materials, 21 (2009) 1609-1612.

[51] Z. Ding, X. Chen, M. Antonietti, X. Wang, Synthesis of transition metal-modified carbon nitride polymers for selective hydrocarbon oxidation, ChemSusChem, 4 (2011) 274-281.

[52] H. Pan, Y.-W. Zhang, V.B. Shenoy, H. Gao, Ab initio study on a novel photocatalyst: functionalized graphitic carbon nitride nanotube, ACS Catalysis, 1 (2011) 99-104.

[53] T. Xiong, W. Cen, Y. Zhang, F. Dong, Bridging the g-C_3N_4 interlayers for enhanced photocatalysis, ACS Catalysis, 6 (2016) 2462-2472.

[54] M. Zhang, X. Bai, D. Liu, J. Wang, Y. Zhu, Enhanced catalytic activity of potassium-doped graphitic carbon nitride induced by lower valence position, Applied Catalysis B: Environmental, 164 (2015) 77-81.

[55] A.M. Dimiev, J.M. Tour, Mechanism of graphene oxide formation, ACS nano, 8 (2014) 3060-3068.

[56] G. Williams, B. Seger, P.V. Kamat, TiO_2-graphene nanocomposites. UV-assisted photocatalytic reduction of graphene oxide, ACSNano, 2 (2008) 1487.

[57] H. Zhang, X. Lv, Y. Li, Y. Wang, J. Li, P25-Graphene Composite as a High Performance Photocatalyst, ACSNano, 4 (2010) 380.

[58] X. Zhang, X. Xie, H. Wang, J. Zhang, B. Pan, Y. Xie, Enhanced photoresponsive ultrathin graphitic-phase C_3N_4 nanosheets for bioimaging, Journal of the American Chemical Society, 135 (2013) 18-21.

[59] J. Xu, L. Zhang, R. Shi, Y. Zhu, Chemical exfoliation of graphitic carbon nitride for efficient heterogeneous photocatalysis, Journal of Materials Chemistry A, 1 (2013) 14766-14772.

[60] P. Niu, L. Zhang, G. Liu, H.M. Cheng, Graphene-like carbon nitride nanosheets for improved photocatalytic activities, Advanced Functional Materials, 22 (2012) 4763-4770.

[61] J. Zhang, F. Guo, X. Wang, An optimized and general synthetic strategy for fabrication of polymeric carbon nitride nanoarchitectures, Advanced Functional Materials, 23 (2013) 3008-3014.

[62] J. Sun, J. Zhang, M. Zhang, M. Antonietti, X. Fu, X. Wang, Bioinspired hollow semiconductor nanospheres as photosynthetic nanoparticles, Nature Communications, 3 (2012) 1139.

[63] J. Wang, C. Zhang, Y. Shen, Z. Zhou, J. Yu, Y. Li, W. Wei, S. Liu, Y. Zhang, Environment-friendly preparation of porous graphite-phase polymeric carbon nitride using calcium carbonate as templates, and enhanced photoelectrochemical activity, Journal of Materials Chemistry A, 3 (2015) 5126-5131.

[64] Z. Yang, Y. Zhang, Z. Schnepp, Soft and hard templating of graphitic carbon nitride, Journal of Materials Chemistry A, 3 (2015) 14081-14092.

[65] F. He, G. Chen, Y. Yu, Y. Zhou, Y. Zheng, S. Hao, The sulfur-bubble template-mediated synthesis of uniform porous g-C$_3$N$_4$ with superior photocatalytic performance, Chemical Communications, 51 (2015) 425-427.

[66] J. Barrio, M. Shalom, Rational Design of Carbon Nitride Materials by Supramolecular Preorganization of Monomers, ChemCatChem, 10 (2018) 5573-5586.

[67] Y. Xiao, G. Tian, W. Li, Y. Xie, B. Jiang, C. Tian, D. Zhao, H. Fu, Molecule self-assembly synthesis of porous few-layer carbon nitride for highly efficient photoredox catalysis, Journal of the American Chemical Society, (2019).

[68] J. Zhang, Y. Wang, J. Jin, J. Zhang, Z. Lin, F. Huang, J. Yu, Efficient visible-light photocatalytic hydrogen evolution and enhanced photostability of core/shell CdS/g-C3N4 nanowires, ACS Applied Materials & Interfaces, 5 (2013) 10317-10324.

[69] J. Zhang, M. Zhang, R.Q. Sun, X. Wang, A facile band alignment of polymeric carbon nitride semiconductors to construct isotype heterojunctions, Angewandte Chemie International Edition, 51 (2012) 10145-10149.

[70] L. Jiang, X. Yuan, G. Zeng, J. Liang, Z. Wu, H. Wang, Construction of an all-solid-state Z-scheme photocatalyst based on graphite carbon nitride and its enhancement to catalytic activity, Environmental Science: Nano, 5 (2018) 599-615.

[71] J. Yu, S. Wang, J. Low, W. Xiao, Enhanced photocatalytic performance of direct Z-scheme g-C$_3$N$_4$-TiO$_2$ photocatalysts for the decomposition of formaldehyde in air, Physical Chemistry Chemical Physics, 15 (2013) 16883-16890.

[72] B. Qiao, A. Wang, X. Yang, L.F. Allard, Z. Jiang, Y. Cui, J. Liu, J. Li, T. Zhang, Single-atom catalysis of CO oxidation using Pt 1/FeO$_x$, Nature Chemistry, 3 (2011) 634-641.

[73] J. Wang, Z. Li, Y. Wu, Y. Li, Fabrication of Single-Atom Catalysts with Precise Structure and High Metal Loading, Advanced Materials, 30 (2018) 1801649.

[74] H. Jeong, S. Shin, H. Lee, Heterogeneous Atomic Catalysts Overcoming the Limitations of Single-Atom Catalysts, ACS nano, (2020).

[75] B. Lu, Q. Liu, S. Chen, Electrocatalysis of Single Atom Sites: Impacts of Atomic Coordination, ACS Catalysis, (2020).

[76] X.-F. Yang, A. Wang, B. Qiao, J. Li, J. Liu, T. Zhang, Single-atom catalysts: a

new frontier in heterogeneous catalysis, Accounts of Chemical Research, 46 (2013) 1740-1748.

[77] J. Li, M.F. Stephanopoulos, Y. Xia, Introduction: Heterogeneous Single-Atom Catalysis, ACS Publications, 2020.

[78] W. Auwärter, Hexagonal boron nitride monolayers on metal supports: Versatile templates for atoms, molecules and nanostructures, Surface Science Reports, 74 (2019) 1-95.

[79] B.J. Morgan, G.W. Watson, A DFT+ U description of oxygen vacancies at the TiO_2 rutile (1 1 0) surface, Surface Science, 601 (2007) 5034-5041.

[80] L. Ran, J. Hou, S. Cao, Z. Li, Y. Zhang, Y. Wu, B. Zhang, P. Zhai, L. Sun, Defect engineering of photocatalysts for solar energy conversion, Solar RRL, 4 (2020) 1900487.

[81] X. Chen, L. Liu, P.Y. Yu, S.S. Mao, Increasing solar absorption for photocatalysis with black hydrogenated titanium dioxide nanocrystals, Science, 331 (2011) 746-750.

[82] G. Wang, Y. Ling, Y. Li, Oxygen-deficient metal oxide nanostructures for photoelectrochemical water oxidation and other applications, Nanoscale, 4 (2012) 6682-6691.

[83] Z. Wang, Y. Huang, M. Chen, X. Shi, Y. Zhang, J.-j. Cao, W. Ho, S.C. Lee, The Roles of N-vacancies over Porous $g-C_3N_4$ Microtubes during Photocatalytic NO_x Removal, ACS Applied Materials & Interfaces, (2019).

Chapter 2 High yield post-thermal treatment of bulk graphitic carbon nitride with tunable band structure for enhanced deNO$_x$ photocatalysis

2.1 Introduction

Energy crisis and environmental problem are two major challenges in the word Air pollution such as NO$_x$, SO$_2$ and CO, has become a serious environmental problem due to the combustion of fossil fuels and industrial processes [4, 5]. Recently, semiconductor photocatalysis has been regarded as a green chemistry technology to dispose of the hazardous gas [6, 7]. Graphitic carbon nitride (CN) is considered as the most promising photocatalyst owing to its visible-light activity, the facile synthesis, low cost, high thermal and chemical stability, and nontoxicity [8]. However, the pristine CN suffers from high photogenerated charge carrier recombination and low specific surface area, resulting in low photocatalytic activity [9]. With the industrial development and social progress, the environmental pollution and energy shortage have become the most serious issues in the world.

Even though the bulk CN exhibits a small surface area, the theoretical specific surface area of monolayer CN is very large [10]. In 2012, Niu et al. first reported the thermal oxidation etching of bulk CN in air to obtain CN nanosheets [11], which was simple and environmentally friendly. However, the yield of CN nanosheets was very low (6%), which cannot satisfy the requirements of the practical applications. Recently, Niu et al. reported the photocatalytic activity of pristine CN could be significantly enhanced via thermal treatment in H$_2$ [12]. Yang et al. reported high activity CN nanosheets were fabricated by a simple ammonia etching treatment [13]. These results demonstrating that the high temperature may play more important role than the atmosphere during the thermal treatment. Motivated by these developments, the research about thermal treatment to improve the photocatalytic activity of pristine CN could be further developed.

In the present work, we demonstrated that bulk CN could be easily exfoliated into nanosheets via post-thermal treatment in air. Totally different from Niu et al. reported thermal oxidation etching of bulk CN [11], which obviously resulted in very low yield, here we reported the very high yield of CN nanosheets could be realized, even higher than that of reported liquid exfoliation [14]. Unexpectedly, the band structure of CN nanosheets were also changed after post-thermal treatment. Due to the large specific surface areas and optimal band structure, the CN nanosheets displayed excellent photocatalytic oxidation of NO_x activity compared to that of bulk CN under visible light. Moreover, the parameters of temperature, time and dosage on the yield were systematically investigated. This work might provide new insight into the thermal treatment of pristine CN for improved visible-light photocatalytic activity.

2.2 Experiment

Bulk CN was synthesized by melamine pyrolysis according to previous literature [15]. CN nanosheets were prepared as follows: l g of bulk CN was placed in an alumina boat (103× 40×21mm) without a cover and heated to a certain temperature (i.e., 450, 480, 500, 520, or 550 ˚C) for 2 h with heating rate of 5 ˚C min^{-1} in a muffle furnace in air and cooled to room temperature naturally. The as-prepared products were designated as CN-450, CN-480, CN-500, CN-520 and CN-550, respectively. In comparison, bulk CN was also calcined at 500 ˚C for 2 h in argon atmosphere tube furnace and the obtained sample was index as CN-500-Ar. To study the parameters of thermal treatment time and dosage, 1g of bulk CN was calcined at 500 ˚C for designed time (i.e., 0.5, 1, 2, 3, or 4 h) by the similar process and a serious of bulk CN (i.e., 0.25, 0.5, 1, 2, or 3g) was calcined at 500 ˚C for 2 h.

Powder X-ray diffraction (XRD) pattern was carried out over a Bruker AXS D2 Phaser diffractometer equipped with Cu Kα source. Fourier transformed infrared (FTIR) spectra were conducted on a JASCO FTIR-660D-ATR spectrometer. UV-vis diffuse reflectance spectra (DRS) were recorded on a JASCO UV-vis spectrophotometer. Electron paramagnetic resonance (EPR) spectra were performed on Bruker E580 EPR

spectrometer at room temperature. Photoluminescence (PL) data were measured using a JASCO FP-8500 spectrofluorometer. X-ray photoelectron spectroscopy (XPS) analysis was conducted on a ULVAC PHI5600 machine. The Brunauer-Emmett-Teller (BET) specific surface areas of the samples were determined on a NOVA4200e, Quantachrome Instruments. Scanning emission microscopy (SEM) investigation was performed using a JSM-7800F microscope. Transmission electron microscopy (TEM) analysis was obtained on a JEM-2000 EXII microscope. Atomic force microscopy (AFM) was carried on a SPA-400 microscope.

The performance of the catalysts was evaluated in a flow type reactor (373 cm^3 of internal volume) at room temperature [5]. A 450 W high pressure mercury lamp equipped with a UV cut-off filter ($\lambda > 400$ nm) was used as the light source for photocatalytic decomposition of NO (DeNO$_x$). The sample was carefully spread in the hole (20mm×16mm×0.5mm) of a glass plate which was placed on the bottom center of the reactor. The concentration of NO was determined using a NO$_x$ analyzer (Yanaco, ECL-88A).

2.3 Results and discussion

The post-thermal treatment of bulk CN for enhanced visible light activity is illustrated in **Fig.2.1**(A). Different from previously reported thermal oxidation etching of bulk CN in air [11], here we developed a combined strategy to increase the specific surface area of bulk CN by thermal oxidation etching and high temperature self-fragmentation into nanosheets simultaneously. Moreover, the high temperature self-fragmentation into nanosheets played the most important role in the improvement of photocatalytic activity, which was confirmed by thermal treatment of bulk CN in argon.
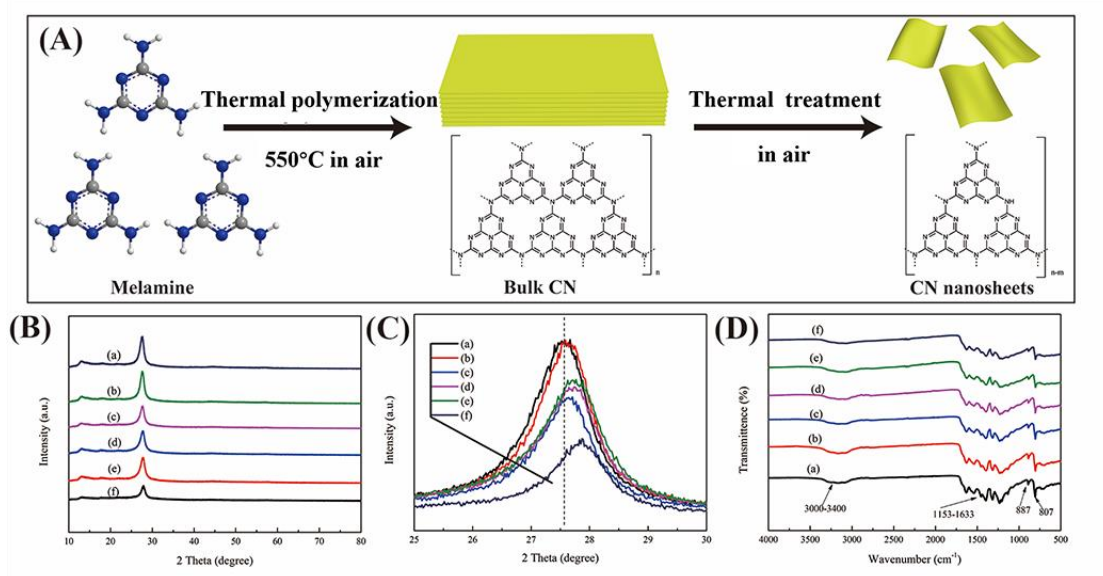
Fig.2.1. (A) Schematic illustration of post-thermal treatment to form CN nanosheets with tunable band structure. (B) The XRD patterns, (C) the amplified diffraction profiles, (D) the FTIR spectra of post-thermal treated CN samples. (a) bulk CN, (b) CN-450, (c) CN-480, (d) CN-500, (e) CN-520, and (f) CN-550.

The chemical structure of the samples treated at different temperatures was investigated by XRD patterns and FTIR spectroscopy. As shown in **Fig.2. 1** (B), all the CN exhibited two characteristic diffraction peaks at 13.5° and 27.8°, which could be index to the (100) and (002) crystal planes of CN, representing in-plane structural packing motif and interplanar stacking of CN sheets, respectively [16]. However, it is important to note that the intensity and position of (002) diffraction changed (**Fig.2. 1** (C)), suggesting the few-layers and denser packing morphology of CN nanosheets after thermal treatment [17]. FTIR spectra depicted in **Fig.2.1** (D) showed the typical peaks at 3000-3400, 1153-1623, 887, and 807 cm^{-1}, which could be assigned N–H stretching indicating the partial hydrogenation of some nitrogen atoms in the samples, typical stretching mode of CN heterocycles, N-H in amino groups, and breathing mode of tris-s-triazine cycles, respectively [18, 19]. Notably, the FTIR spectrum of CN nanosheets resembled that of bulk CN, meaning that the post-thermal treatment did not change general structure of CN, which was consistent with the XRD patterns.
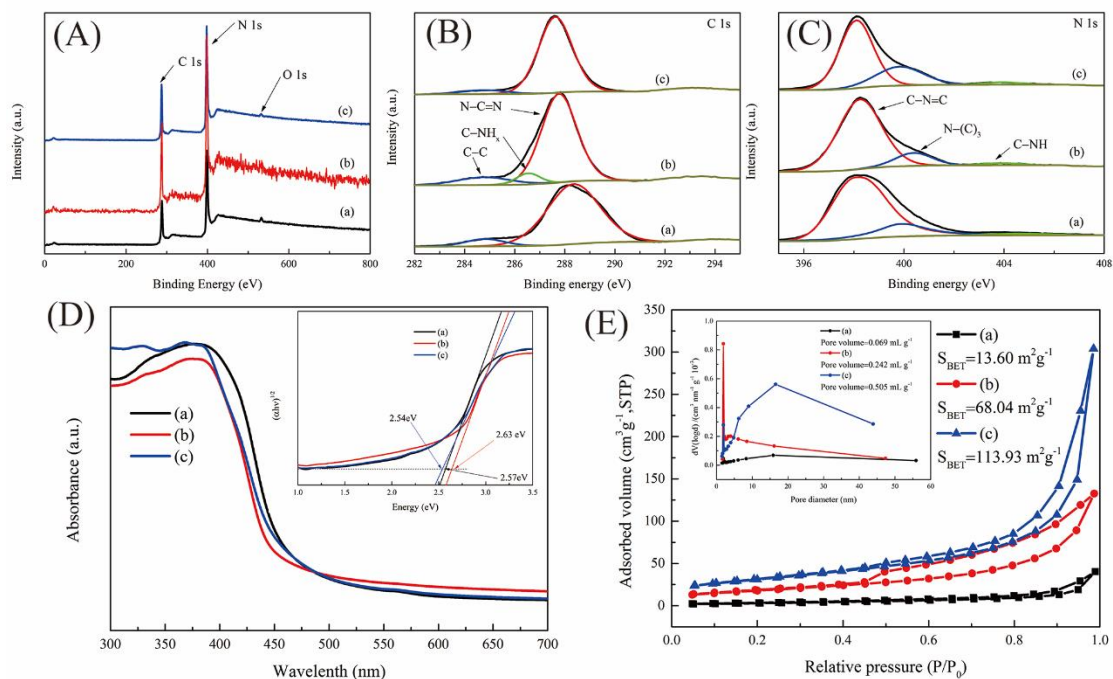
Fig.2.2. The XPS spectra of (A) survey, (B) C1s, and (C) N1s, (D) Diffuse reflectance spectra and plots of $(\alpha h\nu)^{1/2}$ versus $h\nu$ for the corresponding reflectance spectra (inset), (E) N$_2$ adsorption-desorption isotherms and corresponding pore size distribution curves (inset). (a) bulk CN, (b) CN-500, and (c) CN-550.

The compositions and chemical states of the as-prepared photocatalysts were studied by XPS. As shown in XPS survey (**Fig.2.2** (A)), all the samples were mainly composed of C and N, and trace amounts of O were detected on account of surface adsorbed oxygen-containing species. For bulk CN and CN-550 (**Fig.2.2** (B)), the C1s contained two components centered at 288.1 and 284.8 eV, which were ascribed to N–C=N coordination in the framework of CN and surface carbon impurities, respectively [20]. As to CN-500, apart from these two peaks, another peak located at 286.4 eV was observed, corresponding to C-NH$_x$ on the edges of heptazine unites and adsorbed hydrocarbons [18]. In the Figure 2 (C), the N 1s of all the samples could be fitted into three peaks at 398.1, 400.0, and 403.4 eV, attributing to C–N=C, N–(C)$_3$, and C–NH$_x$ in the heptazine framework, respectively [21].

The optical properties of the samples were measured by UV-vis DRS. As shown in **Fig.2.2** (D), all the samples could absorb visible light. Moreover, the CN-500

nanosheet samples showed a slight blue shift of the absorption edge with respect to bulk CN, indicating the narrower visible-light absorption range. The bandgaps of the samples were calculated by transformed Kubelka-Munk function. The bandgaps were 2.57 eV for bulk CN, 2.63 eV for CN-500, and 2.54 eV for CN-550, respectively. The larger band gap of CN-500 could be ascribed to the quantum confinement effect due to the nature of ultrathin nanosheets [22], which gave indirect evidence to the successful exfoliation of bulk CN.

The BET surface areas and pore structures of the as-obtained samples were investigated by nitrogen adsorption-desorption measure measurement. **Fig.2.2** (E) depicted the nitrogen adsorption-desorption isotherms for the CN-500 and CN-550 samples, which were typical type IV curves, suggesting the presence of mesopores and macropores [10]. The BET surface areas of CN-500 (68.0 m^2g^{-1}) and CN-550 (113.9 m^2g^{-1}) samples are much higher than that of bulk CN (13.6 m^2g^{-1}), which showed that post-thermal treatment was a promising strategy to enlarge the specific surface of bulk CN, compared with previously reported methods (Table S1). In addition, the total pore volume of CN-500 and CN-550 were much higher than that of bulk CN, which were 0.24 mLg^{-1} and 0.50 mLg^{-1}, respectively. As it shown in **Fig.2.2** (E), the pore size distribution peak of pristine CN was negligible. By contrast, the pore size distribution curve of CN-500 had obvious peak at about 2 nm and the pore size distribution curve of CN-550 exhibited two strong peaks at around 2 nm and 16.5 nm, separately.
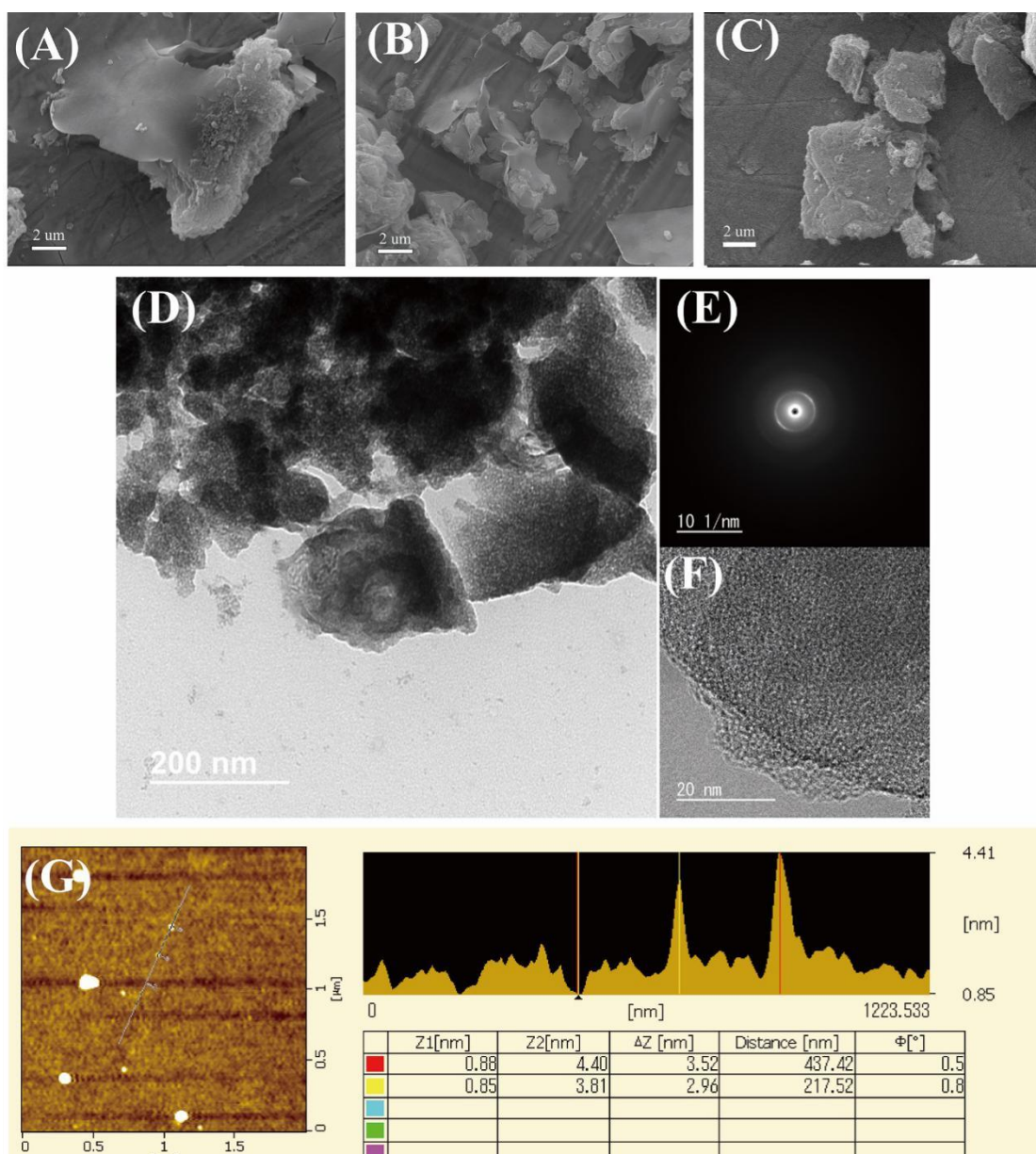
Fig.2.3. SEM images of (A) bulk CN, (B) CN-500, and (C) CN-550. TEM(D), SAED(E), HRTEM (F) and AFM images of CN-500.

SEM, TEM, and AFM were conducted to investigate the morphology and microstructure of the resultant samples. As shown in the **Fig.2.3** (A), the pristine CN was extensively agglomerated lamellar structure with a size of 15 micrometers. After thermal treatment, CN-500 (Figure 3 (B)) and CN-550 **Fig.2.3** (C)) became sheet-like due to the high temperature decomposition into small fragments and the thermal oxidation etching to exfoliate bulk CN into nanosheets. Also, the ultrathin sheets were proved by TEM (**Fig.2.3** (D)) and AFM (**Fig.2.3** (G)) images. The representative AFM

image of the CN-500 samples showed that the thickness of small ultrathin nanosheets ranged from 0.85 nm to 4.81 nm, suggesting the nanosheets around 2-10 layers. After thermal treatment, the CN-500 became amorphous demonstrated by HRTEM (**Fig.2.3** (E)) and SAED (**Fig.2.3** (F)) [15].
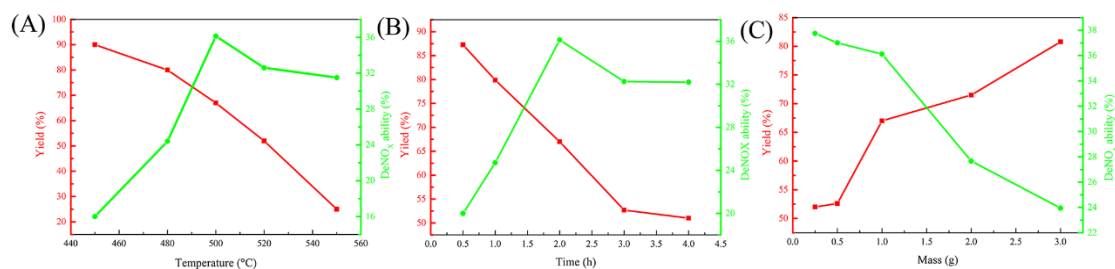
Fig.2.4. The impact of (A) thermal treatment temperature, (B) thermal treatment temperature time, and (C) dosage on the photocatalytic activity and yield of the samples, respectively.

The photocatalytic activities of the obtained samples were evaluated by measuring photocatalytic decomposition of NO_x under visible light irradiation ($\lambda > 400$ nm). **Fig.2.4** (A) illustrated the impact of thermal treatment temperature on the photocatalytic activity and yield of the samples. The $deNO_x$ activity improved along with thermal treatment temperature increasing at first and when temperature reached 500 ˚C, the photocatalytic activity slightly decreased, but the yield had a continuous decline with temperature increasing. To study the effect of thermal treatment deeply, the parameters of thermal treatment time and dosage were also investigated, as shown in the **Fig.2.4** (B) and **Fig.2.4** (C), respectively. Taking into consideration of the actual production, the optimal thermal treatment condition was 500 ˚C for 2 h with 1 g dosage, resulting the excellent catalytic performance and high yield.
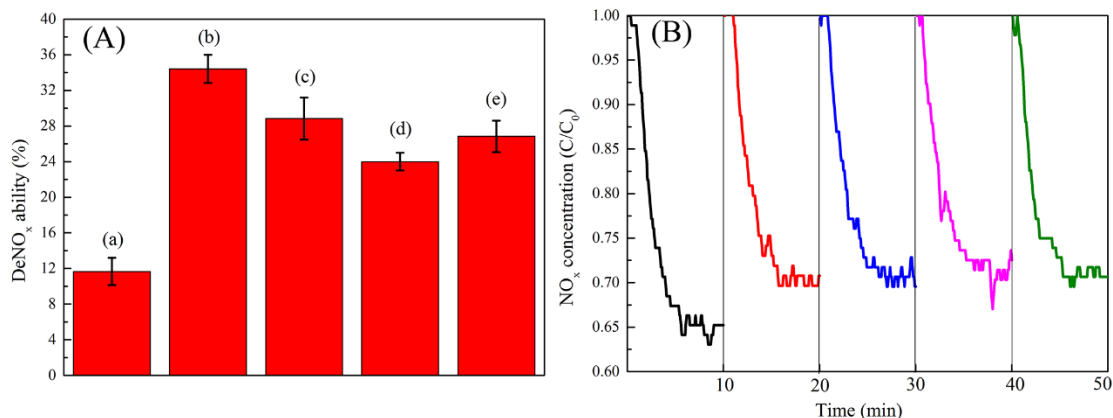
Fig.2.5. (A) DeNO$_x$ ability of the samples under visible light irradiation (λ>400nm). (a) bulk CN, (b) CN-500, (c) CN-550, (d) P25, and (e) CN-500-Ar. (B) Cycling stability test on CN-500 photocatalytic decomposition of NOx under visible light irradiation (λ>400nm).

The **Fig.2.5** (A) showed the deNO$_x$ performance of the sample bulk CN, CN-500 nanosheets, CN-550 nanosheets and P25 under visible light irradiation (λ>400 nm). By contrast, the activity of the sample CN-500-Ar thermal treated in argon was also listed. The CN-500 exhibited the highest activity among the samples, which was about 3.0 times higher than that of bulk CN. Interestingly, the sample CN-500-Ar showed significantly enhanced photocatalytic activity, even higher than that of P25, indicating that the improvement not only due to the thermal oxidation etching, but also the high temperature self-fragmentation into nanosheets. In addition, the catalytic stability of the sample CN-500 was evaluated by performing the recycle experiment under the same reaction conditions. As shown in **Fig.2.5** (B), after five circles, there was no obvious deactivation, which indicated the stability of the sample for photocatalytic decomposition of NO$_X$. Moreover, the stability of the photocatalyst could be further confirmed by XRD (**Fig.2.6**) and FTIR (**Fig.2.7**) characterization [24].
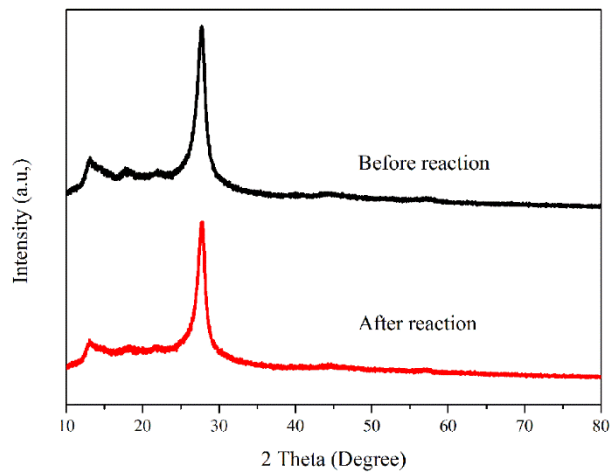
Fig.2.6. XRD patterns of CN-500
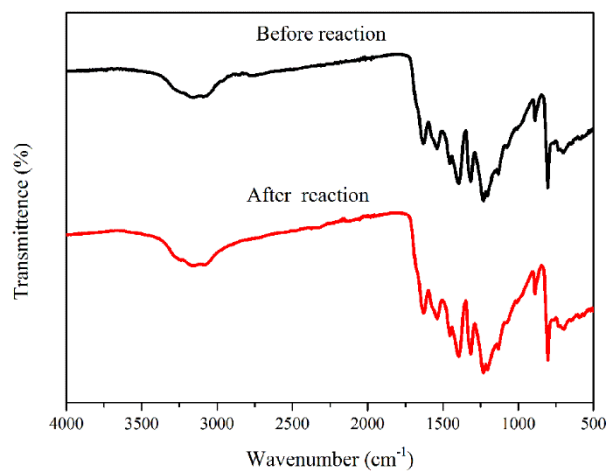
Fig.2.7. FTIR spectra of CN-500
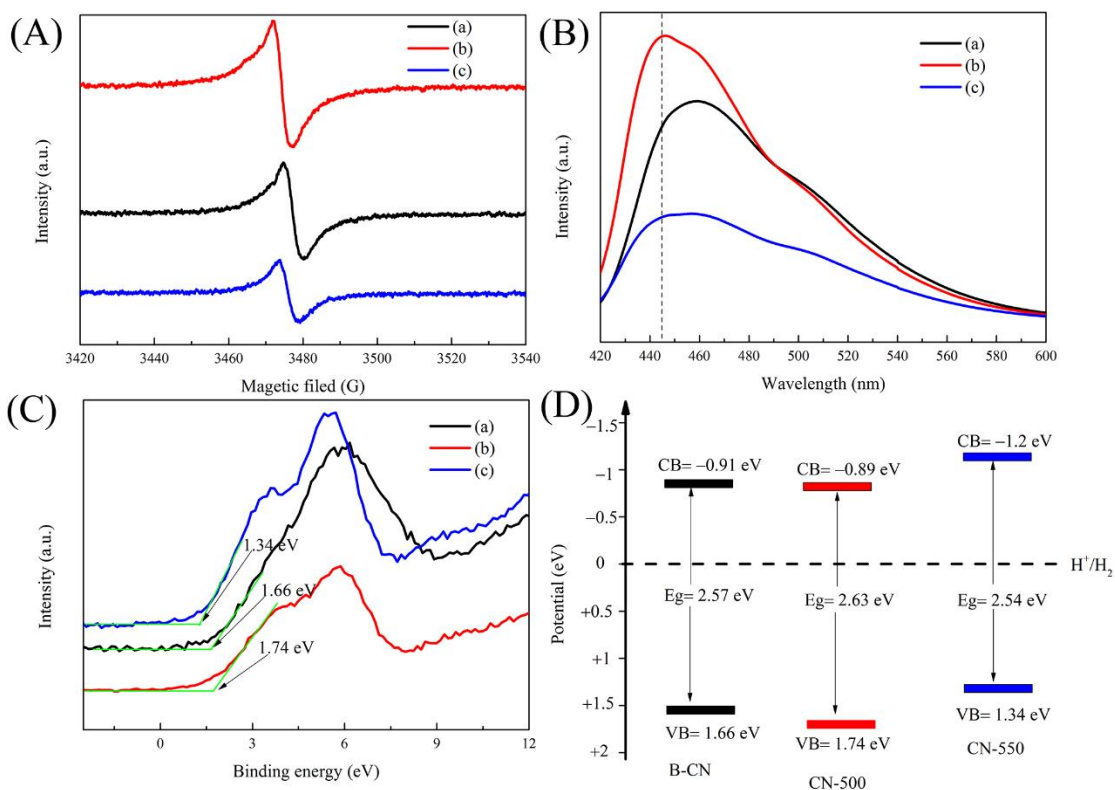
Fig.2.8. (A) EPR spectra, (B) PL spectra, (C) VB-XPS, and (D) schematic illustration for the electronic structures of (a) bulk CN, (b) CN-500, and (c) CN-550

It is well understood that large specific surface could increase active sites for adsorbing reactant molecules and thus facilitate mass and charge carriers transfer for enhanced photocatalytic reactions [11]. Curiously, compared to CN-550 with the higher specific the area of 113.9 m^2/g, the sample CN-500 with lower specific surface area of 68.0 m^2/g exhibited the higher photocatalytic activity. To get insight into the photocatalytic mechanism, further study needs to be carried out. The presence of nitrogen defect was further confirmed by EPR spectroscopy (**Fig.2.8** (A)) which was used for probing unpaired electrons in materials [25]. Taking CN-550 with rare defect as a reference, an enhanced signal was observed in CN-500, which could be ascribed to an unpaired electron on the carbon atoms of the tri-s-triazine units. Due to the introduction of nitrogen vacancy, the extra electrons would redistribute to adjacent carbon atoms by the delocalized π-conjugated networks, which means that a different band structure achieved [26]. In addition, as shown in the PL spectra (**Fig.2.8** (B)), the blue shifts happened in the CN-500 and CN-550 were in favor of the transfer of photo-

induced electrons, which would restrict recombination of photo-induced charge carriers and thus improve the photocatalytic activity [27]. The phenomenon of the photocatalytic activity of the photocatalysts increased a with stronger PL intensity was the same with the previous literature [11].

At last, the nitrogen vacancy induced band structure change was examined by valence band (VB) XPS [27, 28]. From the **Fig.2.8** (C), the VB of bulk CN, CN-500, and CN-550 were 1.66 eV, 1.74 eV, and 1.34 eV, respectively. The VB of CN-500 increased significantly due to the nitrogen vacancy, compared with that of CN-550, which resulted in the higher thermodynamic driving force during the photocatalytic decomposition of NO_x. Therefore, even though the CN-550 exhibited the higher specific surface area, it performed lower photocatalytic activity compared with CN-500, owing to the low oxidizing power. Combined with bandgap values [27, 28], it is safe to get a schematic illustration of band structure of bulk CN, CN-500, and CN-550, respectively. Under different post thermal treatment temperatures, tunable band structures of CN nanosheets were obtained (**Fig.2.8** (D)). All in all, there were various factors such as specific surface area and electronic structure affecting the activity of photocatalysts [29]. And the defect played an important role in the photocatalytic process, resulting the improved the photocatalytic activity [30-33].

2.4 Conclusion

In summary, our study provides a facile strategy to enhance the photocatalytic decomposition of NO_x of bulk CN via a high yield post-thermal treatment. The resultant CN-500 nanosheets exhibited about 3.0 times higher photocatalytic activity than that of bulk CN under visible light irradiation due to the synergic advantages of enlarged specific surface areas and optimized band structure. The enlarged specific surface areas are ascribed to not only thermal oxidation etching bulk CN to CN nanosheets, but also high temperature induced bulk CN self- fragmentation into CN nanosheets, which results in the high yield (70%) of nanosheets. The suitable band structure is attributed to the quantum confinement effect and formation of nitrogen vacancy. The facile and

high yield post-thermal treatment is expected to have a promising future to enhance the photocatalytic activity of bulk CN.

2.5 References

[1] S. Yin, Creation of advanced optical responsive functionality of ceramics by green processes, Journal of the Ceramic Society of Japan, 123 (2015) 823-834.

[2] S. Yin, Y. Asakura, Recent research progress on mixed valence state tungsten based materials, Tungsten, 1 (2019) 5-18.

[3] S. Yin, A. Riapanitra, Y. Asakura, Nanomaterials for infrared shielding smart coatings, Functional Materials Letters, 11 (2018) 1830004.

[4] Z. Zhao, J. Fan, H. Chang, Y. Asakura, S. Yin, Recent progress on mixed-anion type visible-light induced photocatalysts, Science China Technological Sciences, 60 (2017) 1447-1457.

[5] X. Wu, S. Yin, Q. Dong, C. Guo, H. Li, T. Kimura, T. Sato, Synthesis of high visible light active carbon doped TiO_2 photocatalyst by a facile calcination assisted solvothermal method, Applied Catalysis B: Environmental, 142 (2013) 450-457.

[6] H. Li, X. Wu, S. Yin, K. Katsumata, Y. Wang, Effect of rutile TiO_2 on the photocatalytic performance of g-C_3N_4/brookite-$TiO_{2-x}N_y$ photocatalyst for NO decomposition, Applied Surface Science, 392 (2017) 531-539.

[7] J. Ma, C. Wang, H. He, Enhanced photocatalytic oxidation of NO over g-C_3N_4-TiO_2 under UV and visible light, Applied Catalysis B: Environmental, 184 (2016) 28-34.

[8] X. Wang, K. Maeda, A. Thomas, K. Takanabe, G. Xin, J.M. Carlsson, K. Domen, M. Antonietti, A metal-free polymeric photocatalyst for hydrogen production from water under visible light, Nature materials, 8 (2009) 76-80.

[9] J. Fu, J. Yu, C. Jiang, B. Cheng, g-C3N4-Based heterostructured photocatalysts, Advanced Energy Materials, 8 (2018) 1701503.

[10] W.-J. Ong, L.-L. Tan, Y.H. Ng, S.-T. Yong, S.-P. Chai, Graphitic carbon nitride (g-C3N4)-based photocatalysts for artificial photosynthesis and environmental remediation: are we a step closer to achieving sustainability? Chemical reviews, 116 (2016) 7159-7329.

[11] P. Niu, L. Zhang, G. Liu, H.M. Cheng, Graphene-like carbon nitride nanosheets

for improved photocatalytic activities, Advanced Functional Materials, 22 (2012) 4763-4770.

[12] P. Niu, L.C. Yin, Y.Q. Yang, G. Liu, H.M. Cheng, Increasing the visible light absorption of graphitic carbon nitride (Melon) photocatalysts by homogeneous self-modification with nitrogen vacancies, Advanced Materials, 26 (2014) 8046-8052.

[13] P. Yang, J. Zhao, W. Qiao, L. Li, Z. Zhu, Ammonia-induced robust photocatalytic hydrogen evolution of graphitic carbon nitride, Nanoscale, 7 (2015) 18887-18890.

[14] J. Xu, L. Zhang, R. Shi, Y. Zhu, Chemical exfoliation of graphitic carbon nitride for efficient heterogeneous photocatalysis, Journal of Materials Chemistry A, 1 (2013) 14766-14772.

[15] T. Sano, S. Tsutsui, K. Koike, T. Hirakawa, Y. Teramoto, N. Negishi, K. Takeuchi, Activation of graphitic carbon nitride (g-C_3N_4) by alkaline hydrothermal treatment for photocatalytic NO oxidation in gas phase, Journal of materials chemistry A, 1 (2013) 6489-6496.

[16] M. Zhu, S. Kim, L. Mao, M. Fujitsuka, J. Zhang, X. Wang, T. Majima, Metal-free photocatalyst for H_2 evolution in visible to near-infrared region: black phosphorus/graphitic carbon nitride, Journal of the American Chemical Society, 139 (2017) 13234-13242.

[17] H. Wang, W. Zhou, P. Li, X. Tan, Y. Liu, W. Hu, J. Ye, T. Yu, Enhanced visible-light-driven hydrogen production of carbon nitride by band structure tuning, The Journal of Physical Chemistry C, 122 (2018) 17261-17267.

[18] Q. Liang, Z. Li, X. Yu, Z.H. Huang, F. Kang, Q.H. Yang, Macroscopic 3D porous graphitic carbon nitride monolith for enhanced photocatalytic hydrogen evolution, Advanced Materials, 27 (2015) 4634-4639.

[19] J. Wen, J. Xie, X. Chen, X. Li, A review on g-C_3N_4-based photocatalysts, Applied surface science, 391 (2017) 72-123.

[20] L. Ming, N. Sun, L. Xu, F. Chen, Fluoride ion-promoted hydrothermal synthesis of oxygenated g-C_3N_4 with high photocatalytic activity, Colloids and Surfaces A: Physicochemical and Engineering Aspects, 549 (2018) 67-75.

[21] H. Yu, R. Shi, Y. Zhao, T. Bian, Y. Zhao, C. Zhou, G.I. Waterhouse, L.Z. Wu, C.H.

Tung, T. Zhang, Alkali-assisted synthesis of nitrogen deficient graphitic carbon nitride with tunable band structures for efficient visible-light-driven hydrogen evolution, Advanced Materials, 29 (2017) 1605148.

[22] S.L. Wang, X. Luo, X. Zhou, Y. Zhu, X. Chi, W. Chen, K. Wu, Z. Liu, S.Y. Quek, G.Q. Xu, Fabrication and properties of a free-standing two-dimensional titania, Journal of the American Chemical Society, 139 (2017) 15414-15419.

[23] Y. Li, R. Jin, Y. Xing, J. Li, S. Song, X. Liu, M. Li, R. Jin, Macroscopic foam-like holey ultrathin g-C_3N_4 nanosheets for drastic improvement of visible-light photocatalytic activity, Advanced Energy Materials, 6 (2016) 1601273.

[24] Y. Xiao, G. Tian, W. Li, Y. Xie, B. Jiang, C. Tian, D. Zhao, H. Fu, Molecule self-assembly synthesis of porous few-layer carbon nitride for highly efficient photoredox catalysis, Journal of the American Chemical Society, 141 (2019) 2508-2515.

[25] J. Xue, M. Fujitsuka, T. Majima, The role of nitrogen defects in graphitic carbon nitride for visible-light-driven hydrogen evolution, Physical Chemistry Chemical Physics, 21 (2019) 2318-2324.

[26] C. Lv, Y. Qian, C. Yan, Y. Ding, Y. Liu, G. Chen, G. Yu, Defect engineering metal-free polymeric carbon nitride electrocatalyst for effective nitrogen fixation under ambient conditions, Angewandte Chemie, 130 (2018) 10403-10407.

[27] T. Song, P. Zhang, T. Wang, A. Ali, H. Zeng, Alkali-assisted fabrication of holey carbon nitride nanosheet with tunable conjugated system for efficient visible-light-driven water splitting, Applied Catalysis B: Environmental, 224 (2018) 877-885.

[28] X. Song, D. Tang, Y. Chen, M. Yin, Q. Yang, Z. Chen, L. Zhou, A Facile and Green Combined Strategy for Improving Photocatalytic Activity of Carbon Nitride, ACS Omega, 4 (2019) 6114-6125.

[29] P. Niu, G. Liu, H.-M. Cheng, Nitrogen vacancy-promoted photocatalytic activity of graphitic carbon nitride, The Journal of Physical Chemistry C, 116 (2012) 11013-11018.

[30] Z. Chen, T.-T. Fan, X. Yu, Q.-L. Wu, Q.-H. Zhu, L.-Z. Zhang, J.-H. Li, W.-P. Fang, X.-D. Yi, Gradual carbon doping of graphitic carbon nitride towards metal-free visible light photocatalytic hydrogen evolution, Journal of Materials Chemistry A, 6 (2018)

15310-15319.

[31] S. Gao, B. Gu, X. Jiao, Y. Sun, X. Zu, F. Yang, W. Zhu, C. Wang, Z. Feng, B. Ye, Highly efficient and exceptionally durable CO_2 photoreduction to methanol over freestanding defective single-unit-cell bismuth vanadate layers, Journal of the American Chemical Society, 139 (2017) 3438-3445.

[32] X. Jiao, Z. Chen, X. Li, Y. Sun, S. Gao, W. Yan, C. Wang, Q. Zhang, Y. Lin, Y. Luo, Defect-mediated electron–hole separation in one-unit-cell $ZnIn_2S_4$ layers for boosted solar-driven CO_2 reduction, Journal of the American Chemical Society, 139 (2017) 7586-7594.

[33] Z. Wang, Y. Huang, M. Chen, X. Shi, Y. Zhang, J. Cao, W. Ho, S.C. Lee, Roles of N-Vacancies over Porous $g\text{-}C_3N_4$ Microtubes during Photocatalytic NO x Removal, ACS Applied Materials &Interfaces, 11 (2019) 10651-10662.

Chapter 3 Defect engineering

The defect engineering involves two works. The first one is about preparing carbon vacancies and hydroxyls co-modified CN via the green hydrothermal method. The related research work is entitled "**Carbon vacancies and hydroxyls in graphitic carbon nitride: promoted photocatalytic NO removal activity and mechanism**" **(Chapter 3.1).**

The second one is about improving the crystallinity of pristine CN via a modified molten salt method. The related research work is entitled **"Synthesis of crystalline carbon nitride with enhanced photocatalytic NO removal performance: an experimental and DFT theoretical study" (Chapter 3.2).**

3.1 Carbon vacancies and hydroxyls in graphitic carbon nitride: promoted photocatalytic NO removal activity and mechanism

3.1.1 Introduction

Due to rapid industrial development and population growth, environmental pollution has become an issue of worldwide concern [1-4]. Nitric oxide (NO), one of the major air pollutants, have severe effects on the air quality such as acid rain, photochemical smog and ozone accumulation [5-8]. Besides, they could cause respiratory illness and heart attacks in human [9, 10]. To address the air pollution, photocatalysis has attracted much attention because of its potential in utilizing solar energy to remove the NO[9, 11]. It is accepted that the basic and prerequisite of effective photocatalysis is to prepare and develop high-sensitive photocatalysts[12-17]. Since 2009[18], graphitic carbon nitride (CN) has attracted increasing attention due to its low cost, easy preparation, good stability, nontoxicity, and visible-light response[19-21]. However, the bulk CN still suffers from low specific surface area and rapid recombination of photogenerated electron-hole pairs, which results in unsatisfactory of photocatalytic activity[22]. Thus, tremendous efforts have been made to improve the catalytic activity of bulk CN, such as metal and nonmetal doping, forming vacancies, creating heterojunctions and constructing nanostructures[19, 23].

Among these strategies, defect design is viewed as a reliable and effective way to enhance the photocatalytic activity of pristine CN[11, 24, 25]. It has been well understood that constructing defects enable to optimize the electronic structure, charge carrier separation, and active sites of semiconductor photocatalyst[26]. For example, Wang et al. reported that the photocatalytic NO removal ratio of CN microtubes with nitrogen vacancies was 1.8 times higher than that of pristine CN[11]. This is because the surface nitrogen vacancies not only enhanced the light harvesting capability but also acted as reaction sites to activate NO and O_2. Li et al. demonstrated CN with carbon

vacancies showed 2.0 times higher photocatalytic NO decomposition rate than that of pristine CN due to the negatively shifted conduction band potential[27]. Additionally, surface hydroxylation has also been demonstrated to improve the photocatalytic performance of CN effectively[28]. For instance, Wang et al. synthesized surface hydroxylation modified porous CN via a hydrothermal route in the presence of ammonium hydroxide [29]. The tailored CN showed 4.2 times higher photocatalytic hydrogen production than that of bulk CN, which could be ascribed to the accelerated the interfacial charge transfer and enlarged specific surface area. Yu et al. unraveled that surface hydroxylation facilitated local spatial charge separation efficiency and proton activation of CN, resulting in significantly increased photocatalytic hydrogen generation [30]. However, introducing the carbon vacancies and hydroxyls simultaneously into CN has thitherto not been reported.

Herein, we reported a green strategy to fabricate carbon vacancies and hydroxyls co-modified CN (CH-CN) via a post hydrothermal treatment. To the best of our knowledge, this is the first time to report the carbon vacancies and hydroxyls co-modified CN to enhance the photocatalytic NO removal performance. During the hydrothermal process, the water etched the unstable domains of bulk CN to introduce the carbon vacancies and hydroxyls into CH-CN, resulting in the modulated the electronic structure. At the same time, the small fragments formed to increase its specific surface area. The obtained CH-CN nanosheets exhibited 2.2 times higher photocatalytic NO removal performance than that of pristine CN. Combined experimental investigations and density functional theory (DFT) calculations were systematically applied to study the carbon vacancies and hydroxyls in CH-CN nanosheets. It revealed that the improved photocatalytic NO removal performance of CH-CN nanosheets was mainly owing to the synergistic effects of carbon vacancies and hydroxyls. Also, the enlarged specific surface areas had some positive effects to enhance the photocatalytic activity. This study could bring new perspectives into the defect engineering for enhancing the photocatalytic performance of CN based photocatalysts.

3.1.2 Experiment

Sample preparation

The bulk CN was prepared by calcining the melamine at 550 ˚C for 2 h with a heating rate 10 ˚C/min [5, 31]. Then the obtained bulk CN was grounded by ball-milling for further use. The carbon vacancies and hydroxyls co-modified CH-CN was prepared via a post hydrothermal treatment. In detail, 1.0 g of the obtained bulk CN was added into 70 mL of deionized water and stirred for 0.5 h. Then the resultant suspension was transferred into a Teflon-lined autoclave (100mL internal volume) and heated at 180 °C for a certain time (i.e., 3, 6, or 9 h). After the reaction, the solid product was centrifuged, washed with deionized water and finally dried in a vacuum at 60 °C. For abbreviation, the CN treated by the hydrothermal process for 3 h, 6 h, and 9 h was designated CH-CN3, CH-CN6, and CH-CN9, respectively.

Characterization

Powder X-ray diffraction (XRD) patterns were performed on a Bruker D2 Phaser with monochromatized Cu Kα radiation. Fourier transform infrared (FTIR) spectra were carried out on a FTIR spectrometer (JASCO, FTIR-660D-ATR). UV-vis diffuse reflectance spectra (DRS) were obtained on a UV-vis spectrophotometer (JASCO, V-670). X-ray photoelectron spectroscopy (XPS) analysis was conducted with a Perkin Elmer PHI 5600 X-ray photoelectron spectrometer. N_2 adsorption-desorption isotherms and pore-size distributions were carried out using Quantachrome Instruments, NOVA4200e. Scanning electron microscopy (SEM) investigation was identified using a JSM-7800F. Transmission electron microscopy (TEM) images were recorded on a JEM-2000 EXII microscope. High-resolution transmission electron microscopy (HRTEM) analysis was carried out on a ZEISS LEO-9522 microscope. Electron paramagnetic resonance (EPR) spectra were obtained on Bruker E580 EPR spectrometer at room temperature. Photoluminescence (PL) data were recorded with a spectrofluorometer (JASCO, FP-8500). Time-resolved PL spectroscopy was carried out on a time-correlated single-photon counting system comprising a pulsed picosecond diode laser operating at a wavelength of 375 nm (PLP-10-038, Hamamatsu Photonics,

Japan), a monochromator (Acton SP2150, Princeton Instruments, USA), a photosensor module equipped with a photomultiplier tube (H7422P-50, Hamamatsu Photonics, Japan), and a photon-counting board (SPC-130, Becker and Hickl, Germany) at room temperature.

DFT calculations

The electronic structures and adsorption energy were computed by Vienna ab initio Simulation package (VASP) of DFT. The projector augmented wave (PAW) model with Perdew-Burke-Ernzerhof (PBE) function was employed to describe the interactions between core and electrons. An energy cutoff of 500 eV was used for the planewave expansion of the electronic wave function. The Brillouin zones of all systems were sampled with gamma-point centered Monkhorst-Pack grids. A $3 \times 3 \times 1$ Monkhorst Pack k-point setup was used for slab geometry and self-consistent optimization. The force and energy convergence criterion were set to 0.01 eV Å^{-1} and 10^{-5} eV, respectively. A vacuum space of 15 Å was added in the z-direction to shield the periodic effects between layers.

Photocatalytic NO removal test

The photocatalytic NO removal experiments were performed to evaluate the photocatalytic activity of the as-obtained samples [5, 32, 33]. A mercury lamp (450 W) with a cutoff filter (λ>400 nm) was employed as the visible-light source to execute the rection. The as-prepared sample was tightly coated on the cell (20mm×16mm×0.5mm) of a glass plate, which was placed at the bottom of a flow-type reactor (373cm^3 of internal volume). The initial flow of NO gas (200 ml/min) consisted of 2 ppm of NO (N$_2$ balanced)-air mixture. The NO concentration was measured using a NO$_x$ detector (Yanaco, ECL-88A). The removal ratio of NO (%) was calculated as follows:

$$NO(\%) = \frac{C_0 - C}{C_0} \times 100 \tag{3.1-1}$$

Where C_0 and C were the concentration of NO in the feed and outlet streams, respectively.

3.1.3 Results and discussion

Crystal structure and chemical composition
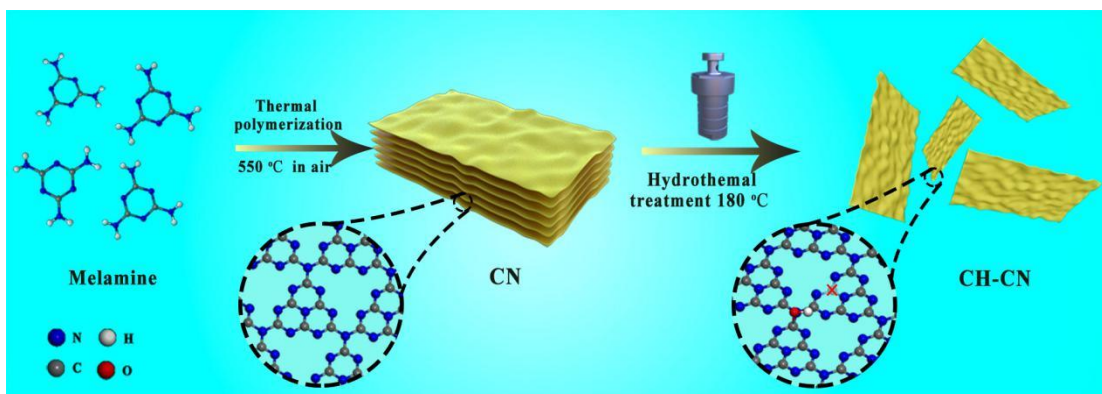
Fig. 3.1.1. Schematic illustration of the formation process for the CH-CN nanosheets

Carbon vacancies and hydroxyls co-modified CH-CN was prepared via a hydrothermal process illustrated in **Fig. 3.1.1**. Firstly, the bulk CN was synthesized by solid state thermal polymerization of melamine. Then, post hydrothermal treatment was employed to modify the bulk CN. During the hydrothermal process, the water would induce the unstable domains of bulk CN to partially hydrolyze[34], which introduce the carbon vacancies and hydroxyls into the resultant CH-CN. At the same time, the bulk CN decomposed into small fragments.
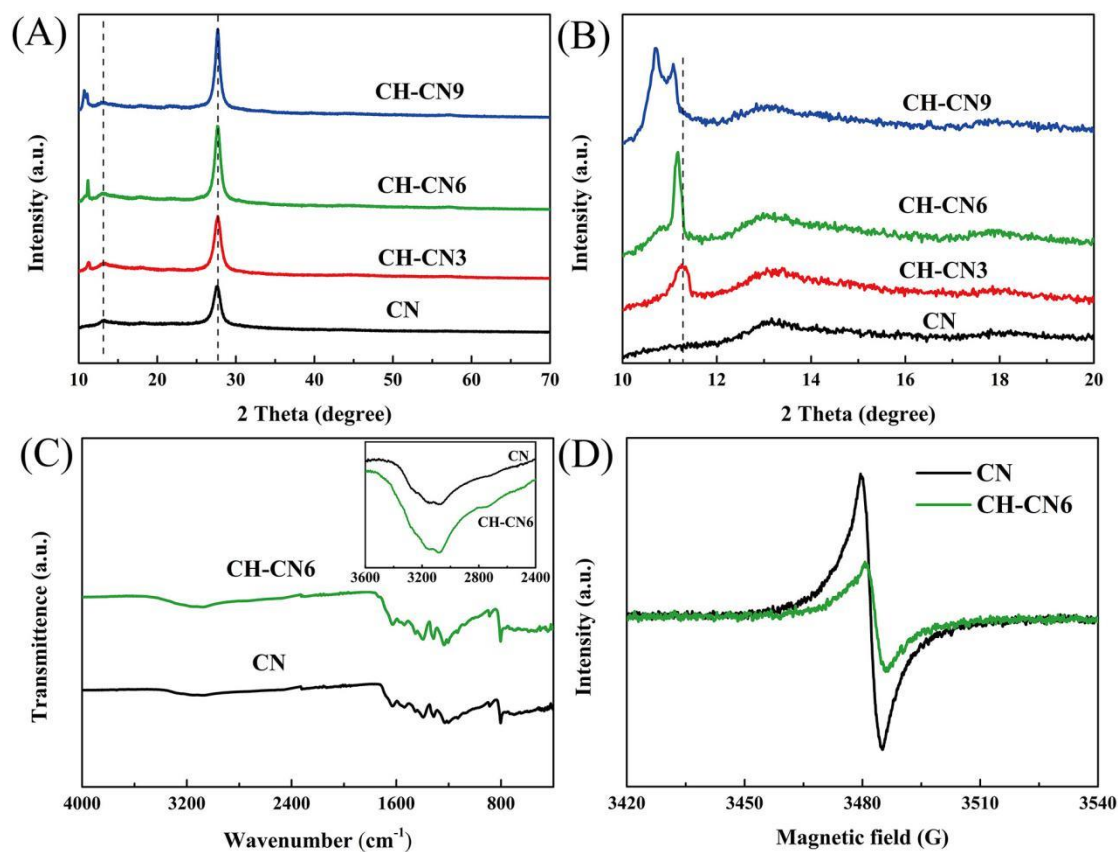
Fig. 3.1.2. (A) XRD patterns of the obtained samples; (B) corresponding the amplified diffraction profiles between 10 and 20°; (C) FTIR spectra of CN and HC-CN6; (D) EPR spectra of CN and HC-CN6.
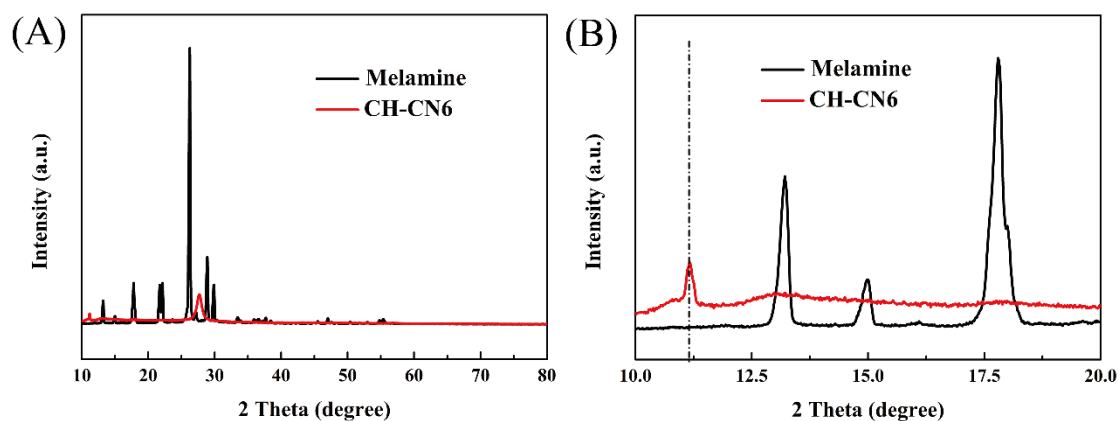
Fig. 3.1.3. (A) XRD patterns of melamine and CH-CN6; (B) corresponding enlarged diffraction profiles in the range 10 to 20°.

To study the crystallographic and purity of the obtained samples, XRD was performed and displayed in **Fig. 3.1.2**A. All the obtained samples displayed two clear

peaks at 13.0° and 27.3°, which were indexed to (100) in-plane structural packing motif and (002) interlayer stacking of conjugated aromatic segments, respectively[35]. This showed that the general structure maintained after hydrothermal treatment[36]. However, with the increasing hydrothermal reaction time, impurity peaks at around 10.6° were clearly observed in **Fig. 3.1.2** B due to the partial destruction of the periodic tri-s-triazine units of CH-CN samples[37]. Further, the impurity peaks could not be ascribed to the depolymerization process because they were not consistent with the peaks of pure melamine (**Fig. 3.1.3** A and **Fig. 3.1.3**B)[38]. **Fig. 3.1.2** C represented the FTIR spectra of pristine CN and CH-CN6. The typical peaks at 810 and 1200-1600 cm^{-1} of all the samples were designated to the breathing mode of tris-s-triazine units and characteristic stretching mode of CN heterocycles, respectively [23]. Compared with CN, CH-CN6 displayed stronger peaks between 3000 and 3500 cm^{-1}, which could be ascribed to much more adsorption of surface O-H [39]. Moreover, the increased surface O-H was demonstrated by the elemental analysis (**Table 3.1.1**). The CH-CN6 sample possessed higher percentages of O and H elements than that of CN, which indicated that more hydroxyls were introduced into HCN samples [36]. In addition, the decreased C/N atomic ratios were observed in CH-CN6 samples, showing the presence of carbon vacancies [19]. To further verify the formation of carbon vacancies in CH-CN6 samples, EPR spectroscopy was performed and results were shown in **Fig. 3.1.2** D. For CH-CN6, apparently a decreased EPR signal appeared, which could be ascribed to the fewer unpaired electrons due to the C atom loss [26]. This result confirmed the formation of carbon vacancies in CH-CN6. To conclude, carbon vacancies and hydroxyls were simultaneously introduced into CH-CN6 after the hydrothermal treatment. **Fig. 3.1.4** depict the optimized configuration of CN and CH-CN based on the DFT calculations, respectively.

CN   CH-CN
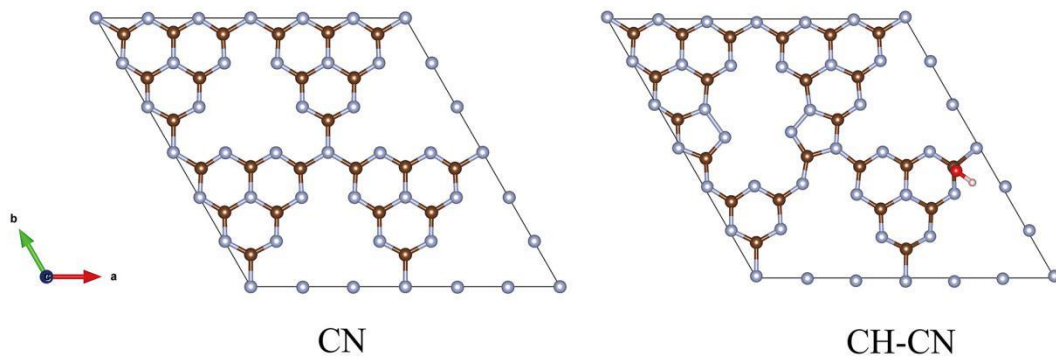
Fig. 3.1.4. The optimized pristine CN and carbon vacancies and hydroxyls co-modified CH-CN configuration. H, C, N, and O atoms are represented by the white, dark gray, light gray, and red balls, respectively.

Table 3.1.1. C/N and O/N atomic ratios of the samples determined by the elemental analysis and XPS analysis

(a) Element analysis						
Samples	C (wt%)	N (wt%)	O (wt%)	H (wt%)	C/N (atomic)	O/N (atomic)
CN	31.35	56.03	10.87	1.74	0.6528	0.1698
CH-CN6	30.07	54.42	13.38	2.13	0.6446	0.2151
(b) XPS element analysis						
Samples	C (wt%)	N (wt%)	O (wt%)	H (wt%)	C/N (atomic)	O/N (atomic)
CN	43.46	55.14	1.40	---	0.9195	0.0222
CH-CN6	39.56	55.03	5.41	---	0.8387	0.0860
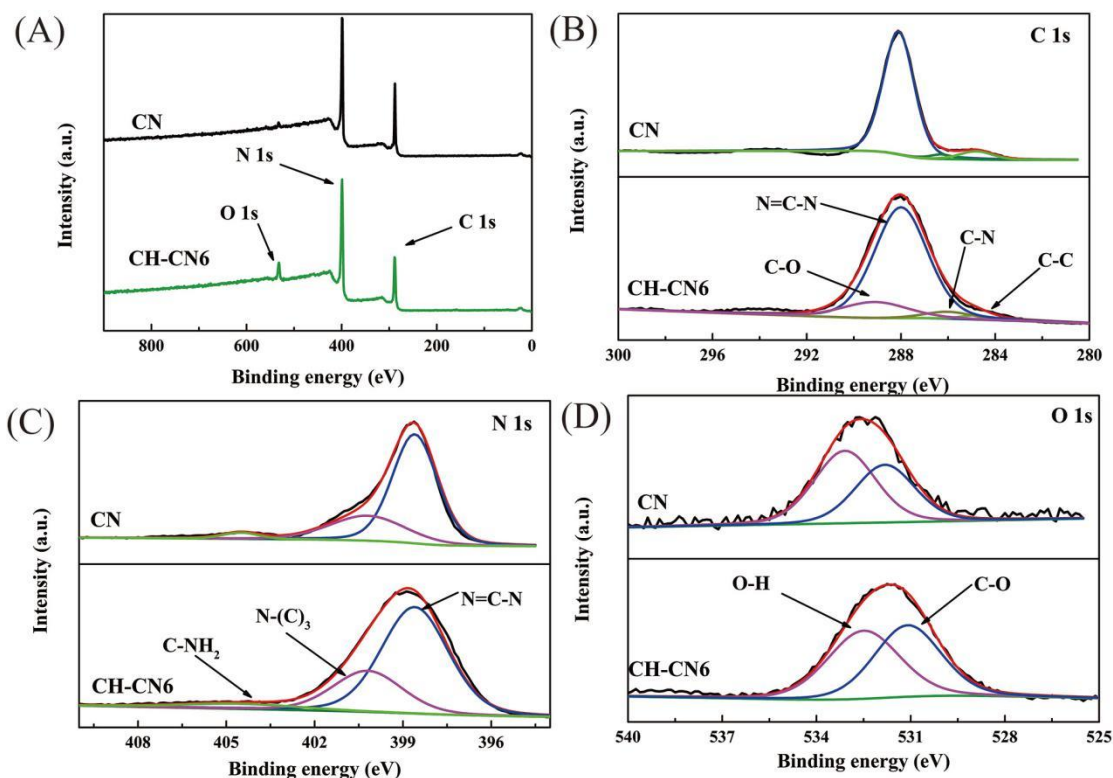
Fig. 3.1.5. XPS spectra of (A) survey, (B) C1s, (C) N1s, and (D) O1s of CN and HC-CN6.

XPS analysis was also performed to investigate the surface chemical composition and chemical state of the as-prepared samples. From the XPS survey spectra (**Fig. 3.1.5**A), it could confirm the existence of carbon, nitrogen and oxygen in CN and CN-CN6. In addition, the intensity of O 1s for CN-CN6 was slightly higher than that for CN, revealing more oxygen elements in CH-CN6. This result was also supported by the XPS element analysis (**Table 3.1.1**). The C/N atomic ratio was decreased in CH-CN6, which was in good agreement with element analysis. As displayed in high-resolution C 1s spectra (**Fig. 3.1.5**B), the CN exhibited peaks located at 288.0, 280.6, and 284.8 eV, which was related to C-C, C-N, and N=C-N, respectively. As for CH-CN6, a new peak at 289.1eV was observed, which was attributed C-O-H band. At the same time, the high-resolution N1s spectra was also analyzed to investigate the true location of oxygen atoms. Both the spectrum of B-CN and CH-CN6 could be deconvoluted into three N species (**Fig. 3.1.5**C), which were centered at 398.6, 400.2, and 404.5 eV, correlated with C-N=C, N-$(C)_3$, C-NH_2, respectively. As shown in the high-resolution O 1s (**Fig.**

3.1.5D), the binding energy at 532.5 eV was ascribed to the C-O of CN caused by the inevitable O doping during the thermal polymerization process in the air[36]. As for the peak at 531.1 eV, it corresponded to the O-H group on the surface of CN. Based on the XPS element analysis (**Table 3.1.1**), more oxygen elements were observed, demonstrating a much O-H group absorbed on the surface of CH-CN6. This result was consistent with the FTIR spectra, which further confirmed the formation of hydroxyls on the surface of CH-CN6.

Morphology and microstructure

The morphology and microstructures of the samples were investigated by SEM, TEM, and HRTEM. As shown in **Fig. 3.1.6**A, the bulk CN exhibited the lamellar structure with smooth surface, which was unfavorable to absorb the light [40]. However, after hydrothermal treatment for 3 h, the size of CH-CN3 (**Fig. 3.1.6**B) decreased to form small fragments. Interestingly, some of CH-CN6 (**Fig. 3.1.7**A) had become nanotubes to minimize the surface energy [39]. Furthermore, the distinct effect of thermal treatment was supported by the TEM images (**Fig. 3.1.6**E and **Fig. 3.1.6**F). No clear lattice was observed in CN (**Fig. 3.1.7**C) and CH-CN6 (**Fig. 3.1.6**G) owing to the low-quality crystallinity, which was consistent with the result of SAED ((**Fig. 3.1.7**A and **Fig. 3.1.6**H)[41, 42].
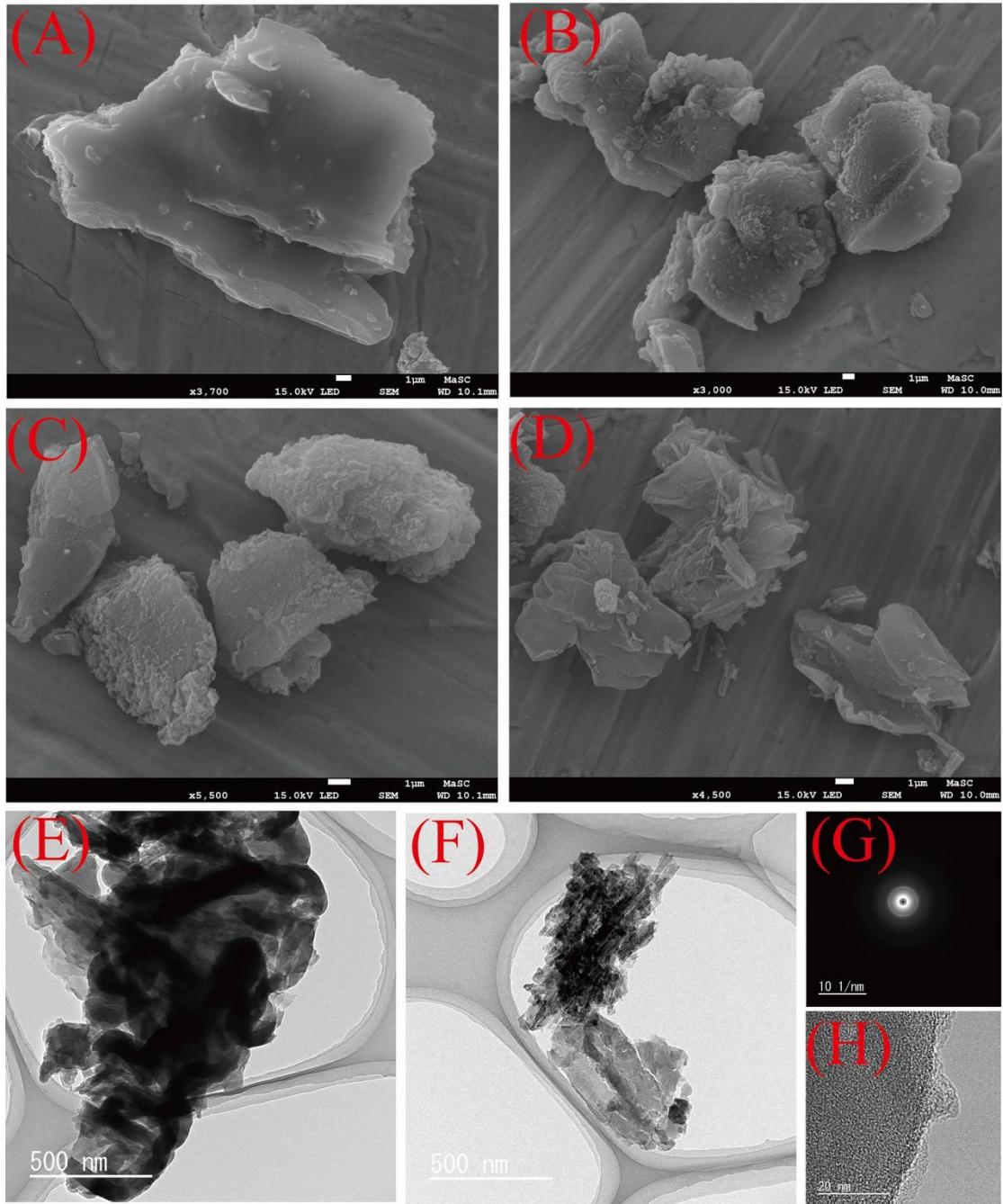
Fig. 3.1.6. (A-D) SEM images of CN, CH-CN3, CH-CN6, and CH-CN9, respectively; (E-F) TEM images of CN and CH-CN6, respectively; (G) SAED and (H) HRTEM of CH-CN6.
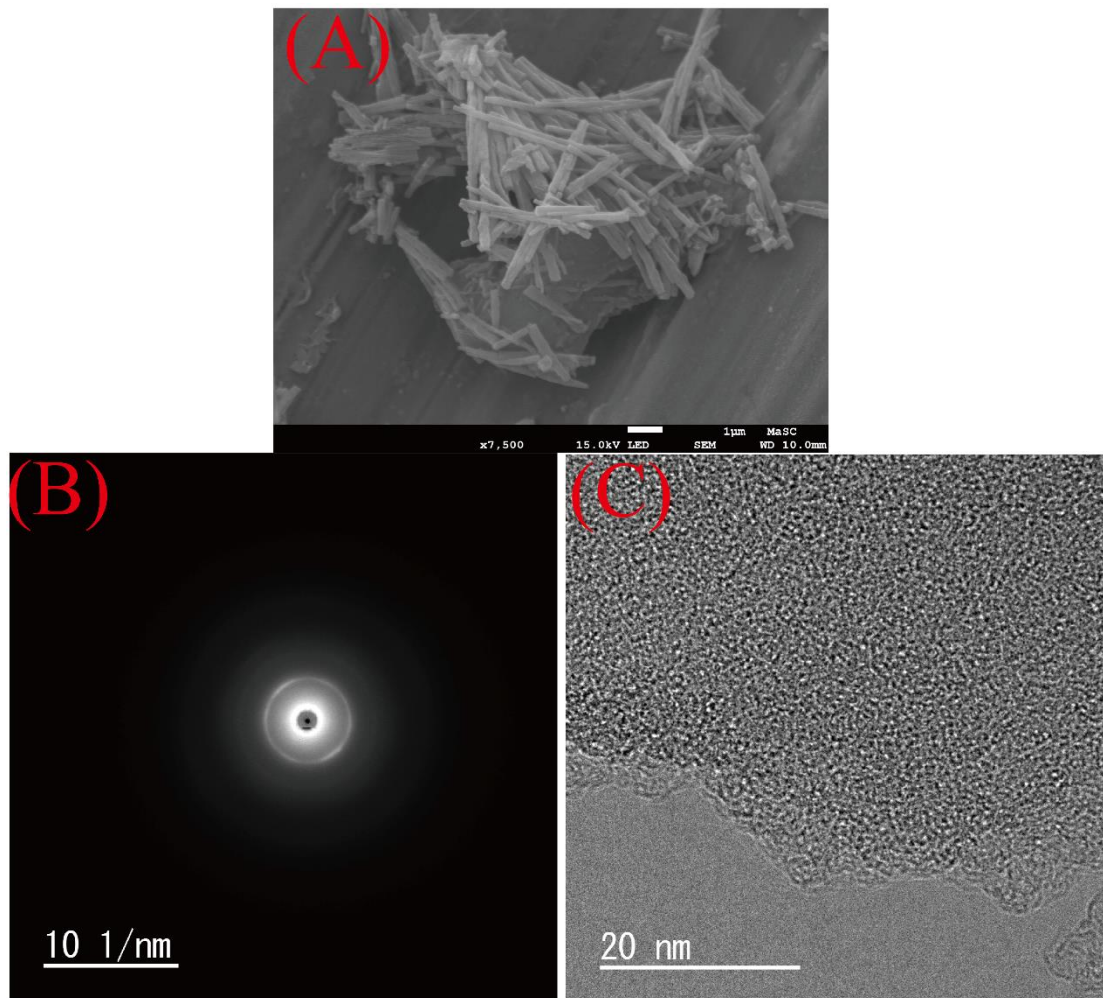
Fig. 3.1.7. (A) SEM image of CH-CN6; (B) SAED and (C) HRTEM of CN.
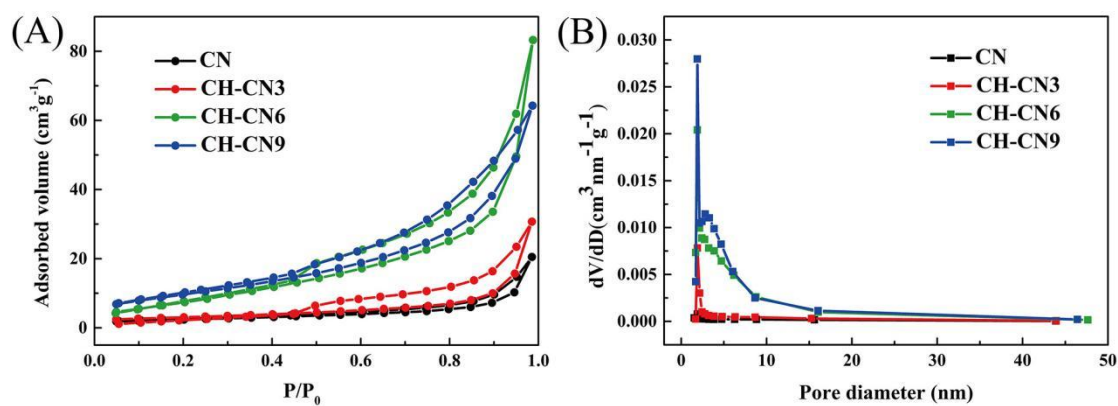
Fig. 3.1.8. (A) Nitrogen gas adsorption isotherms, and (B) corresponding pore size distribution of CN, CH-CN3, CH-CN6 and CH-CN9.

Fig. 3.1.8A shows the N_2 adsorption-desorption isotherms of the obtained samples. All the samples exhibited the typical type-IV curves with a H3-type hysteresis loop,

which indicated the presence of macropores and mesopores in the samples [43]. In addition, the highly porous structure of the samples was proved by the pore size distributions (**Fig. 3.1.8**B). The specific surface area of the samples was calculated using the BET mode and summarized in **Table 3.1.2**. Along with increasing the hydrothermal treatment time, the specific surface area of the samples was slightly enlarged from 8.3(CN) to 35.0 cm^3 g^{-1} (CH-CN6). Notably, during the first 3 hours the specific surface area of CH-CN3 remained almost unchanged (9.8 cm^3 g^{-1}), suggesting that the hydrothermal treatment only had small effects to increase the specific surface area.

Table 3.1.2 BET specific surface area and total pore volume of the obtained samples

Samples	BET surface area (m^2 g^{-1})	Total pore volume (cm^3 g^{-1})
CN	8.3	0.023
CH-CN3	9.8	0.114
CH-CN6	33.3	0.675
CH-CN9	35.5	0.729

Optical property and band structure
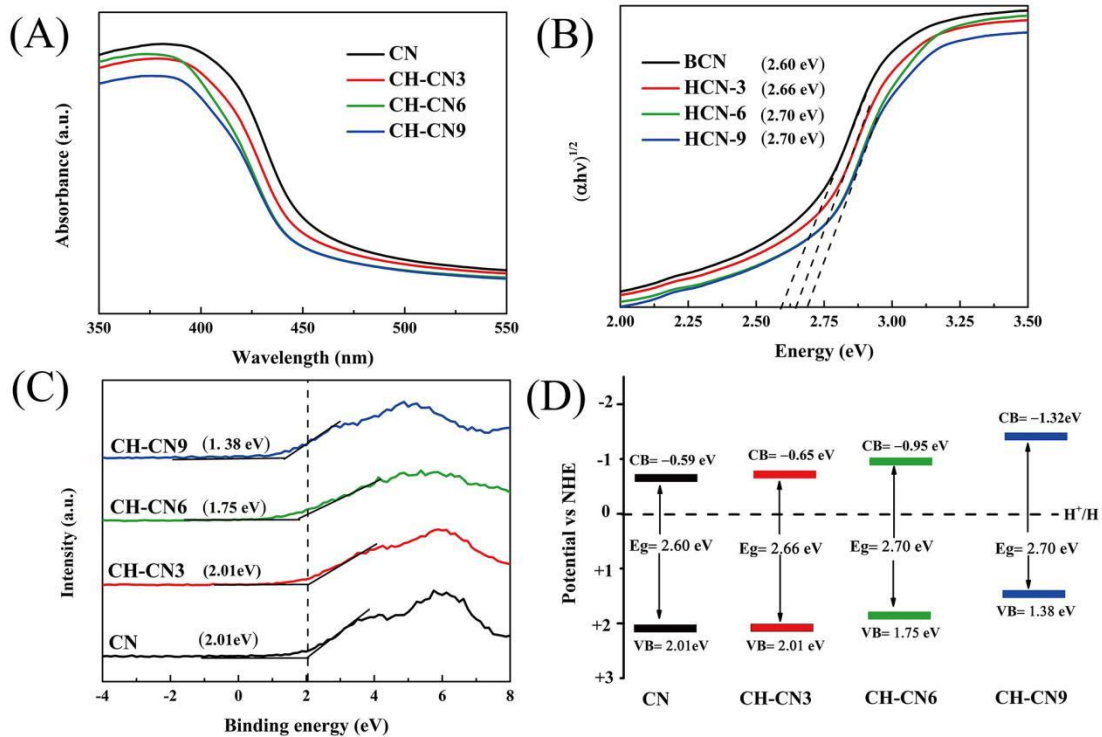
Fig. 3.1.9. (A) UV-vis absorption spectra; (B) corresponding band gap energies; (C) VB-XPS, and (D) schematic illustration for the electronic structures of CN, CH-CN3, CH-CN6 and CH-CN9, respectively.

The optical properties of the resultant samples were analyzed by UV-vis DRS spectra. As can be seen from **Fig. 3.1.9**A, all the samples absorbed visible light. Moreover, the bandgaps of the samples treated by the hydrothermal process enlarged gradually with prolonging the hydrothermal process time (**Fig. 3.1.9**B), which could be ascribed to the hydroxyls and morphology change [29]. Concretely, the hydrothermal treatment could exfoliate the bulk CN into small fragments to increase the bandgaps owing the quantum confine effect [44]. Further, the valance band of the obtained samples were measured by VB XPS. As depicted in **Fig. 3.1.9**C, the valance band of the CH-CN samples decreased obviously after the thermal treatment. This resulted in the photogenerated holes with lower oxidizing ability, which was detrimental to improve the photocatalytic NO removal performance [5]. Therefore, appropriate hydrothermal treatment time should be employed to enhance the photocatalytic

performance of CH-CN samples. Together with the results of bandgaps [5, 45], a schematic illustration of the electronic structure of the samples was displayed in Fig. 7D, which revealed that the band structures of the obtained samples were optimized during the hydrothermal process.

In order to study the effects of carbon vacancies and hydroxyls on the electronic structure of CN, the total density of states (TDOS) and projected density of states (PDOS) of CN and CH-CN were calculated by DFT. The TDOS revealed that the bandgap of CN was only 1.19 eV (**Fig. 3.1.10**B), which was smaller than the experiment value owing to the well-understood limitation of GGA-PBE functional [46]. However, it still made sense to help us to investigate the effects of carbon vacancies and hydroxyls in CH-CN. Compared with CN, the bandgap of CH-CN (0.92 eV) was narrowed due to
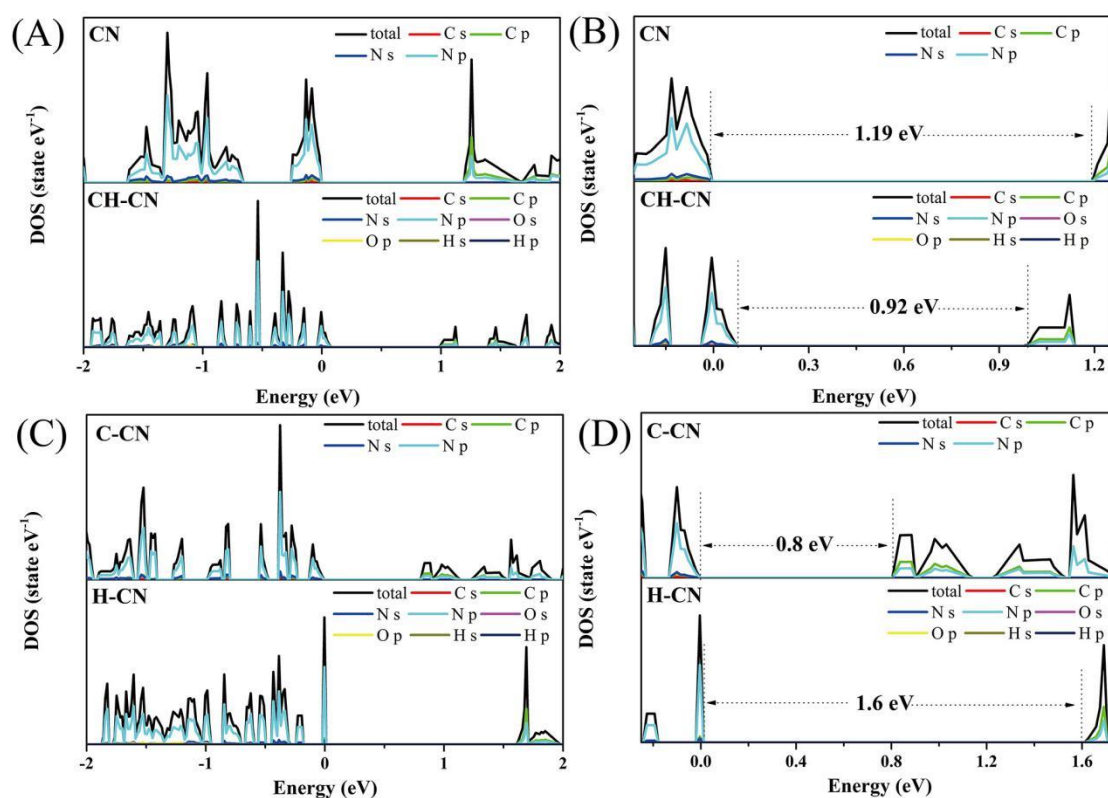
Fig. 3.1.10. (A) Calculated DOS for CN and CH-CN, (B) corresponding enlarged view of the DOS; (C) calculated DOS for C-CN and H-CN, (D) corresponding enlarged view of the DOS. The Fermi level is taken to be zero.

the introduction of carbon vacancies and hydroxyls in CH-CN. The narrowed bandgap was beneficial for light absorption and photogenerated electron-hole pairs generation, causing promoted photocatalytic performance. It is important to note that the theoretical results seemed contradictory to the experimental results. This was because the experimental bandgap of CH-CN was not only related to the carbon vacancies and hydroxyls but also to the quantum confine effect owing to the nanosheet structure of CH-CN, which caused the enlarged bandgap of CH-CN. The valence band edge of CH-CN was shifted upward in good agreement with the experiment results. To analyze the roles of carbon vacancies and hydroxyls deeply, the CN with only carbon vacancies (C-CN) and CN with only hydroxyls (H-CN) were also studied based on the DFT calculations (**Fig. 3.1.11**). As can be learned from the **Fig. 3.1.10**C and **Fig. 3.1.10**D, the carbon vacancies played a positive role in narrowing the bandgap of CN while the hydroxyls had a damaging effect on reducing the bandgap of CN. Although the hydroxyls tended to enlarged the bandgap of CN, giving rise to a lower solar energy absorbing capacity, it enabled to facilitate the local charge separation, which would be further discussed below.
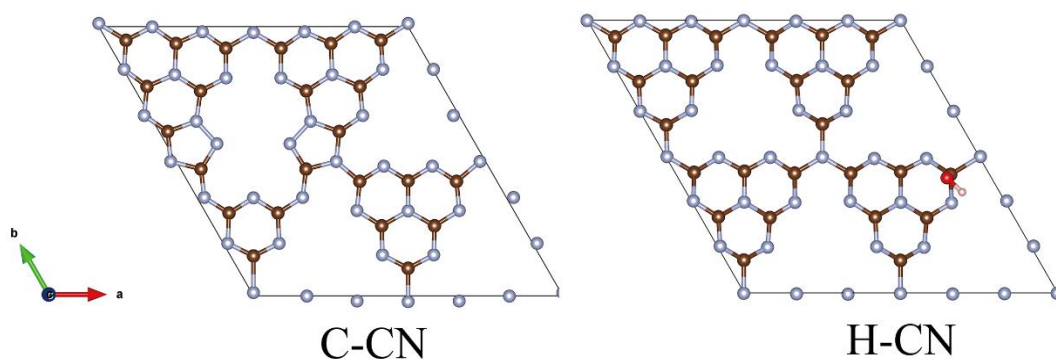
Fig. 3.1.11. The optimized C-CN and H-CN configurations. H, C, N, and O atoms are represented by the white, dark gray, light gray, and red balls, respectively.

Charge carrier separation and transport

It was well-understood that charge carrier separation played crucial roles in determining the photocatalytic activity [20, 47, 48]. Firstly, PL spectra were recorded to unravel the charge carrier separation process. As shown in **Fig. 3.1.12**A, a distinct blue shift of the PL emission peak of CH-CN6 was observed, which was in good

agreement with its enlarged bandgap [35]. Besides, the PL intensity of CH-CN6 was higher than that of CN. It is important to note that this phenomenon could not be simply attributed to the high recombination rates of charge carriers, but was due to the increased concentration of photogenerated electrons and holes because of the enlarged specific surface area [26]. This result was consistent with previous studies [5]. Time-resolved PL spectroscopy was employed to reveal the charge carrier lifetime further. **Fig. 3.1.12**B shows the PL lifetime decay curves of CN and CH-CN6, respectively. The PL lifetime of the samples were calculated by fitting exponentially using the following equation [47, 49-51]:

$$Y = y_0 + A_1 exp\left(-\frac{t}{\tau_1}\right) + A_2 exp\left(-\frac{t}{\tau_2}\right) \tag{3.1-2}$$

where y_0, A_1, and A_2 were calculated after fitting the PL lifetime decay curves. As for τ_1 and τ_2, they were the values of shorter lifetime and longer lifetime, respectively [47]. In addition, the average lifetimes (τ) of the CN and CH-CN6 were calculated by the following equation [52, 53]:

$$\tau = \frac{A_1\tau_1^2 + A_2\tau_2^2}{A_1\tau_1 + A_2\tau_2} \tag{3.1-3}$$

The **Table 3.1.3** summaries the average lifetime of CN and CH-CN6. Compared with CN (1.29 ns), the CH-CN6 (3.07 ns) displayed an obviously increased lifetime, which was indicative of promoted charge carrier separation efficiency [54]. The increased PL lifetime means that the charge carrier had the greater possibilities of involving the subsequent surface redox reactions [35].

Table 3.1.3 Exponential decay-fitted parameters of PL lifetime for CN and CH-CN6.

Samples	τ_1 (ns)	Rel. (%)	τ_2 (ns)	Rel. (%)	τ (ns)
CN	0.86	70.0	4.02	30.0	1.29
CH-CN6	0.95	60.0	3.84	40.0	3.07
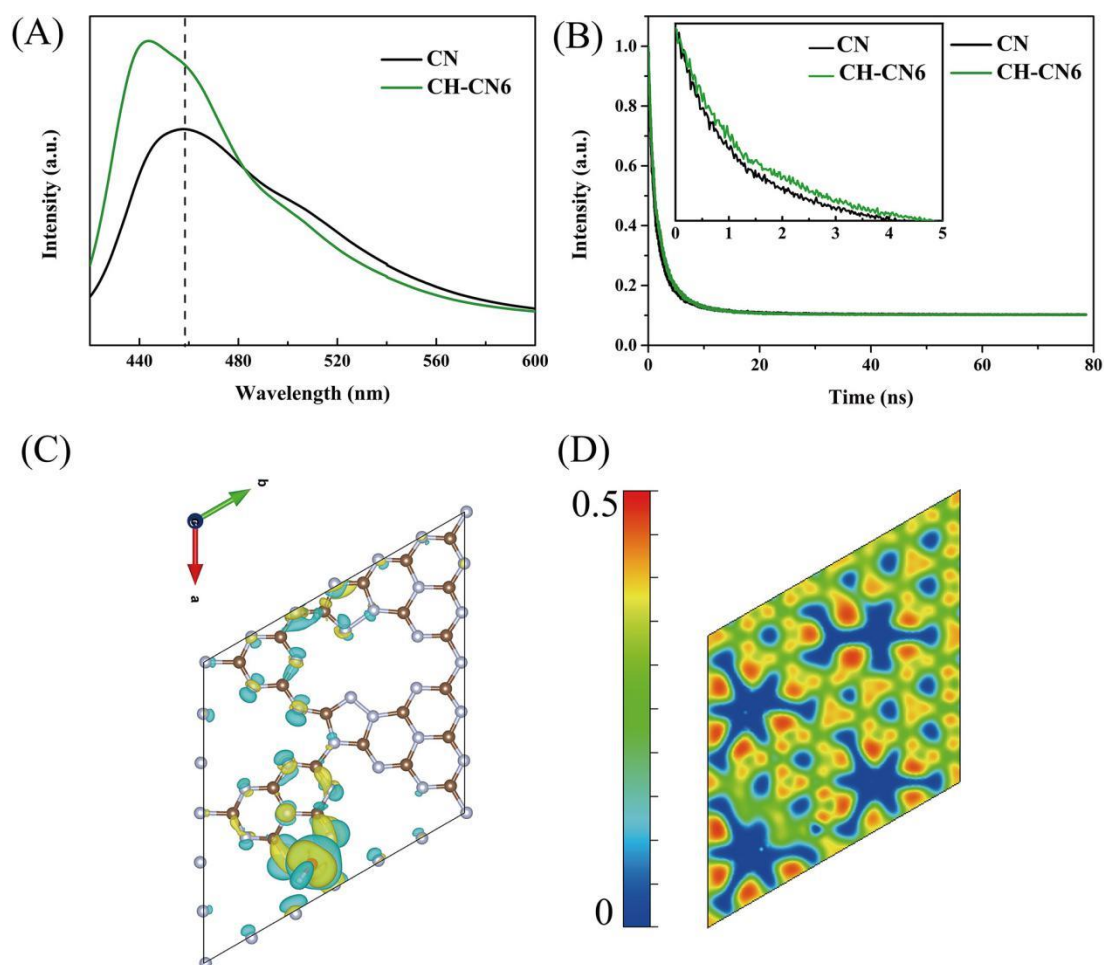
Fig. 3.1.12. (A) steady-state PL spectra; (B) time-resolved PL spectra of CN and CH-CN; respectively. (C) the three-dimensional charge density difference (iso values: 0.005 e/Å^3); and (D) electronic localization function of CH-CN6

In order to characterize the charge separation efficiency deeply, DFT calculations were also performed. As is illustrated in **Fig. 3.1.12**C, the charges were inclined to deplete from C atoms (light-blue isosurfaces) and accumulate around O atoms (yellow isosurfaces), which revealed that the electrons tended to transport from CN lattice skeleton to the surface hydroxyls, resulting in the three-dimensional (3D) conjugate electron system and local spatial charge separation [36, 55-57]. This was supported by the electronic localization function displayed in **Fig. 3.1.12**D. There was a stable covalent bond (H-O-C=N) between -OH and -C=N acted as electron transport channel among the atoms. At the same time, it must be mentioned that the charge carrier separation efficiency largely depended on the charge transfer rate, which could be

explained using the following equation [19]:

$$v = \hbar\kappa/m^*$$
(3.1-4)

Where v and m^* were the charge transfer rate and effective mass of the photogenerated electrons and holes, respectively. $\hbar$ was the reduced Plank constant, and κ was the wave vector. Consequently, smaller m^* brought about higher charge carrier separation efficiency. Based on the band structures (Fig.S5), the effective masses of electrons (m_e^*) and holes (m_h^*) were calculated by fitting parabolic function around the conduction band minimum (CBM) and valence band maximum (VBM) according to the following equation[58]:

$$m^* = \hbar^2 \left[\frac{\partial^2 \varepsilon(k)}{\partial k^2}\right]^{-1}$$
(3.1-5)

Where $\varepsilon(k)$ was the band edge eigenvalues. The obtained results of the charge carrier effective mass along different directions are summarized in **Table 3.1.4**. Both the average m_e^* and m_h^* of CH-CN samples were smaller than those of CN, which indicated the faster charge transfer rate and promoted charge carrier separation efficiency[59]. Also, there were differences in the effective masses of photogenerated electrons and holes of CH-CN, which promotes the electron-hole pairs separation efficiency. This had been demonstrated by the steady-state and time-resolved PL spectroscopy. Single carbon vacancies and hydroxyls were also simulated respectively to reveal their synergistic effects on photocatalytic performance deeply. Compared with CN, the average m_e^* and m_h^* of C-CN was decreased significantly, suggesting that carbon vacancies were beneficial for improving the charge carrier separation efficiency. However, the average m_h^* of H-CN was increased, which was harmful to enhance the photogenerated electrons and holes separation. But as mentioned before, the surface hydroxyls could induce the local spatial charge separation to enhance the charge carrier separation efficiency. Now, it is reasonable to conclude that the synergistic effects of carbon vacancies and hydroxyls caused the promoted charge carrier separation efficiency.

Table 3.1.4. Calculated effective masses of electrons and holes for CN, CH-CN, C-CN and H-CN by parabolic fitting to the CBM and VBM along a specific direction in the reciprocal space. m_0 was the mass of free electrons.

Species					$m_h{}^*/m_0$
$m_e{}^*/m_0$					
CN H→G	Direction	G→L	G→H	G→H	H→L
	Calculation	3.93	3.60	0.59	8.86
	Average	3.77		4.73	
CH-CN G→H	Direction	G→L	G→H	G→H	G→L
	Calculation	1.85	2.95	0.79	2.01
	Average	2.40		1.4	
C-CN G→H	Direction	G→L	G→H	G→H	G→L
	Calculation	1.69	2.31	1.31	4.89
	Average	2.0		3.1	
H-CN G→H	Direction	G→L	G→H	G→H	G→L
	Calculation	121	45	2.16	5.20
	Average	83		3.68	

Photocatalytic performance and mechanism

The photocatalytic NO removal activities of the as-prepared samples were evaluated under visible light irradiation ($\lambda>400$ nm). As shown in **Fig. 3.1.13**A, the CN displayed limited photocatalytic NO removal activity (15%), and the photocatalytic activity of the samples were enhanced along with hydrothermal treatment time increasing. The CH-CN6 exhibited the highest NO removal performance, which was

2.2 times higher than that of CN. Notably, too much hydrothermal treatment time resulted in decreased photocatalytic performance owing to the destroyed structure of CH-CN9. In addition, photocatalytic stability test of H-CN6 indicated its excellent stability (**Fig. 3.1.13**B), which could be further supported by XRD patterns (**Fig. 3.1.14**A) and FTIR spectra (**Fig. 3.1.14**B). Considering its excellent photocatalytic NO removal performance and low-cost metal-free property, the CH-CN6 photocatalyst was superior to our lab previously reported metal-based photocatalysts. To demonstrate the photocatalytic performance of CH-CN6 was competitive, we also compared the photocatalytic performance of CH-CN6 with CN based photocatalyst developed by different strategies such as metal doping (Rb-CN) [1], nonmetal doping (B-CN) [60], nitrogen vacancies [11], rGO/CN [61] and heterostructure constructing (CN/BiOBr) [62] , by the enhanced ratio, i.e., modified CN/pristine CN (**Fig. 3.1.13**C).
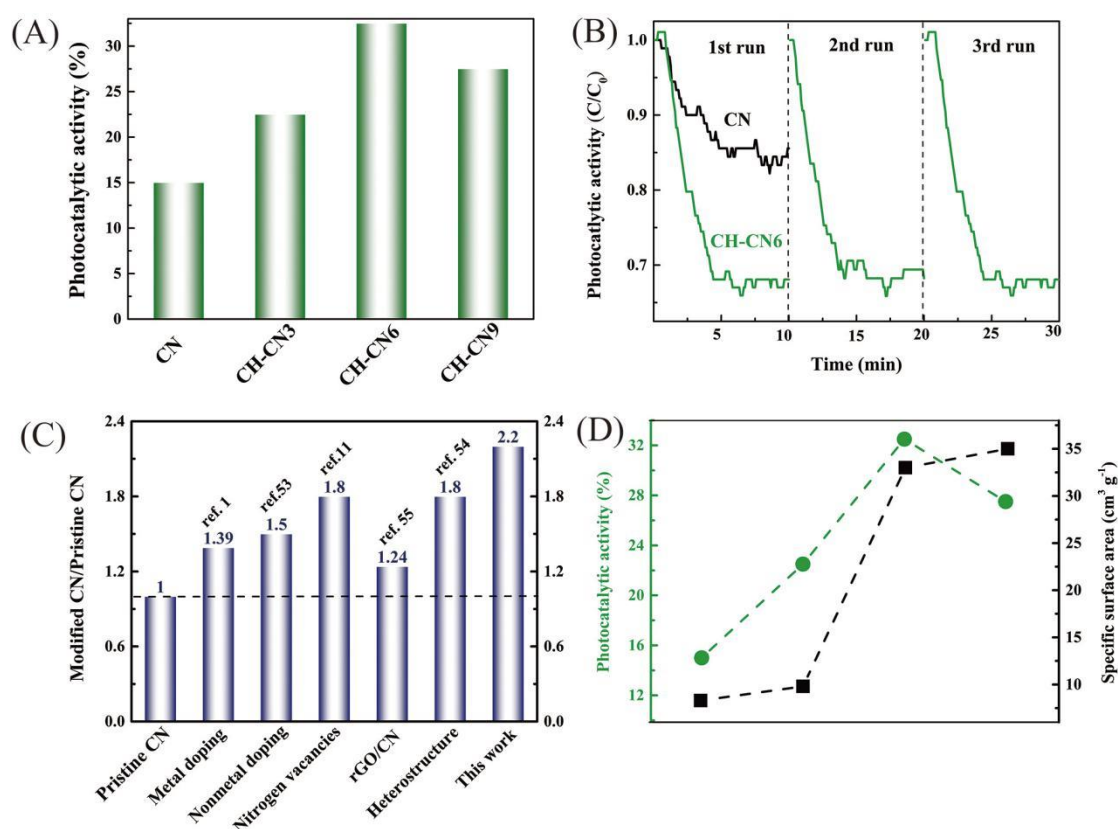
Fig. 3.1.13. (A) Photocatalytic NO removal performance of the obtained samples (λ>400nm), and (B) cycling of CH-CN6 photocatalyst for photocatalytic NO removal; (C) comparisons of different strategies to enhance the photocatalytic NO removal

performance of CN-based photocatalysts.
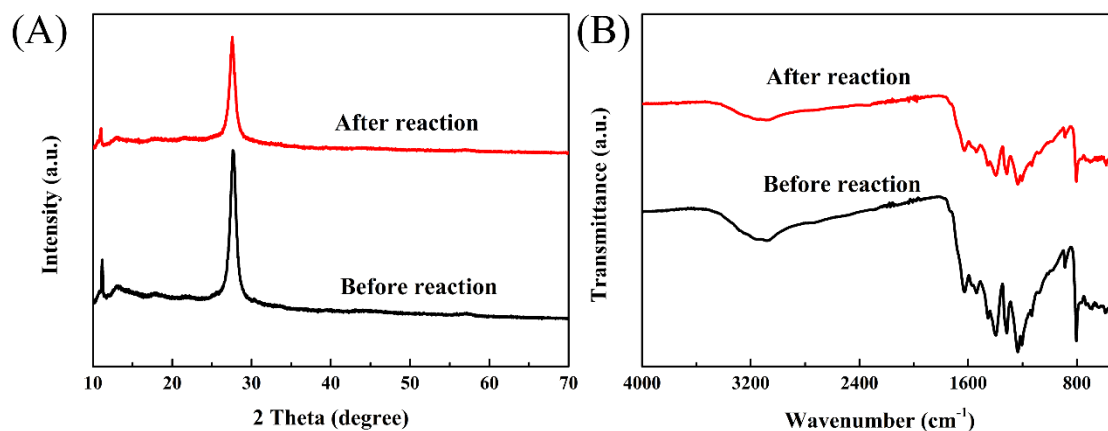
Fig. 3.1.14. (A) XRD patterns and (B) FTIR spectra of CH-CN6 after recycling test.

Based on the above discussions related to the properties of CH-CN6, a possible mechanism was proposed to explain the enhanced photocatalytic NO removal activity. It was commonly known that there are four consecutive steps in various photocatalytic reactions as follows: (i) light absorption; (ii) charge carrier generation; (iii) charge carrier separation; and (iv) surface redox reactions [63]. Firstly, we admitted that the enlarged the specific surface area of CH-CN6 was beneficial for promoting adsorption and the improvement of photocatalytic activity. However, the enlarged specific surface area had only a small role in enhancing the photocatalytic activity, which was supported by the relationship between the specific surface area and the photocatalytic activity (**Fig. 3.1.13**D): the higher specific surface area did not mean higher photocatalytic activity. As depicted in **Fig. 3.1.15**, the synergistic effect of carbon vacancies and hydroxyls played decisive roles in enhancing the photocatalytic NO removal performance. Specifically, the carbon vacancies could reduce the bandgap to absorb more solar energy, resulting in more charge carrier generation [64, 65]; the hydroxyls enable to form the stable covalent bond (H-O-C=N) acted as electron transport channels among the atoms, causing the promoted charge carries separation. It is also important to point out that the accelerated transfer rate of photogenerated electrons and holes of CH-CN could promote photoinduced charge carries separation and keep more charge carriers.

At last, the more remained charge carrier attended the surface redox reactions to enhance the photocatalytic NO removal performance [5, 63]. All in all, the synergistic effects of carbon vacancies and hydroxyls played the pivotal roles in enhancing the photocatalytic NO removal performance during the whole the photocatalysis process.
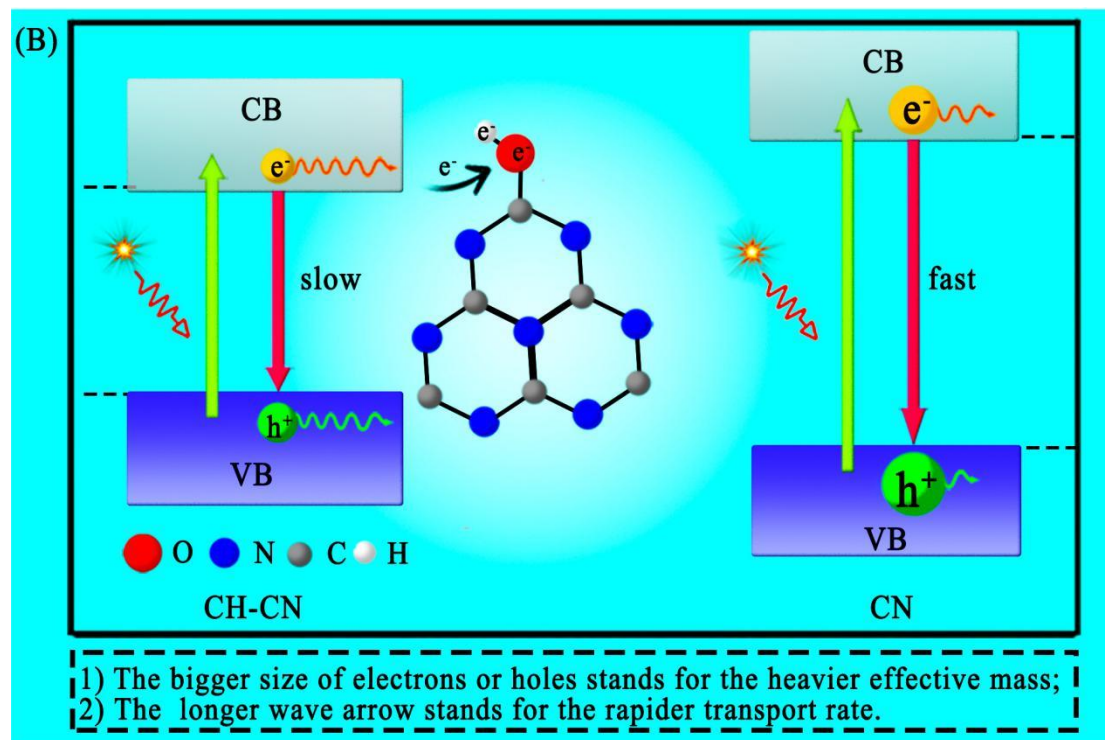
Fig. 3.1.15. Proposed mechanism of the synergistic effects of carbon vacancies and hydroxyls in CH-CN6

3.1.4 Conclusion

In summary, this work demonstrated that carbon vacancies and hydroxyls could be simultaneously introduced into CH-CN samples using a facile hydrothermal method. During the hydrothermal process, the water would induce the unstable domains of bulk CN to hydrolyze partially, which introduced the carbon vacancies and hydroxyls into the resultant CH-CN. The obtained CH-CN6 samples exhibited 2.2 times photocatalytic NO removal performance than that of pristine CN, which could be primarily attributed to the synergistic effects of carbon vacancies and hydroxyls. More specifically, the carbon vacancies could reduce the bandgap of HC-CN to improve the light-absorption;

the hydroxyls enabled to form stable covalent bonds acted as electron transport channels to facilitate the charge carrier separation. Also, the accelerated transfer rate of photogenerated electrons and holes of CH-CN could promote photoinduced charge carries separation and keep more charge carriers. Consequently, the more remained charge carrier attended the surface redox reactions to enhance the photocatalytic NO removal performance. This study may open a new window to prepare CN-based photocatalysts for the enhanced photocatalytic performance.

3.1.5 References

[1] J. Li, W. Cui, Y. Sun, Y. Chu, W. Cen, F. Dong, Directional electron delivery via a vertical channel between g-C$_3$N$_4$ layers promotes photocatalytic efficiency, Journal of Materials Chemistry A, 5 (2017) 9358-9364.

[2] X.-L. Wang, W.-L. An, F. Tian, Y. Yang, H.-X. Xu, D. Wang, X. Zhao, P.-P. Xu, S. Xu, Y.-Z. Wang, Fast microwave-assisted hydrolysis of unsaturated polyester resin into column packing for rapid purifying of dye wastewater, Journal of Hazardous Materials, 384 (2020) 121465.

[3] X.-L. Wang, W.-L. An, Y. Yang, Z.-Y. Hu, S. Xu, W. Liao, Y.-Z. Wang, Porous gel materials from waste thermosetting unsaturated polyester for high-efficiency wastewater treatment, Chemical Engineering Journal, 361 (2019) 21-30.

[4] F. Ding, D. Yang, Z. Tong, Y. Nan, Y. Wang, X. Zou, Z. Jiang, Graphitic carbon nitride-based nanocomposites as visible-light driven photocatalysts for environmental purification, Environmental Science: Nano, 4 (2017) 1455-1469.

[5] Z. Gu, Y. Asakura, S. Yin, High yield post-thermal treatment of bulk graphitic carbon nitride with tunable band structure for enhanced deNOx photocatalysis, Nanotechnology, 31 (2019) 114001.

[6] J. Liao, W. Cui, J. Li, J. Sheng, H. Wang, P. Chen, G. Jiang, Z. Wang, F. Dong, Nitrogen defect structure and NO$^+$ intermediate promoted photocatalytic NO removal on H2 treated g-C$_3$N$_4$, Chemical Engineering Journal, 379 (2020) 122282.

[7] H. Wang, Y. Sun, G. Jiang, Y. Zhang, H. Huang, Z. Wu, S. Lee, F. Dong, Unraveling the mechanisms of visible light photocatalytic NO purification on earth-abundant insulator-based core–shell heterojunctions, Environmental Science & Technology, 52 (2018) 1479-1487.

[8] H. Shang, M. Li, H. Li, S. Huang, C. Mao, Z. Ai, L. Zhang, Oxygen vacancies promoted the selective photocatalytic removal of NO with blue TiO$_2$ via simultaneous molecular oxygen activation and photogenerated hole annihilation, Environmental Science & Technology, 53 (2019) 6444-6453.

[9] A. Nikokavoura, C. Trapalis, Graphene and g-C$_3$N$_4$ based photocatalysts for NO$_x$

removal: a review, Applied Surface Science, 430 (2018) 18-52.

[10] H. Nie, M. Ou, Q. Zhong, S. Zhang, L. Yu, Efficient visible-light photocatalytic oxidation of gaseous NO with graphitic carbon nitride (g-C$_3$N$_4$) activated by the alkaline hydrothermal treatment and mechanism analysis, Journal of Hazardous Materials, 300 (2015) 598-606.

[11] Z. Wang, Y. Huang, M. Chen, X. Shi, Y. Zhang, J.-j. Cao, W. Ho, S.C. Lee, The Roles of N-vacancies over Porous g-C$_3$N$_4$ Microtubes during Photocatalytic NO$_x$ Removal, ACS applied materials & interfaces, (2019).

[12] J. Nowotny, M.A. Alim, T. Bak, M.A. Idris, M. Ionescu, K. Prince, M.Z. Sahdan, K. Sopian, M.A.M. Teridi, W. Sigmund, Defect chemistry and defect engineering of TiO$_2$-based semiconductors for solar energy conversion, Chemical Society Reviews, 44 (2015) 8424-8442.

[13] S.G. Ullattil, S.B. Narendranath, S.C. Pillai, P. Periyat, Black TiO$_2$ nanomaterials: a review of recent advances, Chemical Engineering Journal, 343 (2018) 708-736.

[14] T. Yang, J. Xue, H. Tan, A. Xie, S. Li, W. Yan, Y. Shen, Highly ordered ZnO/ZnFe$_2$O$_4$ inverse opals with binder-free heterojunction interfaces for high-performance photoelectrochemical water splitting, Journal of Materials Chemistry A, (2017).

[15] A. Riapanitra, Y. Asakura, S. Yin, Improved thermochromic and photocatalytic activities of F-VO$_2$/Nb-TiO$_2$ multifunctional coating films, Tungsten, 1 (2019) 306-317.

[16] Y. Wang, T. Liu, H. Li, B. Liu, L. Yang, Tungsten-based photocatalysts with UV–Vis–NIR photocatalytic capacity: progress and opportunity, Tungsten, 1-11.

[17] J. Xue, X. Zhu, Y. Zhang, W. Wang, W. Xie, J. Zhou, J. Bao, Y. Luo, X. Gao, Y. Wang, Nature of conduction band tailing in hydrogenated titanium dioxide for photocatalytic hydrogen evolution, ChemCatChem, 8 (2016) 2010-2014.

[18] X. Wang, K. Maeda, A. Thomas, K. Takanabe, G. Xin, J.M. Carlsson, K. Domen, M. Antonietti, A metal-free polymeric photocatalyst for hydrogen production from water under visible light, Nature Materials, 8 (2009) 76-80.

[19] J. Xue, M. Fujitsuka, T. Majima, The role of nitrogen defects in graphitic carbon nitride for visible-light-driven hydrogen evolution, Physical Chemistry Chemical

Physics, 21 (2019) 2318-2324.

[20] J. Xue, M. Fujitsuka, T. Majima, Near Bandgap Excitation Inhibits the Interfacial Electron Transfer of Semiconductor/Cocatalyst, ACS Applied Materials & Interfaces, (2020).

[21] J. Xue, M. Fujitsuka, T. Majima, Shallow Trap State Induced Efficient Electron Transfer at the Interface of Heterojunction Photocatalysts: The Crucial Role of Vacancy Defects, ACS Applied Materials & Interfaces, (2019).

[22] J. Fu, J. Yu, C. Jiang, B. Cheng, g-C$_3$N$_4$-Based Heterostructured Photocatalysts, Advanced Energy Materials, 8 (2018) 1701503.

[23] J. Wen, J. Xie, X. Chen, X. Li, A review on g-C3N4-based photocatalysts, Applied Surface Science, 391 (2017) 72-123.

[24] S. Bai, N. Zhang, C. Gao, Y. Xiong, Defect engineering in photocatalytic materials, Nano Energy, 53 (2018) 296-336.

[25] L. Ran, J. Hou, S. Cao, Z. Li, Y. Zhang, Y. Wu, B. Zhang, P. Zhai, L. Sun, Defect engineering of photocatalysts for solar energy conversion, Solar RRL.

[26] M. Shen, L. Zhang, M. Wang, J. Tian, X. Jin, L. Guo, L. Wang, J. Shi, Carbon-vacancy modified graphitic carbon nitride: enhanced CO$_2$ photocatalytic reduction performance and mechanism probing, Journal of Materials Chemistry A, 7 (2019) 1556-1563.

[27] Y. Li, W. Ho, K. Lv, B. Zhu, S.C. Lee, Carbon vacancy-induced enhancement of the visible light-driven photocatalytic oxidation of NO over g-C$_3$N$_4$ nanosheets, Applied Surface Science, 430 (2018) 380-389.

[28] L. Wang, G. Zhou, Y. Tian, L. Yan, M. Deng, B. Yang, Z. Kang, H. Sun, Hydroxyl decorated g-C$_3$N$_4$ nanoparticles with narrowed bandgap for high efficient photocatalyst design, Applied Catalysis B: Environmental, 244 (2019) 262-271.

[29] X.-j. Wang, X. Tian, F.-t. Li, Y.-p. Li, J. Zhao, Y.-j. Hao, Y. Liu, Synchronous surface hydroxylation and porous modification of g-C3N4 for enhanced photocatalytic H2 evolution efficiency, International Journal of Hydrogen Energy, 41 (2016) 3888-3895.

[30] Y. Zheng, Z. Zhang, C. Li, S. Proulx, Surface hydroxylation of graphitic carbon

nitride: Enhanced visible light photocatalytic activity, Materials Research Bulletin, 84 (2016) 46-56.

[31] X. Wu, S. Yin, Q. Dong, C. Guo, H. Li, T. Kimura, T. Sato, Synthesis of high visible light active carbon doped TiO_2 photocatalyst by a facile calcination assisted solvothermal method, Applied Catalysis B: Environmental, 142 (2013) 450-457.

[32] J. Wang, Y. Asakura, S. Yin, Preparation of $(Zn_{1+x}Ge)$ $(N_2 O_x)$ nanoparticles with enhanced NO_x decomposition activity under visible light irradiation by nitridation of Zn_2GeO_4 nanoparticles designed precisely, Nanoscale, 11 (2019) 20151-20160.

[33] M. Kobayashi, Y. Suzuki, T. Goto, S.H. Cho, T. Sekino, Y. Asakura, S. Yin, Low-temperature hydrothermal synthesis and characterization of $SrTiO_3$ photocatalysts for NO_x degradation, Journal of the Ceramic Society of Japan, 126 (2018) 135-138.

[34] T. Sano, S. Tsutsui, K. Koike, T. Hirakawa, Y. Teramoto, N. Negishi, K. Takeuchi, Activation of graphitic carbon nitride (g-C_3N_4) by alkaline hydrothermal treatment for photocatalytic NO oxidation in gas phase, Journal of materials chemistry A, 1 (2013) 6489-6496.

[35] Y. Xiao, G. Tian, W. Li, Y. Xie, B. Jiang, C. Tian, D. Zhao, H. Fu, Molecule self-assembly synthesis of porous few-layer carbon nitride for highly efficient photoredox catalysis, Journal of the American Chemical Society, (2019).

[36] S. Yu, J. Li, Y. Zhang, M. Li, F. Dong, T. Zhang, H. Huang, Local spatial charge separation and proton activation induced by surface hydroxylation promoting photocatalytic hydrogen evolution of polymeric carbon nitride, Nano Energy, 50 (2018) 383-392.

[37] X. Wu, F. Chen, X. Wang, H. Yu, In situ one-step hydrothermal synthesis of oxygen-containing groups-modified g-C_3N_4 for the improved photocatalytic H_2-evolution performance, Applied Surface Science, 427 (2018) 645-653.

[38] T. Song, P. Zhang, T. Wang, A. Ali, H. Zeng, Alkali-assisted fabrication of holey carbon nitride nanosheet with tunable conjugated system for efficient visible-light-driven water splitting, Applied Catalysis B: Environmental, 224 (2018) 877-885.

[39] J. Fu, B. Zhu, C. Jiang, B. Cheng, W. You, J. Yu, Hierarchical porous O-doped g-C_3N_4 with enhanced photocatalytic CO_2 reduction activity, Small, 13 (2017) 1603938.

[40] J. Wang, C. Zhang, Y. Shen, Z. Zhou, J. Yu, Y. Li, W. Wei, S. Liu, Y. Zhang, Environment-friendly preparation of porous graphite-phase polymeric carbon nitride using calcium carbonate as templates, and enhanced photoelectrochemical activity, Journal of Materials Chemistry A, 3 (2015) 5126-5131.

[41] Y. Zheng, Z. Yu, H. Ou, A.M. Asiri, Y. Chen, X. Wang, Black Phosphorus and Polymeric Carbon Nitride Heterostructure for Photoinduced Molecular Oxygen Activation, Advanced Functional Materials, (2018).

[42] M. Zhu, S. Kim, L. Mao, M. Fujitsuka, J. Zhang, X. Wang, T. Majima, Metal-Free Photocatalyst for H_2 Evolution in Visible to Near-Infrared Region: Black Phosphorus/Graphitic Carbon Nitride, Journal of the American Chemical Society, 139 (2017) 13234-13242.

[43] Q. Liang, Z. Li, Z.H. Huang, F. Kang, Q.H. Yang, Holey graphitic carbon nitride nanosheets with carbon vacancies for highly improved photocatalytic hydrogen production, Advanced Functional Materials, 25 (2015) 6885-6892.

[44] P. Niu, L. Zhang, G. Liu, H.M. Cheng, Graphene-like carbon nitride nanosheets for improved photocatalytic activities, Advanced Functional Materials, 22 (2012) 4763-4770.

[45] J. Xue, M. Fujitsuka, T. Majima, Shallow trap state-enhanced photocatalytic hydrogen evolution over thermal-decomposed graphitic carbon nitride, Chemical Communications, (2020).

[46] B. Zhu, L. Zhang, B. Cheng, J. Yu, First-principle calculation study of tri-s-triazine-based g-C_3N_4: a review, Applied Catalysis B: Environmental, 224 (2018) 983-999.

[47] J. Ran, T.Y. Ma, G. Gao, X.-W. Du, S.Z. Qiao, Porous P-doped graphitic carbon nitride nanosheets for synergistically enhanced visible-light photocatalytic H 2 production, Energy & Environmental Science, 8 (2015) 3708-3717.

[48] P. Tiong, H.O. Lintang, S. Endud, L. Yuliati, Improved interfacial charge transfer and visible light activity of reduced graphene oxide–graphitic carbon nitride photocatalysts, RSC Advances, 5 (2015) 94029-94039.

[49] P. Kumar, E. Vahidzadeh, U.K. Thakur, P. Kar, K.M. Alam, A. Goswami, N.

Mahdi, K. Cui, G.M. Bernard, V.K. Michaelis, C_3N_5: A Low Bandgap Semiconductor Containing an Azo-Linked Carbon Nitride Framework for Photocatalytic, Photovoltaic and Adsorbent Applications, Journal of the American Chemical Society, 141 (2019) 5415-5436.

[50] M. Liu, S. Wageh, A.A. Al-Ghamdi, P. Xia, B. Cheng, L. Zhang, J. Yu, Quenching induced hierarchical 3D porous g-C_3N_4 with enhanced photocatalytic CO_2 reduction activity, Chemical Communications, 55 (2019) 14023-14026.

[51] Z. Gu, B. Zhang, Y. Asakura, S. Tsukuda, H. Kato, M. Kakihana, S. Yin, Alkali-assisted hydrothermal preparation of g-C_3N_4/rGO nanocomposites with highly enhanced photocatalytic NOx removal activity, Applied Surface Science, (2020) 146213.

[52] Z. Zhang, J. Huang, M. Zhang, Q. Yuan, B. Dong, Ultrathin hexagonal SnS2 nanosheets coupled with g-C_3N_4 nanosheets as 2D/2D heterojunction photocatalysts toward high photocatalytic activity, Applied Catalysis B: Environmental, 163 (2015) 298-305.

[53] Y. Li, R. Jin, Y. Xing, J. Li, S. Song, X. Liu, M. Li, R. Jin, Macroscopic foam-like holey ultrathin g-C_3N_4 nanosheets for drastic improvement of visible-light photocatalytic activity, Advanced Energy Materials, 6 (2016) 1601273.

[54] Z. Chen, T.-T. Fan, X. Yu, Q.-L. Wu, Q.-H. Zhu, L.-Z. Zhang, J.-H. Li, W.-P. Fang, X.-D. Yi, Gradual carbon doping of graphitic carbon nitride towards metal-free visible light photocatalytic hydrogen evolution, Journal of Materials Chemistry A, 6 (2018) 15310-15319.

[55] Z. Li, X. Meng, Z. Zhang, An Effective Approach to Improve the Photocatalytic Activity of Graphitic Carbon Nitride via Hydroxyl Surface Modification, Catalysts, 9 (2019) 17.

[56] S.L. Wang, J. Li, S. Wang, J.e. Wu, T.I. Wong, M.L. Foo, W. Chen, K. Wu, G.Q. Xu, Two-Dimensional C/TiO_2 Heterogeneous Hybrid for Noble-Metal-Free Hydrogen Evolution, ACS Catalysis, 7 (2017) 6892-6900.

[57] Z. Ma, Z. Cui, C. Xiao, W. Dai, Y. Lv, Q. Li, R. Sa, Theoretical screening of efficient single-atom catalysts for nitrogen fixation based on a defective BN monolayer,

Nanoscale, (2020).

[58] W. Yu, D. Xu, T. Peng, Enhanced photocatalytic activity of g-C_3N_4 for selective CO_2 reduction to CH_3OH via facile coupling of ZnO: a direct Z-scheme mechanism, Journal of Materials Chemistry A, 3 (2015) 19936-19947.

[59] H. Zhang, L. Liu, Z. Zhou, First-principles studies on facet-dependent photocatalytic properties of bismuth oxyhalides (BiOXs), RSC advances, 2 (2012) 9224-9229.

[60] Z. Wang, M. Chen, Y. Huang, X. Shi, Y. Zhang, T. Huang, J. Cao, W. Ho, S.C. Lee, Self-assembly synthesis of boron-doped graphitic carbon nitride hollow tubes for enhanced photocatalytic NO_x removal under visible light, Applied Catalysis B: Environmental, 239 (2018) 352-361.

[61] B. Tang, X. Yang, X. Cao, M. Deng, rGO/g-C_3N_4 photocatalyst with an enhanced catalytic activity for NO removal, Materials Research Express, 6 (2019) 125509.

[62] D. Liu, D. Chen, N. Li, Q. Xu, H. Li, J. He, J.-M. Lu, Surface engineering of g-C_3N_4 by stacked oxygen vacancies-rich BiOBr sheets for boosting photocatalytic performance, Angewandte Chemie, (2019).

[63] H. Li, J. Li, Z. Ai, F. Jia, L. Zhang, Oxygen vacancy-mediated photocatalysis of BiOCl: reactivity, selectivity, and perspectives, Angewandte Chemie International Edition, 57 (2018) 122-138.

[64] Y. Zeng, H. Li, J. Luo, J. Yuan, L. Wang, C. Liu, Y. Xia, M. Liu, S. Luo, T. Cai, Sea-urchin-structure g-C_3N_4 with narrow bandgap (2.0 eV) for efficient overall water splitting under visible light irradiation, Applied Catalysis B: Environmental, (2019).

[65] J. Li, B. Shen, Z. Hong, B. Lin, B. Gao, Y. Chen, A facile approach to synthesize novel oxygen-doped g-C_3N_4 with superior visible-light photoreactivity, Chemical communications, 48 (2012) 12017-12019.

3.2 Synthesis of crystalline carbon nitride with enhanced photocatalytic NO removal performance: an experimental and DFT theoretical study

3.2.1 Introduction

Nowadays, tremendous attention is focused on air pollution due to the increasing utilization of conventional fossil fuels [1-3]. Nitric oxide (NO) is one of the primary components of air pollutants, which is harmful to the environment, human and animal health [3, 4]. For example, it could bring about environmental problems including acid rain, urban photochemical smog, ozone depletion, greenhouse effect and so on. To make matters worse, it would raise the chance of getting disease such as emphysema, bronchitis and cardiopathy [5, 6]. Photocatalysis is considered as an innovative and promising technique to remove the NO by using solar energy [7, 8]. It is accepted that the core challenge of photocatalysis lies in the development of highly-efficient photocatalysts [9, 10]. Since 1972 [11], a variety of photocatalysts have been explored for the energy and environment applications [12-14], following in the pioneering work of Fujishima and Honda. Carbon nitride (CN), as a metal-free semiconductor photocatalyst, has attracted considerable attention since 2009 owing to its excellent physical and chemical properties, good stability, visible-light response and low-cost [15-18]. However, the pristine CN suffers from the marginal visible light absorption and low charge carrier separation efficiency, which results in unsatisfactory photocatalytic activity and limits its further application [19, 20].

To date, different strategies have adopted to improve the photocatalytic performance of pristine CN, including metal and no-metal doping, surface sensitization, dimensionality tuning, heterojunction construction and so on [14, 21]. Recently, Wang et al. has revealed that crystallinity is an important factor in enhancing the photocatalytic hydrogen of CN [22, 23]. Normally, the pristine CN derived from the thermally-induced polymerization of nitrogen-containing precursors (e.g. cyanamide,

dicyanamide, melamine and urea) displays low crystallinity because of the predominantly kinetic hindrance [24]. To address this issue, molten-salts (i.e. KCl and LiCl) were used as high-temperature solvent to guide the polymerization process and tailor the electronic structure of CN [22, 23, 25-27]. However, previously reported molten-salts methods were performed under nitrogen atmosphere, which was complex and expensive in comparison with under ambient atmosphere. Can we extend the molten-salts methods from nitrogen atmosphere to ambient atmosphere? More importantly, the effects of crystallinity on the photocatalytic NO removal performance of CN has not been studied thus far.

In this work, we reported a modified molten-salts method to fabricate the crystalline CN under air atmosphere instead of nitrogen atmosphere. To the best of our knowledge, this is the first time to report preparation of crystalline CN via the modified molten-salts method operated under ambient atmosphere. The modified molten-salts method was facile and had the potential for large-scale application. The photocatalytic performance of the obtained crystalline CN was tested by photocatalytic NO removal irradiated under visible light (λ>400nm). Compared with pristine CN, the resultant crystalline CN exhibited outstanding photocatalytic NO removal performance. Experimental characterizations and theoretical calculations were employed to probe the mechanism of highly enhanced photocatalytic NO removal performance of crystalline CN. This research not only extend the molten-salts methods operated under ambient atmosphere, but also revealed the crucial effects of crystallinity on the photocatalytic NO removal performance of CN.

3.2.2 Experiment

Synthesis of pristine CN

Pristine CN was synthesized by calcining dicyanamide (DCDA) (10 g) in a crucible with a cover at 550 ° C for 4h with a heating rate of 2.2 ° C/min in a muffle furnace. After cooling to room temperature, the resultant yellow product was collected and ground into powder for further use.

Synthesis of crystalline CN

The obtained pristine CN (2 g) and molten-salts (11g of KCl and 9 g of LiCl) was mixed and ground to make them homogeneously. Then the mixture was calcined in a crucible with cover at 550 ° C for 4 h at a heating rate of 5 ° C/min in a muffle furnace. (It is important to note that the mixture was calcined under ambient atmosphere different previously reported under nitrogen atmosphere.) After cooling to room temperature, the product was washed with large amount of hot water (85° C) to remove the molten-salts and collected by vacuum filtration, followed by vacuum drying at 60° C. For abbreviation, the pristine CN and crystalline CN were designated as PCN and CCN, respectively. In comparison, the crystalline CN prepared by the molten salts method with a closed nitrogen system. For abbreviation, the crystalline CN prepared by the molten salts method with a closed nitrogen system is index as CCN-N_2. The yield of CCN-N_2 prepared in nitrogen atmosphere was around 70%, which was almost the same with CCN prepared ambient atmosphere (68%).

Characterizations

The phase and crystallinity of PCN and CCN was determined by the X-ray diffraction analysis (XRD, Bruker D2 Phaser) using monochromatized Cu Kα radiation. Fourier transform infrared spectroscopy (FTIR) analysis of the samples was performed FTIR-660D-ATR (JASCO). The UV-visible absorption spectroscopy was measured using UV-vis-NIR V-670 spectrophotometer (JASCO). The morphology and microstructure of PCN and CCN were observed by transmission electron microscopy (TEM) and selected area electron diffraction (SAED) with ZEISS LEO-9522 microscope. The binding energy of the contained elements were confirmed via x-ray photoelectron spectroscopy (XPS, ULVAC PHI 5600). Photoluminescence (PL) spectra of PCN and CCN was obtained using a FP-8500 fluorescence spectrometer ((JASCO). The fluorescence lifetimes of PCN and CCN were detected on a single photon counting spectrometer using a microsecond pulse lamp as the excitation source (375 nm). Electron Spin resonance (ESR) measurements were collected using Bruker E580 spectrometer. The specific surface area was calculated according to the Brunauer-Emmett-Teller (BET) mode using a Quantachrome Instruments (NOVA4200e) at liquid

nitrogen temperature (-196 ° C).

Photocatalytic experiment.

The catalytic performance of PCN and CCN was tested by photocatalytic NO removal at ambient temperature. The 450 W mercury lamp with a cut filter (λ>400 nm) was used as the visible-light source [2, 8]. The samples were spread in the hollow (20 mm × 16 mm × 0.5 mm) of a glass plate and then set at the bottom center of the flow type reactor (373 cm^3 of internal volume). The experimental NO (2ppm) gas was obtained by diluting the compressed NO gas with air stream. The real-time concentration of NO was recorded by NO$_x$ detector (Yanaco, ECL-88A), which controlled the gas flow rate of 200 mL/min. The photocatalytic NO removal efficiency (ŋ) was defined according to the following equation:

$$\text{ŋ}(\%) = \frac{C_0 - C}{C_0} \times 100 \tag{3.2-1}$$

Where C_0 and C were the initial and final concentrations of NO, respectively.

DFT calculations.

All of the calculations were performed using Vienna ab initio simulation package (VASP) based on density functional theory (DFT). The ion-electron interactions were described by the projected augmented wave (PAW) method. The generalized gradient approximation (GGA) with Perdew-Burke-Emzerhof (PBE) was used to describe the exchange-correction functional. The 2×2×1CCN supercell and 2×2×1 PCN were chosen to carry out first-principles calculations, with a 15 Å vacuum region between the layers in z direction to avoid effects of periodic interlayer interaction. For CCN, the Γ-centered 5×5×1 (geometry optimization) and 7×7×1 (self-consistent) Monkhorst-Pack grids for the Brillouin zone sampling (for PCN, geometry optimization 4×3×1; self-consistent: 8×6×1) and cutoff energy of 500eV for plane wave expansion were used. For geometry optimizations, all atoms were relaxed until the force acting on each atom was less than 0.02 eV/Å and the total energy was converged to $1.0×10^{-4}$ eV. The long-range van der Walls (vdW) interaction was of great significance in describing the geometry optimization of 2D materials. In this work, the Grimme's scheme (D3) was used to modify the long-range dispersion interactions.

The adsorption energy (E_{ads}) of molecules adsorption on CCN and PCN (substrate) were calculated by the following equations:

$$E_{ads} = E_{m@substrate} - E_{substrate} - E_m \qquad (3.2\text{-}2)$$

where $E_{m@substrate}$, $E_{substrate}$ and E_m were the total self-consistent energy of the adsorbed system, substrate and the adsorbate (NO and O_2), respectively. In general, as the first step of the catalytic reaction, the adsorption characteristics of the reactants on the catalyst played a vital role. Usually, the reactant molecules need to be chemically adsorbed on the catalyst surface, because the subsequent steps are closely linked with the adsorption process. The electron density difference was an effective method to study the change of electron density in the adsorption process of small molecule, which was calculated by the following equations:

$$\Delta\rho_{Abs} = \rho_{m@substrate} - \rho_{substrate} - \rho_m \qquad (3.2\text{-}3)$$

where $\rho_{m@substrate}$ was the total electron density of the adsorption system, $\rho_{substrate}$ and ρ_m are the electron density of the CCN and PCN (substrate) surface and the isolated NO and O_2, respectively. To focus on the roles of crystallinity and simplify the calculation process, the amino groups of the CCN was not considered in DFT calculation.

3.2.3 Results and discussion

Crystal structure and chemical composition
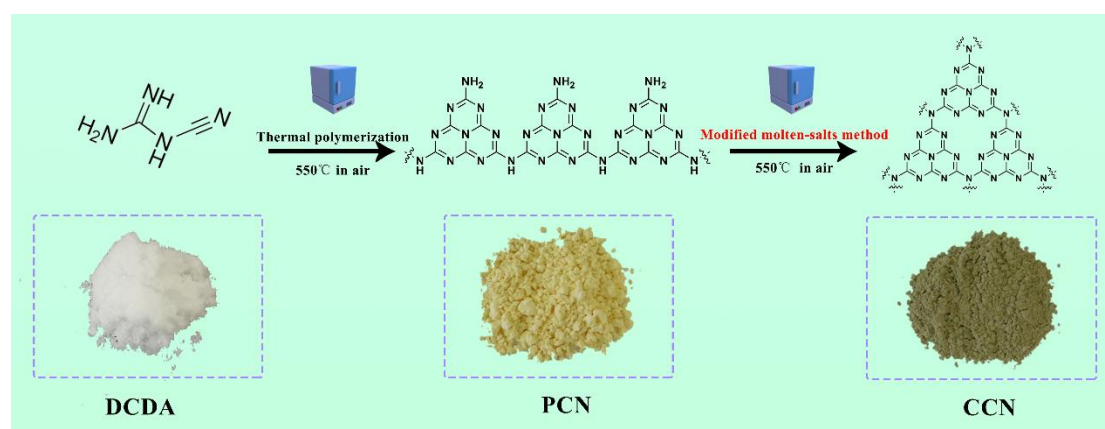
Fig. 3.2.1. Schematic illustration for the preparation of CCN via a modified molten-salts method.

The conventional synthesis of CCN was performed by heating a mixture of PCN and eutectic salts (i.e. KCl and LiCl) under a closed nitrogen system, which was a bottleneck for the scale-up of CCN [22, 23, 25, 28]. To solve the drawback, a modified molten-salts method was developed as depicted in **Fig. 3.2.1**. Firstly, we used DCDA as precursor to prepare PCN. Then the resultant PCN was mixed with eutectic salts (i.e. KCl and LiCl) uniformly as a precursor of CCN. After that, the obtained mixtures were calcined to obtain CCN under ambient atmosphere instead of nitrogen atmosphere. During the calcination process, the eutectic salts (i.e. KCl and LiCl) could increase mobility of PCN [29, 30], which enabled to tailor the electronic structure and crystallinity of PCN [24, 31]. It is important to note that the ambient atmosphere in an open system allows one to prepare CCN in less specialized labs and holds the potential for the scalable production of CCN.
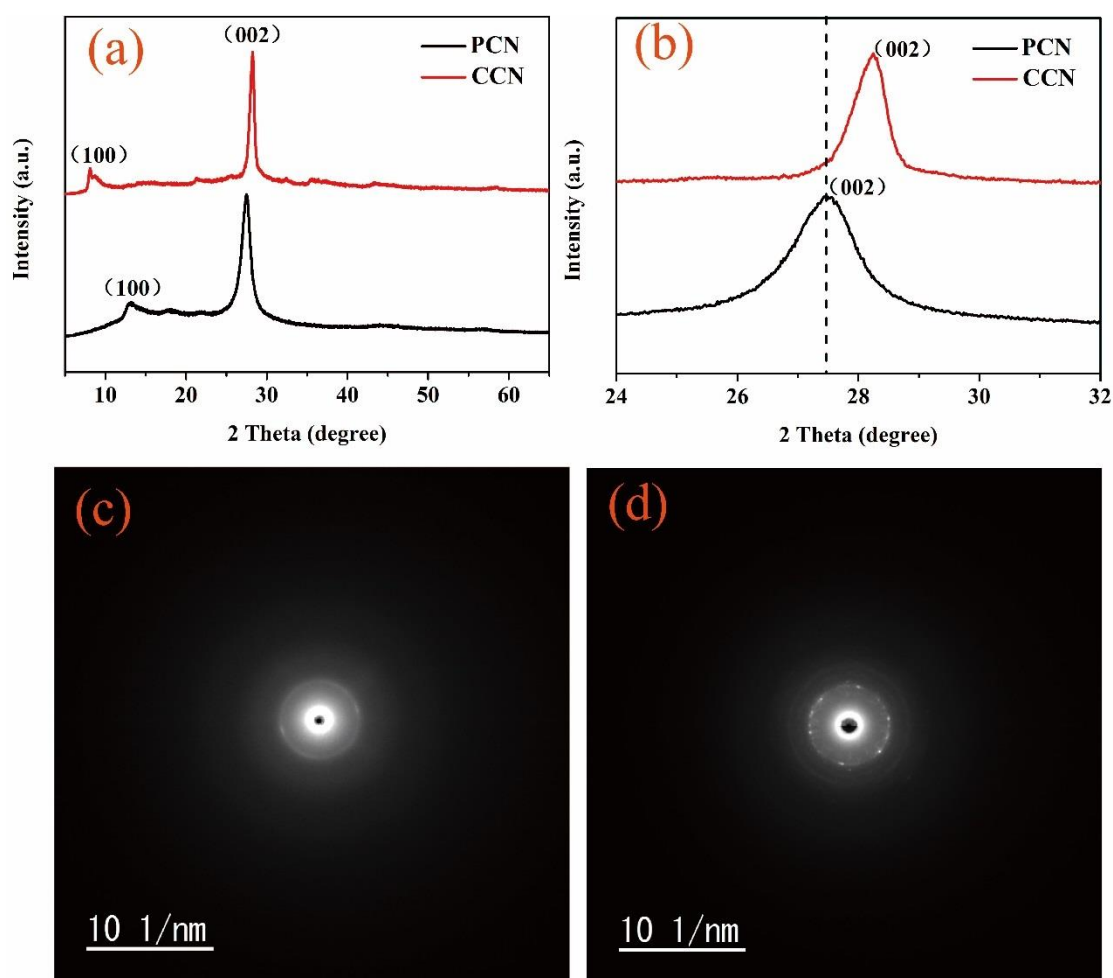
Fig. 3.2.2. (a) Normalized patterns of PCN and CCN, (b) corresponding enlarged XRD

patterns in the range of 24°-32°; SAED images of PCN (c) and CCN(d).

Table 3.2.1. C/N ratios of PCN and CCN determined by the elemental analysis and XPS analysis

Samples	(c) Element analysis		
	C (wt%)	N (wt%)	C/N (atomic)
PCN	34.18	60.62	0.6578
CCN	29.19	49.61	0.6865
Samples	(d) XPS element analysis		
	C (atomic)	N (atomic)	C/N (atomic)
PCN	42.49	56.01	0.7586
CCN	41.36	51.77	0.7989

The crystal structures of PCN and CCN were investigated using XRD as displayed in **Fig. 3.2.2**a and **Fig. 3.2.2**b. The PCN exhibited two characteristic peaks at 13.0 and 27.4 °, corresponding to the (100) and (002) crystal planes of carbon nitride, which could be attributed to the in-plane packing and interfacial stacking of carbon nitride nanosheets, respectively. As for CCN, the peak of (100) was shifted to approximately 8.0 ° consistent with previous literatures, which demonstrated the enlarged in-plane periodicity. In other words, the highly crystalline structure of CCN was confirmed. Moreover, the (002) peak of CCN was slightly shifted to a higher angle in comparison with PCN **Fig. 3.2.2**b), which brought about decreased interlayer distance. This result suggested enhanced interaction between layers of CCN after modified molten-salts treatment. It should be noted that no peaks corresponded the KCl and LiCl crystals,

indicating the removal of the molten-salts by washing with water. Also, the enhanced crystallinity of CCN was strongly demonstrated by the SAED images (**Fig. 3.2.2**c and **Fig. 3.2.2**d). Compared with PCN, the diffraction ring of CCN was more clear owing to the high level of crystallization, which was in good agreement with results of XRD patterns. Based on the XRD patterns and SAED images, it is reasonable to conclude that the crystallinity of CCN wad distinctly improved via the modified molten-salts method.
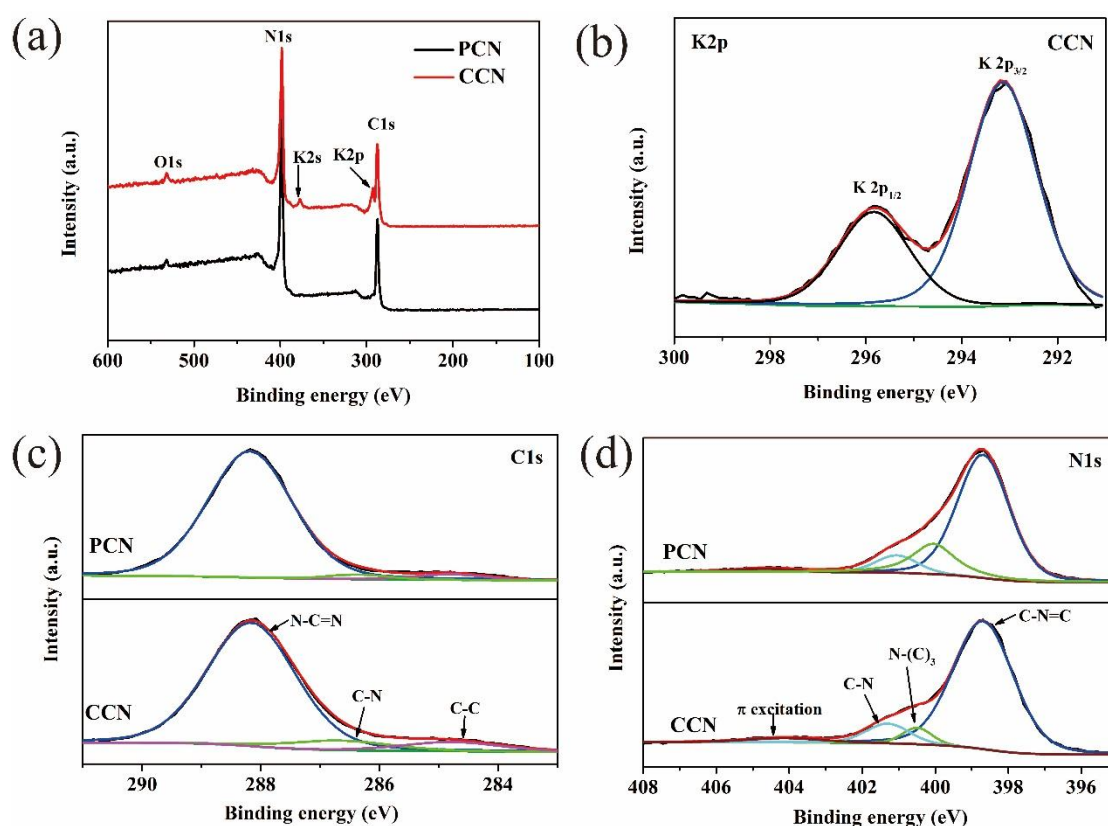
Fig. 3.2.3. (a)XPS spectra of survey for PCN and CCN, (b) XPS spectra of K 2p for CCN, (c) N1s and (c) C1s of spectra for PCN and CCN, respectively.

The composition of PCN and CCN were determined by XPS analysis. There are three elements (C, N, and O) in the survey spectrum of PCN (**Fig. 3.2.3**a). As for CCN, additional K element was observed in the survey spectrum. **Fig. 3.2.3**b exhibited the high-resolution K2p XPS spectrum of CCN. It had been studied that the K ions could not affect the electronic structure of CCN, but enhanced the conductivity, which was

beneficial for the charge carrier separation [16, 32, 33]. It is important to note that no signals corresponding to Cl and Li, which was consistent with previous literatures [23]. For the C 1s spectrum of PCN and CCN (**Fig. 3.2.3**c), three main peaks were observed at the binding energies of 284.8, 286.4, and 288.2 eV. The C 1s peak at 284.8 eV was ascribed to the impurity carbon, which was used as the standard reference carbon. The peaks at 286.4 and 288.2 eV were attributed to bridge functions (C-N) and sp^2-bonded carbon (N-C=N), respectively [16]. For the N1s spectrum of PCN and CCN (**Fig. 3.2.3**d), it could be fitted to four peaks centered at 398.7, 400. 5, 401.5 and 404.3 eV, respectively. The peak at 398.7 eV was attributed to the sp^2-hybridized nitrogen corresponding to the tris-s-triazine rings (C-N=C). The peak centered at 400. 5 eV was assigned to the tertiary nitrogen N-(C)₃ groups. The peak at 401.5 eV was index as bridge functions (C-N) or the terminal amino groups on the surface. The weakest peak located at 404.3 eV was related to the charging effects in the heterocycles [22, 34].
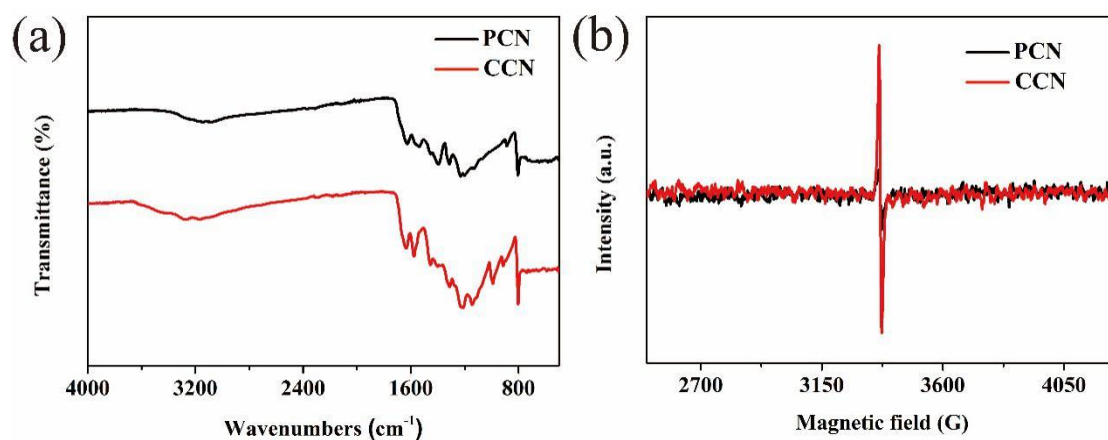
Fig. 3.2.4. (a) FTIR spectra of PCN and CCN; (b) ESR spectra of PCN and CCN.

The FT-IR spectra of PCN and CCN were shown in **Fig. 3.2.4**a. The broad peak between 3000 and 3500 cm^{-1} was ascribed to the terminal amino groups and hydroxyls. The set of peaks in the region from1200 to1700 cm^{-1} were assigned to the tris-s-triazine derivatives[31]. A new peak located at 982 cm^{-1} was observed in CCN due to the symmetric vibration of C-N-C bonds, which was consistent with previous reports [35, 36]. As for the two peaks centered approximately at 805 and 890 cm^{-1}, they were index

as the characteristic breathing mode of tris-s-triazine cycles and deformation mode of N-H in amino groups, respectively [21]. The FTIR spectrum of CCN was similar to that of PCN, which indicated that the modified molten-salts method could retain the basic chemical structure of carbon nitride.

ESR spectra of PCN and CCN were collected at room-temperature to elucidate the electronic nature [37]. As displayed in **Fig. 3.2.4**b, both PCN and CCN showed a single Lorentzian line centered at a g value of 2.0034 owing to the presence of unpaired electrons in the aromatic rings of carbon atoms, which was in good consistent with previous reports [38, 39]. The CCN exhibited the similar ESR signal with that of PCN, suggesting that the basic graphitic heptazine skeleton remains intact in CCN after the modified molten-salts treatment [31, 37]. In addition, CCN showed a much higher EPR signal intensity in comparison with PCN, which was ascribed to the larger number of unpaired electrons in CCN. This result in turn could give an indirect evidence of the increased C/N ratio in CCN [16, 40]. Indeed, according to the element analysis (Table S1), the C/N atomic ratio was increased from 0.6578 (PCN) to 0.6865 (CCN) owing to the removal of amino group in CCN, which brought about the enhanced crystallinity of CCN in comparison with PCN. Similar results were also observed in the XPS element analysis. Considering the XRD patterns, SAED images and element analysis, it is reasonable to conclude that the crystallinity of CCN was significantly improved via the modified molten-salts method.

Morphology and microstructure

The morphology and microstructure of PCN and CCN was characterized using TEM (**Fig. 3.2.5**). The PCN exhibited bulk nanosheet structures, while the CCN displayed plentiful of regular nanorods after the modified molten-salts method, which was beneficial for increasing the specific surface area and pore structure. In addition, the nitrogen adsorption-desorption isotherms for PCN and CCN were carried out to evaluate the specific surface area and porosity (**Fig. 3.2.6**). The CCN exhibited reversible type IV isotherm with a typical H3-type hysteresis loop, which was one of the main characteristics of mesoporous structure. According to the Brunauer-Emmett-Teller (BET) mode, the specific surface areas of PCN and CCN were calculated to be

9.85 and 76.68 m^2g^{-1}, respectively. The pore size distribution curve of CCN disclosed the mesoporous structure, as shown in **Fig. 3.2.6**b. As expected, the pore volume of CCN (0.589 cm^3g^{-1}) was much larger than that of PCN (0.051 cm^3g^{-1}). The enlarged specific surface area could provide more active sites and highly porous structure enabled to shorten the diffusion path of molecular reactants, which was of advantage to enhance the photocatalytic performance of CCN.
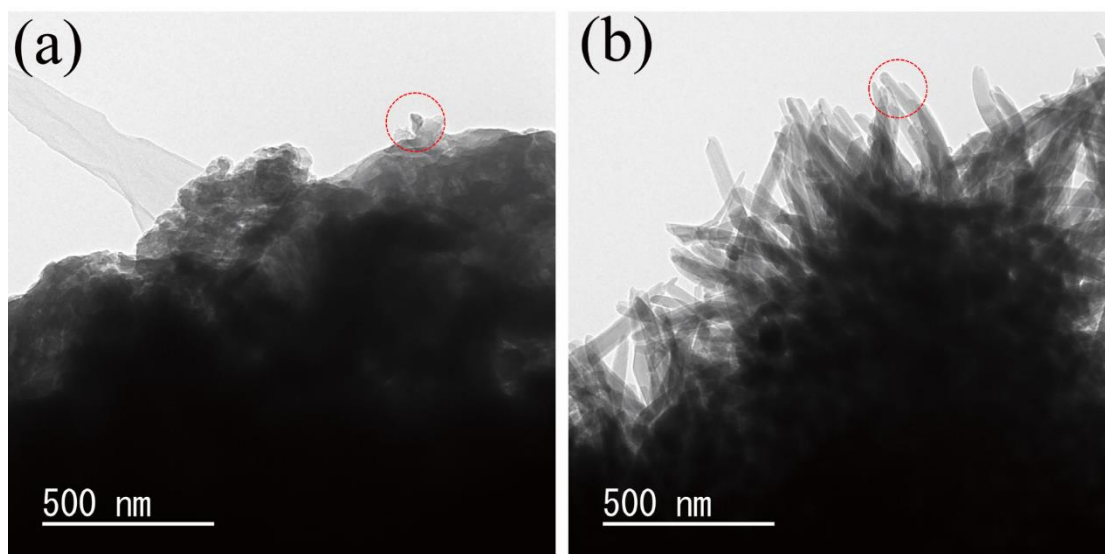
Fig. 3.2.5. TEM images of PCN (a) and CCN (b), respectively. The areas circled by red lines was used for SAED.

The molten salts could simultaneously increase the crystallinity and the surface of CCN. The reasons were as follows: the PCN prepared by thermal-induced polymerization displayed low crystallinity owing to the predominantly kinetic hindrance. The molten-salts acted as high-temperature solution to address this issue, which resulted in the enhanced crystallinity of CCN. At the same time, during the molten-salts process, the deamination would happen in the PCN to obtain large CCN nanosheets, which increased the specific surface areas. For minimizing the surface energy, these formed nanosheets tended to become nanorods, which was consistent with previous reports [22, 23].

Table 3.2.2 BET specific surface area and total pore volume of the obtained samples

Samples	BET surface area	Total pore volume
PCN	9.85	0.051
CCN	76.68	0.589
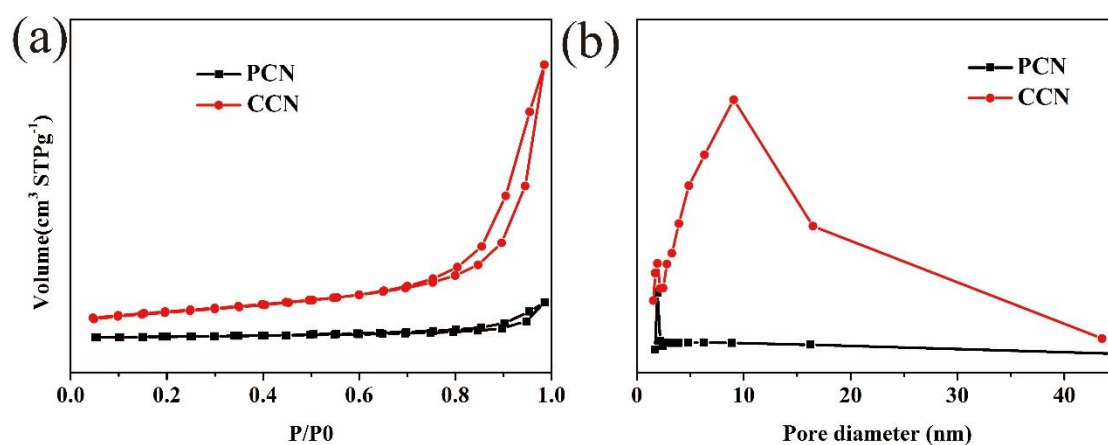
Fig. 3.2.6. (a) Nitrogen gas adsorption isotherms, and (b) corresponding pore size distribution of PCN and CCN

Optical property and band structure

The optical and electronic properties of PCN and CCN were tested by UV-vis DRS (**Fig. 3.2.7**a). The CCN showed significantly enhanced light-harvesting capability above 450 nm in the optical spectrum in comparison with PCN, which was beneficial for improving the photocatalytic performance [41]. The results were also reflected by the smaller bandgap energy of CCN (2.28 eV) than that of PCN (2.50 eV) (**Fig. 3.2.7**b). It was reported that the light-harvesting capability of the polymeric carbon nitride was related to its structural rigidity [29, 35]. Therefore, the enhanced optical property of CCN was ascribed to the increased chain stiffness and interaction between the subunits. In addition, the valence band (VB) of PCN and CCN was calculated by the VB-XPS. As shown in **Fig. 3.2.7**c, the VB of PCN and CCN were nearly identical (1.13eV). This

meant that improving the crystallinity of CCN did not change its VB [24]. Combing with the bandgap values, a schematic diagram of the electronic structure of PCN and CCN was illustrated in **Fig. 3.2.7**d.
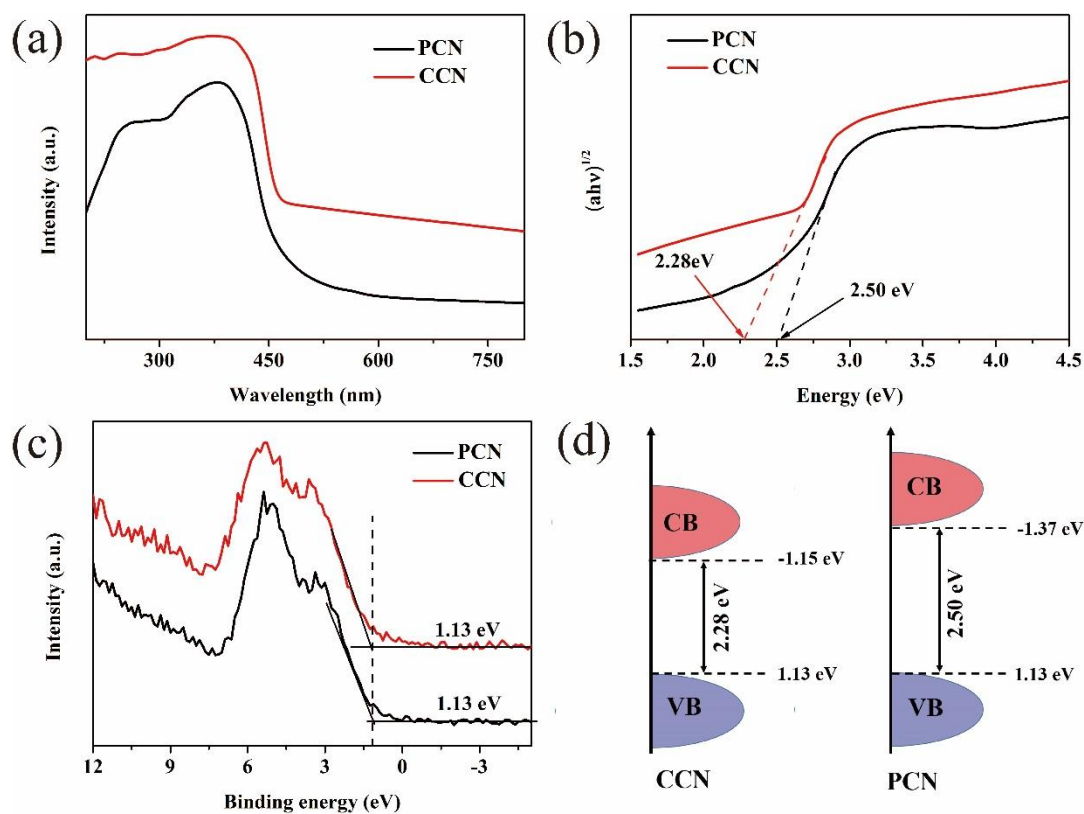
Fig. 3.2.7. (a) UV-vis DRS; (b) Tauc plots for the band gap calculation; (c) VB-XPS spectra, and (d) Energy band structures of PCN and CCN, respectively.

DFT calculation was carried out to study the electronic structure of PCN and CCN deeply (**Fig. 3.2.8**). Considering that the K ions did not change the band structure of CCN significantly, the structural mode of CCN was built without the K ions [16, 42, 43]. **Fig. 3.2.8**a and **Fig. 3.2.8**b displayed the optimized structure mode of CCN and PCN, respectively. Obviously, the major differences between CCN and PCN lied in the removal of amino group in CCN, resulting in the increased C/N ratio in CCN, which was in good agreement with the results of element analysis and XPS element analysis. The bandgap energies of PCN and CCN were 2.50 eV and 1.24 eV, respectively. Moreover, the calculated UV-vis DRS spectra showed the enhanced light-harvesting

capability of CCN in comparison with PCN (**Fig. 3.2.9**). The theoretical results were good consistent with experimental results, qualitatively. It is important to note that both the bandgap of PCN and CCN were underestimated owing to the drawbacks of PBE method.[44] To reveal the contributions of each related orbital to the band structure, the total density of states (TDOS) and partial density of states (PDOS) of PCN and CCN were also obtained. The conduction band minimum (CBM) of PCN mainly consisted of C 2p and N 2p orbitals, while the valance band maximum (VBM) was dominated by the N 2p orbital, which was in agreement with previous reports [45, 46]. Similar results were also observed for CCN. Both experimental characterization and theoretical calculations demonstrated the CCN exhibited a narrower bandgap, which was beneficial for light absorption to enhance the photocatalytic performance.
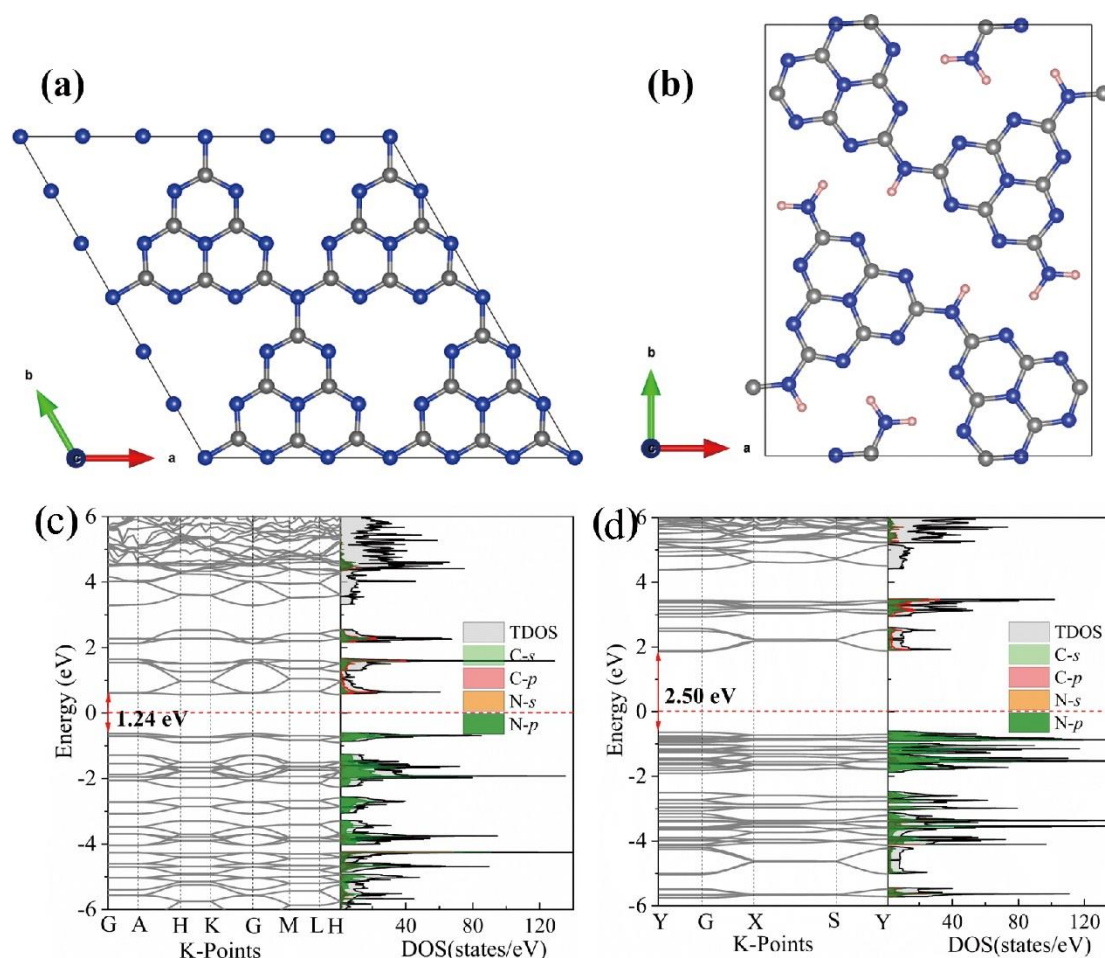
Fig. 3.2.8. The optimized configuration of CCN (a) and PCN (b). C, N and H atoms were represented by the dark, blue and red balls, respectively. The energy band

structures and corresponding calculated DOS of (a) CCN and (b) PCN. The Fermi level is taken as zero.
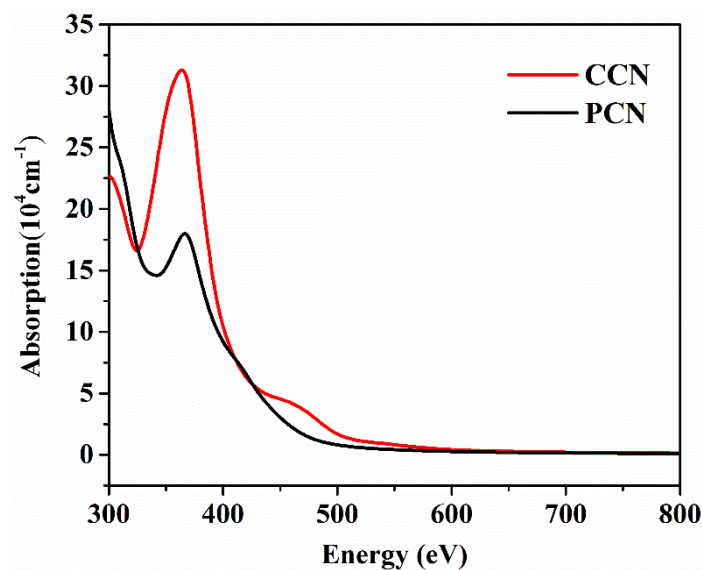
Fig. 3.2.9. Calculated UV-vis DRS spectra of CCN and PCN

Charge carrier separation and transport
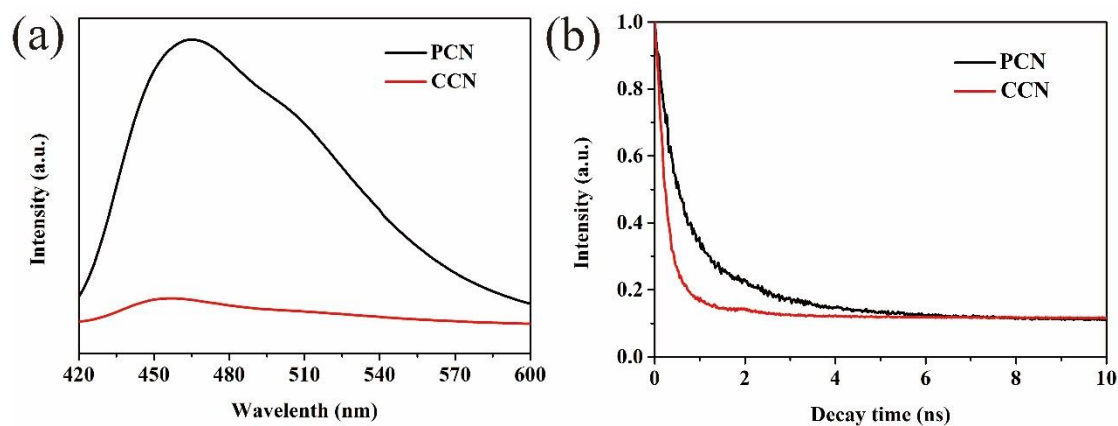
Fig.3.2.10. (a) Steady-state photoluminescence spectra;(b) time-resolved photoluminescence spectra PCN and CCN; respectively.

It is universally acknowledged that the effective separation of photogenerated carriers would be favorable for improving the photocatalytic activity [17, 18, 47, 48]. Steady state and time-resolved photoluminescence (PL) spectroscopy were performed to investigate the migration, transfer and separation efficiency of the photogenerated electron-holes. In general, the PL emission of photocatalysts originated from the charge

carrier recombination [49]. As shown in **Fig.3.2.10**a, there was a distinct decrease in the PL intensity of CCN, compared with that of the PCN, which indicated the enhanced charge carrier separation efficiency of CCN. In addition, **Fig.3.2.10**b showed the time-resolved PL decay spectra of PCN and CCN. The PL lifetimes of PCN and CCN were calculated according the exponential equation [40, 41].

$$Y = y_0 + A_1 exp\left(-\frac{t}{\tau_1}\right) + A_2 exp\left(-\frac{t}{\tau_2}\right) \tag{3.2-4}$$

where y_0 was the baseline correction. A_1 and A_2 were the preexponential factors. The τ_1 and τ_2 were the excited-state luminescence decay time, corresponding to A_1, and A_2, respectively (**Fig.3.2.11**). In addition, the average lifetimes of PCN and CCN could be calculated by the following equation [40, 41].

$$\tau = \frac{A_1\tau_1^2 + A_2\tau_2^2}{A_1\tau_1 + A_2\tau_2} \tag{3.2-5}$$

The average lifetimes of PCN and CCN were 1.46 ns and 0.75 ns, respectively. The decreased lifetime of CCN in comparison to PCN coupled with weak PL of CCN was indicative of fast quenching of the CCN luminescence [37]. This could be ascribed to increased charge migration rate owing to the extended π conjugated system and delocalized electrons, which would be beneficial for the separation of charge carrier [22, 25, 29].
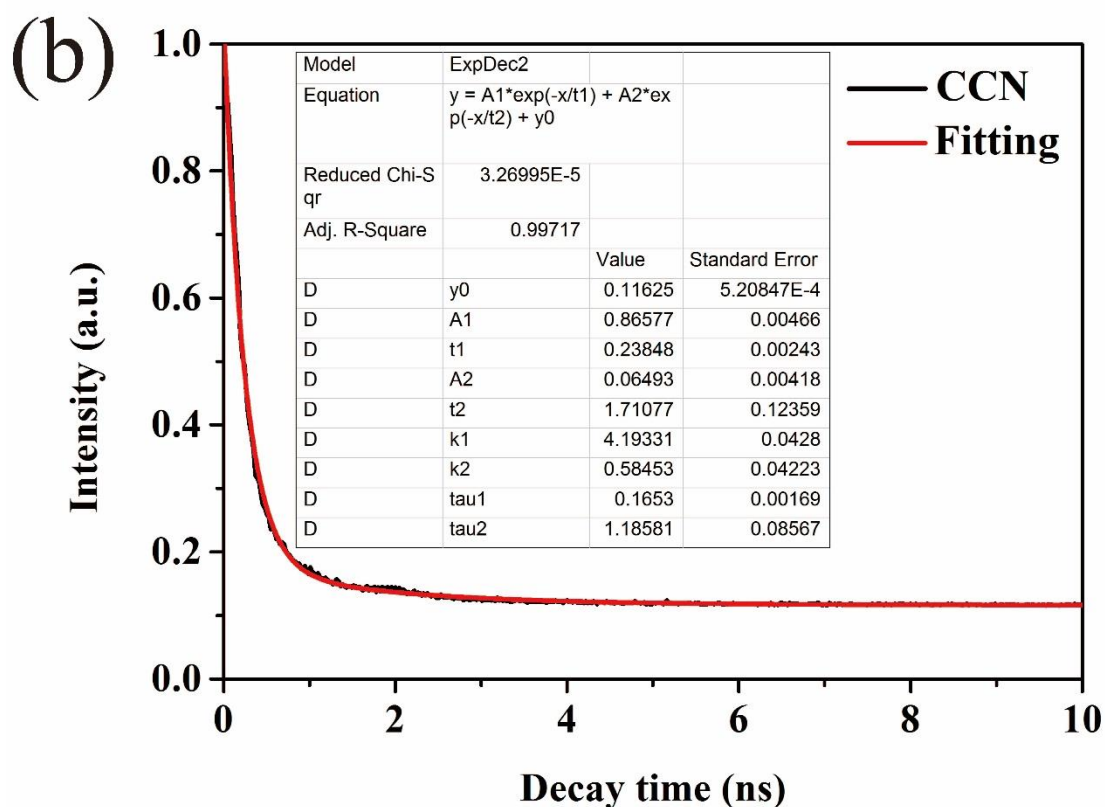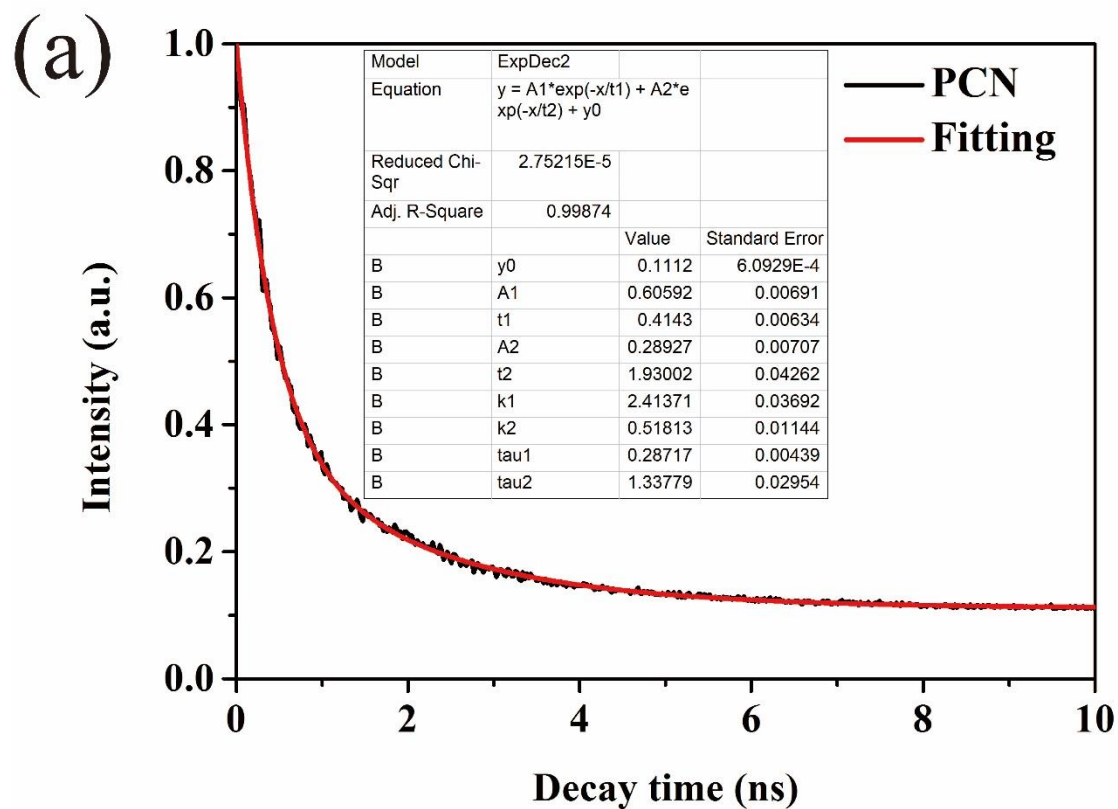
Fig.3.2.11. Exponential decay-fitted parameters of PL lifetime for PCN and CCN.
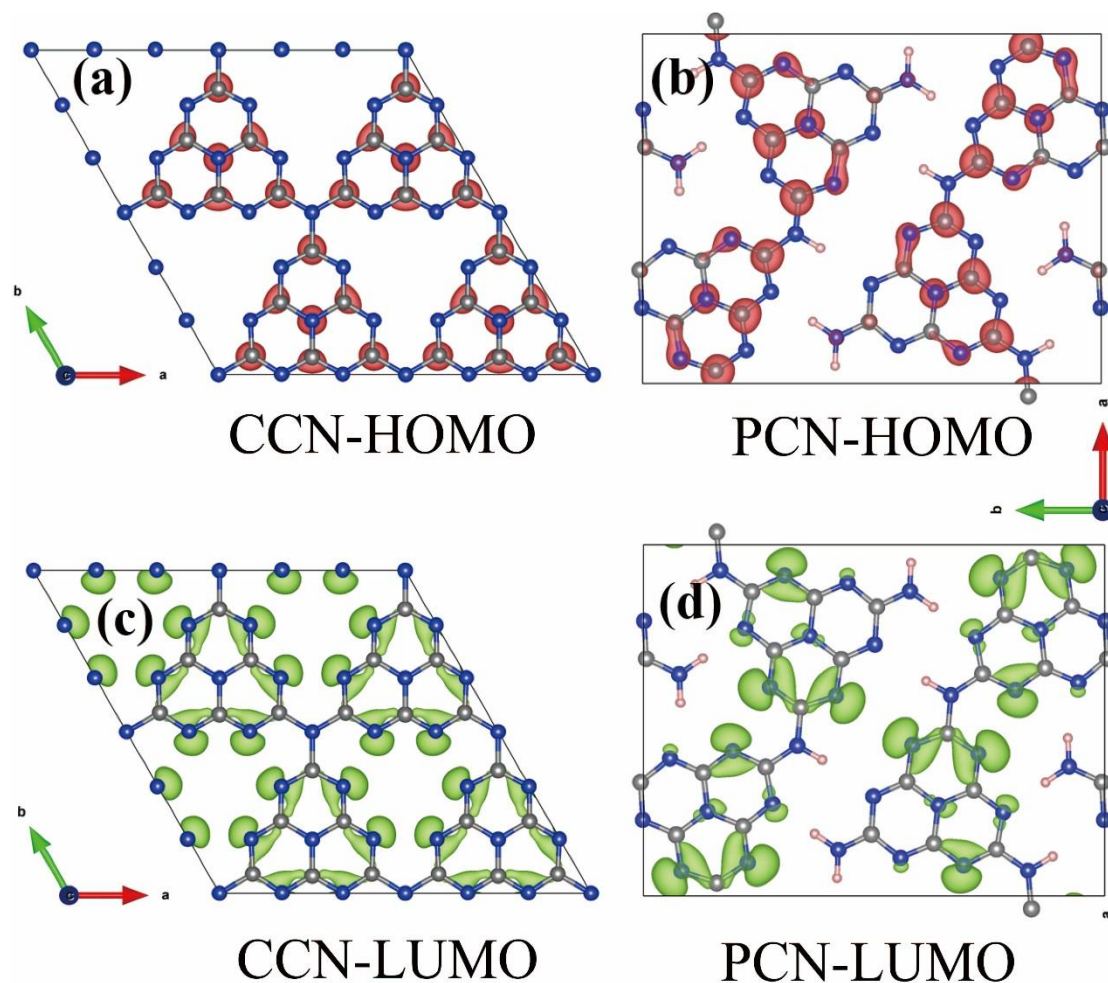
Fig.3.2.12 (a-b) HOMO and LUMO of CCN and PCN, respectively.

In addition, the DFT calculation was performed to investigate the charge carrier separation deeply. The highest occupied molecular orbital (HOMO) and lowest unoccupied molecular orbital (LUMO) of PCN and CCN were shown in **Fig.3.2.12**. Compared with PCN, the photogenerated electrons (corresponding to the LUMO) and holes (corresponding to the HOMO) were located around different atoms of CCN, which reduced the possibility of recombination of photogenerated electrons and holes [42]. In other words, the CCN exhibited better charge carrier separation efficiency than PCN. These results were in good agreement with the experimental results, which indicated the enhanced photocatalytic performance of CCN.

Photocatalytic performance and mechanism
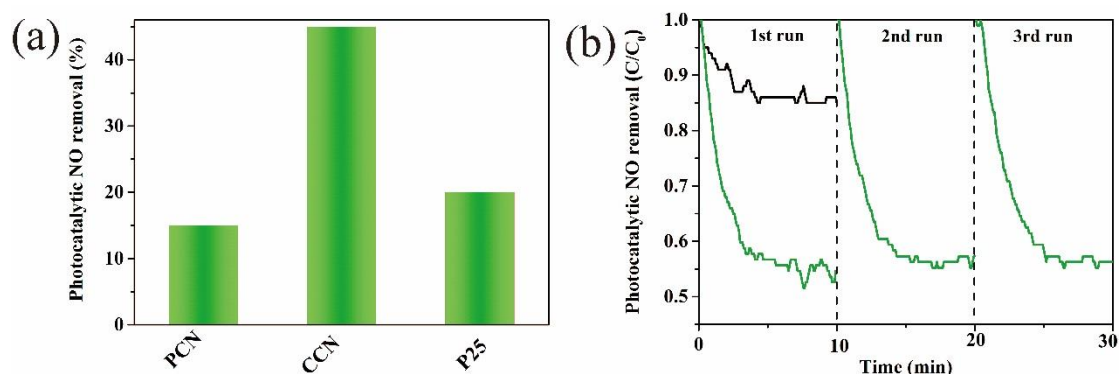
Fig.3.2.13. (a) Photocatalytic performance of PCN and CCN under visible light irradiation(λ>400nm), (b) cycling stability test of CCN photocatalyst.

The photocatalytic performance of PCN and CCN were evaluated under visible-light irradiation (λ>400nm) at room temperature (**Fig.3.2.13**a). The PCN displayed limited photocatalytic activity owing to its low crystallinity. In contrast, the CCN exhibited significantly enhanced photocatalytic NO removal performance after the modified molten-salts thermal treatment, which was 3.0 times higher than that of PCN. Moreover, there was no noticeable decrease in photocatalytic NO removal performance after three cycles (**Fig.3.2.13**b), which indicated the high stability of CCN. The photocatalytic stability of CCN was further demonstrated by the XRD patterns **Fig.3.2.14**a) and FT-IR spectra (**Fig.3.2.14**b). Due to the good catalytic performance and stability, the metal-free CCN held the potential in practical application compared with the reported photocatalysts.
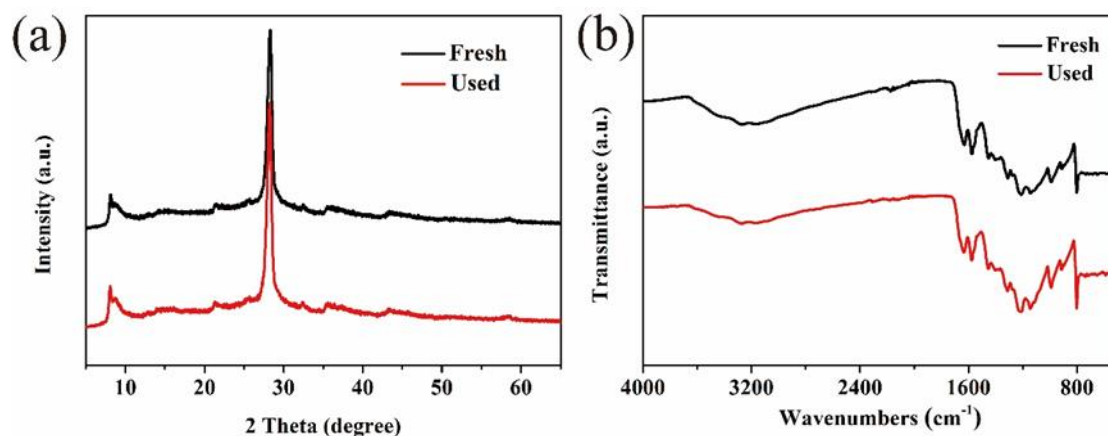
Fig.3.2.14. (a) XRD patterns and (b) FTIR spectra of CCN before and after recycling test.

In addition, the photocatalytic NO removal performance of CCN-N$_2$ was about 46% (**Fig.3.2.15**), which was nearly the same with CCN (45%). The reasons were as follows: in the present modified molten-salts method, the mass ratio of PCN/molten-salts was 1/10. During the post-calcination process, the molten-salts not only acted as high-temperature solution to optimized the crystallinity of PCN, but also protected the PCN from contacting with air. As shown in **Fig.3.2.16**, the PCN was immersed in the molten-salts-solution, which was isolated from the air atmosphere. That is to say, thanks to the large amount of molten-salts-solution, the air nearly could not affect the PCN or CCN. That was why CCN-N$_2$ and CCN displayed the almost the same photocatalytic activity.
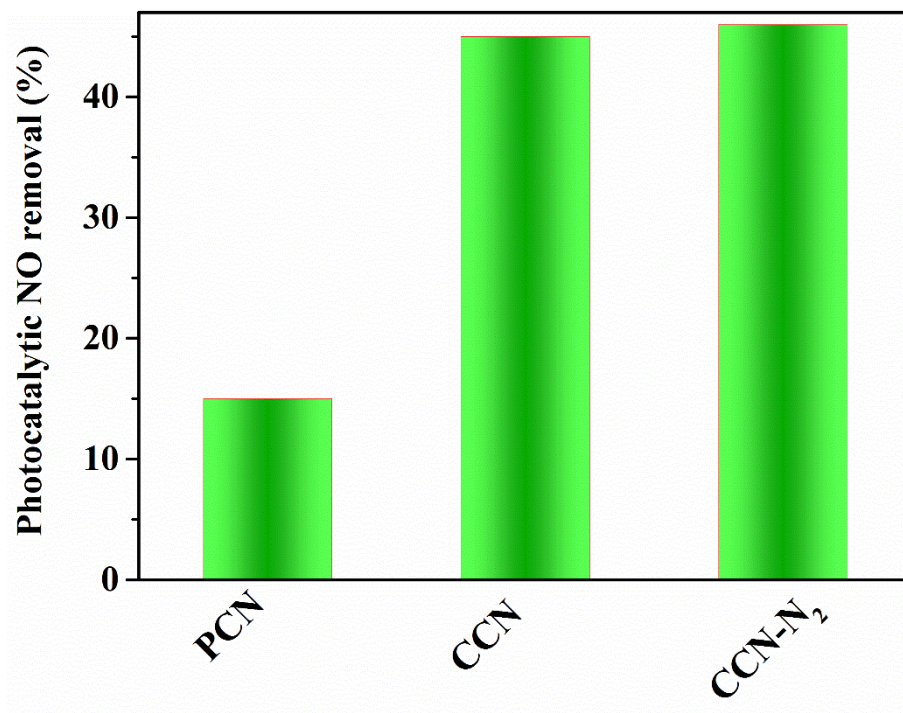
Fig.3.2.15. Photocatalytic performance of PCN, CCN and CCN-N_2 under visible light irradiation(λ>400nm).
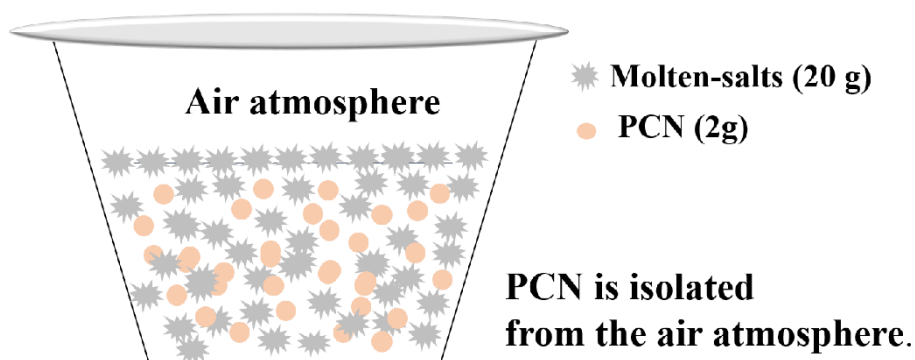
Fig.3.2.16. Illustration of the modified molten-salts method.

$E_{ads}=-1.57$ eV $\Delta Q(NO)=-0.20e$

$E_{ads}=-0.80$ eV, $\Delta Q(O_2)=0.074e$

$E_{ads}=0.945$ eV $\Delta Q(NO)=-0.004e$

$E_{ads}=0.956$ eV, $\Delta Q(O_2)=0.009e$
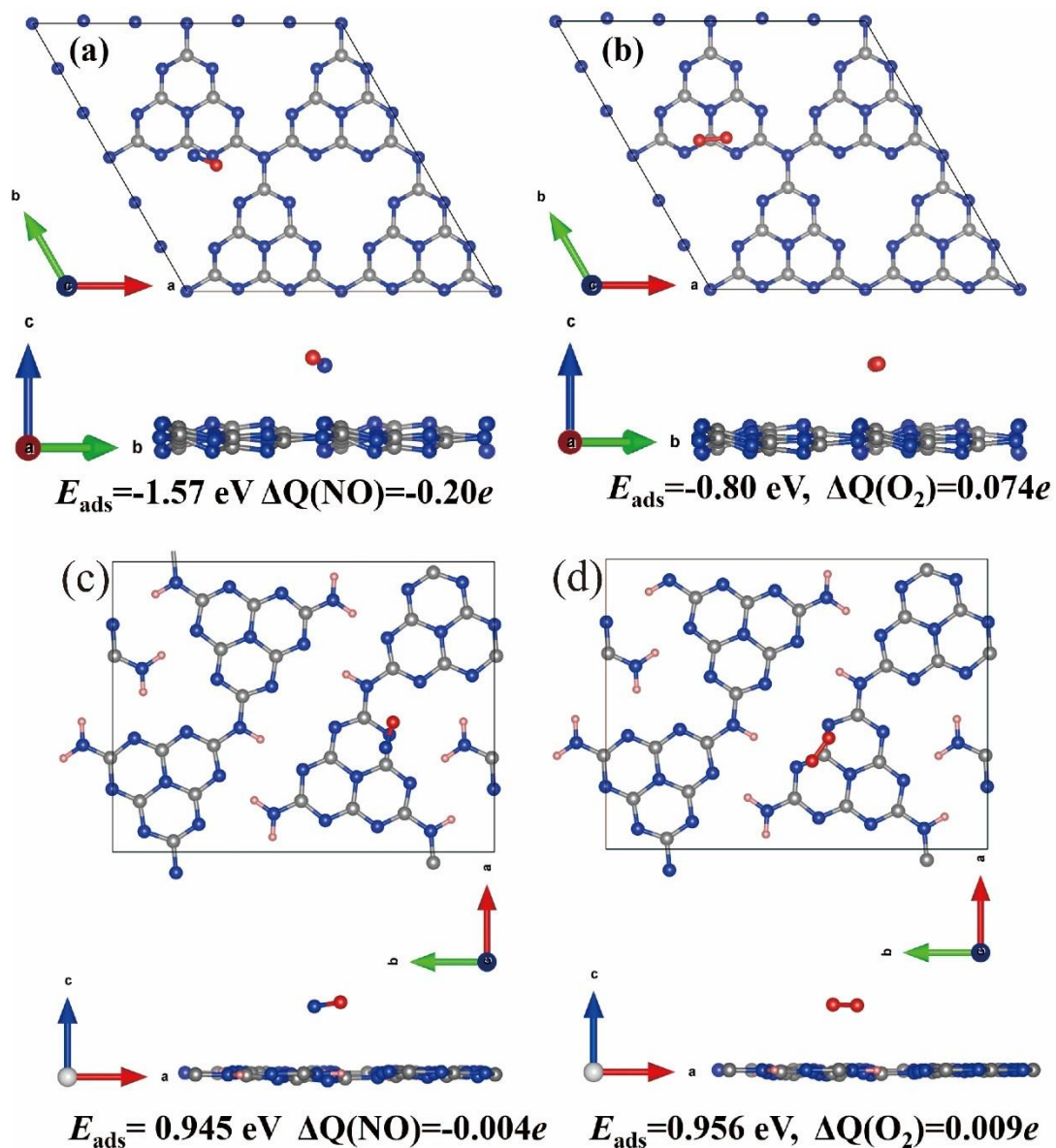
Fig.3.2.17(a-b) The optimized configurations of NO and O_2 molecules adsorbed on CCN; (c-d) the optimized configurations of NO and O_2 molecules adsorbed on PCN

isovalues: 0.0025 e/Å³

isovalues: 0.0025 e/Å³
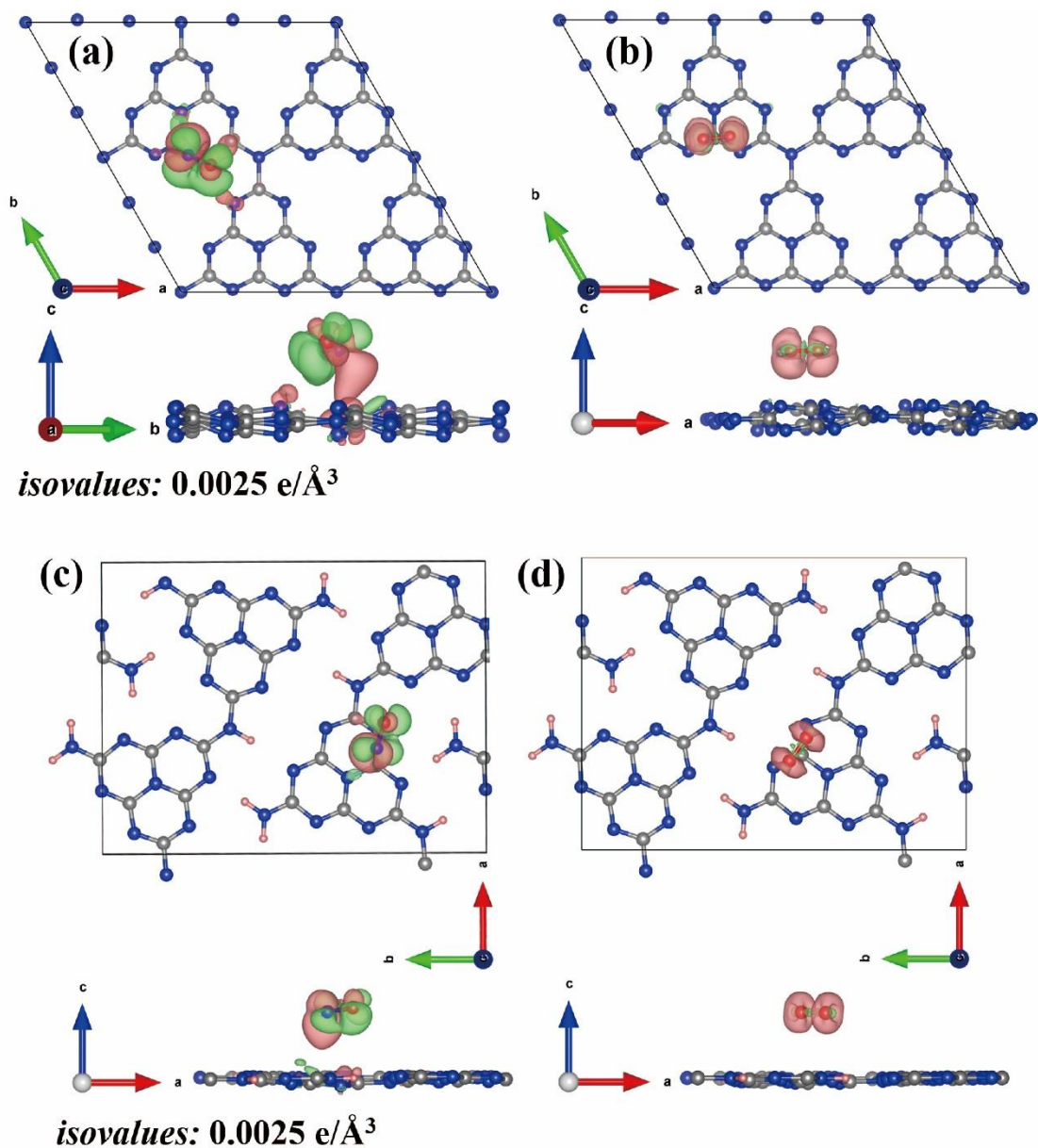
Fig.3.2.18. The charge density difference iso-surface of CCN resulting from adsorption of (a) NO and (b) O$_2$; the charge density difference iso-surface of PCN resulting from adsorption of (c) NO and (d) O$_2$.

It is accepted that the adsorption of reactant molecules on photocatalysts played a pivotal role in the photocatalytic performance [38, 50-54]. Therefore, the adsorption of NO and O$_2$ on PCN and CCN were investigated by DFT calculations. As shown in **Fig.3.2.17**, the stable adsorption configurations of PCN and CCN were obtained after optimizing the initial structures. It is obvious that the molecules (NO and O$_2$) were

much easier to be adsorbed on the surface of CCN than that of PCN because the distance between the molecules (NO and O_2) and CCN was shorter than that of PCN. Concretely, the distance between the NO and CCN was 2.682 Å, while the distance between the NO and PCN was 2.989Å. Similar results were also observed for O_2 (2.863Å for CCN and 2.970 Å for PCN). Based on the calculation results, the CCN displayed lower adsorption energies of NO (-1.57 eV) and O_2 (0.80 eV) than that of PCN, whose adsorption energies were 0.945 eV and 0.956 eV for NO and O_2, respectively. Moreover, the total charge (ΔQ) of NO increased from -0.004 e for PCN and -0.200 e for CCN according to the Bader charge analysis, which revealed that the NO molecules are prone to effortless adsorption and easy activation [51]. Similar results were observed related to the absorption of O_2 on PCN and CCN. Charge density difference could reflect the change in electron density during the small molecule adsorption [52]. **Fig.3.2.18** displayed the charge density difference of CCN and PCN resulting from adsorption of molecules (NO and O_2). Charge accumulation was in red and depletion in green. As shown in **Fig.3.2.18**a and **Fig.3.2.18**, the charges are mainly depleted from NO and accumulated around CCN and PCN. That is to say, the electrons were more likely to transfer from NO to CCN and PCN. It is important to note that the CCN exhibited a larger electron cluster than that of PCN due to the more electrons transfer between NO and substrate, which was in good consistent with the Bader charge analysis. Similar results were observed related to the absorption of O_2 on PCN and CCN. Therefore, it is safe to conclude that the CCN exhibited relatively stronger reactant molecules adsorption and activation ability, which was beneficial for enhancing the photocatalytic NO.

On the basis of the discussions above, a plausible mechanism was proposed to reveal the excellent photocatalytic performance of CCN. It is common knowledge that the typical photocatalytic reactions could be divided into three basic process as follows: (I) light absorption and charge generation; (II) charge separation and migration; (III) surface redox reaction.[55, 56] As illustrated in **Fig.3.2.19**, the CCN exhibited the narrowed bandgap to extend the light absorption and produce much more charge carrier owing to the improved crystallinity. In addition, the improved crystallinity of CCN

brought about the increased charge migration rate due to the extended conjugated system, resulting in facilitated charge separation and migration. Moreover, CCN showed smaller surface adsorption energy of NO and O_2, which was beneficial for reactants activation to improve the photocatalytic activity. Last but not least, the specific surface area of CCN was enlarged to improve the photocatalytic activity. All in all, thanks to the high crystallinity and enlarged specific surface area, the CCN displayed 3.0 times higher photocatalytic NO removal performance than PCN under visible-light irradiation ($\lambda > 400nm$).
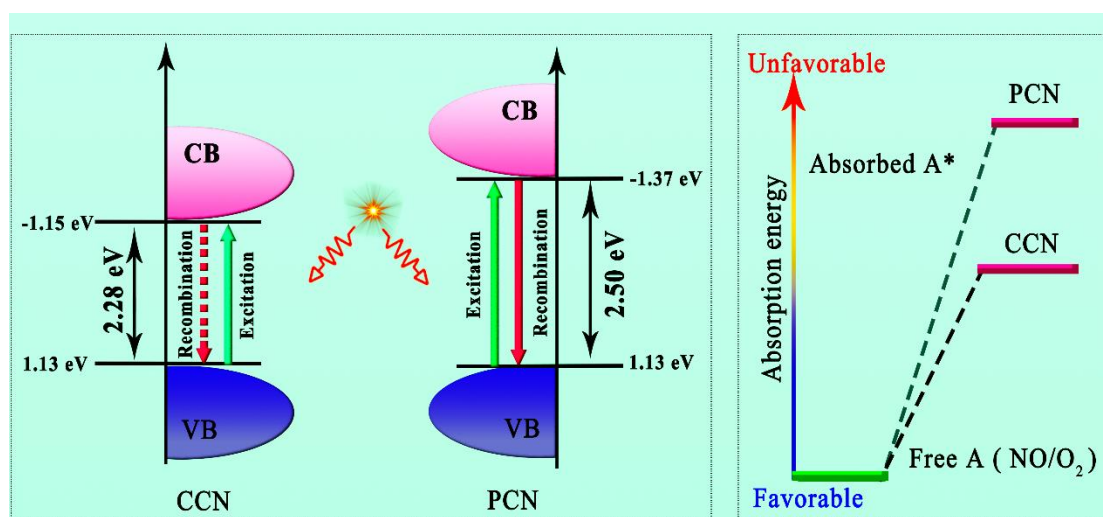
Fig.3.2.19. Proposed mechanism for the crucial role of crystallinity in the photocatalytic NO removal process

3.2.4 Conclusion

In summary, we demonstrated a facile route to synthesize highly crystalline CCN via a modified salts-molten method. The modified salts-molten method was carried out in a scalable and ambient pressure, which is expected to the large-scale production of CCN. The photocatalytic NO removal performance of the resultant CCN was significantly enhanced, which was 3.0 times higher than that of PCN. Detailed experimental characterization and theoretical calculation revealed the crucial role of crystallinity in CCN for the enhanced photocatalytic NO removal performance. The advantages of high crystallinity in CCN were as follows: (1) it would narrow the

bandgap to enhance the light absorption; (2) it could increase the conductivity to facilitate the charge carrier separation; (3) it enabled to decrease the adsorption energy of molecules (i.e. NO and O_2) to activate them for photocatalytic reactions. Our results provided deep insights into the crucial role of crystallinity in CCN for the enhanced photocatalytic NO removal performance. More importantly, the approach used in present work could be extended to improve the crystallinity of other polymeric carbon nitride-based materials (for example C_3N_5) for photocatalytic, photovoltaic and sensor applications.

3.2.5 References

[1] H. Wang, Y. Sun, G. Jiang, Y. Zhang, H. Huang, Z. Wu, S. Lee, F. Dong, Unraveling the mechanisms of visible light photocatalytic NO purification on earth-abundant insulator-based core–shell heterojunctions, Environmental Science & Technology, **52** (2018) 1479-1487.

[2] Z. Gu, Y. Asakura, S. Yin, High yield post-thermal treatment of bulk graphitic carbon nitride with tunable band structure for enhanced deNO$_x$ photocatalysis, Nanotechnology, **31** (2019) 114001.

[3] J. Lasek, Y.-H. Yu, J.C. Wu, Removal of NOx by photocatalytic processes, Journal of Photochemistry and Photobiology C: Photochemistry Reviews, 14 (2013) 29-52.

[4] X. Wu, S. Yin, Q. Dong, C. Guo, H. Li, T. Kimura, T. Sato, Synthesis of high visible light active carbon doped TiO2 photocatalyst by a facile calcination assisted solvothermal method, Applied Catalysis B: Environmental, 142 (2013) 450-457.

[5] J. Ma, C. Wang, H. He, Enhanced photocatalytic oxidation of NO over g-C$_3$N$_4$-TiO$_2$ under UV and visible light, Applied Catalysis B Environmental, 184 (2016) 28-34.

[6] G. Dong, D.L. Jacobs, L. Zang, C. Wang, Carbon vacancy regulated photoreduction of NO to N$_2$ over ultrathin g-C$_3$N$_4$ nanosheets, Applied Catalysis B: Environmental, 218 (2017) 515-524.

[7] H. Shang, M. Li, H. Li, S. Huang, C. Mao, Z. Ai, L. Zhang, Oxygen vacancies promoted the selective photocatalytic removal of NO with blue TiO$_2$ via simultaneous molecular oxygen activation and photogenerated hole annihilation, Environmental Science & Technology, 53 (2019) 6444-6453.

[8] Z. Gu, B. Zhang, Y. Asakura, S. Tsukuda, H. Kato, M. Kakihana, S. Yin, Alkali-assisted hydrothermal preparation of g-C$_3$N$_4$/rGO nanocomposites with highly enhanced photocatalytic NOx removal activity, Applied Surface Science, (2020) 146213.

[9] L. Jiang, X. Yuan, G. Zeng, J. Liang, Z. Wu, H. Wang, Construction of an all-solid-state Z-scheme photocatalyst based on graphite carbon nitride and its enhancement to catalytic activity, Environmental Science: Nano, 5 (2018) 599-615.

[10] F. Ding, D. Yang, Z. Tong, Y. Nan, Y. Wang, X. Zou, Z. Jiang, Graphitic carbon nitride-based nanocomposites as visible-light driven photocatalysts for environmental purification, Environmental Science: Nano, 4 (2017) 1455-1469.

[11] A. Fujishima, K. Honda, Electrochemical photolysis of water at a semiconductor electrode, nature, 238 (1972) 37.

[12] A. Kudo, Y. Miseki, Heterogeneous photocatalyst materials for water splitting, Chemical Society Reviews, 7 (2003) 31-38.

[13] A. Li, W. Zhu, C. Li, T. Wang, J. Gong, Rational design of yolk–shell nanostructures for photocatalysis, Chemical Society Reviews, 48 (2019) 1874-1907.

[14] W.J. Ong, L.L. Tan, H.N. Yun, S.T. Yong, S.P. Chai, Graphitic Carbon Nitride (g-C_3N_4)-Based Photocatalysts for Artificial Photosynthesis and Environmental Remediation: Are We a Step Closer To Achieving Sustainability?, Chemical Reviews, 116 (2016) 7159-7329.

[15] X. Wang, K. Maeda, A. Thomas, K. Takanabe, G. Xin, J.M. Carlsson, K. Domen, M. Antonietti, A metal-free polymeric photocatalyst for hydrogen production from water under visible light, Nature Materials, 8 (2009) 76-80.

[16] J. Xue, M. Fujitsuka, T. Majima, The role of nitrogen defects in graphitic carbon nitride for visible-light-driven hydrogen evolution, Physical Chemistry Chemical Physics, 21 (2019) 2318-2324.

[17] J. Xue, M. Fujitsuka, T. Majima, Shallow Trap State-Induced Efficient Electron Transfer at the Interface of Heterojunction Photocatalysts: The Crucial Role of Vacancy Defects, ACS Applied Materials & Interfaces, 11 (2019) 40860-40867.

[18] J. Xue, M. Fujitsuka, T. Majima, Near Bandgap Excitation Inhibits the Interfacial Electron Transfer of Semiconductor/Cocatalyst, ACS Applied Materials & Interfaces, (2020).

[19] J. Xue, M. Fujitsuka, T. Majima, Shallow trap state-enhanced photocatalytic hydrogen evolution over thermal-decomposed polymeric carbon nitride, Chemical Communications (Cambridge, England), (2020).

[20] J. Fu, J. Yu, C. Jiang, B. Cheng, g-C3N4-Based Heterostructured Photocatalysts, Advanced Energy Materials, 8 (2018) 1701503.

[21] J. Wen, J. Xie, X. Chen, X. Li, A review on g-C3N4-based photocatalysts, Applied Surface Science, 391 (2017) 72-123.

[22] L. Lin, H. Ou, Y. Zhang, X. Wang, Tri-s-triazine-based crystalline graphitic carbon nitrides for highly efficient hydrogen evolution photocatalysis, ACS Catalysis, 6 (2016) 3921-3931.

[23] L. Lin, W. Ren, C. Wang, A. Asiri, J. Zhang, X. Wang, Crystalline carbon nitride semiconductors prepared at different temperatures for photocatalytic hydrogen production, Applied Catalysis B: Environmental, 231 (2018) 234-241.

[24] X. Liu, B. Jing, G. Lun, Y. Wang, X. Wang, C. Fang, Z. Ao, C.-H. Li, Integrating nitrogen vacancies into crystalline graphitic carbon nitride for enhanced photocatalytic hydrogen production, Chemical Communications, (2020).

[25] H. Ou, L. Lin, Y. Zheng, P. Yang, Y. Fang, X. Wang, Tri-s-triazine-based crystalline carbon nitride nanosheets for an improved hydrogen evolution, Advanced Materials, 29 (2017) 1700008.

[26] L. Tian, J. Li, F. Liang, J. Wang, S. Li, H. Zhang, S. Zhang, Molten salt synthesis of tetragonal carbon nitride hollow tubes and their application for removal of pollutants from wastewater, Applied Catalysis B: Environmental, 225 (2018) 307-313.

[27] X. Liu, B. Jing, G. Lun, Y. Wang, X. Wang, C. Fang, Z. Ao, C. Li, Integrating nitrogen vacancies into crystalline graphitic carbon nitride for enhanced photocatalytic hydrogen production, Chemical Communications, 56 (2020) 3179-3182.

[28] L.F. Villalobos, M.T. Vahdat, M. Dakhchoune, Z. Nadizadeh, M. Mensi, E. Oveisi, D. Campi, N. Marzari, K.V. Agrawal, Large-scale synthesis of crystalline g-C$_3$N$_4$ nanosheets and high-temperature H$_2$ sieving from assembled films, Science Advances, 6 (2020) 851.

[29] L. Lin, Z. Yu, X. Wang, Crystalline carbon nitride semiconductors for photocatalytic water splitting, Angewandte Chemie, 131 (2019) 6225-6236.

[30] M.J. Bojdys, J.O. Müller, M. Antonietti, A. Thomas, Ionothermal synthesis of crystalline, condensed, graphitic carbon nitride, Chemistry–A European Journal, 14 (2008) 8177-8182.

[31] W. Ren, J. Cheng, H. Ou, C. Huang, M.M. Titirici, X. Wang, Enhancing visible-

light hydrogen evolution performance of crystalline carbon nitride by defect engineering, ChemSusChem, 12 (2019) 3257-3262.

[32] Y. Li, X. Li, H. Zhang, J. Fan, Q. Xiang, Design and application of active sites in g-C3N4-based photocatalysts, Journal of Materials Science & Technology, 56 (2020) 69-88.

[33] W. Iqbal, B. Qiu, Q. Zhu, M. Xing, J. Zhang, Self-modified breaking hydrogen bonds to highly crystalline graphitic carbon nitrides nanosheets for drastically enhanced hydrogen production, Applied Catalysis B: Environmental, 232 (2018) 306-313.

[34] Y. Li, R. Jin, Y. Xing, J. Li, S. Song, X. Liu, M. Li, R. Jin, Macroscopic foam-like holey ultrathin g-C3N4 nanosheets for drastic improvement of visible-light photocatalytic activity, Advanced Energy Materials, 6 (2016) 1601273.

[35] W. Ren, J. Cheng, H. Ou, C. Huang, M. Anpo, X. Wang, Optimizing the Crystallization Process of Conjugated Polymer Photocatalysts to Promote Electron Transfer and Molecular Oxygen Activation, Journal of Catalysis, (2020).

[36] G. Zhang, G. Li, Z.A. Lan, L. Lin, A. Savateev, T. Heil, S. Zafeiratos, X. Wang, M. Antonietti, Optimizing optical absorption, exciton dissociation, and charge transfer of a polymeric carbon nitride with ultrahigh solar hydrogen production activity, Angewandte Chemie, 129 (2017) 13630-13634.

[37] P. Kumar, E. Vahidzadeh, U.K. Thakur, P. Kar, K.M. Alam, A. Goswami, N. Mahdi, K. Cui, G.M. Bernard, V.K. Michaelis, C3N5: A Low Bandgap Semiconductor Containing an Azo-Linked Carbon Nitride Framework for Photocatalytic, Photovoltaic and Adsorbent Applications, Journal of the American Chemical Society, 141 (2019) 5415-5436.

[38] M. Shen, L. Zhang, M. Wang, J. Tian, X. Jin, L. Guo, L. Wang, J. Shi, Carbon-vacancy modified graphitic carbon nitride: enhanced CO 2 photocatalytic reduction performance and mechanism probing, Journal of materials chemistry A, 7 (2019) 1556-1563.

[39] Y. Li, W. Ho, K. Lv, B. Zhu, S.C. Lee, Carbon vacancy-induced enhancement of the visible light-driven photocatalytic oxidation of NO over g-C$_3$N$_4$ nanosheets, Applied Surface Science, 430 (2018) 380-389.

[40] Z. Gu, Z. Cui, Z. Wang, K.S. Qin, Y. Asakura, T. Hasegawa, S. Tsukuda, K. Hongo, R. Maezono, S. Yin, Carbon vacancies and hydroxyls in graphitic carbon nitride: promoted photocatalytic NO removal activity and mechanism, Applied Catalysis B: Environmental, (2020) 119376.

[41] J. Ran, T.Y. Ma, G. Gao, X.-W. Du, S.Z. Qiao, Porous P-doped graphitic carbon nitride nanosheets for synergistically enhanced visible-light photocatalytic H 2 production, Energy & Environmental Science, 8 (2015) 3708-3717.

[42] Z. Ma, Z. Cui, Y. Lv, R. Sa, K. Wu, Q. Li, Three-in-One: Opened Charge-transfer channel, positively shifted oxidation potential, and enhanced visible light response of g-C3N4 photocatalyst through K and S Co-doping, International Journal of Hydrogen Energy, 45 (2020) 4534-4544.

[43] H. Gao, S. Yan, J. Wang, Y.A. Huang, P. Wang, Z. Li, Z. Zou, Towards efficient solar hydrogen production by intercalated carbon nitride photocatalyst, Physical Chemistry Chemical Physics, 15 (2013) 18077-18084.

[44] B. Zhu, L. Zhang, B. Cheng, J. Yu, First-principle calculation study of tri-s-triazine-based g-C$_3$N$_4$: a review, Applied Catalysis B: Environmental, 224 (2018) 983-999.

[45] J. Cui, S. Liang, X. Wang, J. Zhang, First principle modeling of oxygen-doped monolayer graphitic carbon nitride, Materials Chemistry and Physics, 161 (2015) 194-200.

[46] B. Zhu, B. Cheng, L. Zhang, J. Yu, Review on DFT calculation of s-triazine-based carbon nitride, Carbon Energy, 1 (2019) 32-56.

[47] J. Zhang, S. Wageh, A. Al-Ghamdi, J. Yu, New understanding on the different photocatalytic activity of wurtzite and zinc-blende CdS, Applied Catalysis B: Environmental, 192 (2016) 101-107.

[48] Y. Xiao, G. Tian, W. Li, Y. Xie, B. Jiang, C. Tian, D. Zhao, H. Fu, Molecule self-assembly synthesis of porous few-layer carbon nitride for highly efficient photoredox catalysis, Journal of the American Chemical Society, 141 (2019) 2508-2515.

[49] J. Liqiang, Q. Yichun, W. Baiqi, L. Shudan, J. Baojiang, Y. Libin, F. Wei, F. Honggang, S. Jiazhong, Review of photoluminescence performance of nano-sized

semiconductor materials and its relationships with photocatalytic activity, Solar Energy Materials and Solar Cells, 90 (2006) 1773-1787.

[50] Y. Li, M. Gu, T. Shi, W. Cui, X. Zhang, F. Dong, J. Cheng, J. Fan, K. Lv, Carbon vacancy in C3N4 nanotube: Electronic structure, photocatalysis mechanism and highly enhanced activity, Applied Catalysis B: Environmental, 262 (2020) 118281.

[51] Z. Wang, Y. Huang, M. Chen, X. Shi, Y. Zhang, J. Cao, W. Ho, S.C. Lee, Roles of N-Vacancies over Porous g-C$_3$N$_4$ Microtubes during Photocatalytic NO$_x$ Removal, ACS Applied Materials & Interfaces, 11 (2019) 10651-10662.

[52] Z. Cui, C. Xiao, Y. Lv, Q. Li, R. Sa, Z. Ma, Adsorption behavior of CO, CO$_2$, H$_2$, H$_2$O, NO, and O$_2$ on pristine and defective 2D monolayer Ferromagnetic Fe$_3$GeTe$_2$, Applied Surface Science, (2020) 146894.

[53] B. Zhu, S. Wageh, A.A. Al-Ghamdi, S. Yang, Z. Tian, J. Yu, Adsorption of CO$_2$, O$_2$, NO and CO on s-triazine-based g-C$_3$N$_4$ surface, Catalysis Today, 335 (2019) 117-127.

[54] H.-Z. Wu, S. Bandaru, J. Liu, L.-L. Li, Z. Wang, Adsorption of H2O, H2, O2, CO, NO, and CO2 on graphene/g-C3N4 nanocomposite investigated by density functional theory, Applied Surface Science, 430 (2018) 125-136.

[55] Y. Huang, Y. Yu, Y. Yu, B. Zhang, Oxygen Vacancy Engineering in Photocatalysis, Solar RRL, (2020) 2000037.

[56] H. Li, J. Li, Z. Ai, F. Jia, L. Zhang, Oxygen vacancy-mediated photocatalysis of BiOCl: reactivity, selectivity, and perspectives, Angewandte Chemie International Edition, 57 (2018) 122-138.

Chapter 4 Heterostructure construction

The Heterostructure construction involves two large works, i.e., **carbonaceous/CN hybrid (Chapter 4.1) and CN/TiO₂ heterostructure (Chapter 4.2)**.

To be more specific, CN/rGO nanocomposites are fabricated via an alkali-assisted hydrothermal process. The related research work is entitled **"Alkali-assisted hydrothermal preparation of g-C₃N₄/rGO nanocomposites with highly enhanced photocatalytic NOₓ decomposition activity" (Chapter 4.1).**

Our target is to prepare CN/TiO₂ heterostructure (**Chapter 4.2**) via calcination assisted hydrothermal process. Interestingly, we prepared oxygen vacancies mediated TiO₂ with excellent photocatalytic performance, which include two parts.

The first related research work is entitled **"Intrinsic carbon-doping induced synthesis of oxygen vacancies-mediated TiO₂ nanocrystals: enhanced photocatalytic NO removal performance and mechanism" (Chapter 4.2.1)**

The second related research work is entitled **"Reductant-free synthesis of oxygen vacancies-mediated TiO₂ nanocrystals with enhanced photocatalytic NO removal performance: an experimental and DFT study" (Chapter 4.2.2).**

4.1 Alkali-assisted hydrothermal preparation of g-C₃N₄/rGO nanocomposites with highly enhanced photocatalytic NOₓ decomposition activity

4.1.1 Introduction

Air pollution such as NO_x, SO_2, and CO is increasingly serious, due to the fossil fuel utilization and industrial activities [1, 2]. Photocatalysis as a green chemistry technology is regarded as a promising method for environmental remediation [3, 4]. Clearly, the major focus in photocatalysis is to develop highly efficient catalyst [5-10]. Since Wang et al. first reported a metal-free polymeric photocatalyst for hydrogen production in 2009 [11], graphitic carbon nitride (g-C₃N₄) has drawn considerable attention because of its visible-light responsive activity, facile preparation process using low-cost precursors, physicochemical stability and very unique two-dimensional (2D) structure [12-14]. Nevertheless, the pristine g-C₃N₄ photocatalyst still faces several drawbacks, such as limited absorption range, small specific surface area, rapid recombination of photogenerated carriers and weak redox ability, which hampers its practical applications [15, 16]. Therefore, enormous efforts have been made to improve the photocatalytic activity of g-C₃N₄ including constructing heterostructures, metal and nonmetal doping, and morphology control [17, 18].

Particularly, g-C₃N₄/graphene composites have attracted much attention due to the promoted charge carrier separation efficiency and also enhanced photocatalytic activity [19, 20]. For instance, Xiang et al. reported that g-C₃N₄/graphene composites exhibited about 3.0 times higher hydrogen production rate than that of pure g-C₃N₄ [21]. Zhang et al. reported that cross-linked g-C₃N₄/graphene nanocomposites showed 2.7 times photocatalytic degradation of 4-nitrophenol activity, compared with pure g-C₃N₄ [22]. The conventional thermal polymerization of g-C₃N₄ precursor (such as melamine, dicyandiamide, and cyanamide) with graphene oxide (GO) has proved to be an effective strategy to prepare g-C₃N₄/reduced GO (rGO) nanocomposites [21-23]. However, g-

C_3N_4 in the g-C_3N_4/rGO nanocomposites obtained from high temperature solid state reaction is still bulk and suffers from low surface area and few active sites [15, 24], which is disadvantageous to the improvement of their photocatalytic activity [25, 26]. Moreover, the thermal reduction of GO could result in inevitable structural damage of rGO owing to the released gas during thermal polymerization [27], thus weakening the electronic conductivity of rGO and decreasing the electron-hole separation efficiency [28]. Therefore, it remains challenging to prepare g-C_3N_4/rGO nanocomposites for the enhanced photocatalytic activity.

Herein, we developed a facile process to prepare g-C_3N_4/rGO nanocomposites via an alkali-assisted hydrothermal process. Interestingly, the alkali involved two roles for preparation of g-C_3N_4/rGO nanocomposites, simultaneously. The NaOH not only played an important role in etching the bulk g-C_3N_4 to increase specific the surface area [25, 26], but also significantly promoted the deoxygenation of GO to obtain rGO [29]. To our best knowledge, this was the first time to report preparation of g-C_3N_4/rGO nanocomposites via a one-pot alkali-assisted hydrothermal process. The morphologies, structures, and optical properties of bulk g-C_3N_4, g-C_3N_4 nanosheets, and g-C_3N_4/rGO nanocomposites were characterized in detail. The photocatalytic activity of g-C_3N_4/rGO nanocomposites was evaluated by photocatalytic decomposition NO_x under visible-light irradiation ($\lambda > 400$nm). The results indicated that the obtained g-C_3N_4/rGO nanocomposites exhibited significantly enhanced photocatalytic activity, compared with that of bulk g-C_3N_4. Furthermore, a possible mechanism related the charge transfer and separation was proposed to clarify the excellent photocatalytic performance of g-C_3N_4/rGO nanocomposites. This work demonstrated a novel and facile strategy to prepare g-C_3N_4/rGO nanocomposites, which may provide fresh insights for preparation of photocatalyst with high efficient.

4.1.2 Experiment

Sample preparation

Melamine and NaOH were purchased from Wako. GO was bought from Sigma-

Aldrich. All the chemical reagents were used as received without further purification. Pristine g-C_3N_4 was prepared by thermal polymerization of melamine according to previous literature [30]. In detail, melamine (10 g) was introduced into a crucible and heated to 520 ˚C for 2 h with heating rate 5 ˚C/min. After cooling down to room temperature, the obtained bulk g-C_3N_4 was ground by an agate mortar for further use. The g-C_3N_4/rGO nanocomposites were prepared by a facile alkali-assisted hydrothermal process. In a typical synthesis, g-C_3N_4 (1.0 g) and NaOH (0.36 g) was put into 85 mL of water, and then different amounts of GO were added in (Supporting Information). The resultant solution was stirred for 0.5 h followed by ultrasound treatment for 0.5 h. Subsequently, the obtained suspension was introduced into a Teflon-lined autoclave (100 mL) and heated at 120 °C for 18 h. After reaction, the obtained products were centrifuged and washed by deionized water and ethanol for several times, and finally vacuum dried at 60 °C overnight. For abbreviation, the bulk g-C_3N_4 and g-C_3N_4/rGO nanocomposites was denoted as BCN and CNG, respectively. In comparison, no GO was added and kept the other parameters constant, and the g-C_3N_4 nanosheet product was designated as CNN.

Characterization

X-ray diffraction (XRD) measurement was carried out using a Bruker AXS D2 Phaser unit equipped with Cu Kα source. Diffuse reflectance spectrum (DRS) was recorded using a UV-vis spectrophotometer (JASCO, V-670). Fourier transform infrared (FTIR) spectrum was determined on a FTIR spectrometer (JASCO, FTIR-660D-ATR). X-ray photoelectron spectroscopy (XPS) measurement was performed on a PerkinElmer PHI 5600. The morphology and microstructure of samples were observed by transmission electron microscopy (TEM, JEM-2000EXII), high-resolution transmission electron microscopy (HRTEM, ZEISS LEO 9522) and field emission scanning electron microscopy (FESEM, JSM-7800F). Nitrogen gas adsorption-desorption isotherms and pore-size distributions were obtained using Quantachrome Instruments, NOVA4200e. The specific surface areas of the samples were determined using the BET method. Thermogravimetry analysis (TGA) was performed on RIGAKU Thermoplus TG8120. Photoluminescence (PL) data was measured by a

spectrofluorometer (JASCO, FP-8500) with a laser (λ=400 nm) at room temperature. Time-resolved PL emission decay was recorded by a time-correlated single-photon counting system at 375 nm (PLP-10-038, Hamamatsu Photonics), equipped with a monochromator (Acton SP2150, Princeton Instruments, USA), a photon-counting board (SPC-130, Becker and Hickl) and a photosensor module with a photomultiplier tube (H7422P-50, Hamamatsu Photonics) at room temperature. Electrochemical impedance spectroscopy (EIS) curves were tested on with electrochemical workstation (Bio-logic, France) in a three electrode, utilizing a Pt pieces as the counter electrode and an Ag/AgCl electrode as the reference electrode. 0.1 mol. L^{-1} sodium sulfate purged with nitrogen was used as electrolyte solution.

Photocatalytic decomposition NO_x

The catalytic performances of as-obtained samples were evaluated by the decomposition of NO_x ($deNO_x$) in a flow type reactor ($373 cm^3$ of internal volume) under 450 W mercury lamp irradiation with a cutoff filter (λ>400nm) [1]. The photocatalyst was spread in the cell (20mm×16mm×0.5mm) of a glass substrate, which was set at the bottom center of the photocatalytic reactor. The NO_x concentration was determined by a NO_x detector (Yanaco, ECL-88A). The initial flowed 200 ml/min of NO_x gas consisted of 2 ppm of NO (N_2 balanced)-air mixture, and its concentration was determined using NO_x detector (Yanaco, ECL-88A). It is important to note that the measured NO_x concentration included NO_2 which could be ascribed to the oxidation of NO. The NO_x removal percentage (%) was defined as follows:

$$DeNO_x(\%) = \frac{C_0 - C}{C_0} \times 100 \qquad (4.1\text{-}1)$$

Where C_0 was the initial NO_x concentration and C was the final NO_x concentration after 10 minutes photocatalytic decomposition of NO_x at room temperature.

4.1.3 Results and discussion

The CNG nanocomposites were prepared as illustrated schematically in **Fig. 4.1.1**. The details were elaborated in the experimental section. The alkaline etching could

break the bulk BCN into small fragments to increase the specific surface area and active sites [25, 26]. Simultaneously, the GO experienced deoxygenation to become rGO under alkaline conditions [28, 29]. Therefore, the CNG nanocomposites were successfully fabricated via an alkali-assisted hydrothermal process.
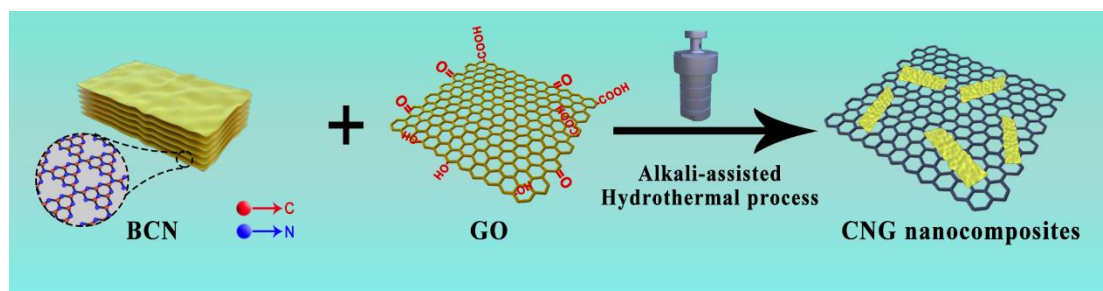
Fig. 4.1.1. Illustration for the preparation of CNG nanocomposites via an alkali-assisted hydrothermal process.

The crystal structures of as-obtained samples were studied by XRD patterns. As shown in **Fig. 4.1.2**A, all the samples possessed two distinct diffraction peaks around 13.5° and 27.8°, which were related to the (100) and (002) crystal planes of g-C$_3$N$_4$, respectively[31, 32]. **Fig. 4.1.2**B displayed the enlarged diffraction region between 8° and 16°. Compared with BCN, the XRD patterns of CNN and CNG nanocomposites exhibited peaks around 10.6°, which was ascribed to the partial destroy of the periodic tri-s-triazine units of graphitic carbon nitride owing to the alkali-assisted hydrothermal treatment. This was similar to previously reported results [33]. It is important to note that no apparent peaks of rGO appeared owing to the trace amount of rGO, which was difficult to be resolved by XRD [34]. However, the rGO sheets in the CNG nanocomposites could be easily detected by the HRTEM and SAED. From the **Fig. 4.1.2**C and **Fig. 4.1.3**, it was safe to conclude that no obvious fringe could be found in BCN due to the low crystallinity of BCN [35]. But in **Fig. 4.1.2**D, clear lattice fringes with d-spacing of 0.34 nm were observed in the CNG nanocomposites, which could be attributed to the (002) lattice plane of rGO sheets [36]. Also, the existence of graphene in the CNG nanocomposites could be demonstrated by the SAED image (**Fig. 4.1.3**B).
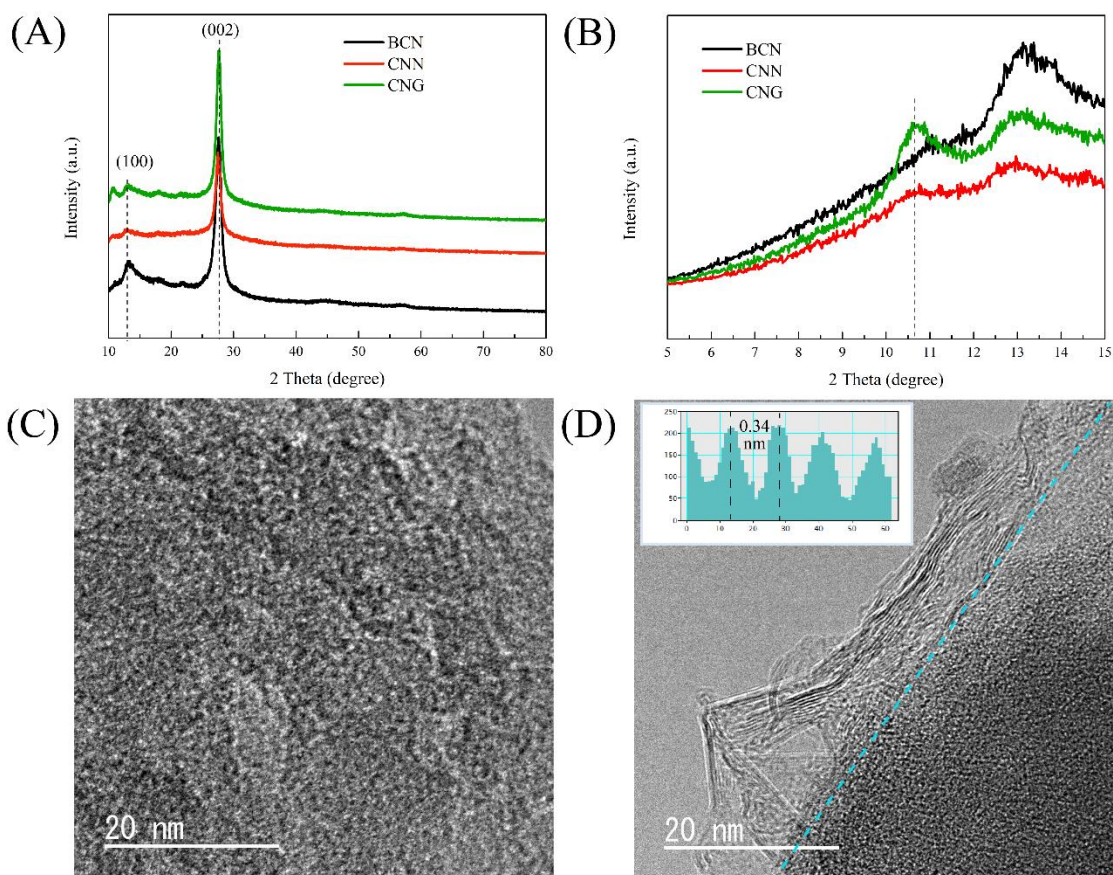
Fig. 4.1.2. (A) XRD patterns of BCN, CNN and CNG; (B) the enlarged diffraction profiles in the range between 5 and 15°; (C) the HRTEM image of BCN; (D) the HRTEM image of CNG. The inset in (D) is the profile plots of the calibration for measuring the spacings in panel.
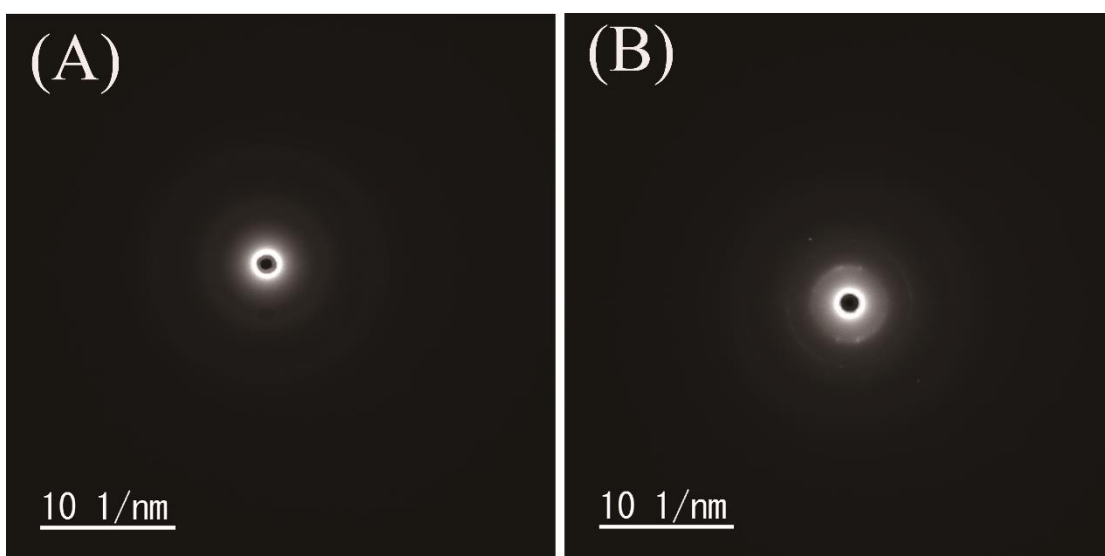
Fig. 4.1. 3. (A) SAED image of BCN; (B) SAED image of CNG (graphene part)

FTIR analysis was further carried out to identify the resultant samples. As shown in **Fig. 4.1.4**A, the main characteristic peaks for BCN in the region between 1200 cm^{-1} and 1700 cm^{-1} could be assigned to the typical stretching mode of g-C$_3$N$_4$ heterocycles [37], while the sharp peak at 808 cm^{-1} resulted from the characteristic breathing mode of tris-s-triazine cycles [14]. In addition, the deformation mode of N-H in amino groups at 887 cm^{-1} were observed [17], and the broad bands between 3000 and 3500 cm^{-1} were related to the N-H stretching vibration in the bridging C-NH-C units [13]. Notably, the FTIR spectrum of CNN and CNG nanocomposites resembled that of bulk BCN, indicating that the alkali-assisted hydrothermal treatment did not change the basic structure of g-C$_3$N$_4$, agreed with the XRD patterns. Similar results were also demonstrated by Raman spectra (**Fig. 4.1.5**).
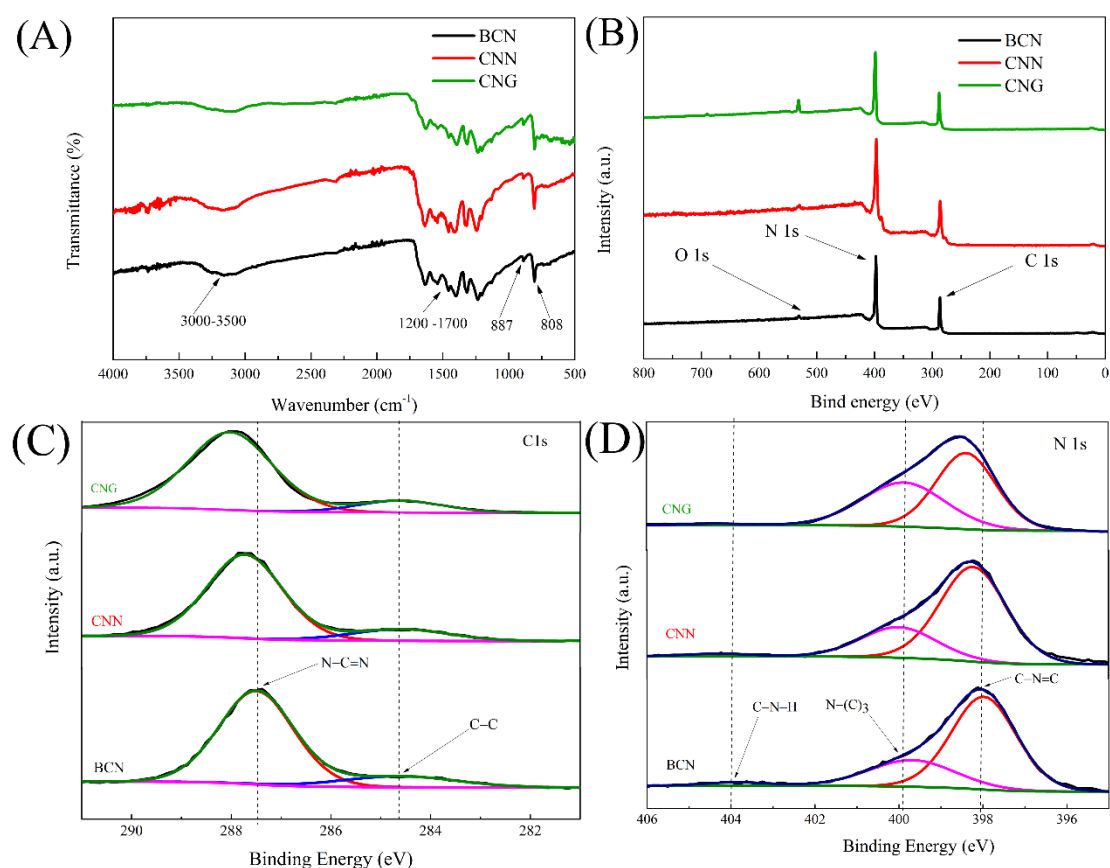
Fig. 4.1.4. (A) FTIR spectra of BCN, CNN and CNG; (B) the XPS survey spectra and (C), (D) high-resolution C1s, N1s XPS spectra of BCN, CNN and CNG, respectively.

XPS spectra were collected to reveal the chemical configurations of the samples

and interfacial interactions between CNN and rGO. Based on the survey spectra (F **Fig. 4.1.4**B), all the samples mainly consisted of C and N elements, and very small amounts of O were observed, which could be attributed to the O_2 or H_2O absorbed on the surface of the samples [16]. For the high-resolution C 1s of BCN (**Fig. 4.1.4**C), two peaks at 284.6 and 287.5 eV could be observed, which were index as carbon-containing contaminants and sp^2-bonded carbon (N–C=N), respectively [38]. Interestingly, for CNN, the binding energies of C 1s shifted to high binding energy by ca. 0.3eV due to the hydrothermal treatment [39]. When it comes to CNG nanocomposites, the binding energies of C 1s possessed the highest binding energy shift owing to the interfacial interaction between CNN and rGO sheets, which was similar with previously reported results [5]. Meanwhile, the N 1s spectrum of all the samples could be deconvoluted into three peaks (Fig. 3D), assign to N (sp^2) in tri-s-triazine units bonded to N–C=N, N–$(C)_3$, and C–N–H, respectively [38]. It was important to note that the N 1s spectrum of CNN and CNG nanocomposites shifted to high binding energies, compared with BCN, which was consistent with the results of C 1s. Based on the binding energy shifts of C 1s and N 1s, it might be concluded that the hydrothermal treatment and rGO had a great effect on bulk BCN [33, 39]. Also, it demonstrated indirectly the existence of rGO sheets due to the interfacial interactions between CNN and rGO [5].
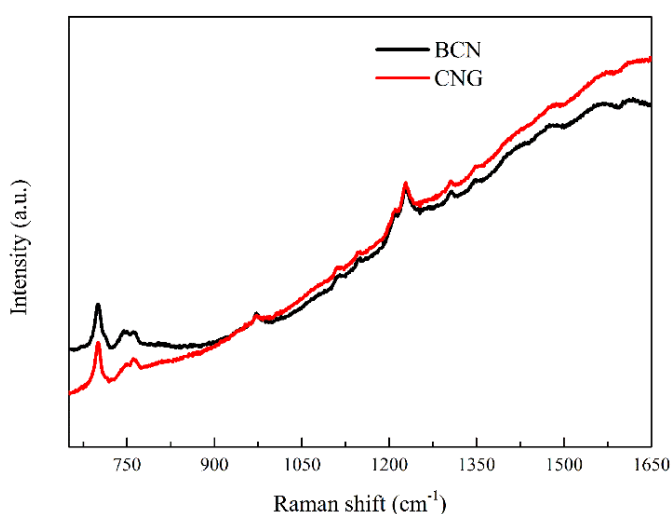
Fig. 4.1.5. Raman spectra of BCN and CNG.
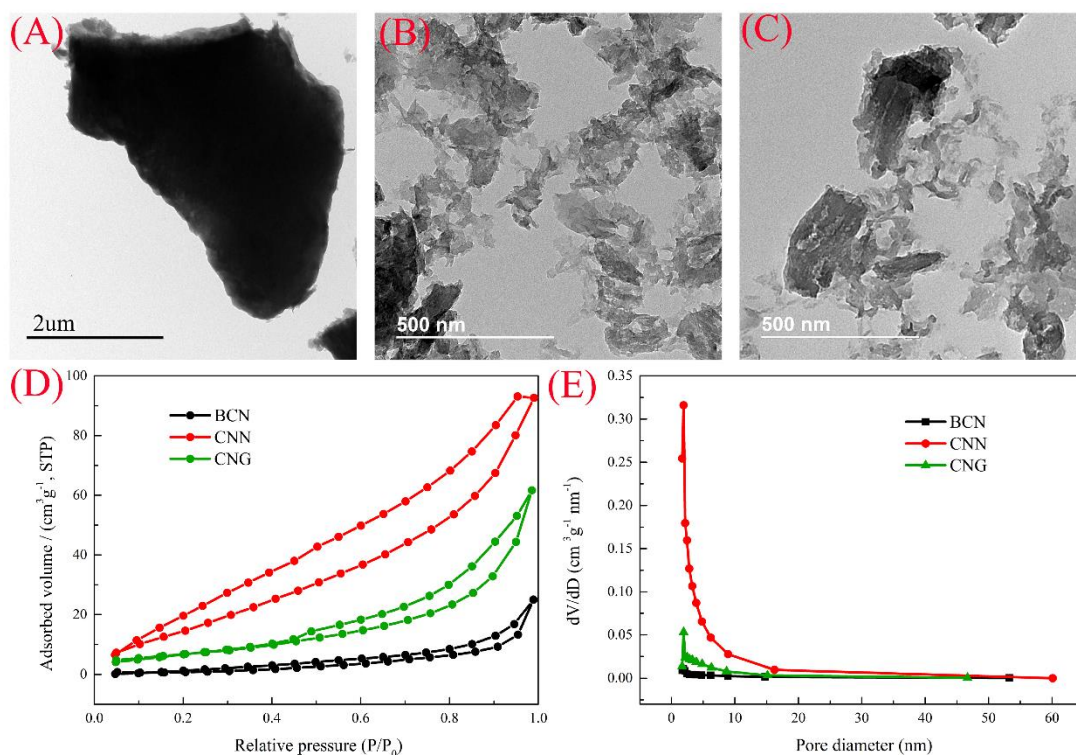
Fig.4.1.6. (A-C) TEM images of BCN, CNN and CNG respectively; (D) Nitrogen gas adsorption isotherms, and (E) corresponding pore size distribution of BCN, CNN and CNG.

Table 4.1.1 BET specific surface area, total pore volume and average size of BCN, CNN, and CNG

Samples	Abbreviation	BET surface area ($m^2\ g^{-1}$)	Total pore volume ($cm^3\ g^{-1}$)
Bulk g-C_3N_4	BCN	6.9	0.699
g-C_3N_4 nanosheets	CNN	74.2	7.578
g-C_3N_4 /rGO	CNG	27.0	1.930
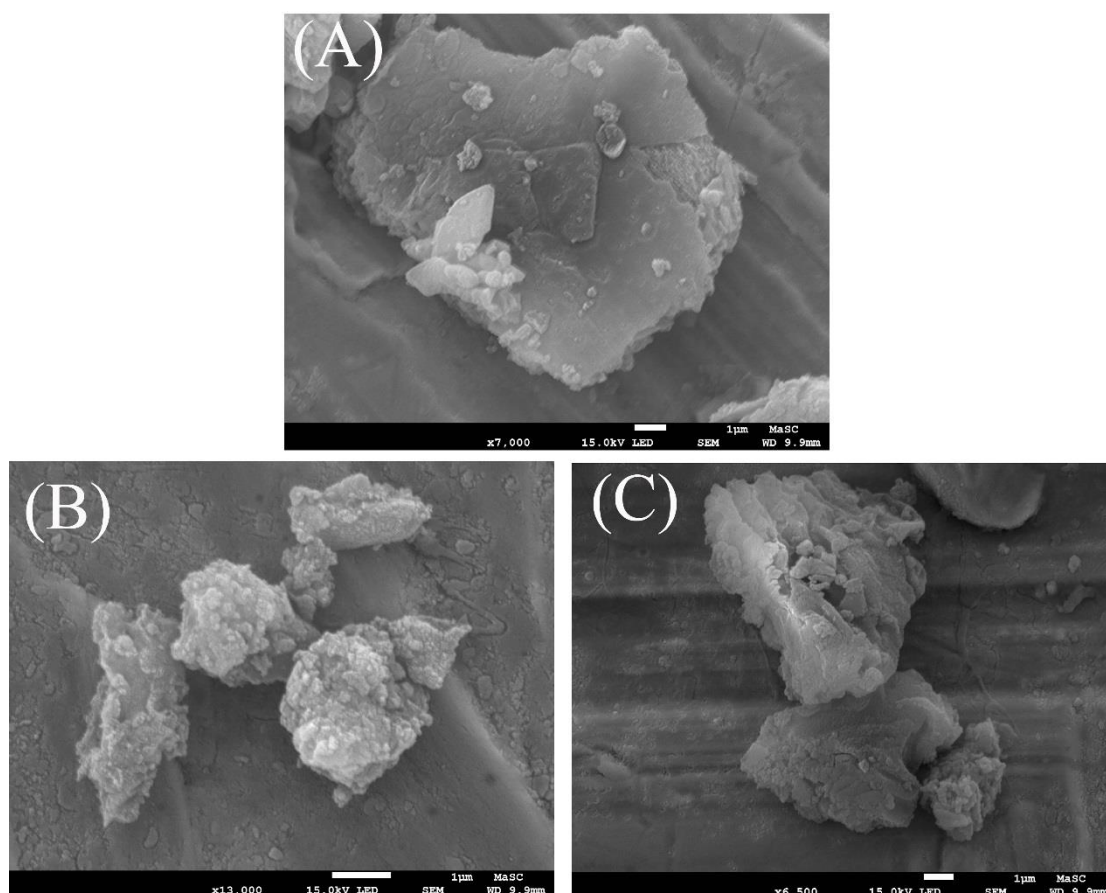
Fig. 4.1.7. SEM images of (A) BCN, (B) CNN and (C) CNG.

The morphology of bulk BCN, CNN nanosheets, and CNG nanocomposites were identified with SEM and TEM (**Fig.4.1.6** (A-C) and **Fig. 4.1.7**). The pristine BCN exhibited a lamellar structure with a size of 10 um and had a smooth surface, which was detrimental to light absorption and charge carrier transport [40]. After alkali-assisted hydrothermal treatment, the CNN and CNG nanocomposites were broken into small fragment to increase the specific surface areas and edge active sites. Moreover, the CNN nanosheets and CNG nanocomposites displayed a short migration distance of charge carriers, which could enhance the charge transfer and reduce the recombination of electrons and holes [18]. Also, CNN nanosheets and CNG nanocomposites could be accumulated into porous structure to increase the multiple reflections of incident light [41], resulting improved light harvesting ability.

The nitrogen adsorption was conducted to evaluate the BET specific surface areas and porous structures of bulk BCN, CNN nanosheets and CNG nanocomposites.

Fig.4.1.6A illustrated that the nitrogen adsorption-desorption isotherms of all the obtained samples were representative type-IV with H3-type hysteresis loop, which demonstrated the existence of mesopores and macropores [16]. Compared with bulk BCN, CNN nanosheets exhibited a distinct hysteresis loop, which was in good consistent with the pore size distribution plotted in **Fig.4.1.6**B. The pore volumes of bulk BCN and CNN nanosheets were 0.699 and 7.578 cm^3 g^{-1}, respectively (**Table 4.1.1**). Moreover, the CNN nanosheets showed specific surface area of 74.2 m^2 g^{-1}, which was around 10.8 times higher than that of bulk BCN (6.9 m^2 g^{-1}). Unexpectedly, the specific surface area of CNG nanocomposites was found to be only 27.0 m^2 g^{-1}, which was much less than that of CNN nanosheets. However, it was still almost 4.0 times higher than that of bulk BCN. Also, the similar porous structure of CNN nanosheets and CNG nanocomposites could be demonstrated by TG curves (**Fig. 4.1.8**), as they displayed almost the same weight loss before 200 °C owing to the evaporation of much absorbed H_2O [42]. The enlarged specific surface area of CNN nanosheets and CNG nanocomposites could increase the active sites to enhance their photocatalytic activity [43].
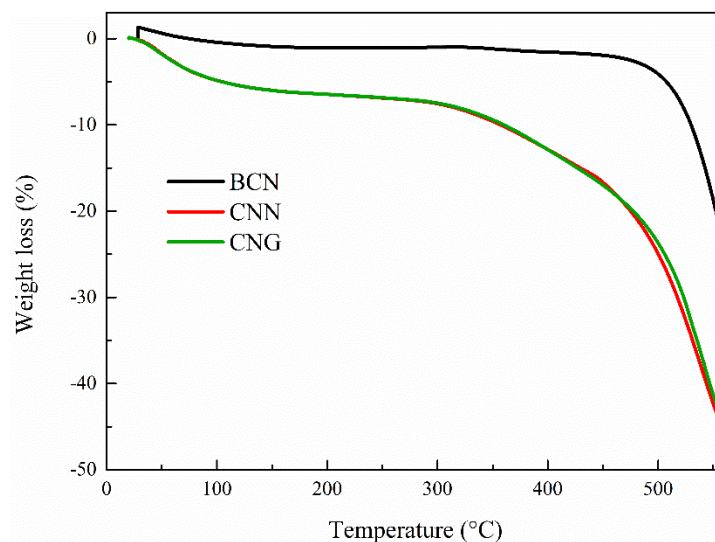
Fig. 4.1.8. TG curves of BCN, CNN, and CNG heated in the air.
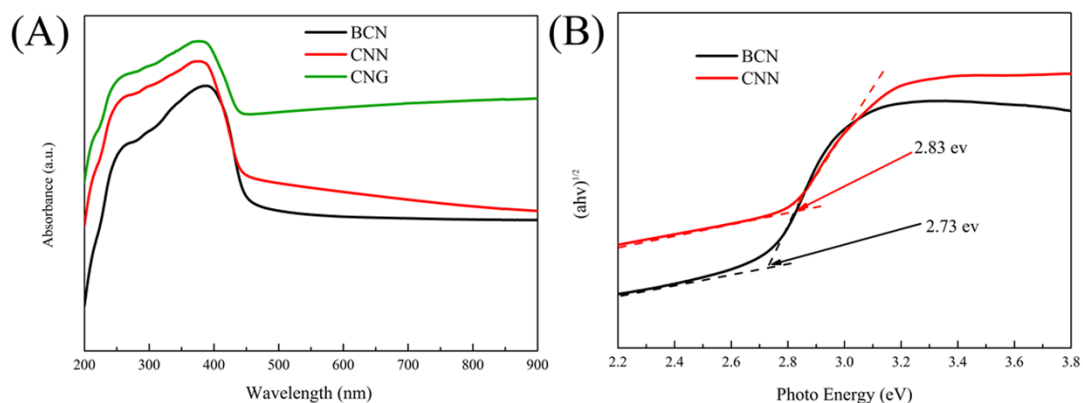
Fig. 4.1.9. (A) UV-vis absorption spectra of BCN, CNN and CNG respectively; and (B) corresponding band gap energies of BCN and CNN.

The optical properties of BCN, CNN, and CNG nanocomposites were characterized by UV-vis DRS. All the samples displayed a wide absorbance range from the UV region to the visible region (**Fig. 4.1.9**A). In comparison with BCN, CNN exhibited distinctly enhanced light harvesting ability due to the multiple reflections of incident light within the porous structure of packed CNN nanosheets [44]. Moreover, the bandgap of CNN was enlarged from 2.73eV to 2.83 eV due to the well-known quantum effect (**Fig. 4.1.9**B) [24], which gave indirect evidence to the nanosheets structure CNN [45]. Clearly, CNG nanocomposites exhibited the highest light harvesting ability with an obvious red-shift absorption edge, which could be ascribed to the strong light absorption ability of rGO [21, 22]. The enhanced light absorption could facilitate more electron-hole pairs production to improve the catalytic activity [17].

135
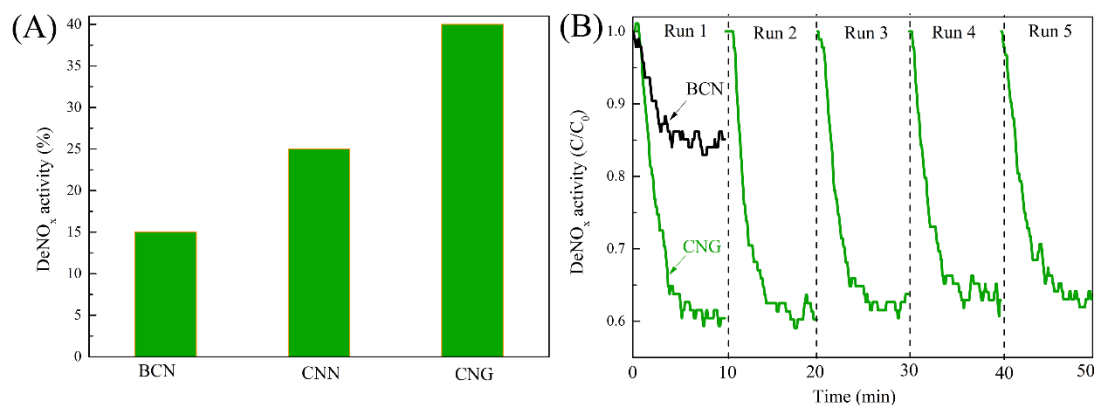
Fig. 4.1.10. (A) Visible light induced photocatalytic decomposition NO$_x$ activity (λ>400nm), and (B) Cycling stability characterization of CNG photocatalyst.
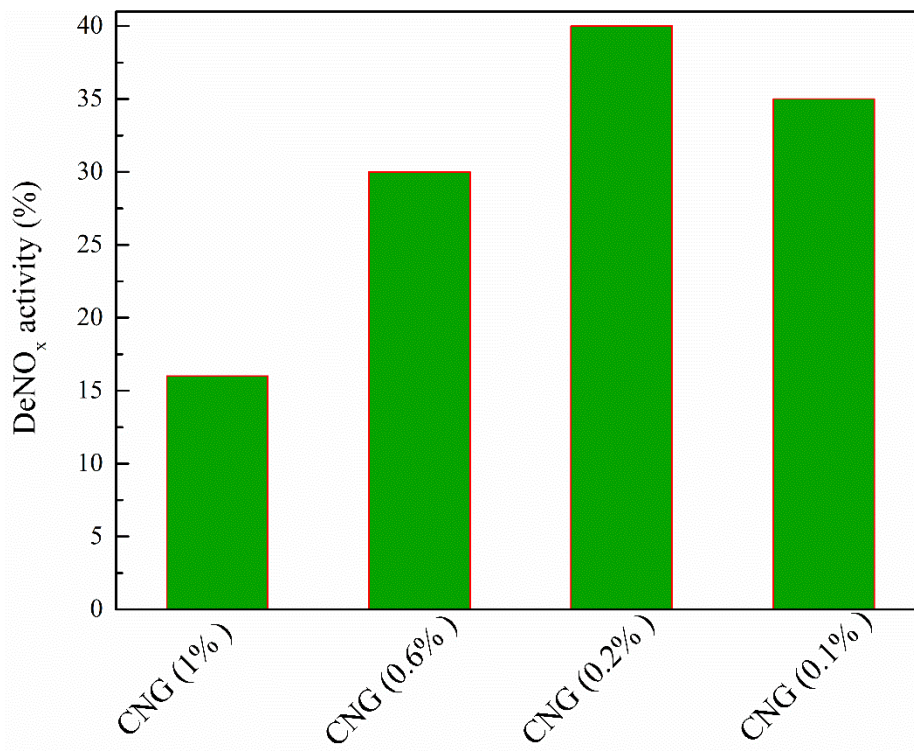
Fig. 4.1.11. Comparison of the photoactivities of CNG nanocomposites with different rGO content under visible-light irradiation (>400 nm)
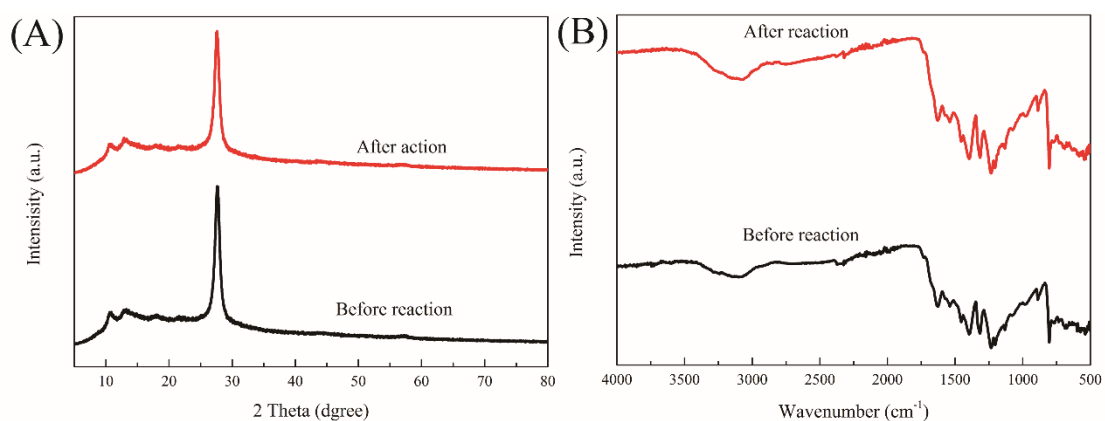
Fig. 4.1.12 (A) XRD patterns of CNG after recycling test; (B) FTIR spectra of CNG after recycling test

The photocatalytic activity of the prepared samples was evaluated by

decomposition NO_x under visible light irradiation (λ>400 nm). As shown in **Fig. 4.1.10**A, the photocatalytic activity of CNG nanocomposites showed the highest DeNO$_x$ activity (40%) among the three samples. It was about 2.7 times higher than that of bulk BCN (15%) and 1.7 times higher than that of CNN (23%), respectively. To determine the optimal rGO in the CNG nanocomposites, a series of rGO was added into CNG nanocomposites to confirm the photocatalytic decomposition of NO$_x$ activity (**Fig. 4.1.11**). It must be mentioned that excessive rGO nanosheet resulted in rapid reduction in the photocatalytic performance because much incident visible light would be absorbed by rGO nanosheet [22]. Moreover, the photocatalytic activity of CNG nanocomposites did not decrease too much after five cycling tests, suggesting the high stability of CNG nanocomposites. This was also supported by the XRD patterns (**Fig. 4.1.12** A) and FTIR spectra (**Fig. 4.1.12** B) since there was no obvious difference between the used sample and fresh sample. Considering the excellent photocatalytic activity, high stability and low cost, this metal-free photocatalyst was more promising than previously our group reported traditional-metal-based semiconductor photocatalysts (**Table 4.1.2**). It is well known that many factors such as (1) the amount of catalyst used, (2) the gas flow rate, (3) the concentration of NO$_x$, (4) the intensity of light could affect the photocatalytic activity of photocatalysts. Therefore, we just compared the photocatalytic activity of CNG with those of traditional metal semiconductor photocatalysts, which are all developed and characterized by our group. In the table 1, all the experimental conditions were the same because they were carried out in the lab of ourselves. Moreover, to demonstrate the photocatalytic activity of CNG was competitive. We also compared the photocatalytic activity of CN based photocatalysts developed by different groups such as Rb doped CN [46], defective CN [47], Ca doped CN [48], and rGO/CN [49], by the enhanced ratio, i.e., modified CN/pristine CN. The results were summarized in **Fig. 4.1.14.**
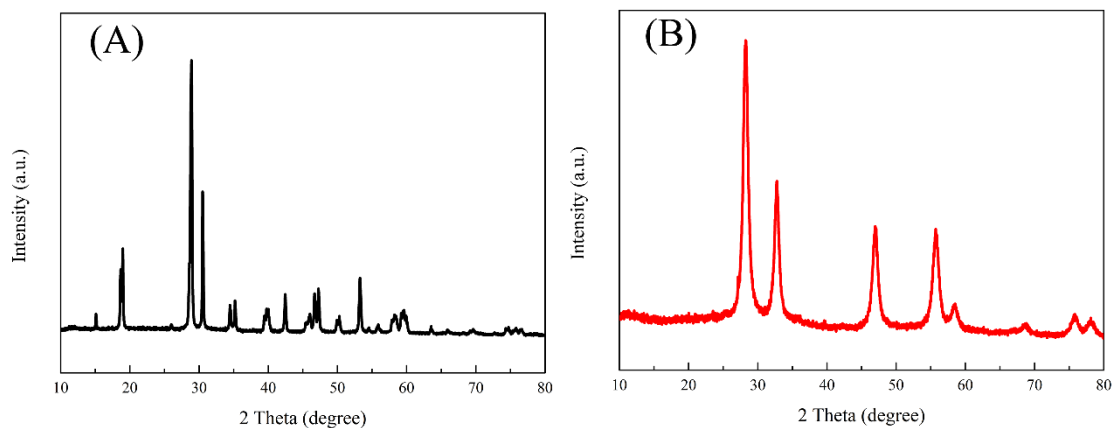
Fig. 4.1.13. (A)XRD pattern of $BiVO_4$; (B) XRD pattern of Bi_2WO_6.

Table 4.1.2. Comparisons of different photocatalysts for decomposition NO_x under visible light irradiation ($\lambda > 400$ nm).

Photocatalysts	DeNO$_x$ activity (%)	Reference
GaON	10	[50]
GaN:ZnO	12	[51]
BiVO$_4$	15	**Fig.4.1.13**. (A)
Ca-siloxene	20	[52]
P25	20	
C-TiO$_2$	29	[53, 54]
N-TiO$_2$	30	[3, 54]
BiOX (X=Cl, Br, I)	25, 30, 2	[54]
C-NaTaO$_3$	30	[55]
Bi$_2$WO$_6$	30	**Fig. 4.1.13**. (B)
SrTiO$_3$	33	[56]
(Zn$_{1+x}$Ge) (N$_2$O$_x$)	35	[4]
g-C$_3$N$_4$/rGO (CNG)	40	This work
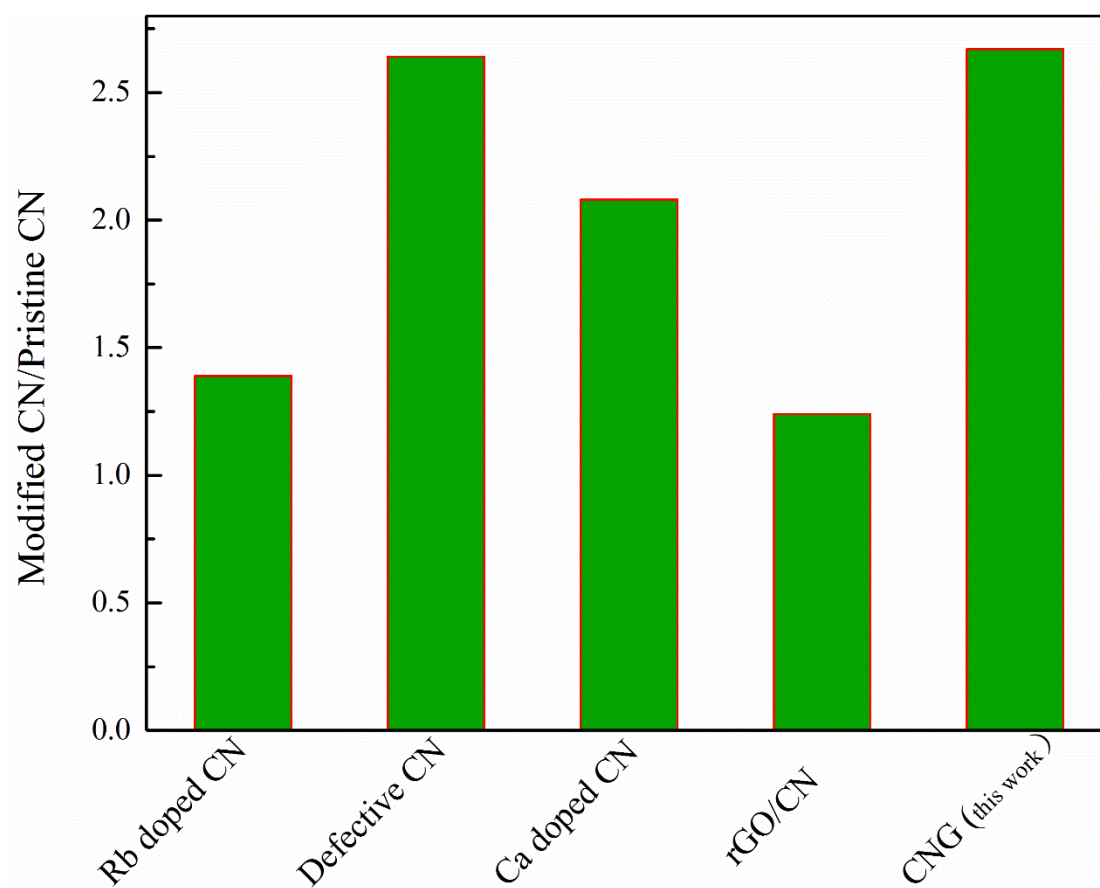
Fig. 4.1.14. Comparisons of CN based photocatalysts developed by different groups for decomposition NO$_x$, by the enhanced ratio, i.e., modified CN/pristine CN.

It is accepted that photocatalytic activity is largely dependent on the charge carrier separation and transport efficiency [15, 57-60]. Therefore, steady state PL spectroscopy was employed to reveal the charge separation and transfer behavior of the obtained samples. Compared with bulk BCN, the intensity for CNN nanosheets was significantly decreased (**Fig. 4.1.15**A), demonstrating that the recombination of photogenerated charge carrier was suppressed [13, 16]. This was because after alkali-assisted hydrothermal process, the bulk BCN was etched into small fragments and the volume recombination of charge carrier was reduced due to the short charge migration distance [17, 18, 61]. The CNG displayed the lowest PL peak intensity among all the samples, suggesting the smallest charge recombination rate, which could be ascribed to the synergistic effect of morphology control and heterostructure. More concretely, CNG nanocomposites not only showed the nanosheets structure to reduce the volume

recombination of charge carrier, but also possessed rGO to suppressed the surface recombination of charge carrier since the graphene could act as an excellent electron acceptor and transfer channel, which enabled to promote the charge carrier separation on the surface of CNG nanocomposites [15, 21, 22].
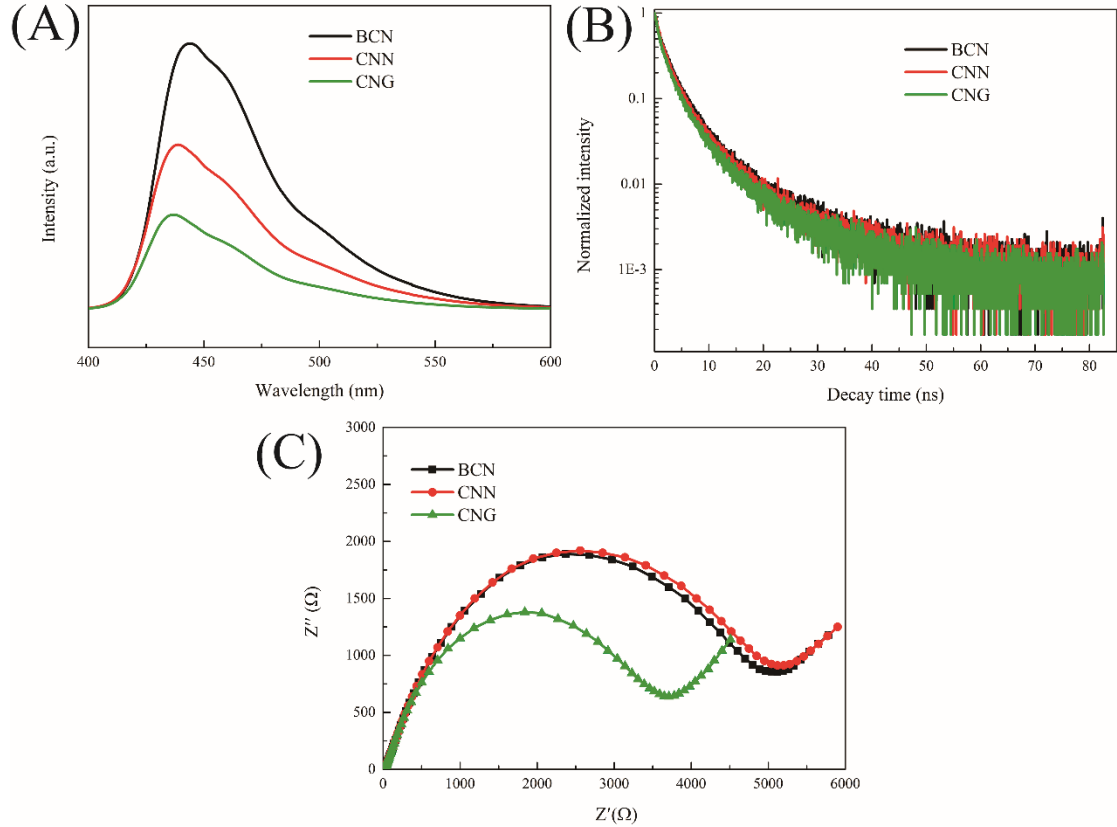
Fig. 4.1.15. (A) steady state PL spectra, (A) time-resolved PL spectra, and EIS Nyquist plots of BCN, CNN and CNG respectively

The time-resolved PL spectroscopy was also carried out to investigate the lifetime of charge carrier and charge separation process. **Fig. 4.1.15**B displayed the PL lifetime decay curves of BCN, CNN, and CNG nanocomposites. The PL decay curves were fitted with the following exponential equation [37, 57]:

$$Y = y_0 + A_1 exp\left(-\frac{t}{\tau_1}\right) + A_2 exp\left(-\frac{t}{\tau_2}\right) \tag{4.1-2}$$

where y_0, A_1, and A_2 are constants and obtained after fitting each PL lifetime decay curve. The τ_1 and τ_2 were the values of fast lifetime component and slow lifetime component, respectively. Based on the fitting data, the average lifetimes of the samples

were calculated from the two lifetime components with the following equation [62, 63]:

$$\tau = \frac{A_1\tau_1^2 + A_2\tau_2^2}{A_1\tau_1 + A_2\tau_2} \qquad (4.1\text{-}3)$$

The resultant PL lifetimes of the samples were summarized and listed in **Table 4.1.3**. Compared with bulk BCN, both the fast lifetime τ_1 and slow lifetime τ_2 of CNN nanosheets decreased from 1.2 to 1.1 ns and 4.5 to 4.3 ns, respectively. Consequently, the average lifetime decreased from 3.5 (BCN) to 3.3 ns (CNN). The reduced average lifetime of CNN nanosheets indicated the fast quenching of luminescence, which was consistent with results of steady state PL spectra [64]. The fast quenching could be attributed to the enhanced charge carrier separation of CNN nanosheets due to the short transfer distance of electron-hole pairs [37, 64, 65]. Notably, the slightly decreased lifetime of CNG nanocomposites (3.1 ns) was related to the efficient interfacial charge transfer from CNN nanosheets to rGO [60], suggesting the positive effect of graphene in promoting the photoinduced electron-hole pairs separation owing to its extraordinary electrical property [18].

Table 4.1.3 Exponential decay-fitted parameters of PL lifetime for BCN, CNN, and CNG.

Samples	τ_1 (ns)	Rel. (%)	τ_2 (ns)	Rel. (%)	τ (ns)
BCN	1.2	62.1	4.5	37.9	3.5
CNN	1.1	64.7	4.3	35.3	3.3
CNG	0.9	64.8	4.0	35.2	3.1

Table 4.1.4 Simulation results of the EIS plots

Samples	R1(Ω)	R2(Ω)
BCN	12.24	5967
CNN	12.22	6168
CNG	11.99	7350

To get insight into the charge transport behaviors of the samples, EIS measurements were performed under dark conditions. **Fig. 4.1.15**C showed the EIS Nyquist plots of BCN, CNN, and CNG nanocomposites. The EIS Nyquist plots could be fitted based on the equivalent circuit illustrated in Fig. 7C inset, where R_1 and R_2 were series resistance and electron transport resistance, respectively [57, 66]. The simulation results of the EIS Nyquist plots were presented in **Table 4.1.4**. Clearly, CNG nanocomposites exhibited the smallest resistances for the interfacial charge transfer, which was correlated with excellent charge separation of photogenerated electron-hole pairs of CNG nanocomposites [66]. The results of EIS measurements were in good consistent with steady state and time resolved PL spectra. Meanwhile, it should be pointed out BCN and CNN displayed almost the same resistance, which could be attributed to the fact that alkali-assisted hydrothermal treatment did not change the electronic structure too much, supported by the XRD patterns and the FTIR spectra.
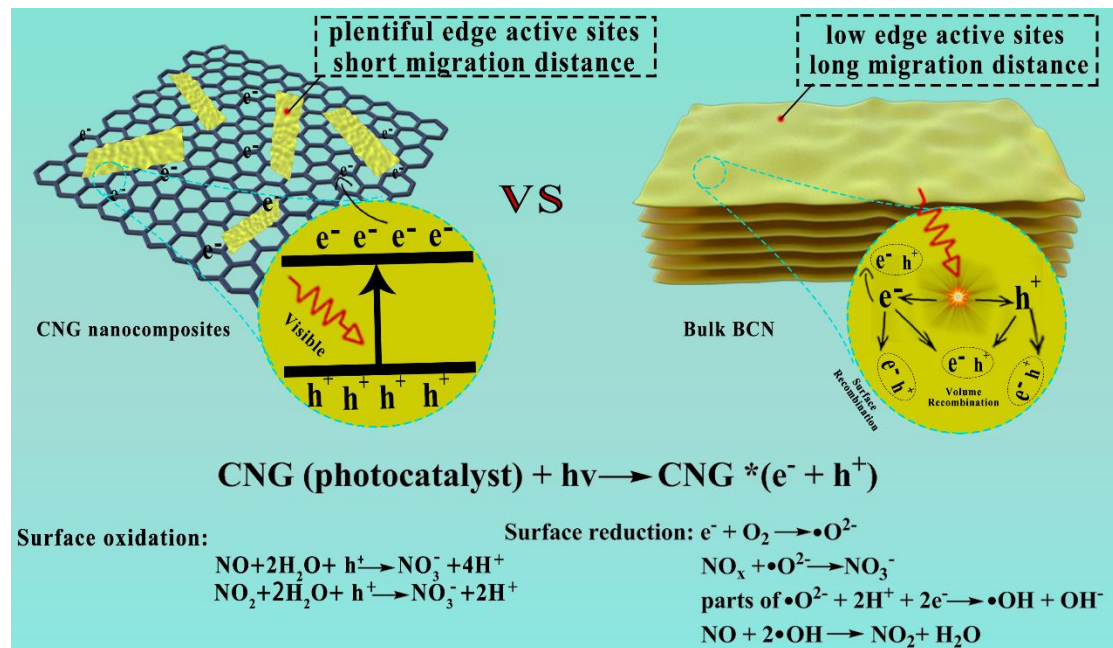
Fig. 4.1.16. Proposed reaction mechanism of CNG nanocomposites with enhanced photocatalytic decomposition NO_x activity

Based on the above discussions, a charge transfer and separation mechanism could be proposed and presented in **Fig. 4.1.16**. Compared with bulk BCN, the CNG

nanocomposites possessed a variety of merits to improve their photocatalytic activity. Firstly, the CNG nanocomposites exhibited large specific surface areas and plentiful edge active sites due to the alkali-assisted hydrothermal treatment. Therefore, it enabled to generate more electron-hole pairs under the visible light irradiation, which was beneficial for the improvement of photocatalytic performance. Secondly, the nanosheets structure of CNG nanocomposites displayed a short migration distance of charge carriers from the interior to the surface for reduction and oxidation reactions, thus reducing the volume recombination of charge carries and promote the photocatalytic activity. More importantly, due to the unique optical and electronic properties of rGO nanosheets, it not only enabled the CNG nanocomposites to have excellent light harvesting ability, but also acted as an extraordinary electron acceptor and transfer channel, which could greatly suppress the surface recombination of charge carries and enhance the photocatalytic activity. Therefore, the CNG nanocomposites in comparison with bulk BNC had much more photoinduced electrons and holes to initiate the surface reduction and oxidation processes for the photocatalytic decomposition NO_x. According to previously reported literatures [46-48, 67, 68], during the surface reduction and oxidation processes, some reactive oxygen species such as $\bullet O^{2-}$ and $\bullet OH$ formed. The photoinduced holes and reactive oxygen species could decompose the NO_x into NO_3^-. Also, as an evidence, in 2004, a Japanese Industrial Standard (JIS R 1701-1:2004(J) [69] on the removal of nitric oxide had been established. It is accepted that the environmental pollutant nitrogen monoxide reacts with some reactive oxygen radicals to mainly produce nitrate nitrous acid or nitric acid (80%), and 20% of the NO could be decomposed directly to nitrogen and oxygen, (see Eqns (1) (2)) [70]

$$NO + \{\cdot OH, \ \cdot OOH, \text{ and/or } O_2\} \rightarrow HNO_2 \text{ and/or } HNO_3 \quad (80\%) \qquad (4.1\text{-}4)$$

$$\rightarrow N_2 + O_2 \qquad (20\%) \qquad (4.1\text{-}5)$$

All in all, owing to the nanosheets structure and rGO nanosheets, the CNG nanocomposites exhibited the outstanding photocatalytic performance. It displayed 2.7 times higher photocatalytic decomposition NO_x than that of bulk BCN, even higher than those of most previously reported traditional-metal-based semiconductor

photocatalysts.

4.1.4 Conclusion

In summary, we had successfully developed a novel strategy to prepare CNG nanocomposites via one-pot alkali-assisted hydrothermal process, in which the NaOH acted as two crucial roles. On one hand, it could etch the bulk BCN into small nanosheets to increase the specific surface areas and edge actives; on the other hand, it promoted the reduction of GO to enhance the electronic conductivity of rGO nanosheets. Moreover, the CNG nanocomposites exhibited 2.7 times higher photocatalytic decomposition NO_x activity than that of bulk BCN, which could be ascribed to the synergistic effect of nanosheets structure and rGO nanosheets. The nanosheets structure allowed the CNG nanocomposites to exhibit large specific surface areas and plentiful edge active sites to generate more electron-hole pairs under the light irradiation. The rGO nanosheets acted as an extraordinary electron acceptor and transfer channel, which could greatly suppress the surface recombination of charge carries and enhance the photocatalytic performance. This work demonstrated that a combined strategy, i.e. morphology control and heterojunction construction, is promising for the synthesis of photocatalysts with high activity in energy conversion and environmental rpurification applications.

4.1.5 References

[1] X. Wu, S. Yin, Q. Dong, C. Guo, H. Li, T. Kimura, T. Sato, Synthesis of high visible light active carbon doped TiO_2 photocatalyst by a facile calcination assisted solvothermal method, Applied Catalysis B: Environmental, **142** (2013) 450-457.

[2] J. Ma, C. Wang, H. He, Enhanced photocatalytic oxidation of NO over g-C_3N_4-TiO_2 under UV and visible light, Applied Catalysis B Environmental, 184 (2016) 28-34.

[3] S. Yin, B. Liu, P. Zhang, T. Morikawa, K.-i. Yamanaka, T. Sato, Photocatalytic oxidation of NO_x under visible LED light irradiation over nitrogen-doped titania particles with iron or platinum loading, The Journal of Physical Chemistry C, 112 (2008) 12425-12431.

[4] J. Wang, Y. Asakura, S. Yin, Preparation of $(Zn_{1+x}Ge)(N_2Ox)$ nanoparticles with enhanced NO_x decomposition activity under visible light irradiation by nitridation of Zn_2GeO_4 nanoparticles designed precisely, Nanoscale, 11 (2019) 20151-20160.

[5] M. Zhu, S. Kim, L. Mao, M. Fujitsuka, J. Zhang, X. Wang, T. Majima, Metal-Free Photocatalyst for H_2 Evolution in Visible to Near-Infrared Region: Black Phosphorus/Graphitic Carbon Nitride, Journal of the American Chemical Society, 139 (2017) 13234-13242.

[6] F. Ding, D. Yang, Z. Tong, Y. Nan, Y. Wang, X. Zou, Z. Jiang, Graphitic carbon nitride-based nanocomposites as visible-light driven photocatalysts for environmental purification, Environmental Science: Nano, 4 (2017) 1455-1469.

[7] S. Yin, Y. Asakura, Recent research progress on mixed valence state tungsten based materials, Tungsten, 1 (2019) 5-18.

[8] S. Wang, L. Wang, Recent progress of tungsten-and molybdenum-based semiconductor materials for solar-hydrogen production, Tungsten, 1 (2019) 19-45.

[9] X. Zhang, G. Ma, J. Wang, Hydrothermal synthesis of two-dimensional MoS_2 and its applications, Tungsten, 1 (2019) 59-79.

[10] J. Xue, M. Fujitsuka, T. Majima, Near Bandgap Excitation Inhibits the Interfacial Electron Transfer of Semiconductor/Cocatalyst, ACS Applied Materials & Interfaces, (2020).

[11] X. Wang, K. Maeda, A. Thomas, K. Takanabe, G. Xin, J.M. Carlsson, K. Domen, M. Antonietti, A metal-free polymeric photocatalyst for hydrogen production from water under visible light, Nature Materials, 8 (2009) 76.

[12] J. Xue, M. Fujitsuka, T. Majima, The role of nitrogen defects in graphitic carbon nitride for visible-light-driven hydrogen evolution, Physical Chemistry Chemical Physics, 21 (2019) 2318-2324.

[13] T. Song, P. Zhang, T. Wang, A. Ali, H. Zeng, Alkali-assisted fabrication of holey carbon nitride nanosheet with tunable conjugated system for efficient visible-light-driven water splitting, Applied Catalysis B: Environmental, 224 (2018) 877-885.

[14] H. Yu, R. Shi, Y. Zhao, T. Bian, Y. Zhao, C. Zhou, G.I. Waterhouse, L.Z. Wu, C.H. Tung, T. Zhang, Alkali‑Assisted Synthesis of Nitrogen Deficient Graphitic Carbon Nitride with Tunable Band Structures for Efficient Visible‑Light‑Driven Hydrogen Evolution, Advanced Materials, 29 (2017).

[15] J. Fu, J. Yu, C. Jiang, B. Cheng, g-C_3N_4-Based Heterostructured Photocatalysts, Advanced Energy Materials, 8 (2018) 1701503.

[16] Y. Xiao, G. Tian, W. Li, Y. Xie, B. Jiang, C. Tian, D. Zhao, H. Fu, Molecule self-assembly synthesis of porous few-layer carbon nitride for highly efficient photoredox catalysis, Journal of the American Chemical Society, (2019).

[17] J. Wen, J. Xie, X. Chen, X. Li, A review on g-C_3N_4-based photocatalysts, Applied Surface Science, 391 (2017) 72-123.

[18] W.J. Ong, L.L. Tan, H.N. Yun, S.T. Yong, S.P. Chai, Graphitic Carbon Nitride (g-C_3N_4)-Based Photocatalysts for Artificial Photosynthesis and Environmental Remediation: Are We a Step Closer To Achieving Sustainability?, Chemical Reviews, 116 (2016) 7159-7329.

[19] Y. Zhao, J. Zhang, L. Qu, Graphitic carbon nitride/graphene hybrids as new active materials for energy conversion and storage, ChemNanoMat, 1 (2015) 298-318.

[20] Q. Han, N. Chen, J. Zhang, L. Qu, Graphene/graphitic carbon nitride hybrids for catalysis, Materials Horizons, 4 (2017) 832-850.

[21] Q. Xiang, J. Yu, M. Jaroniec, Preparation and enhanced visible-light photocatalytic H2-production activity of graphene/g-C_3N_4 composites, The Journal of Physical

Chemistry C, 115 (2011) 7355-7363.

[22] Y. Li, H. Zhang, P. Liu, D. Wang, Y. Li, H. Zhao, Cross-Linked g-C_3N_4/rGO Nanocomposites with Tunable Band Structure and Enhanced Visible Light Photocatalytic Activity, Small, 9 (2013) 3336-3344.

[23] Y. Zhang, T. Mori, L. Niu, J. Ye, Non-covalent doping of graphitic carbon nitride polymer with graphene: controlled electronic structure and enhanced optoelectronic conversion, Energy & Environmental Science, 4 (2011) 4517-4521.

[24] P. Niu, L. Zhang, G. Liu, H.M. Cheng, Graphene‐like carbon nitride nanosheets for improved photocatalytic activities, Advanced Functional Materials, 22 (2012) 4763-4770.

[25] T. Sano, S. Tsutsui, K. Koike, T. Hirakawa, Y. Teramoto, N. Negishi, K. Takeuchi, Activation of graphitic carbon nitride (g-C_3N_4) by alkaline hydrothermal treatment for photocatalytic NO oxidation in gas phase, Journal of Materials Chemistry A, 1 (2013) 6489-6496.

[26] H. Nie, M. Ou, Q. Zhong, S. Zhang, L. Yu, Efficient visible-light photocatalytic oxidation of gaseous NO with graphitic carbon nitride (g-C_3N_4) activated by the alkaline hydrothermal treatment and mechanism analysis, Journal of hazardous materials, 300 (2015) 598-606.

[27] S.P. Sasikala, P. Poulin, C. Aymonier, Advances in Subcritical Hydro‐/Solvothermal Processing of Graphene Materials, Advanced Materials, 29 (2017) 1605473.

[28] S.D. Perera, R.G. Mariano, K. Vu, N. Nour, O. Seitz, Y. Chabal, K.J. Balkus Jr, Hydrothermal synthesis of graphene-TiO_2 nanotube composites with enhanced photocatalytic activity, Acs Catalysis, 2 (2012) 949-956.

[29] X. Fan, W. Peng, Y. Li, X. Li, S. Wang, G. Zhang, F. Zhang, Deoxygenation of exfoliated graphite oxide under alkaline conditions: a green route to graphene preparation, Advanced Materials, 20 (2008) 4490-4493.

[30] K. Wang, Q. Li, B. Liu, B. Cheng, W. Ho, J. Yu, Sulfur-doped g-C_3N_4 with enhanced photocatalytic CO_2-reduction performance, Applied Catalysis B: Environmental, 176 (2015) 44-52.

[31] S. Guo, Z. Deng, M. Li, B. Jiang, C. Tian, Q. Pan, H. Fu, Phosphorus-doped carbon nitride tubes with a layered micro-nanostructure for enhanced visible-light photocatalytic hydrogen evolution, Angewandte Chemie International Edition, 55 (2016) 1830-1834.

[32] Y. Hong, C. Li, D. Li, Z. Fang, B. Luo, X. Yan, H. Shen, B. Mao, W. Shi, Precisely tunable thickness of graphitic carbon nitride nanosheets for visible-light-driven photocatalytic hydrogen evolution, Nanoscale, 9 (2017) 14103-14110.

[33] X. Wu, F. Chen, X. Wang, H. Yu, In situ one-step hydrothermal synthesis of oxygen-containing groups-modified g-C_3N_4 for the improved photocatalytic H2-evolution performance, Applied Surface Science, 427 (2018) 645-653.

[34] S. Pu, R. Zhu, H. Ma, D. Deng, X. Pei, F. Qi, W. Chu, Facile in-situ design strategy to disperse TiO_2 nanoparticles on graphene for the enhanced photocatalytic degradation of rhodamine 6G, Applied Catalysis B Environmental, 218 (2017) 208-219.

[35] Y. Zheng, Z. Yu, H. Ou, A.M. Asiri, Y. Chen, X. Wang, Black phosphorus and polymeric carbon nitride heterostructure for photoinduced molecular oxygen activation, Advanced Functional Materials, 28 (2018) 1705407.

[36] D. Sun, D. Ye, P. Liu, Y. Tang, J. Guo, L. Wang, H. Wang, MoS_2/Graphene nanosheets from commercial bulky MoS_2 and graphite as anode materials for high rate sodium‐Ion batteries, Advanced Energy Materials, 8 (2018) 1702383.

[37] J. Fu, B. Zhu, C. Jiang, B. Cheng, W. You, J. Yu, Hierarchical porous O‐doped g-C_3N_4 with enhanced photocatalytic CO_2 reduction activity, Small, 13 (2017) 1603938.

[38] G. Lei, Y. Cao, W. Zhao, Z. Dai, L. Shen, Y. Xiao, L. Jiang, Exfoliation of Graphitic Carbon Nitride for Enhanced Oxidative Desulfurization: A Facile and General Strategy, ACS Sustainable Chemistry & Engineering, 7 (2019) 4941-4950.

[39] H. Wei, Q. Zhang, Y. Zhang, Z. Yang, A. Zhu, D.D. Dionysiou, Enhancement of the Cr (VI) adsorption and photocatalytic reduction activity of g-C_3N_4 by hydrothermal treatment in HNO_3 aqueous solution, Applied Catalysis A: General, 521 (2016) 9-18.

[40] J. Wang, C. Zhang, Y. Shen, Z. Zhou, J. Yu, Y. Li, W. Wei, S. Liu, Y. Zhang, Environment-friendly preparation of porous graphite-phase polymeric carbon nitride

using calcium carbonate as templates, and enhanced photoelectrochemical activity, Journal of Materials Chemistry A, 3 (2015) 5126-5131.

[41] D. Chen, J. Yang, H. Ding, Synthesis of nanoporous carbon nitride using calcium carbonate as templates with enhanced visible-light photocatalytic activity, Applied Surface Science, 391 (2017) 384-391.

[42] Q. Liang, Z. Li, X. Yu, Z.H. Huang, F. Kang, Q.H. Yang, Macroscopic 3D porous graphitic carbon nitride monolith for enhanced photocatalytic hydrogen evolution, Advanced Materials, 27 (2015) 4634-4639.

[43] M. Xiao, Z. Wang, M. Lyu, B. Luo, S. Wang, G. Liu, H.M. Cheng, L. Wang, Hollow Nanostructures for Photocatalysis: Advantages and Challenges, Advanced Materials, (2018) 1801369.

[44] G. Prieto, H. Tüysüz, N. Duyckaerts, J. Knossalla, G.-H. Wang, F. Schüth, Hollow nano-and microstructures as catalysts, Chemical reviews, 116 (2016) 14056-14119.

[45] Z. Gu, Y. Asakura, S. Yin, High yield post-thermal treatment of bulk graphitic carbon nitride with tunable band structure for enhanced deNO$_x$ photocatalysis, Nanotechnology, 31 (2019) 114001.

[46] J. Li, W. Cui, Y. Sun, Y. Chu, W. Cen, F. Dong, Directional electron delivery via a vertical channel between g-C$_3$N$_4$ layers promotes photocatalytic efficiency, Journal of Materials Chemistry A, 5 (2017) 9358-9364.

[47] J. Liao, W. Cui, J. Li, J. Sheng, H. Wang, P. Chen, G. Jiang, Z. Wang, F. Dong, Nitrogen defect structure and NO$^+$ intermediate promoted photocatalytic NO removal on H$_2$ treated g-C$_3$N$_4$, Chemical Engineering Journal, 379 (2020) 122282.

[48] J. Li, Y. Sun, G. Jiang, Y. Chu, S. Lee, F. Dong, Tailoring the rate-determining step in photocatalysis via localized excess electrons for efficient and safe air cleaning, Applied Catalysis B: Environmental, 239 (2018) 187-195.

[49] B. Tang, X. Yang, X. Cao, M. Deng, rGO/g-C$_3$N$_4$ photocatalyst with an enhanced catalytic activity for NO removal, Materials Research Express, 6 (2019) 125509.

[50] Y. Asakura, Y. Inaguma, K. Ueda, Y. Masubuchi, S. Yin, Synthesis of gallium oxynitride nanoparticles through hydrothermal reaction in the presence of acetylene black and their photocatalytic NO$_x$ decomposition, Nanoscale, 10 (2018) 1837-1844.

[51] Y. Asakura, Y. Nishimura, Y. Masubuchi, S. Yin, Utility of $ZnGa_2O_4$ Nanoparticles Obtained Hydrothermally for Preparation of GaN: ZnO Solid Solution Nanoparticles and Transparent Films, European Journal of Inorganic Chemistry, 2019 (2019) 1999-2005.

[52] H. Imagawa, X. Wu, H. Itahara, S. Yin, K. Kojima, S.F. Chichibu, T. Sato, Photocatalytic NO removal over calcium-bridged siloxenes under ultraviolet and visible light irradiation, Dalton Transactions, 47 (2018) 7070-7076.

[53] X. Wu, S. Yin, Q. Dong, T. Sato, Blue/green/red colour emitting up-conversion phosphors coupled $C-TiO_2$ composites with UV, visible and NIR responsive photocatalytic performance, Applied Catalysis B: Environmental, 156 (2014) 257-264.

[54] X. Wu, K. Zhang, G. Zhang, S. Yin, Facile preparation of BiOX (X= Cl, Br, I) nanoparticles and up-conversion phosphors/BiOBr composites for efficient degradation of NO gas: Oxygen vacancy effect and near infrared light responsive mechanism, Chemical Engineering Journal, 325 (2017) 59-70.

[55] X. Wu, S. Yin, B. Liu, M. Kobayashi, M. Kakihana, T. Sato, A carbon modified $NaTaO_3$ mesocrystal nanoparticle with excellent efficiency of visible light induced photocatalysis, Journal of Materials Chemistry A, 2 (2014) 20832-20840.

[56] M. Kobayashi, Y. Suzuki, T. Goto, S.H. Cho, T. Sekino, Y. Asakura, S. Yin, Low-temperature hydrothermal synthesis and characterization of $SrTiO_3$ photocatalysts for NOx degradation, Journal of the Ceramic Society of Japan, 126 (2018) 135-138.

[57] J. Ran, T.Y. Ma, G. Gao, X.-W. Du, S.Z. Qiao, Porous P-doped graphitic carbon nitride nanosheets for synergistically enhanced visible-light photocatalytic H_2 production, Energy & Environmental Science, 8 (2015) 3708-3717.

[58] J. Xue, M. Fujitsuka, T. Majima, Shallow Trap State Induced Efficient Electron Transfer at the Interface of Heterojunction Photocatalysts: The Crucial Role of Vacancy Defects, ACS Applied Materials & Interfaces, (2019).

[59] S. Komatsuda, Y. Asakura, J.J.M. Vequizo, A. Yamakata, S. Yin, Enhanced photocatalytic NOx decomposition of visible-light responsive $F-TiO_2/(N, C)-TiO_2$ by charge transfer between $F-TiO_2$ and $(N, C)-TiO_2$ through their doping levels, Applied Catalysis B: Environmental, 238 (2018) 358-364.

[60] Y.-J. Yuan, Y. Yang, Z. Li, D. Chen, S. Wu, G. Fang, W. Bai, M. Ding, L.-X. Yang, D.-P. Cao, Promoting charge separation in g-C$_3$N$_4$/graphene/MoS$_2$ photocatalysts by two-dimensional nanojunction for enhanced photocatalytic H$_2$ production, ACS Applied Energy Materials, 1 (2018) 1400-1407.

[61] P. Yang, J. Zhao, W. Qiao, L. Li, Z. Zhu, Ammonia-induced robust photocatalytic hydrogen evolution of graphitic carbon nitride, Nanoscale, 7 (2015) 18887-18890.

[62] Z. Zhang, J. Huang, M. Zhang, Q. Yuan, B. Dong, Ultrathin hexagonal SnS2 nanosheets coupled with g-C$_3$N$_4$ nanosheets as 2D/2D heterojunction photocatalysts toward high photocatalytic activity, Applied Catalysis B: Environmental, 163 (2015) 298-305.

[63] Y. Li, R. Jin, Y. Xing, J. Li, S. Song, X. Liu, M. Li, R. Jin, Macroscopic Foam‐Like Holey Ultrathin g‐C$_3$N$_4$ Nanosheets for Drastic Improvement of Visible‐Light Photocatalytic Activity, Advanced Energy Materials, 6 (2016) 1601273.

[64] P. Kumar, E. Vahidzadeh, U.K. Thakur, P. Kar, K.M. Alam, A. Goswami, N. Mahdi, K. Cui, G.M. Bernard, V.K. Michaelis, C$_3$N$_5$: A Low Bandgap Semiconductor Containing an Azo-Linked Carbon Nitride Framework for Photocatalytic, Photovoltaic and Adsorbent Applications, Journal of the American Chemical Society, 141 (2019) 5415-5436.

[65] N. Tian, Y. Zhang, X. Li, K. Xiao, X. Du, F. Dong, G.I. Waterhouse, T. Zhang, H. Huang, Precursor-reforming protocol to 3D mesoporous g-C$_3$N$_4$ established by ultrathin self-doped nanosheets for superior hydrogen evolution, Nano Energy, 38 (2017) 72-81.

[66] Y. Wang, X. Liu, J. Liu, B. Han, X. Hu, F. Yang, Z. Xu, Y. Li, S. Jia, Z. Li, Carbon quantum dot implanted graphite carbon nitride nanotubes: excellent charge separation and enhanced photocatalytic hydrogen evolution, Angewandte Chemie International Edition, 57 (2018) 5765-5771.

[67] Z. Wang, M. Chen, Y. Huang, X. Shi, Y. Zhang, T. Huang, J. Cao, W. Ho, S.C. Lee, Self-assembly synthesis of boron-doped graphitic carbon nitride hollow tubes for enhanced photocatalytic NO$_x$ removal under visible light, Applied Catalysis B: Environmental, 239 (2018) 352-361.

[68] Z. Wang, Y. Huang, M. Chen, X. Shi, Y. Zhang, J.-j. Cao, W. Ho, S.C. Lee, The Roles of N-vacancies over Porous g-C_3N_4 Microtubes during Photocatalytic NO_x Removal, ACS Applied Materials & Interfaces, (2019).

[69] Japanese Industrial Standard [JIS R 1701-1:2004(J)], Test method for air purification performance of photocatalytic materials – Part 1: Removal of nitric oxide, Japanese Standards Association, established on 2004-01-20.

[70] M. Anpo, (2002), Recent Development on Visible Light Response Type Photocatalyst, NTS, Tokyo, p 9.

4.2 CN/TiO$_2$ heterostructure

Our target is to prepare CN/TiO$_2$ heterostructure (**Chapter 4.2**) via calcination assisted hydrothermal process. Interestingly, we prepared oxygen vacancies mediated TiO$_2$ with excellent photocatalytic performance, which include two parts.

The first related research work is entitled **"Intrinsic carbon-doping induced synthesis of oxygen vacancies-mediated TiO$_2$ nanocrystals: enhanced photocatalytic NO removal performance and mechanism" (Chapter 4.2.1)**

The second related research work is entitled **"Reductant-free synthesis of oxygen vacancies-mediated TiO$_2$ nanocrystals with enhanced photocatalytic NO removal performance: an experimental and DFT study" (Chapter 4.2.2).**

4.2.1 Intrinsic carbon-doping induced synthesis of oxygen vacancies-mediated TiO₂ nanocrystals: enhanced photocatalytic NO removal performance and mechanism

4.2.1.1 Introduction

Environmental pollution and energy crisis are the two major challenges in the world on account of the consumption of fossil fuels and industrial activities [1, 2]. Photocatalysis has been recognized as a promising technology for energy conversion and environmental remediation [3-6]. It is well-understood that the fabrication and development of photocatalysts is the key point of photocatalytic technology [7-11]. Since the pioneering work in 1972 when Fujishima and Honda firstly reported the photocatalytic water splitting using TiO_2 electrodes[12], abundant of photocatalysts were developed such as ZnO [6, 13], BiOCl [14], Bi_2WO_6 [15], $BiVO_4$ [16], CdS [17] and $g-C_3N_4$ [18]. Even so, TiO_2 is still one of the most effective, low-cost and fascinating photocatalyst due to its outstanding properties such as high chemical and thermal stability, environmental benignity and excellent electronic property [19, 20]. However, the relatively large band gap (3.0-3.2eV) of TiO_2 makes it only sensitive to ultraviolet (UV) light, which makes up less than 5% of the natural solar light [21]. Also, pristine TiO_2 suffers from the high recombination of photogenerated charge carriers [22, 23]. These intrinsic shortcomings of TiO_2 seriously hamper its further practical applications. Therefore, much effort has been devoted to solve the problem including metal and non-metal doping, noble metal deposition, sensitization, defect engineering, heterostructure construction and so on [24, 25].

Recently, oxygen vacancies (OVs) have emerged as a promising strategy to modulate the large band gap of TiO_2 since Chen et al. synthesized black TiO_2 with rich OVs by high-pressure hydrogen treatment in 2011 [26]. The OVs have significant effects on the band structure and properties of TiO_2. Concretely, the OVs induced localized states that could narrow the band gap and extend the light response to visible

light, which would promote to generate more charge carriers [27]. Also, the OVs might improve the electronic conductivity to enhance the charge carrier efficiency [28]. In turn, the resultant much more charge carriers are beneficial for surface redox reactions. Moreover, the OVs enable to modify the electronic structure around the reaction sites to facilitate the adsorption of intermediates and realize the improvement of the photocatalytic activity [28]. Up to the present, great progress has been made to synthesize the OVs-mediated TiO_2 (OVs-TiO_2), to meet its requirements for energy and environment [29, 30]. The main methods of preparing OVs-TiO_2 are thermal treatment of TiO_2 in reducing atmospheres (i.e., vacuum atmosphere, pure H_2 or H_2/Ar), chemical reduction (i.e., Al, Li, or $NaBH_4$), and electrochemical reduction. However, these reported strategies have their inevitable drawbacks, such as the requirement of high temperature or high pressure, involvement of toxic reductive agents, and time and cost consuming [27, 29, 31]. Therefore, it is still a great challenge to develop a facile and low-cost route for the preparation OVs-TiO_2.

In this study, we developed a facile strategy to fabricate OVs-TiO_2 anatase TiO_2 nanoparticles by a low-temperature calcination in the N_2 atmosphere assisted water-controlled-releasing solvothermal (WCRS) process using the ethanol, acetic acid and titanium tetraisopropoxide (TTIP) as precursors. The photocatalytic NO removal test was employed to evaluate the photocatalytic performance of the obtained samples. The obtained OVs-TiO_2 nanoparticles displayed outstanding photocatalytic NO removal performance under visible light irradiation (λ>510 nm), in comparison with the commercial P25. In addition, the obtained OVs-TiO_2 displayed about 4.0 times higher catalytic activity than that of carbon-doped TiO_2. With the aid of DFT calculations, we revealed that the carbon-doping was beneficial for the formation of OVs in carbon-doped TiO_2. Moreover, the combination of experimental investigation and theoretical calculation was performed to probe the crucial roles of OVs in OVs-TiO_2 during the photocatalytic NO removal process.

4.2.1.2 Experiment

Sample preparation

Anatase carbon-doped TiO_2 nanoparticles were synthesized by a WCRS process using ethanol, acetic acid and TTIP as precursors. In detail, as the optimized synthesis condition, the ethanol (60 mL), acetic acid (10 mL) and TTIP (5 mL) were introduced into a 100 mL Teflon-lined autoclave followed by heating at 200 ˚C for 18 hours (Table S1). The optimal ratios of the precursors were based on the XRD patterns (**Fig. 4.2.1.1**) and photocatalytic activity (**Fig. 4.2.1.2**). After cooling to room temperature naturally, the product was centrifuged, washed and finally dried under vacuum at 60 ˚C.

To demonstrated that the WCRS process was versatile and to find the optimal ratio of acetic acid/ethanol, a series of TiO_2 samples were synthesized based on the different ratios of acetic acid/ethanol, which were summarized in **Table 4.2.1.1**, **Fig. 4.2.1.1** and **Fig. 4.2.1.2**. As shown in **Fig. 4.2.1.1**, all the as-obtained samples displayed the anatase phase, which was in good agreement with the standard pattern of anatase TiO_2 (JCPDS no. 21-1272) and no other impurities were observed. These results demonstrated that the WCRS process was versatile to synthesize anatase TiO_2. From **Fig. 4.2.1.2**, it can be seen that 10/60-TiO_2 exhibited the highest photocatalytic NO removal performance among all the samples under visible-light irradiation ($\lambda > 400$ nm). Therefore, the 10/60-TiO_2 was chosen as the pristine TiO_2 to prepare the OVs-mediated TiO_2 in the main body.

Table 4.2.1.1. The different ratios of acetic acid/ethanol

Abbr.	5/65-TiO_2	10/60-TiO_2	15/55-TiO_2	20/50-TiO_2	25/45-TiO_2	30/40-TiO_2
Acetic acid (mL)	5	10	15	20	25	30
Ethanol (mL)	65	60	55	50	45	40
TTIP (mL)	5	5	5	5	5	5
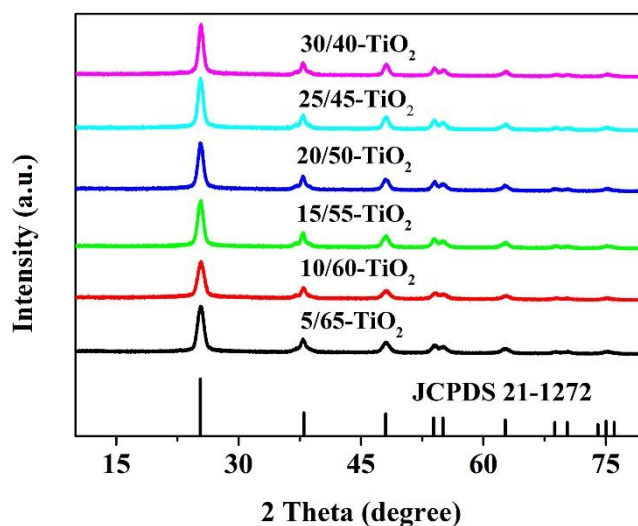
Fig. 4.2.1.1. XRD patterns of the as-obtained samples synthesized via a WCRS process with different solvents ratio
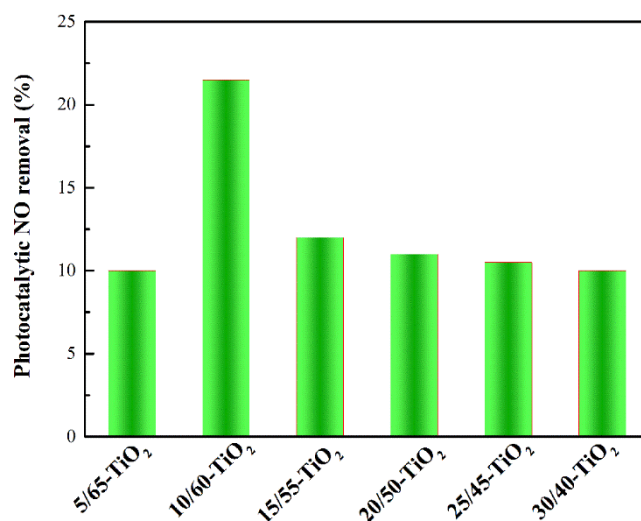
Fig. 4.2.1.2. Photocatalytic NO removal performance of the as-obtained samples synthesized via a WCRS process with different solvent ratio under visible-light irradiation (λ>400 nm)

Synthesis of OVs-TiO₂

To introduce the OVs into anatase carbon-doped TiO_2 nanoparticles, a facile post low-temperature calcination in the N_2 atmosphere was employed. In a typical procedure, 1g of anatase carbon-doped TiO_2 nanoparticles was calcined at a certain temperature (i.e., 250, 325 and 400 ˚C) for 2 h in a tube furnace under a nitrogen atmosphere. For abbreviation, the OVs-TiO_2 nanoparticles calcined under different temperatures (i.e.,

250, 325 and 400 °C) were designated as OVs-TiO$_2$-250, OVs-TiO$_2$-325, and OVs-TiO$_2$-400, respectively.

Characterization

X-ray diffraction with Cu Kα line (XRD, Bruker D2 Phaser) was carried out to determine the crystalline structures of the samples. Fourier transform infrared (FTIR) spectra were recorded on an FTIR spectrometer (JASCO, FTIR-660D-ATR). The optical properties of the samples were measured on a near-infrared spectrophotometer (JASCO, V-670). The morphology and microstructure of the products were characterized by transmission electron microscopy (TEM, JEOL JEM-2000EXII)), high-resolution transmission electron microscopy (HRTEM, JEOL JEM-2010), and selected area electron diffraction (SAED) using ZEISS LEO-9522 microscope. Electron paramagnetic resonance (EPR) spectra were collected on Bruker E580 EPR spectrometer at room temperature. Photoluminescence (PL) data were tested using a spectrofluorometer (JASCO, FP-8500) under excitation of a wavelength of 325 nm. The binding energy of the contained elements was confirmed via x-ray photoelectron spectroscopy (XPS, ULVAC PHI 5600, ULVAC PHI Co., Ltd). Raman spectra were measured by a Raman spectrometer (JASCO, RAM-500DSEII)

Density functional theory calculations

To further understand the electronic structure of OVs-TiO$_2$, density functional theory (DFT) calculation was carried out by using the Vienna Ab Initio Simulation Package (VASP)[32, 33] based on the projected augmented wave (PAW) method. The generalized gradient approximation with the Perdew–Burke–Ernzerhof (GGA/PBE)[34] was employed as the exchange-correlation functional. In addition, an effective U value of 8.0 eV was applied to the $3d$ orbitals of Ti to well reproduce electronic structures for anatase TiO$_2$[35]. Duplicating the primitive cell of anatase TiO$_2$ to a 2 x 2 x 1 supercell (pure bulk TiO$_2$ model), the (001)-(2*2) surface model was slabbed from the supercell, with a vacuum space of 15 Å in the z-direction to avoid the influence of the inter-layer interaction caused by the periodicity. The slab thickness was 9.91 Å. The (001) surface slab model of TiO$_2$ consisting of 48 atoms: 16 Ti atoms and 32 O atoms. 1 O atom was removed and the concentration of O vacancies was about 2%. Moreover, the formation

energies were calculated based on bulk TiO_2 mode. The bulk TiO_2 mode consisting of 48 atoms: 16 Ti atoms and 32 O atoms. 1 O atom was removed on the surface of bulk TiO_2 mode and the concentration of O vacancies was about 2%. And 1 C atom was doped atom into the surface bulk TiO_2 mode and concentration of C atoms was about 2%, too. After introducing O vacancies and the C atom, we fixed the lattice constant and let the atoms fully relax in the unit cell to reach the convergence standards of force and energy in order to determine the formation energy of O vacancies and C doping. The O chemical potential obtained for O-rich and O-poor conditions was determined by the value of -4.98eV. If the O chemical potential was lower than -4.98eV, it meant O-poor conditions. If the O chemical potential was lower than -4.98eV, it meant O-rich conditions. In current work, we assumed that carbon formed during calcination was graphitic not in the form of CO_2 gas because the atmosphere was N_2 during the calcination process. A Γ-centered 6 × 6 × 5 (bulk) and 6 × 6 × 1 (layer) Monkhorst-Pack grids for the Brillouin zone sampling and a plane wave basis set with a cutoff energy of 400 eV were used to calculate self-consistent field (SCF) energies and charge densities. For energy and geometry optimizations, their convergence criteria for the SCF energy and maximum force were set to be 1.0×10^{-4} eV/atom and 0.01 eV/Å, respectively.

Photocatalytic NO removal characterization

The performance of the resultant samples was evaluated by photocatalytic NO removal test in a continuous flow reactor system, using a mercury lamp (450 W) with a cutoff filter (λ>400 nm or λ>510nm) as the visible-light source. Also, the photocatalytic NO removal activity of OVs-TiO_2 samples were measured under irradiation of full spectrum (without the filter), i.e., the light source including the visible-light and UV light [2, 36, 37]. The as-prepared samples were placed in the cell (20mm×16mm×0.5mm) of glass plate and the glass plate containing the photocatalyst was transferred into the continuous flow reactor with the internal volume of $373cm^3$. NO_x detector (Yanaco, ECL-88A) was equipped to determine the concentration of NO. 1 ppm NO gas, prepared by mixing compressed air and N_2 balanced 2 ppm NO with a ratio of 1:1, was introduced continuously into the photocatalysis reactor by the flow

rate of 200 mL min^{-1}. The NO removal percentage (%) was defined as follows:

$$NO(\%) = \frac{C_0 - C}{C_0} \times 100 \qquad (4.2.1\text{-}1)$$

Where C_0 and C were the concentrations of NO in the feed and outlet streams after 10 minutes of photocatalytic NO removal at room temperature.

4.2.1.3 Results and discussion
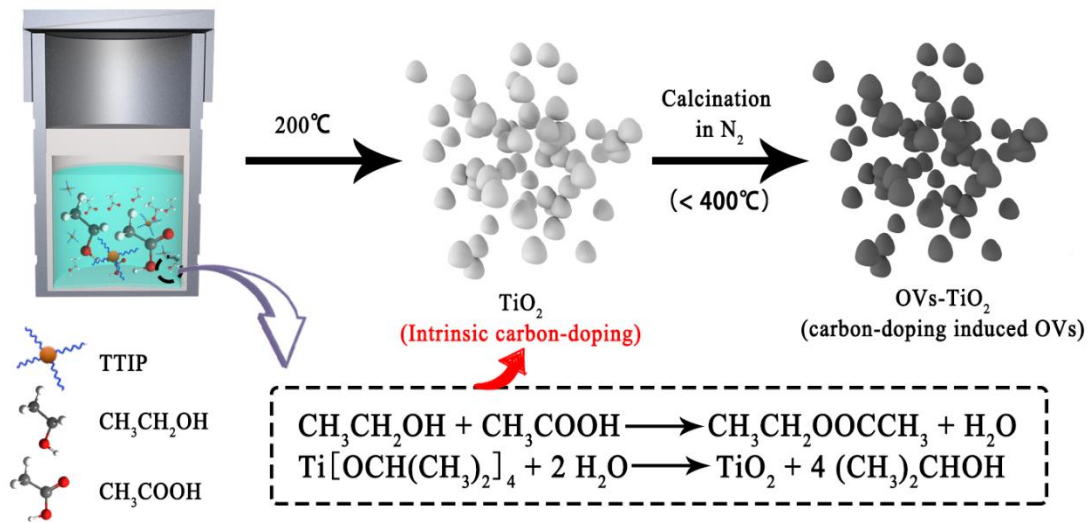
Fig. 4.2.1.3. Schematic illustration for the synthesis of OVs-TiO$_2$ via intrinsic carbon-doping induced strategy

Formation mechanism of OVs-TiO$_2$

The OVs-TiO$_2$ was synthesized via a low-temperature calcination in nitrogen atmosphere after the WCRS process using ethanol, acetic acid and TTIP as precursors, as shown in **Fig. 4.2.1.3**. During the solvothermal process, the esterification reaction between ethanol and acetic acid would generate water gradually, which was employed to induce the hydrolysis of TTIP, resulting in the intrinsic carbon-doped TiO$_2$ nanocrystals [38]. Then the obtained carbon-doped TiO$_2$ nanocrystals were calcined at different low temperatures under N$_2$ atmosphere to introduce the OVs into them and remove the carbon dopant.
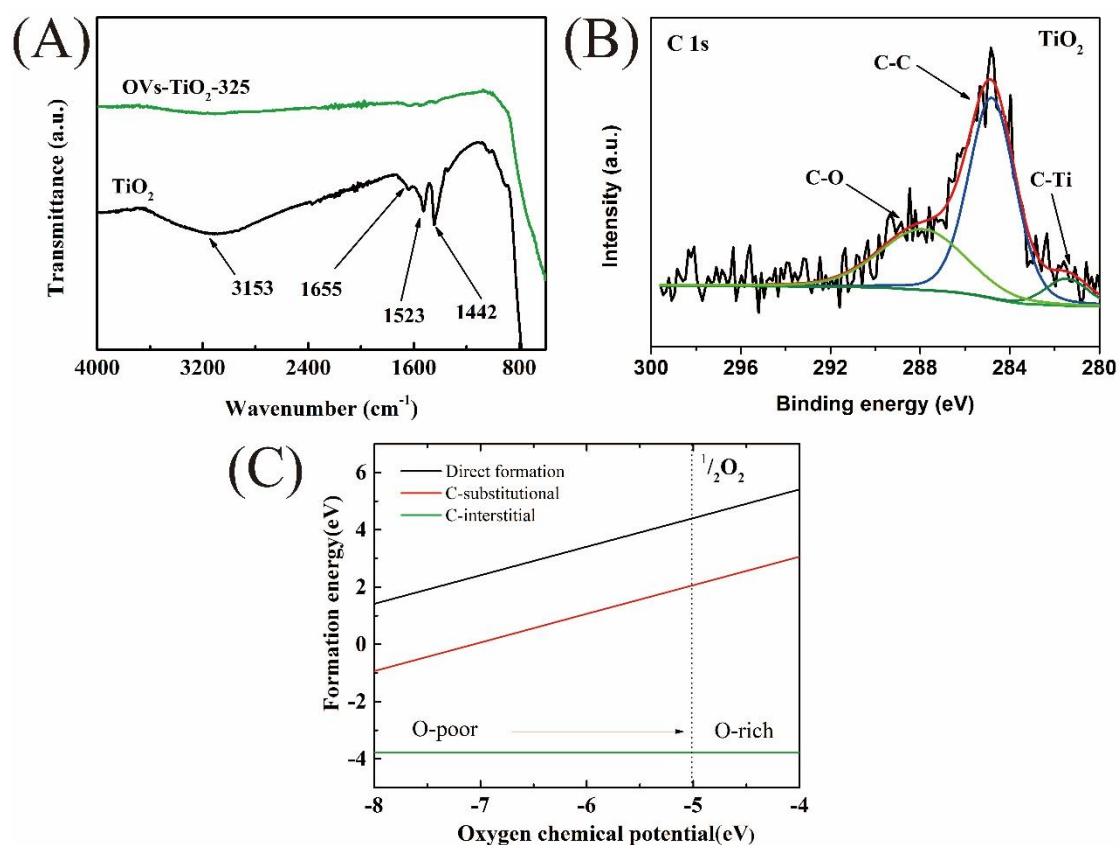
Fig. 4.2.1.4. (A) FTIR spectra of TiO_2 and OVs-TiO_2-325, (B) XPS spectra of C1s for TiO_2, and (C) formation energies as a function of oxygen chemical potential for different carbon species based on the DFT calculations.
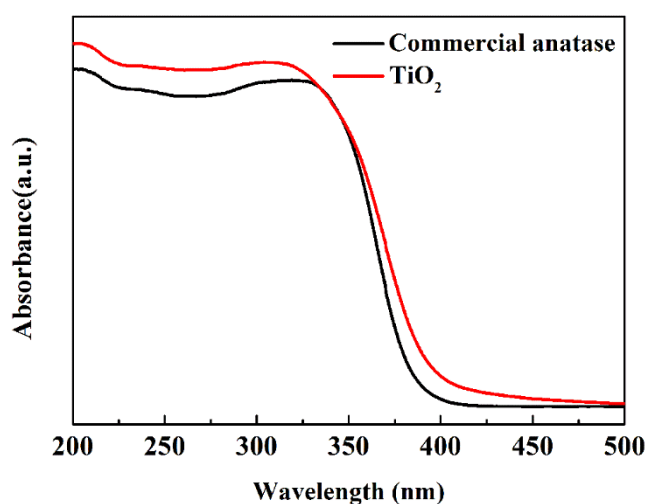
Fig. 4.2.1.5. UV-vis DRS spectra of as-synthesized TiO_2 and commercial anatase

Considering the synthesis process of OVs-TiO_2 samples was facile and

unconventional, experimental and theoretical investigation was adopted to unravel the mechanism. It is easy to understand that the carbon elements were inevitably doped into anatase TiO_2 nanoparticles via substituting oxygen sites or getting into the interstitial of TiO_2, which was due to the involvement of organic materials such as ethanol, acetic acid, and TTIP during the WCRS process [38]. The intrinsic carbon-doping was revealed by the FTIR spectra depicted in **Fig. 4.2.1.4.**A. The TiO_2 exhibited distinct peaks at 1442 and 1523 cm^{-1}, which could be ascribed to the carbon-related substrates including ethanol, acetic acid and ethyl acetate. However, after calcination in N_2, both of them disappeared. The peaks at 1655 and 3153 cm^{-1} was related to the hydroxyls and adsorbed water[36]. Moreover, the XPS spectra provide direct evidence of carbon doping in TiO_2. As shown in **Fig. 4.2.1.4** B, the carbide-related trace could be observed at around 281.3 eV in the TiO_2 after Ar^+ etching, which was ascribed to the Ti-C bond [39, 40].In addition, the intrinsic carbon-doping was demonstrated UV-Vis DRS spectra (**Fig.4.2.1.5**). Compared with commercial anatase, the synthesized anatase TiO_2 showed enhanced visible-light absorption due to the intrinsic carbon-doping. Also, the inherent carbon-doping of TiO_2 was supported by its photocatalytic performance under visible-light irradiation (λ>510 nm)[36].

The effects of carbon doping on the formation energies (ΔE) of OVs are illustrated in **Fig. 4.2.1.4**C. The formation energies of OVs related to different carbon doping was follows:

Direct formation:

$$TiO_2 \rightarrow TiO_{2-x} \text{ (O vacancy)} + O \qquad (\Delta E = 5.073 \text{ eV}) \qquad (4.2.1\text{-}2)$$

C-substitutional TiO_2:

$$TiO_{2-x}C_x \rightarrow TiO_{2-x} \text{ (O vacancy)} + C + O \qquad (\Delta E = -3.7857 \text{ eV}) \qquad (4.2.1\text{-}3)$$

C-interstitial TiO_2:

$$TiO_2C_x \rightarrow TiO_{2-x} \text{ (O vacancy)} + C + O \qquad (\Delta E = 2.0543 \text{ eV}) \qquad (4.2.1\text{-}4)$$

From the DFT calculation results, it is easy to conclude that no matter what the form of carbon doping was, i.e., substitutional carbon or interstitial carbon, the carbon impurities favored the formation of OVs in anatase TiO_2[41]. In other words, thanks to the WCRS process to introduce the carbon-related organic impurities into TiO_2, the

formation of OVs in anatase TiO_2 could be realized by low-temperature calcination in N_2 atmosphere.

Phase structures, OVs analysis and morphologies
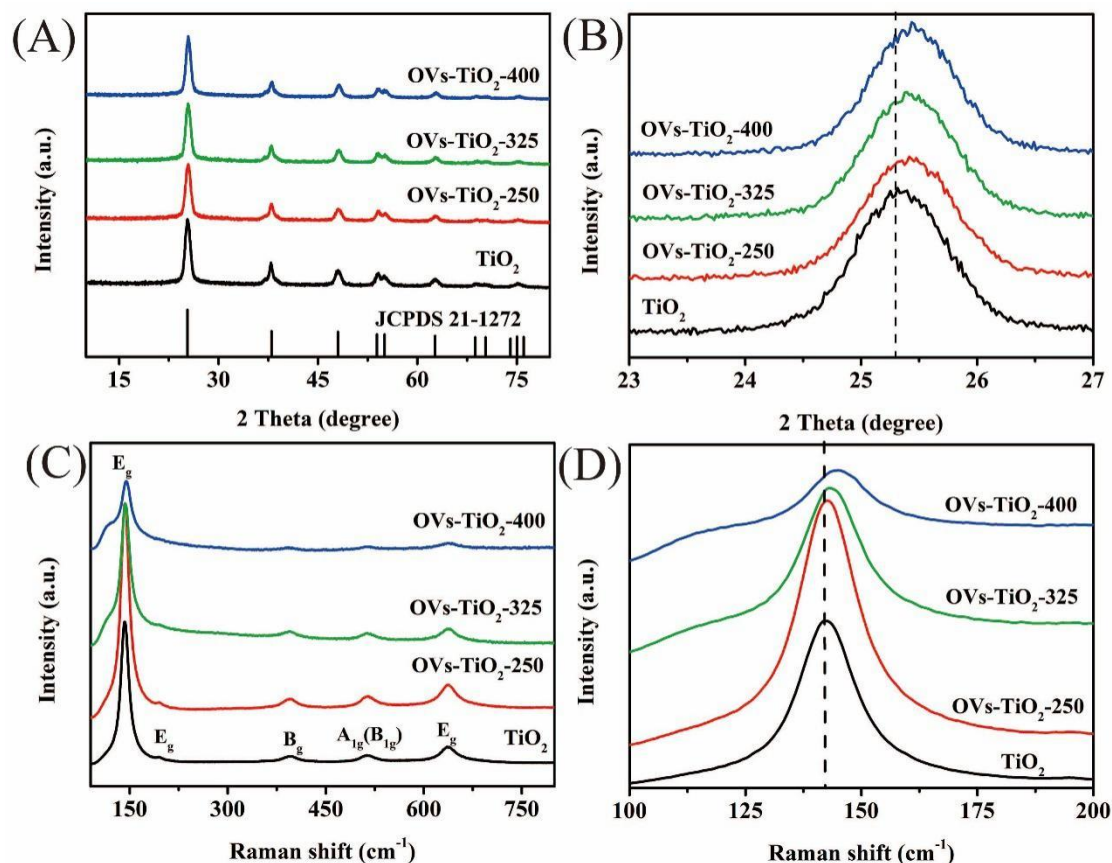
Fig. 4.2.1.6. (A) XRD patterns of the as-obtained samples (TiO_2, OVs-TiO_2-250, OVs-TiO_2-325, and OVs-TiO_2-400), (B) corresponding enlarged XRD patterns in the range between 20°-30°;(C) Raman spectra, (D) corresponding enlarged Raman spectra.

The XRD patterns of carbon-doped TiO_2, OVs-TiO_2-250, OVs-TiO_2-325, and OVs-TiO_2-400 were recorded in **Fig. 4.2.1.6**A to reveal their phase structures. The XRD patterns of all the obtained samples were all good consistent with the standard pattern of anatase TiO_2 (JCPDS no. 21-1272) and no other impurities were observed [42]. **Fig. 4.2.1.6**B displayed the enlarged view of (101) peaks from 23.0 to 27.0°, showing that the diffractions peaks of all OVs-TiO_2 samples distinctly shift to higher diffraction angles in comparison with carbon-doped TiO_2. These results demonstrated the reduction of the interplanar distance of the crystalline phase, which was indicative of

the existence of OVs [43]. These results were consistent with previous results [24]. Moreover, Raman spectroscopy was carried out to further detect the structures of the as-resultant samples. As shown in **Fig. 4.2.1.6**C, six characteristic Raman peaks ($3E_g+2B_{1g}+A_{1g}$) emerged for all the samples, which were index to the Raman modes of the anatase [42]. These results were in good agreement with XRD patterns. In addition, compared with carbon-doped TiO_2, the scattering peaks of OVs-TiO_2 samples shifted to higher wavenumbers (**Fig. 4.2.1.6**D), which was attributed to the presence of the OVs in anatase crystal. This phenomenon was consistent with previously reported[24, 43].
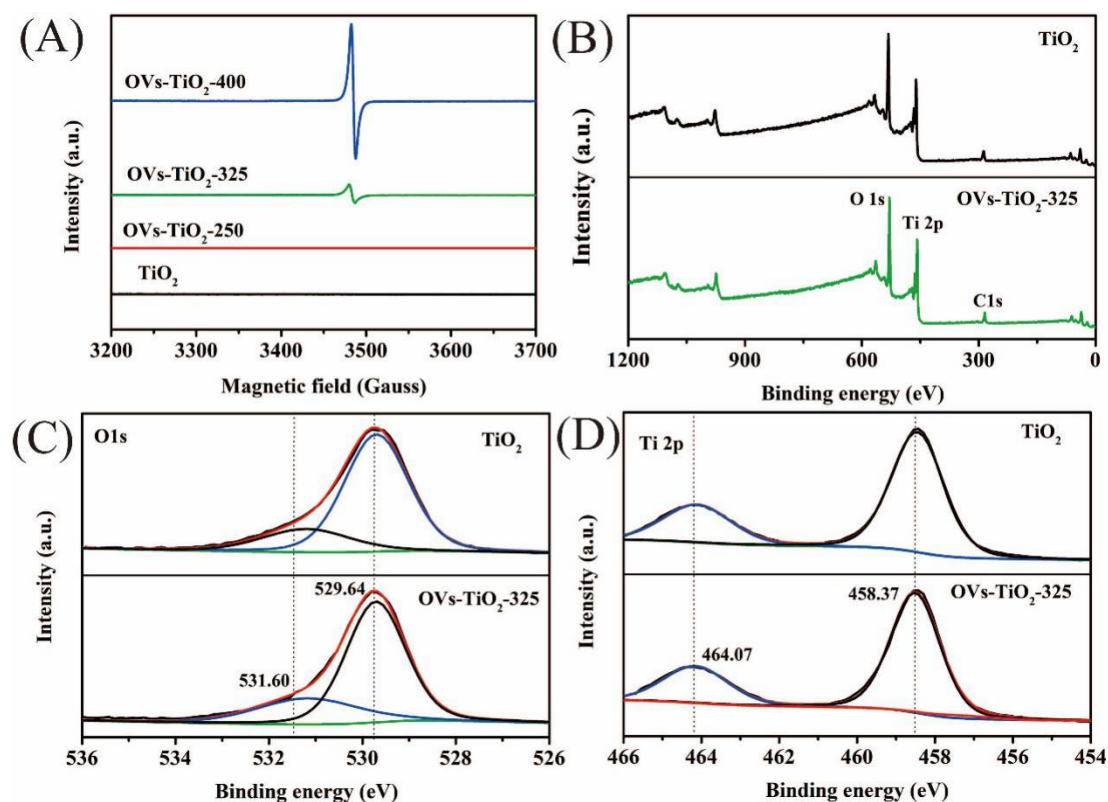
Fig. 4.2.1.7. (A) EPR spectra of the as-obtained samples (TiO_2, OVs-TiO_2-250, OVs-TiO_2-325, OVs-TiO_2-400); XPS spectra of (B) survey spectrum, (C) O1s and (D) Ti 2p for TiO_2 and OVs-TiO_2-325.

EPR was a sensitive and direct technique to confirm the presence of OVs in TiO_2 [19]. **Fig. 4.2.1.7**A shows the EPR spectra of the obtained samples. There was

negligible paramagnetic signal in carbon-doped TiO_2, which suggested no existence of Ti^{3+} or OVs in the synthesized TiO_2[44]. No obvious peak could be found in the OVs-TiO_2-250 sample, which suggested few OVs formed in in the OVs-TiO_2-250 sample. This is because too low calcination temperature hardly introduces the OVs into carbon-doped TiO_2. For OVs-TiO_2-325, a response was clearly observed, suggesting the OVs with trapped electrons. Among the samples, the OVs-TiO_2-400 exhibited the strongest signal intensity, which indicated the highest concentrations of OVs in it. XPS was also performed to study the surface chemistry of the carbon-doped TiO_2 and OVs-TiO_2-325.The XPS survey spectrum indicated the presence of Ti, O, and C (**Fig. 4.2.1.7**B). The trace amount of C element could be ascribed to the organic precursors and adventitious carbon species. It is important to note that the survey XPS spectrum was carried out without Ar^+ etching to remove the adventitious carbon species, therefore, in the survey spectra, both samples showed the C1s spectra coming from the adsorbed carbon species. For high-resolution O 1s of carbon-doped TiO_2 (**Fig. 4.2.1.7**C), two peaks at 531.60 and 529.64 eV could be observed, which were index as surface OH groups and lattice oxygen in TiO_2, respectively. As shown in **Fig. 4.2.1.7**D, the Ti 2p spectra of carbon-doped TiO_2 and OVs-TiO_2-325 were almost identical. All Ti 2p signals were symmetric with no shoulders at the lower energy sides, which demonstrated no Ti^{3+} existed on the surface of OVs-TiO_2-325. These results were due to the electronic interactions between the Ti atoms and OVs are too weak under current conditions to forms stable Ti^{3+} [44]. The phenomenon was consistent previous reports [24]. The XPS spectra were in good agreement with the results of EPR spectra. To be more specific, both the XPS spectra and EPR spectra did not show the existence of Ti^{3+}. In other words, the disordered surface layer could be attributed to the formation of OVs [24], which we would discuss later.

Fig. 4.2.1.8A and **Fig. 4.2.1.8**B show the typical TEM images of carbon-doped TiO_2 and OVs-TiO_2-325, respectively. Both of carbon-doped TiO_2 and OVs-TiO_2-325 were nanoparticles and post-calcination did not change the size of nanoparticles significantly. Moreover, the low-temperature calcination did not affect the specific surface areas of the samples too much. The specific surface areas of carbon-doped TiO_2

and OVs-TiO$_2$-325 were 136.9 m^2/g and120.5 m^2/g **(Fig. 4.2.1.9)**, respectively. HR-TEM was commonly performed to identify the disordered structures in OVs-TiO$_2$ samples. As shown in Fig.5C, the carbon-doped TiO$_2$ exhibited clearly-resolved lattice fringes with a d-spacing of 0.35nm typical for anatase, which indicated the high level of crystallization. In contrast, the lattice fringes of OVs-TiO$_2$-325 became blur after calcination under N$_2$ atmosphere, which demonstrated the structural deviation from the crystalline anatase[26]. In addition, **Fig. 4.2.1.8** (E-F) and **Fig. 4.2.1.10** (A-B) depicted the optimized configuration of pristine TiO$_2$ and OVs-TiO$_2$, based on the DFT calculations, respectively. Compared with TiO$_2$, the disordered structure was formed in the OVs-TiO$_2$ lattice owing to the existence of OVs, which was demonstrated by the HR-TEM images. These DFT results were in good consistent with shifts in the XRD peaks, which indicated the lattice distortions, i.e., the presence of the OVs in the OVs-TiO$_2$ samples.
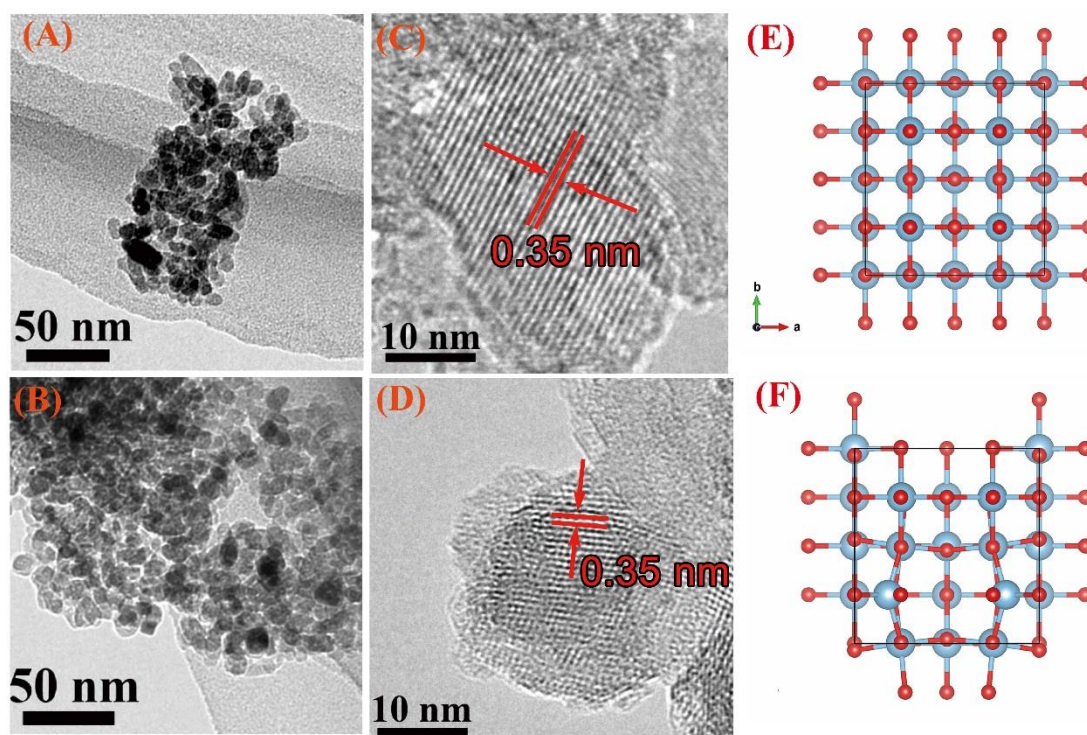
Fig. 4.2.1.8. (A-B) TEM images and (C-D) HR-TEM images of TiO$_2$ (left) and OVs-TiO$_2$-325(right), respectively. (E-F) Top view of the optimized configuration for bulk TiO$_2$ and OVs-TiO$_2$, respectively. Ti and O atoms were index as the red and light blue balls, respectively.
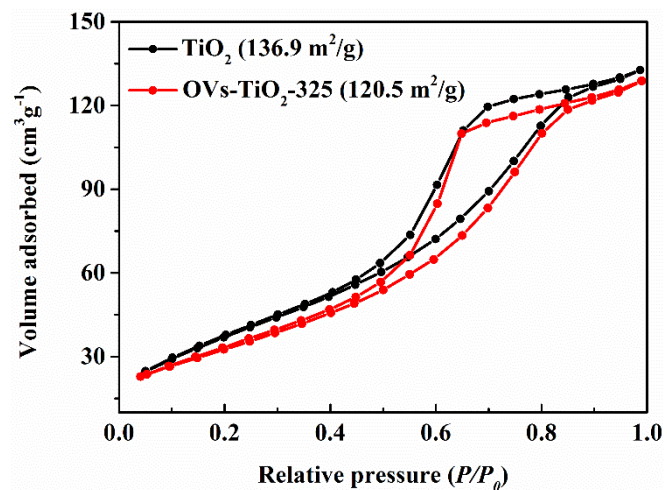
Fig. 4.2.1.9. Nitrogen adsorption isotherms of TiO$_2$ and OVs-TiO$_2$-325, respectively.
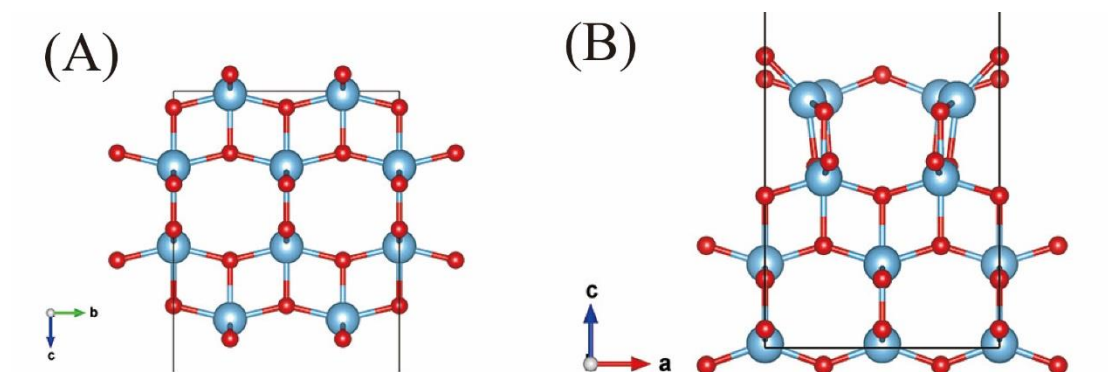
Fig. 4.2.1.10 (A-B) Side view of the optimized configuration for bulk TiO$_2$ and OVs-TiO$_2$, respectively. Ti and O atoms are represented by the red and light blue balls, respectively.

167

Optical and electronic properties
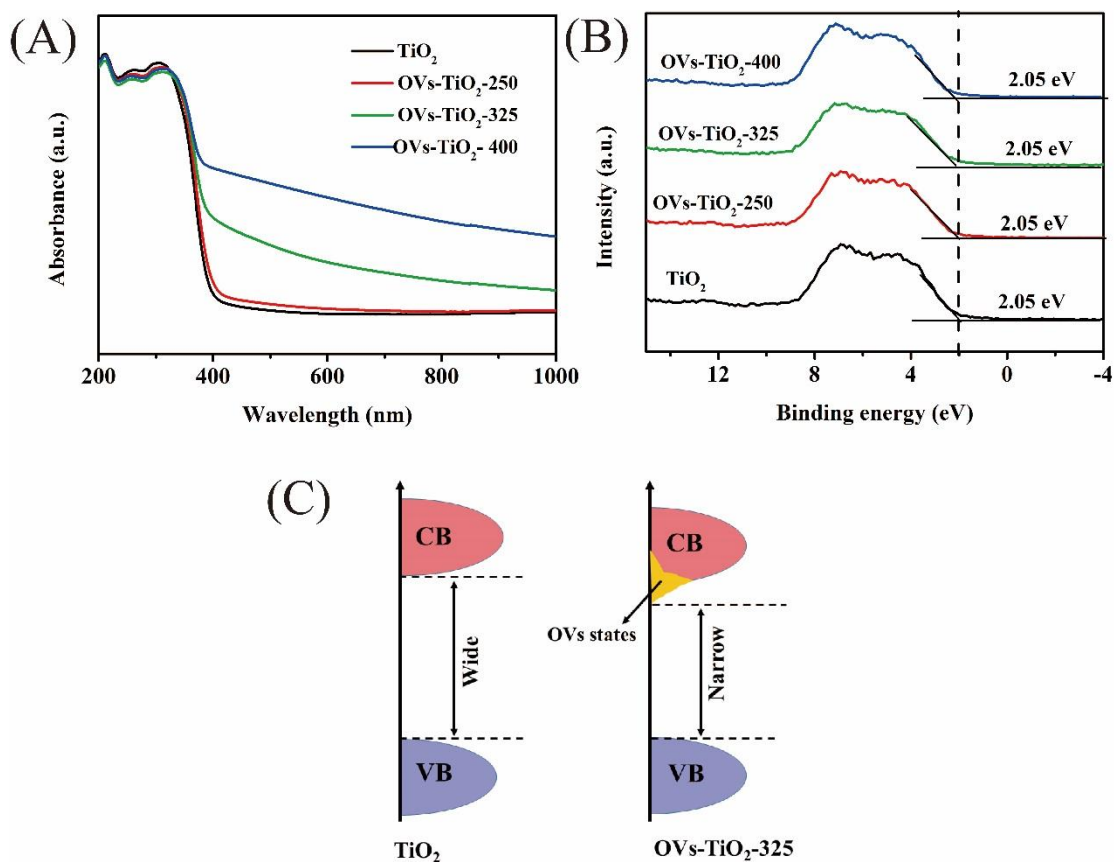
Fig. 4.2.1.11. (A) UV-vis DRS spectra, and (B) VB-XPS spectra of as-obtained samples. (C) schematic illustration for the energy band structures of TiO_2 and OVs-TiO_2-325
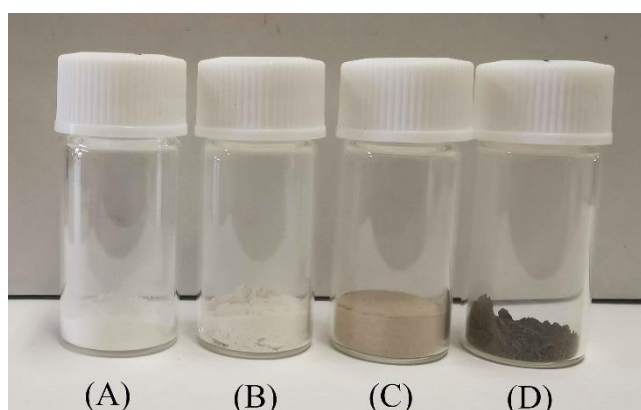
Fig. 4.2.1.12. The digital photograph of the as-synthesized samples with different concentrations of OVs. (A), (B), (C), and (D) were TiO_2, OVs-TiO_2-250, OVs-TiO_2-325, and OVs-TiO_2-400, respectively.

The optical properties of the samples were studied by UV-Vis DRS, as shown in **Fig. 4.2.1.11**A. Compared with carbon-doped TiO_2, OVs-TiO_2 samples showed gradually enhanced light harvesting capability with the increasing concentration of OVs in TiO_2, which clarified the dramatic color change from white to dark grey (**Fig. 4.2.1.12**)[44]. The OVs-TiO_2-400 exhibited the best light absorption ability among all the samples, extending in the near-infrared (NIR) region of the spectrum. It is important to note that both OVs-TiO_2-325 and OVs-TiO_2-400 exhibited distinct tail absorption (Urbach tail) from the visible to the NIR region, which indicated the additional electronic states (well-known as mid-gap states) located within the intrinsic band gap owing to the lattice disorders [45]. The valence band (VB) of the samples was measured by VB XPS (**Fig. 4.2.1.11**B). All the samples showed nearly the same VB edges, which indicated OVs had a negligible influence on the position of VB [44, 46]. In addition, a schematic illustration of the density of states (DOS) distribution in TiO_2 and OVs-TiO_2-325 was depicted in **Fig. 4.2.1.11**C.
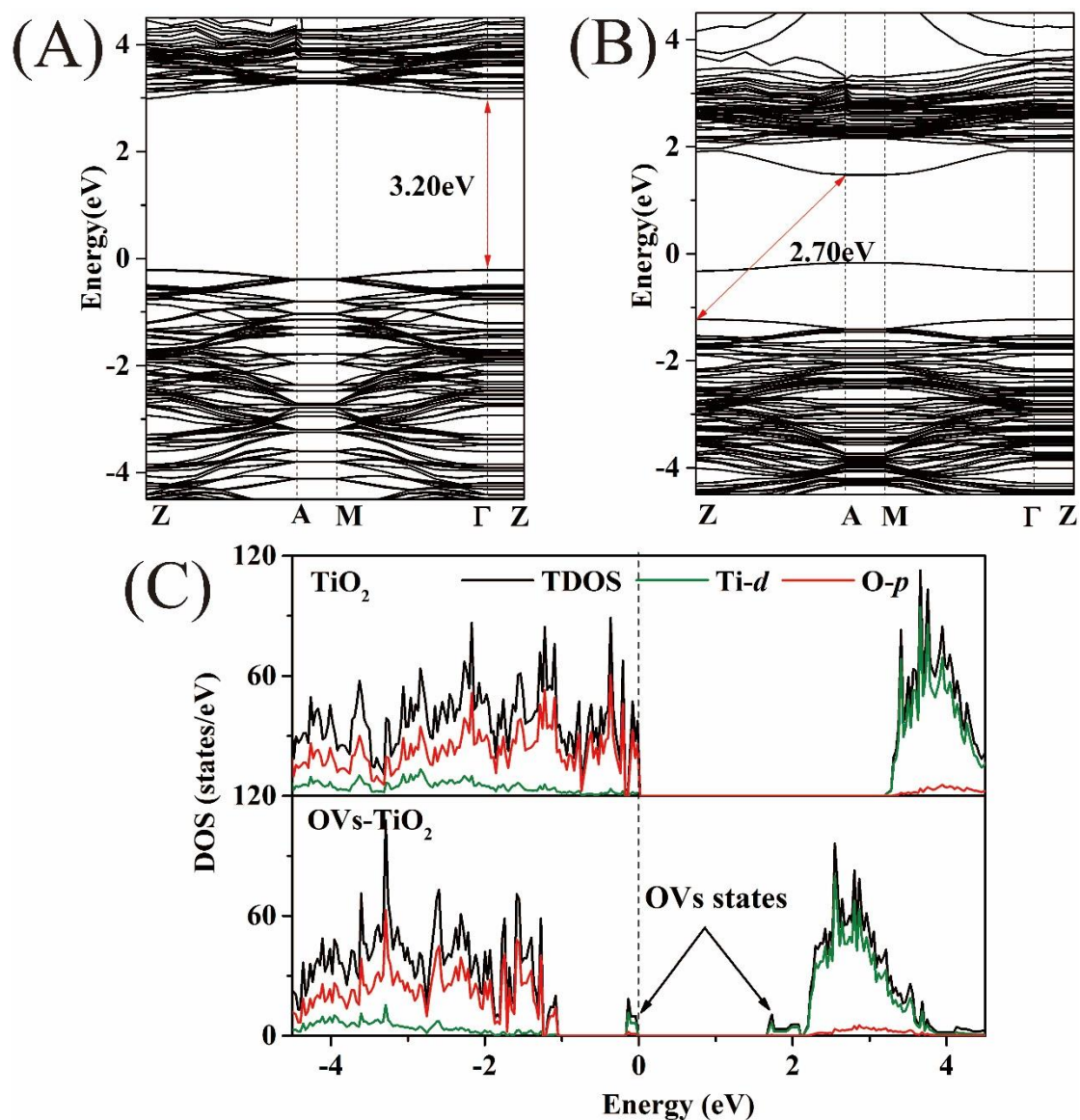
Fig. 4.2.1.13. (A and B) the band structures of TiO_2 and OVs-TiO_2, respectively. (C) Calculated DOS for TiO_2 and OVs-TiO_2, respectively. The Fermi level was taken to be zero.

To understand the crucial roles of OVs in the electronic and optical properties of OVs-TiO_2 deeply, the band structures and DOS were investigated by DFT calculations. As presented in **Fig. 4.2.1.13**A and **Fig. 4.2.1.13**B, OVs-TiO_2 displayed a narrower bandgap of 2.70 eV compared with pristine TiO_2 (3.20 eV), which indicated the higher light absorption property. These theoretical results were qualitatively consistent with the bandgaps unraveled by the UV-vis DRS spectra. Moreover, as indicated in **Fig. 4.2.1.13**C, the valence band maximum (VBM) mainly consisted of O-2p orbitals, and

170

the conduction band maximum (CBM) was mainly composed of Ti-3d orbitals[47]. Compared with pristine TiO_2, the OVs-TiO_2 displayed two groups of OV-induced states: one overlapped with CB derived from Ti-3d orbitals to narrow the bandgap of OVs-TiO_2; another one was considered as mid-gap state derived from the Ti-3d orbitals to enhance the tail absorption[26, 31, 45, 48]. The obtained the VB and CB potentials relative to the Fermi level, that is to say, the VB potentials of pure TiO_2 and OVs-TiO_2 obtained was relative value not absolute value. Therefore, the shift in the VB of OVs-TiO_2 did not contradict the experiment results. In other words, these theoretical calculations were in good agreement with the experimental results, revealing the mechanism of OVs in the optical property and band structure.

Charge carrier transfer and separation
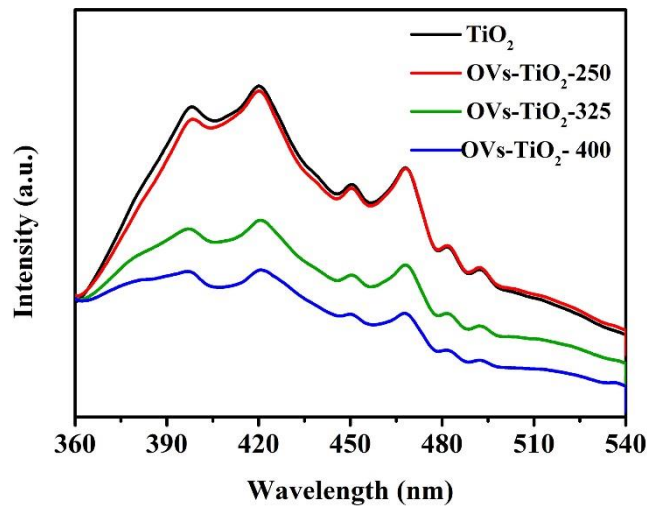
Fig. 4.2.1.14. PL spectra of the obtained samples (TiO_2, OVs-TiO_2-250, OVs-TiO_2-325, and OVs-TiO_2-400)

To study the charge carriers transfer and separation modulated by the OVs, PL analyses were carried out at room temperature (**Fig. 4.2.1.14**). The intensity of PL peaks could be indicative of the recombination of photogenerated electrons and holes. Compared with the carbon doped TiO_2, the intensity of OVs-TiO_2 samples decreased gradually along with increasing the concentration of OVs, suggesting the enhanced charge carrier separation efficiency. It should be noted that the PL intensity of OVs-

TiO$_2$-250 sample hardly decreased owing to few OVs formed in it, which was in good agreement with the EPR spectra results. Among all the samples, the OVs-TiO$_2$-400 exhibited the lowest intensity of PL peaks owing to the highest concentration of OVs. This was because the OVs-induced localized states could trap the photogenerated electrons or holes to suppress the recombination of the charge carriers [27, 31]. Moreover, the OVs enabled to enhance the electrical conductivity by downward shift the conduction band bottom to shorten the migration length for electrons arrival [29]. The enhanced electrical conductivity of OVs-TiO$_2$ samples was beneficial for charge carrier transfer and separation.

It is well-understood that the photocatalytic activity is also affected by the charge transfer rate [49]. The high mobility of photogenerated electrons and holes meant the fast transport speed from bulk to surface, which could promote the charge carrier separation efficiency. Theoretically, the mobility of photogenerated electrons and holes was calculated according to the following equation [2, 50]:

$$v = \hbar \kappa / m^*$$
(4.2.1-5)

Where m^* was the effective mass of electrons or holes, κ was the wave vector, $\hbar$ was the reduced Planck constant, and v was transfer rate of the photogenerated electrons and holes. On the basis of band structure, the effective masses of photogenerated electrons (m_e^*) and holes (m_h^*) along the designated directions were calculated by fitting parabolic functions around the CB minimum (CBM) and VB maximum (VBM) according to the following equation [51]:

$$m^* = \hbar^2 \left[\frac{\partial^2 \varepsilon(k)}{\partial k^2} \right]^{-1}$$
(4.2.1-6)

Where $\varepsilon(k)$ was the band edge energy as a function of wave vector κ. In order to analyze the charge separation efficiency deeply, the relative effective mass (D) of the photogenerated hole to electron was defined according to the following equation:

$$D = \{ \frac{m_h^*}{m_e^*} , \frac{m_e^*}{m_h^*} \} max$$
(4.21.-7)

In general, (I) the smaller effective mass of charge carrier corresponded to the higher mobility, resulting in lower recombination probability of photogenerated electrons and holes; (II) a larger value of D indicated a bigger difference in the mobility of

photogenerated electrons and holes (D>1), leading to promoted charge separation efficiency [17, 51]. As shown in **Table 4.2.1.2**, OVs-TiO$_2$ exhibited the smallest electron effective mass (1.326) and hole effective mass (4.031) along the M→Γ direction. In comparison, TiO$_2$ displayed much higher electron effective mass (2.496) and hole effective mass (8.937) along the Γ→Z direction than those of OVs-TiO$_2$ along the M→Γ direction. It should be noted that both effective mass of charge carrier of TiO$_2$ along the Γ→M direction and effective mass of charge carrier of OVs-TiO$_2$ along the Γ→A direction were too heavy and they could not be taken into consideration [17]. Moreover, the relative effective mass D (3.040) of charge carriers of OVs-TiO$_2$ long the M→Γ direction was nearly the same with that of TiO$_2$ (3.580) along the Γ→Z direction, which meant that relative effective mass D could be ignored in the current work. In other words, only the effective mass of charge carrier played a significant role in determining the charge carrier separation efficiency. Therefore, smaller effective mass of charge carrier of OVs-TiO$_2$ indicates enhanced charge separation efficiency [53]. These theoretical results fall in line with PL spectra. The enhanced charge carrier separation efficiency of OVs-TiO$_2$ suggested much more effective photoinduced electrons and holes involved in the subsequent surface reactions, which would be conductive to promoting the photocatalytic performance.

Table 4.2.1.2. Calculated effective masses of photogenerated electrons and holes of TiO$_2$ and OVs-TiO$_2$ by parabolic fitting to the CBM and VBM along a specific direction in the reciprocal space. m$_0$ was designated as the mass of free electrons.

	Direction	m_e^*/m_0	m_h^*/m_0	D
TiO$_2$	Γ→M	263.555	47.925	5.499
	Γ→Z	2.496	8.937	3.580
OVs-TiO$_2$	M→A	527.109	527.109	1.000
	M→Γ	1.326	4.031	3.040

Photocatalytic NO removal performance

The catalytic activity of the obtained samples was tested under the visible-light irradiation (λ>510 nm and λ>400). In comparison, commercial P25 was used as a standard for showing the excellent photocatalytic activities of OVs-TiO$_2$ samples. As displayed in **Fig. 4.2.1.15**A, the P25 could not exhibit photocatalytic NO removal performance under the visible-light irradiation (λ>510 nm) due to its wide bandgap. However, the carbon-doped TiO$_2$ showed limited photocatalytic NO removal performance, which was ascribed to the inevitable carbon doping originated from the organic precursors during the WCRS process. After the calcination in N$_2$, the OVs-TiO$_2$-250 showed enhanced photocatalytic NO removal performance owing to the introduction of OVs. The OVs-TiO$_2$-325 exhibited the highest visible-light catalytic activity among the samples, which was about 4.0 times higher than that of carbon-doped TiO$_2$.

It should be noted that too much OVs resulted in decreased photocatalytic NO removal performances of OV-TiO$_2$-400. Also, the OV-TiO$_2$-325 displayed the highest photocatalytic NO removal performance among all the samples under the irradiation of visible-light (λ>400 nm) (**Fig. 4.2.1.15**B). In addition, under the full spectrum light irradiation, OVs-TiO$_2$ samples still displayed higher photocatalytic activity than the commercial P25, which demonstrated that OVs played significant roles in enhancing

the photocatalytic NO removal performance (**Fig.4.2.1.16**). Moreover, the photocatalytic stability of OV-TiO$_2$-325 was investigated as shown in Fig. 8C, which confirmed the excellent stability of OVs-TiO$_2$-325 after five cycles. The stability of OVs-TiO$_2$-325 was also supported by the XRD patterns because no crystal phase changed for used OV-TiO$_2$-325 (**Fig. 4.2.1.17**), in comparison with fresh OVs-TiO$_2$-325.
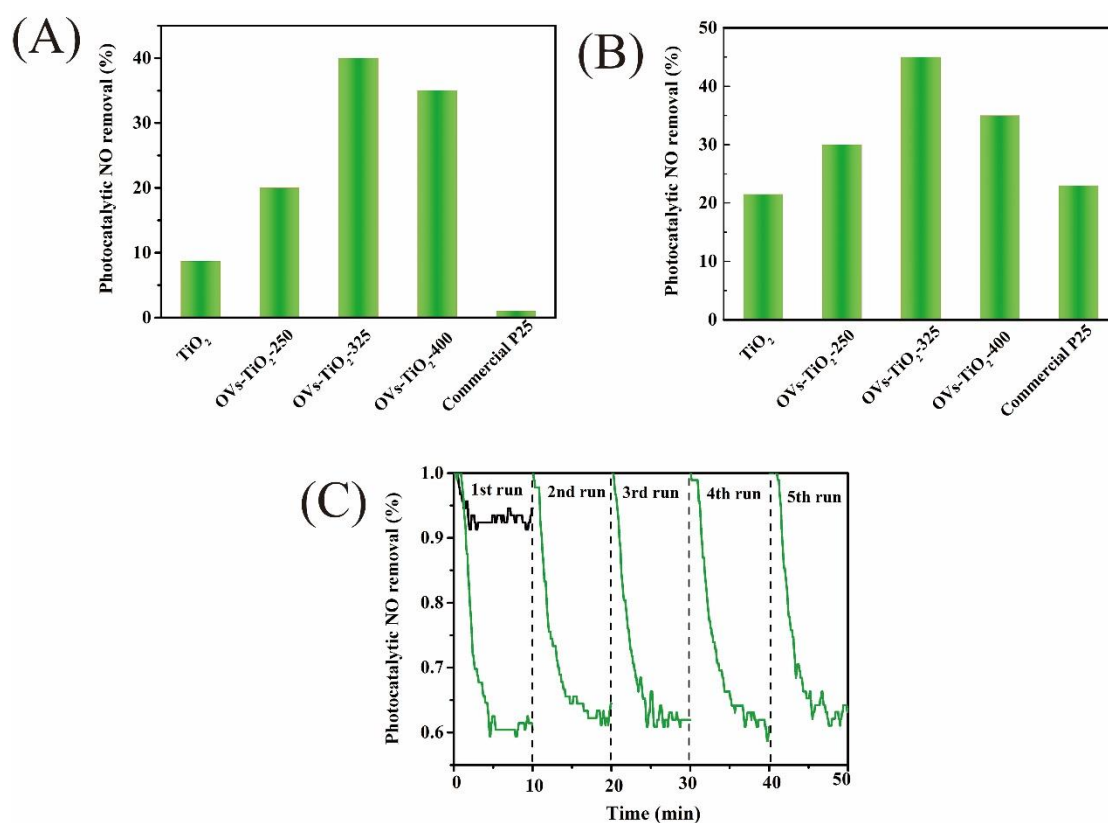
Fig. 4.2.1.15. Catalytic activity of the resultant samples under irradiation of light with wavelength of (A)λ>510 nm, (B)λ>400 nm; and (C) cycling test of OVs-TiO$_2$-325 photocatalyst under visible-irradiation (λ>510 nm). The carbon dopedTiO$_2$ was as used as a standard, whose color was black line
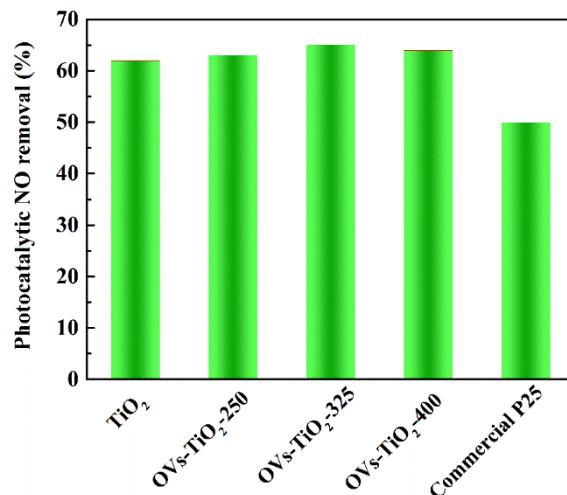
Fig.4.2.1.16. Catalytic activity of the resultant samples under irradiation of full spectrum (without filter)
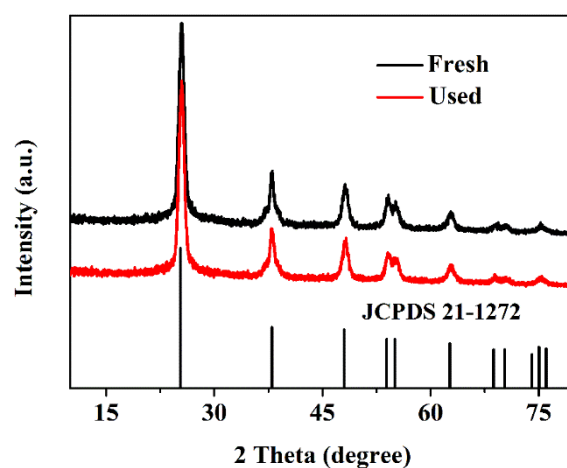
Fig. 4.2.1.17. XRD patterns of OVs-TiO$_2$-325 before and after recycling test.
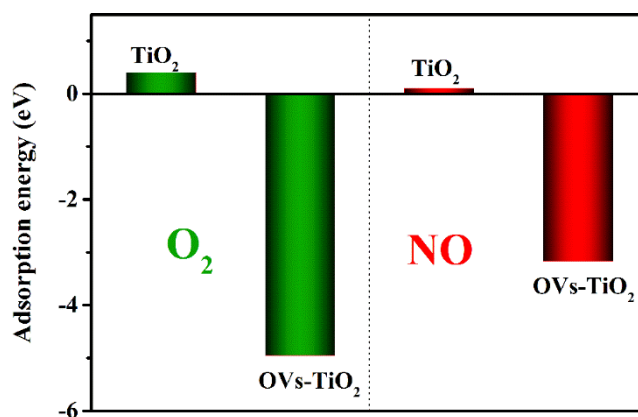
Fig. 4.2.1.18. The adsorption energies of O$_2$ and NO on TiO$_2$ and OVs-TiO$_2$, respectively.
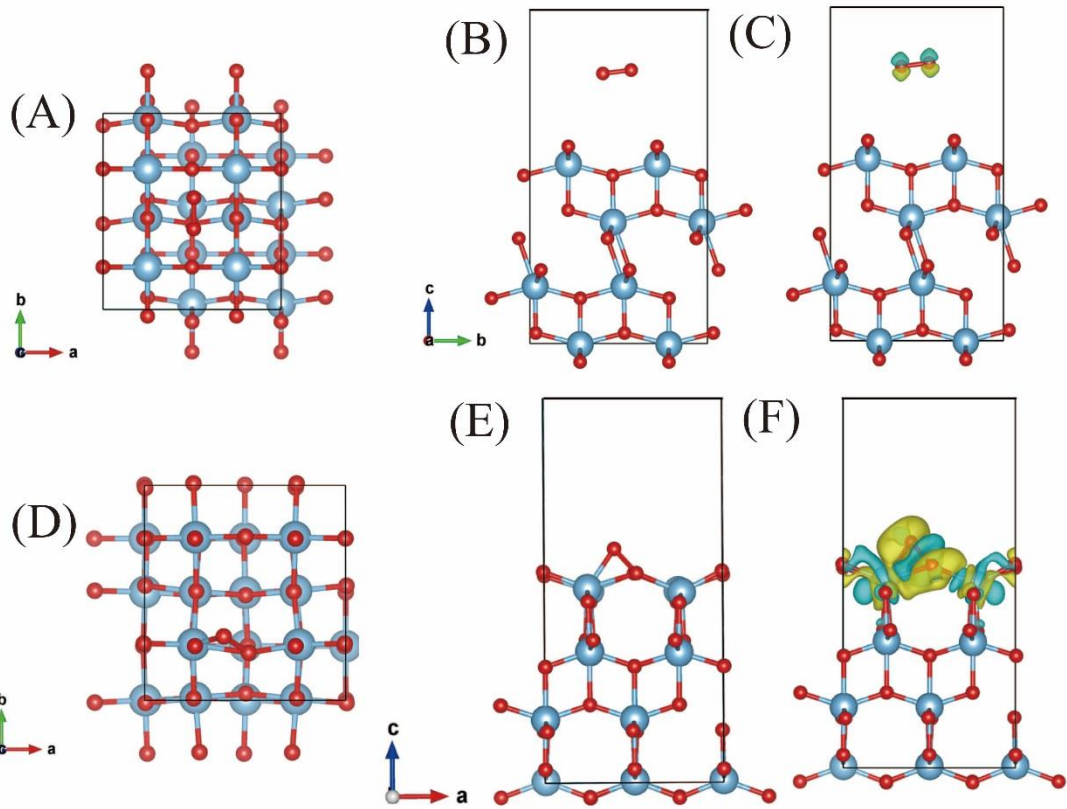
Fig.4.2.1.19. Models of O_2 adsorbed on: (A-B) TiO_2 and (D-E) OVs-TiO_2 after geometry optimization. The corresponding charge density difference of O_2 absorbed on: (C) TiO_2 and (d) OVs-TiO_2. (isovalues: 0.005 e/$Å^3$)
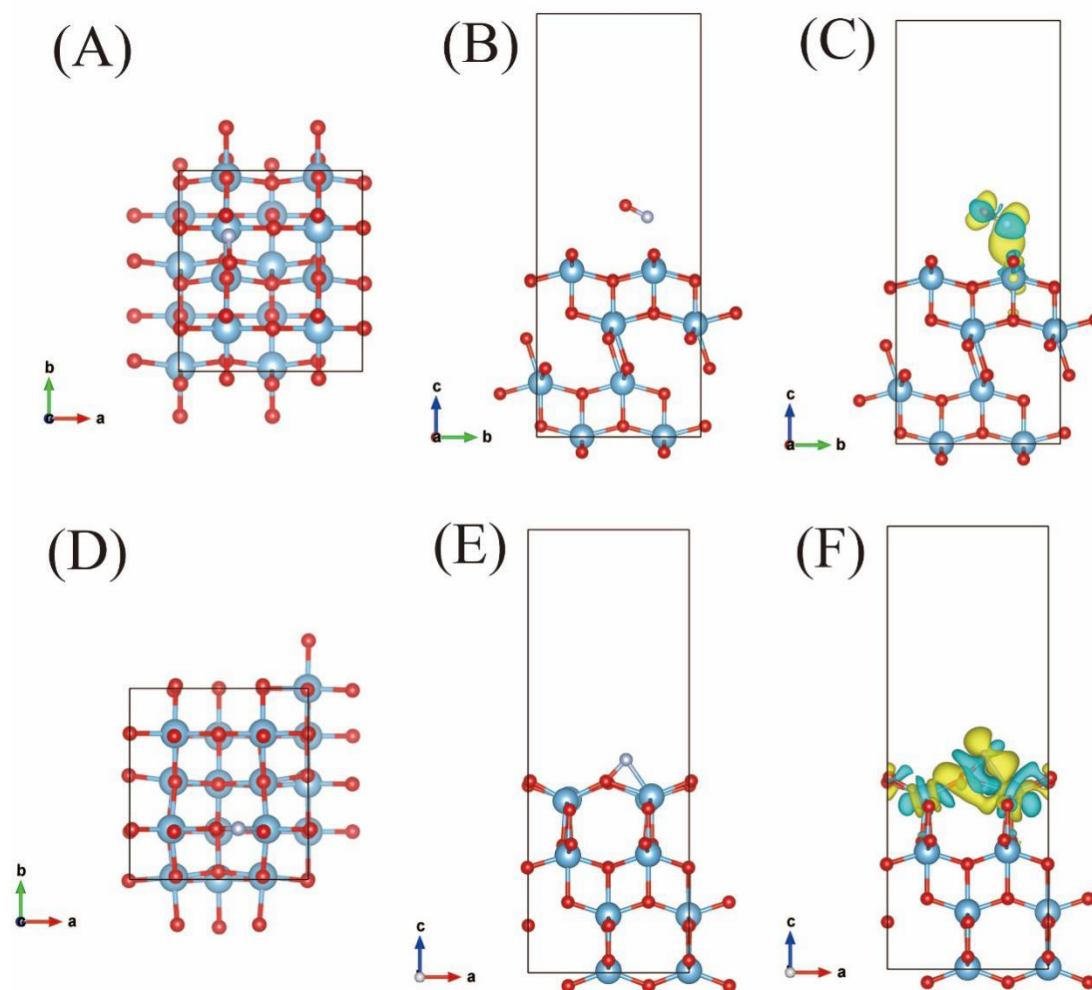
Fig.4.2.1.20. Models of NO adsorbed on: (A-B) TiO_2 and (D-E) OVs-TiO_2 after geometry optimization. The corresponding charge density difference of NO absorbed on: (C) TiO_2 and (d) OVs-TiO_2. (isovalues: 0.005 e/$Å^3$))

Crucial roles of OVs in the photocatalytic NO removal

It is well-understood that the photocatalysis reaction happens at surface active sites[14]. To unravel the crucial roles of OVs in the electronic structure of the surface active sites, theoretical calculations were performed. The mode of O_2 absorbed on the surface of pristine TiO_2 and OVs-TiO_2 following geometry optimization was depicted in **Fig. 4.2.1.19** (A-B and D-E). DFT calculations revealed that O_2 could not be absorbed on the surface of pristine TiO_2, whereas it could be easily absorbed on the surface of OVs-TiO_2 around OVs. According to the data in **Fig. 4.2.1.18**, the adsorption energy for pristine TiO_2 and OVs-TiO_2 were +0.400 eV and –4.951 eV, respectively. The

chemisorption was always accompanied by electrons transfer between the absorbed O_2 and TiO_2, resulting in O_2 activation[54]. To clarify the O_2 activation in pristine TiO_2 and $OVs-TiO_2$ deeply, the charge density difference of O_2 absorbed mode was studied **Fig.4.2.1.19** (C and F), which indicated +1.1995 electrons according to Bader charge analysis (**Table 4.2.1.3**)[55], suggesting the molecular activation[56].

Table 4.2.1.3. The q (in e) was the number of transferred electrons from the absorbed molecules to the substrate via Bader charge analysis (the "+" or "–" denoted gaining or losing electrons)

molecule	atoms	q	q at TiO_2	q at $OVs-TiO_2$
NO	N	–0.4973	–0.4260	+0.1780
	O	+0.4973	+0.4270	+0.8210
	Total	0.0000	+0.0010	+0.9990
O_2	O_1	+0.0571	–0.0349	+0.7160
	O_2	–0.0571	+0.0326	+0.4835
	Total	0.0000	–0.0023	+1.1995

In contrast, the electrons gain and loss of pristine TiO_2 was close to 0, and it could be considered that there was basically no activation. To go a step further, the activated O_2 finally dissociated into two active O atoms at the OVs sites[14, 31]. The resultant active O atoms were more easily reduced to become reactive oxygen species such as $\cdot O_2^-$, H_2O_2, and $\cdot OH$ than that of molecular O_2 by photogenerated electrons reduction[54, 57]. The obtained reactive oxygen species was beneficial for the enhanced photocatalytic NO removal performances. Based on the DFT calculations, we

also found that the OVs could increase the NO adsorption capacities to participate in the surface reactions[30] (**Fig.4.2.1.20**). Therefore, the OVs were vital to capture and activate the reactants (O_2 and NO) to improve the visible-light photocatalytic NO removal activity.
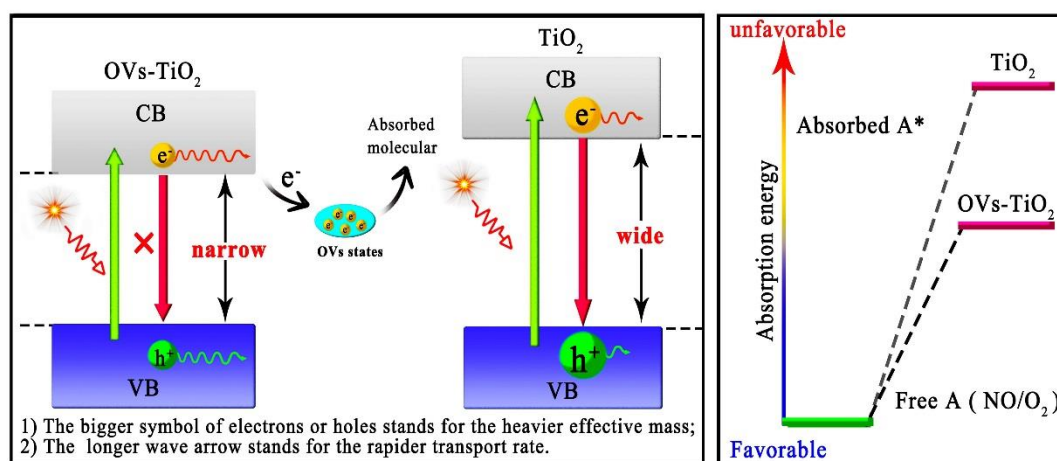
Fig. 4.2.1.21. Proposed mechanism of OVs during photocatalytic NO removal process

Based on the aforementioned optical and electronic properties, charge carrier transfer and separation, and DFT calculations for O_2 and NO adsorption, the crucial role of OVs in improving the photocatalytic activity was proposed illustrated in **Fig. 4.2.1.21**. In general, photocatalytic NO removal by photocatalyst utilizing the solar energy involved the following three steps: (I) light-harvesting by photocatalyst; (II) excited charge carrier transfer and separation; (III) redox reaction between photogenerated charges and reactants absorbed on the surface of photocatalyst [58]. As shown in Fig.10, the OVs could modulate the electronic structure of OVs-TiO_2, narrowing the bandgap and thus extending the light absorption. The enhanced light absorption brought about more charge carriers. Moreover, the OVs-TiO_2 exhibited a smaller effective mass of charge carrier and thus promoted the charge carrier separation efficiency. At the same time, the OVs could increase the conductivity to promote the charge carrier separation efficiency because of narrowed bandgap. Also, the surface OVs tended to serve as the reactive sites and trap the photogenerated electrons,

facilitating the interfacial charge transfer for the subsequent surface redox reaction. Last but not least, OVs were beneficial for molecular O_2 and NO activation to participate in the surface reaction. The OVs not only decreased the chemisorption energy but also strengthened the interaction between O_2 and TiO_2 surface owing to the abundant localized electrons. The activated molecular O_2 and NO promoted the photocatalytic NO removal performance of OVs-enriched TiO_2. All in all, the OVs played a decisive role in improving the NO removal photocatalytic performance during the whole photocatalytic process, i.e., extending light absorption, facilitating charge separation, and activating the surface reaction.

4.2.1.4 Conclusions

In summary, we developed an intrinsic carbon-doping induced synthesis of OVs-TiO_2 nanocrystals. The intrinsic carbon-doping TiO_2 nanocrystals were synthesized by WCRS process using ethanol, acetic acid and TTIP as precursors. Thanks to the organic precursor, the resultant TiO_2 nanocrystals were carbon-doped inherently. Low temperature calcination at 325 °C under N_2 atmosphere could introduce the OVs into TiO_2 nanocrystals. Compared with commercial P25, the obtained OVs-TiO_2 displayed outstanding visible-light-response property and excellent photocatalytic NO removal activity. Experimental investigation and theoretical calculation revealed the crucial roles of OVs during the whole photocatalytic NO removal process: extending light absorption, facilitating charge separation, and activating surface reactions. Also, DFT calculation unraveled why N_2 atmosphere could introduce OVs into TiO_2 nanocrystals easily. This work not only offered new perspectives for the design of OVs-TiO_2, but also contributed to understanding the critical roles of OVs in the photocatalytic process.

4.2.1.5 References

[1] Z. Ma, Z. Cui, C. Xiao, W. Dai, Y. Lv, Q. Li, R. Sa, Theoretical screening of efficient single-atom catalysts for nitrogen fixation based on a defective BN monolayer, Nanoscale, (2020).

[2] Z. Gu, B. Zhang, Y. Asakura, S. Tsukuda, H. Kato, M. Kakihana, S. Yin, Alkali-assisted hydrothermal preparation of g-C_3N_4/rGO nanocomposites with highly enhanced photocatalytic NO_x removal activity, Applied Surface Science, (2020) 146213.

[3] L. Ran, J. Hou, S. Cao, Z. Li, Y. Zhang, Y. Wu, B. Zhang, P. Zhai, L. Sun, Defect engineering of photocatalysts for solar energy conversion, Solar RRL.

[4] J. Xue, M. Fujitsuka, T. Majima, Shallow Trap State-Induced Efficient Electron Transfer at the Interface of Heterojunction Photocatalysts: The Crucial Role of Vacancy Defects, ACS Applied Materials & Interfaces, 11 (2019) 40860-40867.

[5] J. Xue, M. Fujitsuka, T. Majima, Near Bandgap Excitation Inhibits the Interfacial Electron Transfer of Semiconductor/Cocatalyst, ACS Applied Materials & Interfaces, (2020).

[6] T. Yang, J. Xue, H. Tan, A. Xie, S. Li, W. Yan, Y. Shen, Highly ordered ZnO/$ZnFe_2O_4$ inverse opals with binder-free heterojunction interfaces for high-performance photoelectrochemical water splitting, Journal of Materials Chemistry A, 6 (2018) 1210-1218.

[7] H. Wang, H. Guo, N. Zhang, Z. Chen, B. Hu, X. Wang, Enhanced photoreduction of U (VI) on C_3N_4 by Cr (VI) and bisphenol A: ESR, XPS, and EXAFS investigation, Environmental science & technology, 53 (2019) 6454-6461.

[8] X. Wu, Y. Li, G. Zhang, H. Chen, J. Li, K. Wang, Y. Pan, Y. Zhao, Y. Sun, Y. Xie, Photocatalytic CO_2 conversion of $M_{0.33}WO_3$ directly from the air with high selectivity: insight into full spectrum-induced reaction mechanism, Journal of the American Chemical Society, 141 (2019) 5267-5274.

[9] J. Li, X. Wu, W. Pan, G. Zhang, H. Chen, Vacancy-Rich Monolayer BiO_{2-x} as a Highly Efficient UV, Visible, and Near-Infrared Responsive Photocatalyst,

Angewandte Chemie International Edition, 57 (2018) 491-495.

[10] Z. Zhao, J. Fan, H. Chang, Y. Asakura, S. Yin, Recent progress on mixed-anion type visible-light induced photocatalysts, Science China Technological Sciences, 60 (2017) 1447-1457.

[11] S. Yin, Y. Asakura, Recent research progress on mixed valence state tungsten based materials, Tungsten, 1 (2019) 5-18.

[12] A. Fujishima, K. Honda, Electrochemical photolysis of water at a semiconductor electrode, nature, 238 (1972) 37.

[13] X. Wu, S. Yin, D. Xue, S. Komarneni, T. Sato, A $Cs(x)WO_3$/ZnO nanocomposite as a smart coating for photocatalytic environmental cleanup and heat insulation, Nanoscale, 7 (2015) 17048.

[14] H. Li, J. Li, Z. Ai, F. Jia, L. Zhang, Oxygen vacancy-mediated photocatalysis of BiOCl: reactivity, selectivity, and perspectives, Angewandte Chemie International Edition, 57 (2018) 122-138.

[15] J. Tian, Y. Sang, G. Yu, H. Jiang, X. Mu, H. Liu, A Bi_2WO_6 -based hybrid photocatalyst with broad spectrum photocatalytic properties under UV, visible, and near-infrared irradiation, Advanced Materials, 44 (2013) 5075.

[16] W. Wang, P.J. Strohbeen, D. Lee, C. Zhou, J.K. Kawasaki, K.-S. Choi, M. Liu, G. Galli, The role of surface oxygen vacancies in $BiVO_4$, Chemistry of Materials, 32 (2020) 2899-2909.

[17] J. Zhang, S. Wageh, A. Al-Ghamdi, J. Yu, New understanding on the different photocatalytic activity of wurtzite and zinc-blende CdS, Applied Catalysis B: Environmental, 192 (2016) 101-107.

[18] X. Wang, K. Maeda, A. Thomas, K. Takanabe, G. Xin, J.M. Carlsson, K. Domen, M. Antonietti, A metal-free polymeric photocatalyst for hydrogen production from water under visible light, Nature Materials, 8 (2009) 76.

[19] C. Di Valentin, E. Finazzi, G. Pacchioni, A. Selloni, S. Livraghi, M.C. Paganini, E. Giamello, N-doped TiO_2: Theory and experiment, Chemical Physics, 339 (2007) 44-56.

[20] X. Wu, S. Yin, Q. Dong, T. Sato, Blue/green/red colour emitting up-conversion

phosphors coupled C-TiO$_2$ composites with UV, visible and NIR responsive photocatalytic performance, Applied Catalysis B: Environmental, 156 (2014) 257-264.

[21] L. Liu, X. Chen, Titanium dioxide nanomaterials: self-structural modifications, Chemical Reviews, 114 (2014) 9890-9918.

[22] J. Nowotny, M.A. Alim, T. Bak, M.A. Idris, M. Ionescu, K. Prince, M.Z. Sahdan, K. Sopian, M.A.M. Teridi, W. Sigmund, Defect chemistry and defect engineering of TiO$_2$-based semiconductors for solar energy conversion, Chemical Society Reviews, 44 (2015) 8424-8442.

[23] H. Tan, Z. Zhao, M. Niu, C. Mao, D. Cao, D. Cheng, P. Feng, Z. Sun, A facile and versatile method for preparation of colored TiO$_2$ with enhanced solar-driven photocatalytic activity, Nanoscale, 6 (2014) 10216-10223.

[24] X. Chen, L. Liu, F. Huang, Black titanium dioxide (TiO$_2$) nanomaterials, Chemical Society Reviews, 44 (2015) 1861-1885.

[25] Y. Nam, J.H. Lim, K.C. Ko, J.Y. Lee, Photocatalytic activity of TiO$_2$ nanoparticles: a theoretical aspect, Journal of Materials Chemistry A, 7 (2019) 13833-13859.

[26] X. Chen, L. Liu, P.Y. Yu, S.S. Mao, Increasing solar absorption for photocatalysis with black hydrogenated titanium dioxide nanocrystals, Science, 331 (2011) 746-750.

[27] L. Ran, J. Hou, S. Cao, Z. Li, Y. Zhang, Y. Wu, B. Zhang, P. Zhai, L. Sun, Defect engineering of photocatalysts for solar energy conversion, Solar RRL, 4 (2020) 1900487.

[28] K. Zhu, F. Shi, X. Zhu, W. Yang, The roles of oxygen vacancies in electrocatalytic oxygen evolution reaction, Nano Energy, (2020) 104761.

[29] D. Zu, H. Wang, S. Lin, G. Ou, H. Wei, S. Sun, H. Wu, Oxygen-deficient metal oxides: Synthesis routes and applications in energy and environment, Nano Research, (2019) 1-14.

[30] H. Shang, M. Li, H. Li, S. Huang, C. Mao, Z. Ai, L. Zhang, Oxygen vacancies promoted the selective photocatalytic removal of NO with blue TiO$_2$ via simultaneous molecular oxygen activation and photogenerated hole annihilation, Environmental Science & Technology, 53 (2019) 6444-6453.

[31] Y. Huang, Y. Yu, Y. Yu, B. Zhang, Oxygen Vacancy Engineering in

Photocatalysis, Solar RRL, (2020) 2000037.

[32] G. Kresse, J. Furthmüller, Efficiency of ab-initio total energy calculations for metals and semiconductors using a plane-wave basis set, Computational Materials Science, 6 (1996) 15-50.

[33] G. Kresse, J. Furthmüller, Efficient iterative schemes for ab initio total-energy calculations using a plane-wave basis set, Physical review B, 54 (1996) 11169.

[34] J.P. Perdew, K. Burke, M. Ernzerhof, Generalized gradient approximation made simple, Physical review letters, 77 (1996) 3865.

[35] M. Arroyo-de Dompablo, A. Morales-García, M. Taravillo, DFT+ U calculations of crystal lattice, electronic structure, and phase stability under pressure of TiO2 polymorphs, The Journal of chemical physics, 135 (2011) 054503.

[36] X. Wu, S. Yin, Q. Dong, C. Guo, H. Li, T. Kimura, T. Sato, Synthesis of high visible light active carbon doped TiO_2 photocatalyst by a facile calcination assisted solvothermal method, Applied Catalysis B: Environmental, 142 (2013) 450-457.

[37] Z. Gu, Y. Asakura, S. Yin, High yield post-thermal treatment of bulk graphitic carbon nitride with tunable band structure for enhanced $deNO_x$ photocatalysis, Nanotechnology, 31 (2019) 114001.

[38] C. Guo, X. Wu, M. Yan, Q. Dong, S. Yin, T. Sato, S. Liu, The visible-light driven photocatalytic destruction of NO x using mesoporous TiO_2 spheres synthesized via a "water-controlled release process", Nanoscale, 5 (2013) 8184-8191.

[39] D. Zhang, X. Ma, H. Zhang, Y. Liao, Q. Xiang, Enhanced photocatalytic hydrogen evolution activity of carbon and nitrogen self-doped TiO_2 hollow sphere with the creation of oxygen vacancy and Ti^{3+}, Materials today energy, 10 (2018) 132-140.

[40] S. Wei, R. Wu, X. Xu, J. Jian, H. Wang, Y. Sun, One-step synthetic approach for core-shelled black anatase titania with high visible light photocatalytic performance, Chemical Engineering Journal, 299 (2016) 120-125.

[41] C. Di Valentin, G. Pacchioni, A. Selloni, Theory of carbon doping of titanium dioxide, Chemistry of Materials, 17 (2005) 6656-6665.

[42] S. Wei, S. Ni, X. Xu, A new approach to inducing Ti^{3+} in anatase TiO_2 for efficient photocatalytic hydrogen production, Chinese Journal of Catalysis, 39 (2018) 510-516.

[43] S.G. Ullattil, S.B. Narendranath, S.C. Pillai, P. Periyat, Black TiO_2 nanomaterials: a review of recent advances, Chemical Engineering Journal, 343 (2018) 708-736.

[44] J. Xue, X. Zhu, Y. Zhang, W. Wang, W. Xie, J. Zhou, J. Bao, Y. Luo, X. Gao, Y. Wang, Nature of conduction band tailing in hydrogenated titanium dioxide for photocatalytic hydrogen evolution, ChemCatChem, 8 (2016) 2010-2014.

[45] W. Ren, J. Cheng, H. Ou, C. Huang, M.M. Titirici, X. Wang, Enhancing visible-light hydrogen evolution performance of crystalline carbon nitride by defect engineering, ChemSusChem, 12 (2019) 3257-3262.

[46] S. Liu, S. Yuan, Q. Zhang, B. Xu, C. Wang, M. Zhang, T. Ohno, Fabrication and characterization of black TiO_2 with different Ti^{3+} concentrations under atmospheric conditions, Journal of Catalysis, 366 (2018) 282-288.

[47] G. Ou, Y. Xu, B. Wen, R. Lin, B. Ge, Y. Tang, Y. Liang, C. Yang, K. Huang, D. Zu, Tuning defects in oxides at room temperature by lithium reduction, Nature communications, 9 (2018) 1-9.

[48] G. Tang, Z. Xiao, J. Hong, Designing two-dimensional properties in three-dimensional halide perovskites via orbital engineering, The journal of physical chemistry letters, 10 (2019) 6688-6694.

[49] J. Xue, M. Fujitsuka, T. Majima, The role of nitrogen defects in graphitic carbon nitride for visible-light-driven hydrogen evolution, Physical Chemistry Chemical Physics, 21 (2019) 2318-2324.

[50] J. Zhang, W. Yu, J. Liu, B. Liu, Illustration of high-active Ag_2CrO_4 photocatalyst from the first-principle calculation of electronic structures and carrier effective mass, Applied Surface Science, 358 (2015) 457-462.

[51] W. Yu, D. Xu, T. Peng, Enhanced photocatalytic activity of g-C_3N_4 for selective CO_2 reduction to CH_3OH via facile coupling of ZnO: a direct Z-scheme mechanism, Journal of Materials Chemistry A, 3 (2015) 19936-19947.

[52] H. Zhang, L. Liu, Z. Zhou, First-principles studies on facet-dependent photocatalytic properties of bismuth oxyhalides (BiOXs), RSC advances, 2 (2012) 9224-9229.

[53] H. Zhong, M. Yang, G. Tang, S. Yuan, Type-II Lateral Heterostructures of

Monolayer Halide Double Perovskites for Optoelectronic Applications, ACS Energy Letters, (2020).

[54] Z. Wang, Y. Huang, M. Chen, X. Shi, Y. Zhang, J. Cao, W. Ho, S.C. Lee, Roles of N-Vacancies over Porous g-C$_3$N$_4$ Microtubes during Photocatalytic NO$_x$ Removal, ACS applied materials & interfaces, 11 (2019) 10651-10662.

[55] Z. Cui, C. Xiao, Y. Lv, Q. Li, R. Sa, Z. Ma, Adsorption behavior of CO, CO$_2$, H$_2$, H$_2$O, NO, and O$_2$ on pristine and defective 2D monolayer Ferromagnetic Fe$_3$GeTe$_2$, Applied Surface Science, (2020) 146894.

[56] Z. Wang, Y. Huang, M. Chen, X. Shi, Y. Zhang, J.-j. Cao, W. Ho, S.C. Lee, The Roles of N-vacancies over Porous g-C$_3$N$_4$ Microtubes during Photocatalytic NO$_x$ Removal, ACS Applied Materials & Interfaces, (2019).

[57] Y. Nosaka, A.Y. Nosaka, Generation and detection of reactive oxygen species in photocatalysis, Chemical Reviews, 117 (2017) 11302-11336.

[58] J. Wen, J. Xie, X. Chen, X. Li, A review on g-C$_3$N$_4$-based photocatalysts, Applied Surface Science, 391 (2017) 72-123.

4.2.2 Reductant-free synthesis of oxygen vacancies-mediated TiO₂ nanocrystals with enhanced photocatalytic NO removal performance: an experimental and DFT study

4.2.2.1 Introduction

With the development of industrialization and modernization, the environmental pollution, especially air pollution, has become one of the most serious problems in the world [1-3]. Nitrogen oxide (NO) is a significant atmospheric pollutant, which could cause environmental problems such as acid rain, photochemical smog, ozone layer depletion and global warming [4-7]. Besides, NO is harmful to human heath by increasing the risks of respiratory and heart disease [4, 5, 8]. Recently, photocatalysis is considered to be a green technology to remove the air pollutant using the abundant and environmentally friendly solar energy [9-11]. The key to photocatalysis is to develop effective, stable and low-cost semiconductor photocatalysts [12, 13]. Up to present, extensive research has been performed for the development of efficient photocatalyst[14], such as metal oxides[15], metal sulfides[16], and polymer carbon nitrides[17]. Among the semiconductor photocatalysts, titanium dioxide (TiO₂) has received much attention owing to its numerous excellent properties including chemical and thermal stability, low cost, nontoxicity, plentiful polymorphs and so on [18]. However, the photocatalytic process of TiO₂ is only activated by irradiation under UV light because of its relatively wide bandgap (>3.0 eV), which greatly limits its efficiency for solar energy harvesting [19]. Also, the pristine TiO₂ suffers from the rapid photogenerated charge carrier recombination and poor charge transport property, which result in unsatisfactory photocatalytic performance [20]. Therefore, development of visible-light responsive and active TiO₂ is one of the key challenges in the field of semiconductor photocatalysis.

Various strategies have been employed to improve the optical and electronic properties of pristine TiO₂, including meatal and non-meatal doping, dye sensitization,

constructing heterojunction and so on[20, 21]. Recently, oxygen vacancies (OVs) engineering has attracted much attention as it is an effective strategy to tune the electronic structure of TiO_2[22]. For example, Zhang et. reported that the OVs-mediated blue TiO_2 showed significantly promoted photocatalytic NO removal performance in comparison with pristine TiO_2[23]. In addition, Fan demonstrated that Bi_2WO_6 with gradient OVs with highly photocatalytic NO oxidation under visible light irradiation [24]. It is universally accepted that OVs played significant roles in the photocatalytic removal process [22]. Since Chen et al. first reported black TiO_2 by heating white TiO_2 at 200°C under 20.0 bar hydrogen pressure in 2011[25], diverse methodologies have been performed to synthesize the OVs-mediated TiO_2 such as (1) high-temperature treatment under reducing gas atmosphere (i.e. H_2, Ar, H_2/N_2, H_2/Ar, and vacuum); (2) chemical reduction (i.e. $NaBH_4$ reduction, and active metal reduction including Li, Mg, Al and Zn); and (3) electrochemical reduction [15, 22]. However, these reported methods suffer from some inevitable drawbacks including high temperature or pressure condition, involvement of toxic reagent, complex operation process, and time and cost consuming. Therefore, it is still a tough task to develop a facile and low-cost strategy to synthesize OVs-mediated TiO_2 for enhanced photocatalytic performance.

Here, we reported a reductant-free synthesis of OVs-mediated TiO_2 nanocrystals via a low-temperature calcination in nitrogen atmosphere assisted solvothermal process. Firstly, the pristine TiO_2 was synthesized by solvothermal process using the tetra-n-butyl titanate (TBT) as the precursor and ethanol as the solvent. Because of the organic precursor and solvent, the obtained pristine TiO_2 was inevitably carbon-doped during the solvothermal process. In order to introduce the OVs into the pristine TiO_2, low-temperature calcination in nitrogen atmosphere instead of reducing gas atmosphere was carried out, which was different from the conventional reduction process. Experimental characterization and theoretical calculation revealed that the intrinsic carbon-doping was conducive to the formation of OVs. Moreover, the photocatalytic performance of the resultant samples was evaluated by photocatalytic NO removal under visible light irradiation ($\lambda > 510nm$). The obtained OVs-mediated TiO_2 exhibited outstanding photocatalytic performance in comparison with the commercial P25, which was

attributed to the crucial roles of OVs. This work not only provided a novel synthesis of OVs-mediated TiO_2, but also contributed to understanding the crucial roles of OVs.

4.2.2.2 Experiment

Preparation of OVs-mediated TiO_2

OVs-mediated TiO_2 was synthesized by a low-temperature calcination assisted solvothermal method. Typically, 5mL TBT was added into 30 mL ethanol under a magnetic stirring for 30 min. The obtained solution was designed as solution A. 2 mL deionized water was added into 10 mL ethanol under a magnetic stirring for 30 min. The obtained solution was designed as solution B. Then the solution B was added dropwise into solution A under a magnetic stirring for 60 min. Subsequently, the mixed solution was transferred into a 100 mL Teflon-lined autoclave and heated at 190 °C for 3h. Then the product was collected, washed with ethanol and dried in vacuum at 60 °C overnight. To introduce the OVs into TiO_2, the obtained product was calcined in N_2 at 325 °C for 2h with a heating rate of 5 °C/min. For comparison, the TiO_2 was also calcined in air with other parameters remaining the same [26]. For abbreviation, the obtained TiO_2 calcined in N_2 was index as OVs-TiO_2-N_2, while the sample calcined in Air was labeled as TiO_2-Air. At the same time, the commercial anatase TiO_2 was treated under the same treatment conditions, i.e., under 325 ° C in nitrogen atmosphere (Fig.S5), which was used as a controlled experiment

Characterization

UV-vis diffuse reflectance spectroscopy (DRS) was carried out on UV-vis spectrophotometer (JASCO, V-670). The crystalline phases of the as-prepared samples were characterized by X-ray diffraction (XRD) on Bruker D2 Phaser with monochromatized Cu Kα radiation. Electron paramagnetic resonance (EPR) measurement was performed on Bruker E580 EPR spectrometer at room temperature. The transmission electron microscopy (TEM) and high-resolution TEM (HR-TEM) were operated at ZEISS LEO-9522 microscope. Photoluminescence (PL) spectra were measured on a Fluorescence Spectrometer (JASCO, FP-8500). X-ray photoelectron

spectroscopy (XPS) data were obtained on an X-ray photoelectron spectrometer (Perkin Elmer PHI 5600).

Computational method

To further understand the electronic structure of OVs-TiO$_2$, density functional theory (DFT) calculations were carried out using the Vienna Ab Initio Simulation Package (VASP) based on plane-wave basis sets. The generalized gradient approximation with the Perdew–Burke–Ernzerhof (GGA/PBE) was employed to describe the exchange-correlation interactions[27-29]. The primitive anatase cell was expanded to a 2 × 2 × 1 supercell as pure bulk TiO$_2$ model. The (001)-(2*2) surface model was slabbed from the 2 × 2 × 1 bulk TiO$_2$ model, with a vacuum space of 15 Å in the z-direction to avoid the influence of the inter-layer interaction caused by the periodicity. A Γ-centered 6 × 6 × 5 (bulk) and 6 × 6 × 1 (layer) Monkhorst-Pack grids for the Brillouin zone sampling and a plane wave basis set with a cutoff energy of 400 eV were used to calculate self-consistent energy and charge information. Then the geometry optimizations were performed until the forces and energy for each atom was reduced below 0.01 eV/Å and 1.0 ×10^{-4} eV/atom. In addition, an effective U value of 6.0 eV was applied to the 3d orbitals of Ti to obtain a band gap value close to the experimental value.

Photocatalytic NO removal evaluation

The photocatalytic activities of the as-obtained samples were tested by photocatalytic NO removal under visible light irradiation. The visible light source was obtained from a mercury lamp (450 W) with a cutoff filter (λ>510 nm or λ>400 nm). A continuous rectangular flow reactor with internal volume of 373cm^3 was used as chamber for NO removal. The as-synthesized sample was carefully coated onto the cell (20mm×16mm×0.5mm) of a glass dish. Then the glass dish was transferred to the bottom of rectangular flow reactor. The experimental NO gas (2ppm) was obtained by diluting the compressed NO gas cylinder with air stream. The real-time concentration of NO was analyzed online by NO$_x$ detector (Yanaco, ECL-88A), which controlled the gas flow rate of 200 ml/min. The photocatalytic NO removal reacted for 10 minutes at room temperature after the light turned on. The photocatalytic NO removal efficiency (%) was defined as follows:

$$NO(\%) = \frac{C_0 - C}{C_0} \times 100 \qquad (4.2.2\text{-}1)$$

Where C_0 and C were the concentrations of NO in the feeding and outlet streams, respectively.

4.2.2.3 Results and discussion

Formation mechanism of OVs
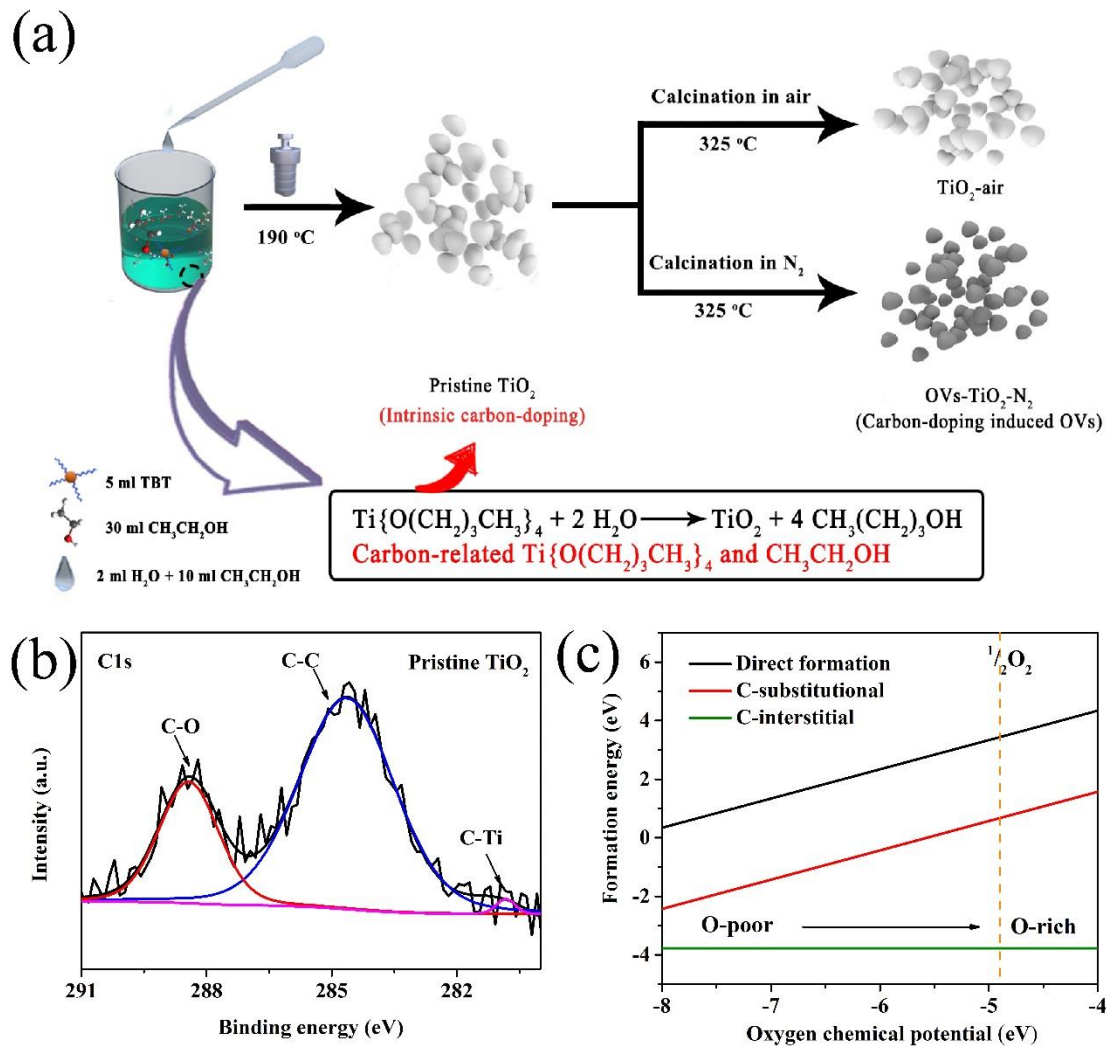
Fig. 4.2.2.1 (a) Schematic synthesis process of the intrinsic carbon-doping induced OVs-TiO$_2$-N$_2$ nanocrystals. (b) High-resolution XPS spectra of C1s for pristine TiO$_2$. (c) Comparison of OVs formation energies for direct formation, carbon-substitutional induced formation, carbon-interstitial induced formation in TiO$_2$

OVs-TiO$_2$-N$_2$ was synthesized as depicted schematically in **Fig. 4.2.2.1**a. Firstly,

the amorphous TiO$_2$ particles were prepared by controlled hydrolysis TBT in ethanol with the mixture of ethanol and water (The ratio of ethanol/water is 10:2) dropwise. Then the solvothermal process was performed to make the amorphous TiO$_2$ into crystallization. To introduce the OVs into pristine TiO$_2$, the as-synthesized TiO$_2$ was calcined at 325 °C in N$_2$. After the OVs was successfully introduced into the pristine TiO$_2$, the grey OVs-TiO$_2$-N$_2$ was synthesized. It should be noted that calcination at 325 °C in air could not introduce the OVs into pristine TiO$_2$.
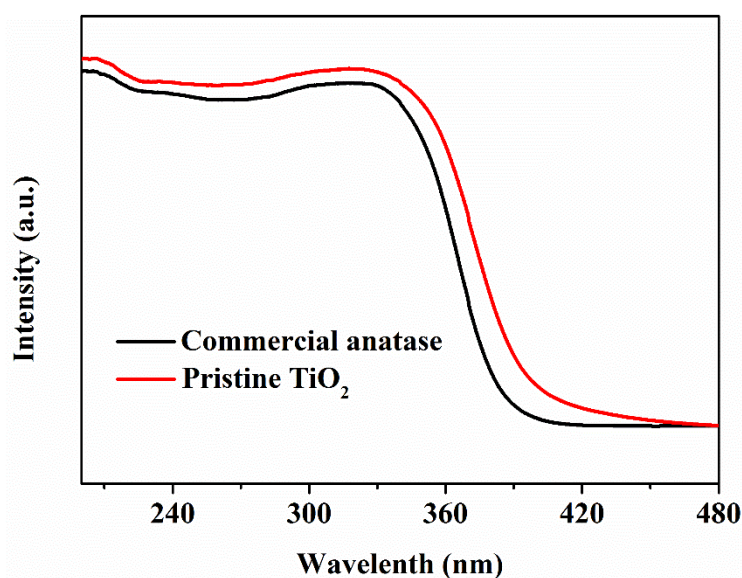
Fig. 4.2.2.2. UV-vis DRS spectra of as-synthesized TiO$_2$ and commercial anatase.

It is accepted that the common strategy to introduce OVs into metal oxides was thermal treatment at high temperatures under reducing gas atmosphere (i.e. H$_2$, CO, NH$_3$ and CH$_4$)[15]. However, in the present work, the calcination process was carried out at low temperature and nitrogen atmosphere. Considering it was facile and novel, combination of experimental characterization and theoretical calculation was adopted to reveal the formation mechanism of OVs in OVs-TiO$_2$-N$_2$. It is easy to understand that carbon impurities were inevitably doped into the pristine TiO$_2$ due to the organic precursors, i.e., TBT and ethanol. Moreover, the high-resolution XSP C1s spectra of pristine TiO$_2$ gave a direct evidence of carbon-doping because the C-Ti band was clearly observed in pristine TiO$_2$ (**Fig. 4.2.2.1**1b)[30, 31]. And the DRS results of

pristine TiO_2 and commercial anatase provided an indirect evidence of intrinsic carbon-doping since the pristine TiO_2 displayed better light-harvesting capability than that of commercial anatase owing to the carbon impurities (**Fig. 4.2.2.2**) [32].
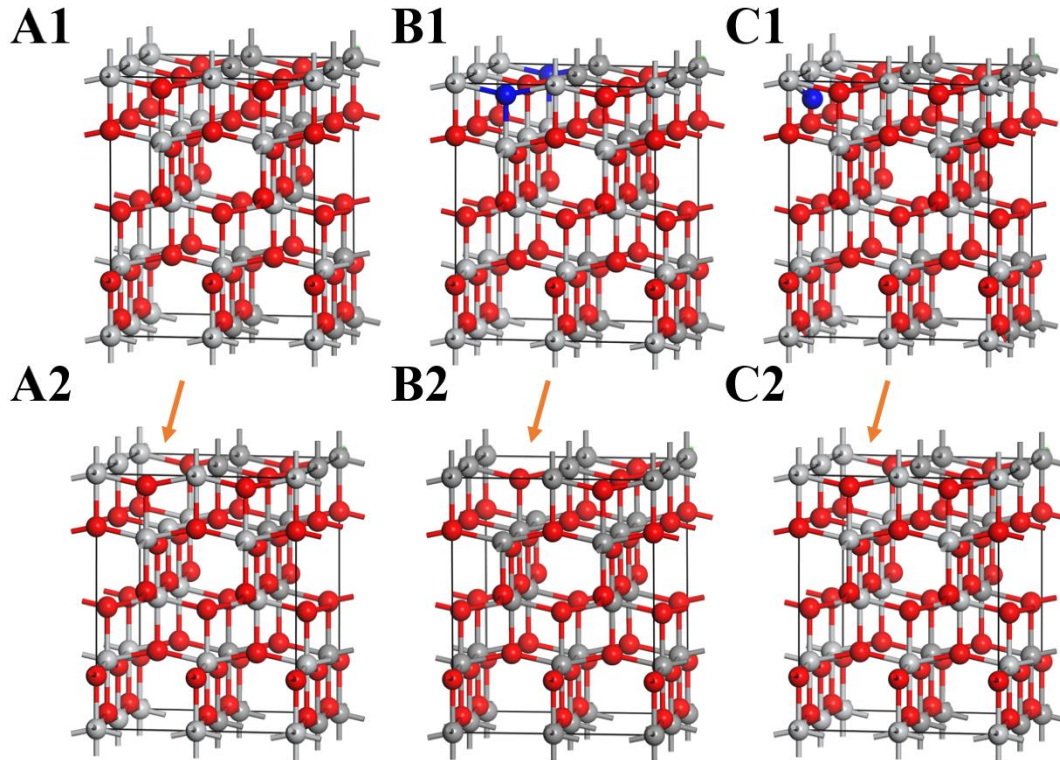
Fig. 4.2.2.3. The supercell modes of perfect anatase TiO_2 (A1), C-substitutional anatase TiO_2 (B1) and C-interstitial anatase TiO_2 (C1). The corresponding supercell modes with OVs (A2-C2) derived from the perfect anatase TiO_2, C-substitutional anatase TiO_2, and C-interstitial anatase TiO_2, respectively. The grey balls represented Ti atoms. The red balls represented O atoms. The blue ball represented C atoms. The removal of O atoms in the supercell modes indicated the OVs. Please note that the carbon element was removed after the calcination in the supercell modes (B2 and C2)

The effect of carbon-doping on the formation energy of OVs was further investigated based on the density functional theory (DFT) calculations (**Fig. 4.2.2.2c** and **Fig.4.2.2.4**) and illustrated as the following reactions:

Direct formation

$TiO_2 \rightarrow TiO_{2-x}$ (O vacancy) + O   ($\triangle E$=3.417eV)   (4.2.2-2)

C-interstitial TiO$_2$:

TiO$_2$C$_y$ → TiO$_{2-x}$ (O vacancy) + C + O   (△E= 0.642eV, C-removed)   (4.2.2-3)

C-substitutional TiO$_2$:

TiO$_{2-y}$C$_y$ → TiO$_{2-x}$ (O vacancy) + C + O (△E=-3.778eV, C-removed)   (4.2.2-4)
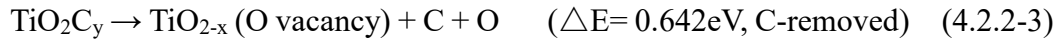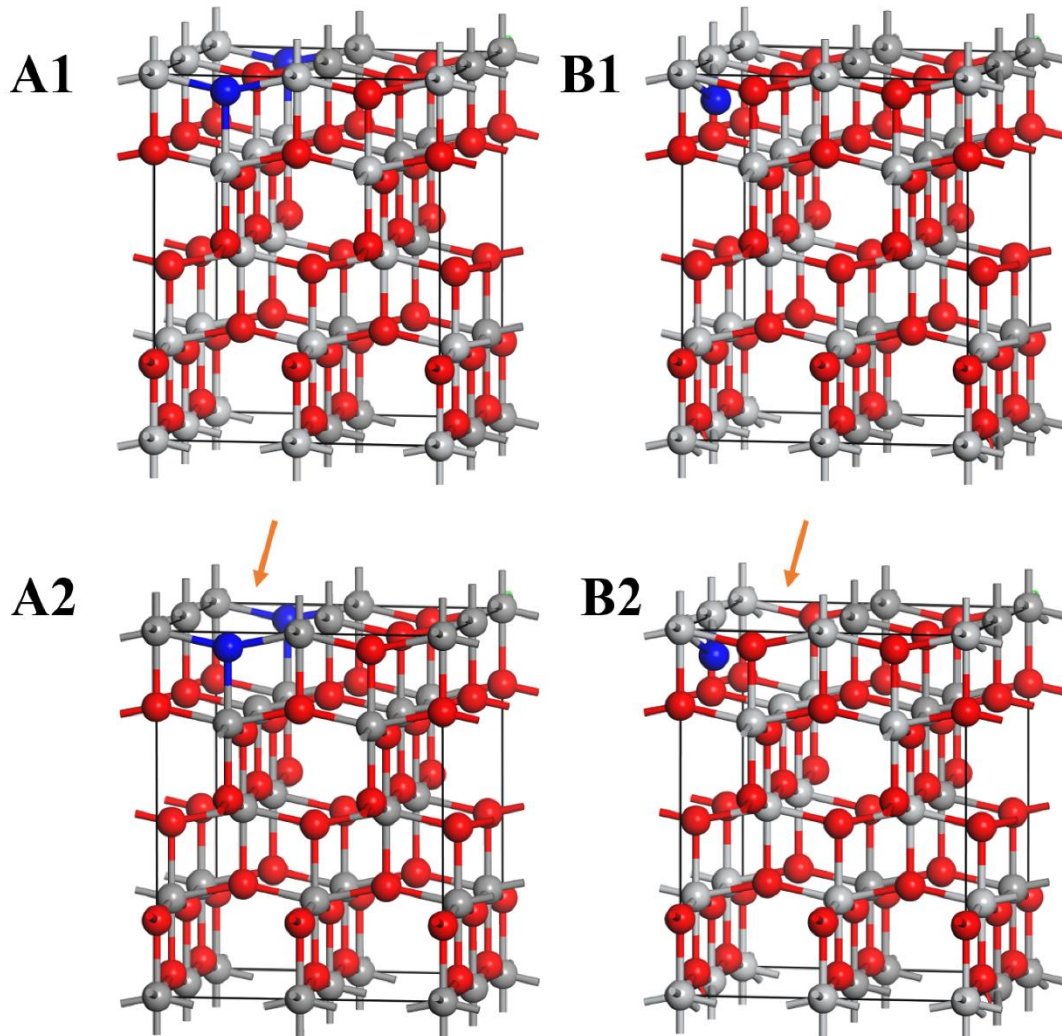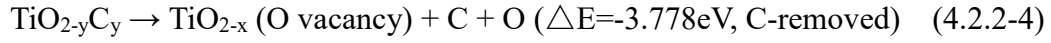
Fig.4.2.2.4. The supercell modes of C-substitutional anatase TiO$_2$ (A1) and C-interstitial anatase TiO$_2$ (B1). The corresponding supercell modes with OVs (A2-B2) derived from the perfect anatase TiO$_2$, C-substitutional anatase TiO$_2$, and C-interstitial anatase TiO$_2$, respectively. The grey balls represented Ti atoms. The red balls represented O atoms. The blue ball represented C atoms. The removal of O atoms in the supercell modes indicated the OVs. Please note that the carbon element was remained after the calcination in the supercell modes (B2 and C2)

These reactions represented the formation energy of OVs in undoped TiO_2, interstitial carbon-doping TiO_2, substitutional carbon-doping TiO_2, respectively. Compared with undoped TiO_2, the formation energy of OVs in interstitial carbon-doping TiO_2 and substitutional carbon-doping TiO_2 both decreased distinctly, which indicated that carbon-doping was beneficial for the formation of OVs in TiO_2[33]. In the current work, it was difficult to determine the type of carbon-doping clearly. However, based on the DFT calculations, no matter what type of carbon-doping it was, i.e. interstitial carbon-doping or substitutional carbon-doping, the carbon doping benefited the formation of OVs in TiO_2[33]. In addition, the modes with both OVs and carbon-doping after the calcination process were taken into consideration (**Fig.4.2.2.5**) and illustrated as the following reactions:

C-interstitial TiO_2:

$TiO_2C_y \rightarrow TiO_{2-x}C_y$ (O vacancy) + O   ($\triangle E$=7.113 eV, C-remained) (4.2.2-5)

C-substitutional TiO_2:

$TiO_{2-y}C_y \rightarrow TiO_{2-y-x}C_y$ (O vacancy) + O   ($\triangle E$= 6.081eV, C-remained) (4.2.2-6)

According to the DFT calculations, carbon elements could not remain after the calcination process because the formation energies of OVs were increased. Therefore, thanks to intrinsic carbon-doping in pristine TiO_2, the OVs could be easily introduced into OVs-TiO_2-N_2 at low temperature under N_2 atmosphere instead of reducing gas atmosphere (i.e. H_2, CO, NH_3 and CH_4).

Phase and structure

XRD was performed to investigate the crystal structure of the samples (**Fig.4.2.2.5**a). All the samples showed the same diffraction peaks, which were well consistent with the standard pattern of anatase TiO_2 (JCPDS No.21-1272)[34]. These results indicated that the calcination process did not damage crystal structure of the samples. Moreover, the EPR spectra were collected to determine the OVs in the samples (**Fig.4.2.2.5**b). No EPR signal was observed for pristine TiO_2 while OVs-TiO_2-N_2 gave rise to a strong EPR signal, which confirm the existence of OVs in the OVs-TiO_2-N_2 samples[35]. These results were in good agreement with previous reports[19, 36]. It

must be pointed out that TiO_2-air did not exhibit EPR signal, which demonstrated that OVs could not be introduced into TiO_2 under air atmosphere.
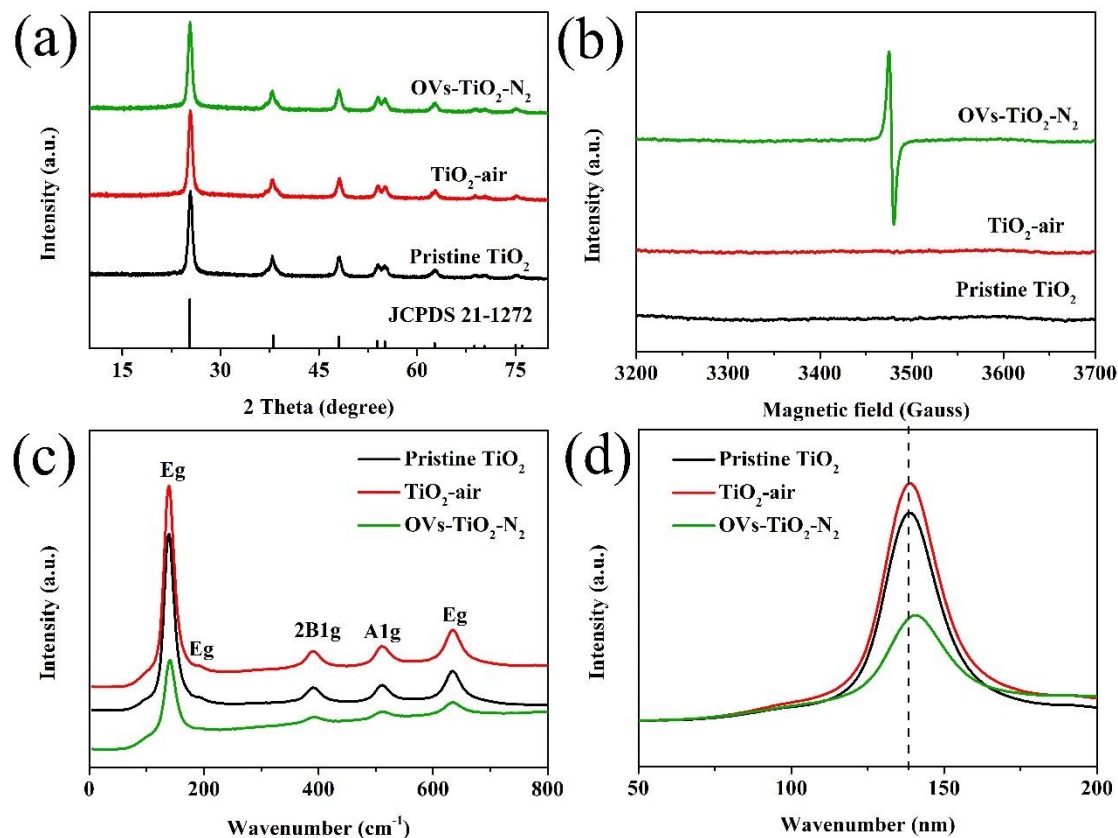
Fig.4.2.2.5 (a)XRD patterns, (b) EPR spectra, (c) Raman spectra and (d) corresponding enlarged Raman spectra of the samples.

The formation of OVs in OVs-TiO_2-N_2 could be further confirmed by Raman spectra (**Fig.4.2.2.5**c and **Fig.4.2.2.5**d). All the samples displayed five bands located at 144,197,397,515 and 638 cm^{-1} (**Fig.4.2.2.5**c), in accordance with the six Raman active modes of anatase ($3Eg+2B1g+A1g$), respectively[37]. The similar Raman spectra of the as-synthesized samples indicated that the calcination process did not distinctly affect the chemical structure of TiO_2, which was in good consistent with the results of XRD patterns. However, a slight red shift at approximately 144 cm^{-1} band was observed in OVs-TiO_2-N_2 (**Fig.4.2.2.5**d), which could be ascribed to the lattice distortion and low crystallinity [18, 19]. In other words, the formation of OVs in OVs-TiO_2-N_2 was again

confirmed by Raman spectra.

To analyze the chemical state of the samples, XPS spectra was obtained and showed in **Fig.4.2.2.6**. The pristine TiO_2 displayed the characteristic Ti 2p peaks located at 464.6 eV and 458.8 eV, corresponding to Ti $2p_{1/2}$ and Ti $2p_{3/2}$, respectively (**Fig.4.2.2.6**a). With respect to OVs-TiO_2-N_2, the peak of Ti $2p_{3/2}$ displayed a distinct shift to lower binding energy owing to the formation of OVs, which was similar to previous literature [36]. In addition, the high-resolution XPS spectra of O 1s of TiO_2 and OVs-TiO_2-N_2 could be deconvolved into two peaks (**Fig.4.2.2.6**b), which were ascribed to lattice oxygen and surface-adsorbed oxygen species, respectively. Similar to Ti 2p, the O 1s of OVs-TiO_2-N_2 showed an obvious shift to lower binding energy due to formation of OVs. Therefore, it is safe to conclude that the XPS spectra demonstrated the existence of OVs in OVs-TiO_2-N_2 again.
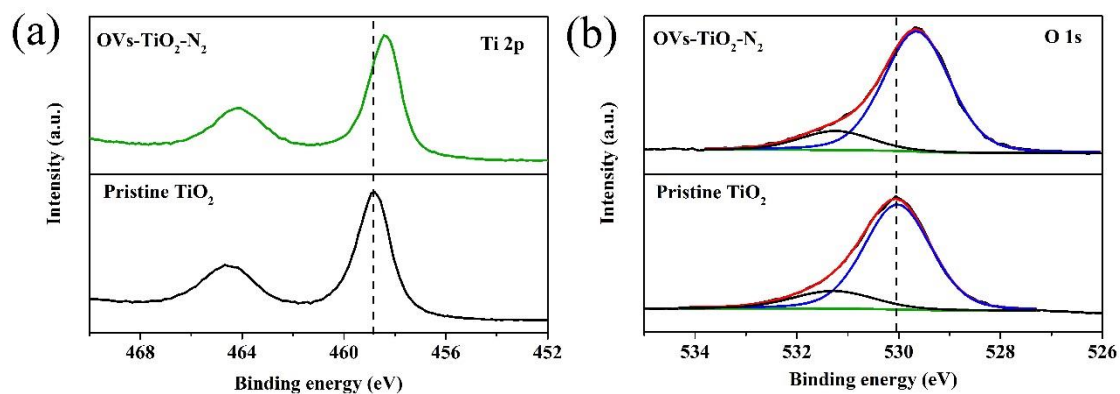
Fig.4.2.2.6 (a) High-resolution XPS spectra of Ti 2p, (b) High-resolution XPS spectra of O1s

Morphological analysis

The morphology and microstructure of the pristine TiO_2 and OVs-TiO_2-N_2 investigated by transmission electron microscopy (TEM) and high-resolution transmission electron microscopy (HRTEM). Both the pristine TiO_2 and OVs-TiO_2-N_2 showed morphologies of nanoparticles (**Fig. 4.2.2.7**a1 and **Fig. 4.2.2.7**a2). In addition, the sizes of pristine TiO_2 and OVs-TiO_2-N_2 were nearly identical. These results

suggested that the low-temperature did not have much effect on the morphology of the samples. In addition, the pristine TiO_2 exhibited ordered lattice fringes with interplanar spacing of 0.35 nm (**Fig. 4.2.2.7**b1) while the OVs-TiO_2-N_2 displayed the lattice disorder owing to the unsaturated Ti atoms derived from the OVs (**Fig. 4.2.2.7**b2)[25]. Also, the decreased crystallinity of OVs-TiO_2-N_2 was supported by its less clear diffraction rings in comparison with pristine TiO_2 (**Fig. 4.2.2.8**a and **Fig. 4.2.2.8**6b). **Fig. 4.2.2.7**c1 and **Fig. 4.2.2.7**c2 illustrated the geometrically optimized structures of perfect TiO_2 and OVs-TiO_2-N_2, respectively. Compared with TiO_2, the OVs-TiO_2-N_2 showed distinct lattice distortion, which was in good consistent the images of HRTEM.
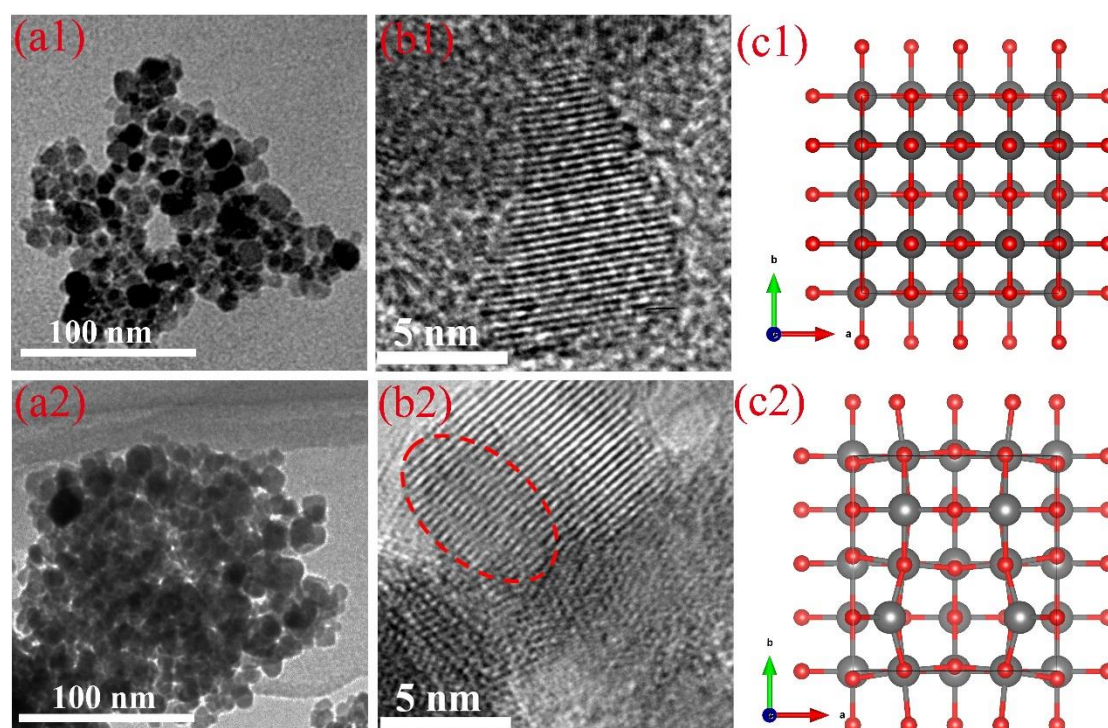
Fig. 4.2.2.7. The TEM images of pristine TiO_2 (a1) and OVs-TiO_2-N_2 (a2); the HRTEM images of pristine TiO_2 (b1) and OVs-TiO_2-N_2 (b2); the optimized configurations (top view) of pristine TiO_2(c1) and OVs-TiO_2 (c2) based on the DFT calculations.
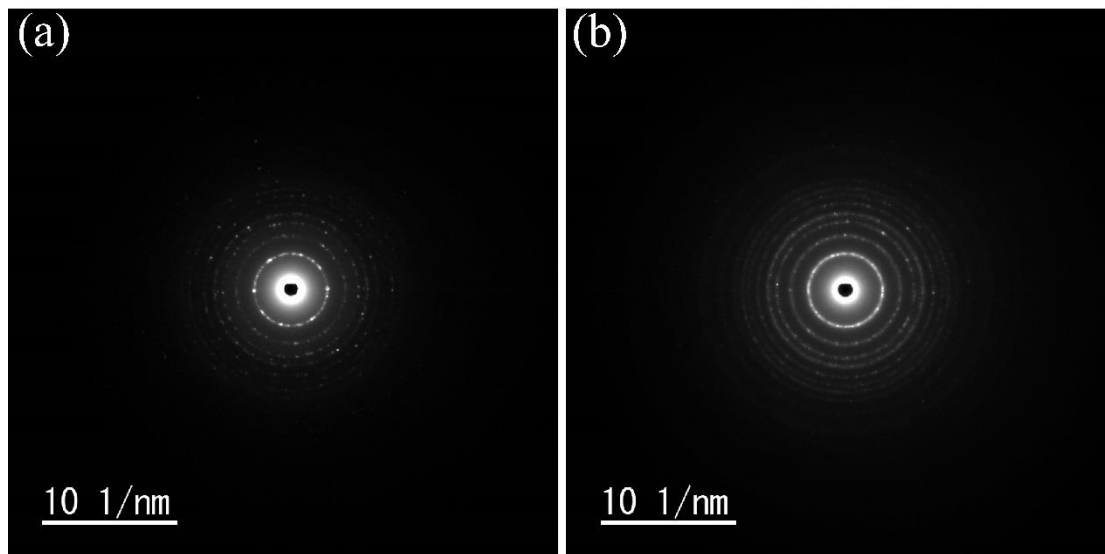
Fig. 4.2.2.8 SAED images of pristine TiO$_2$ (a) and OVs-TiO$_2$-N$_2$ (b).
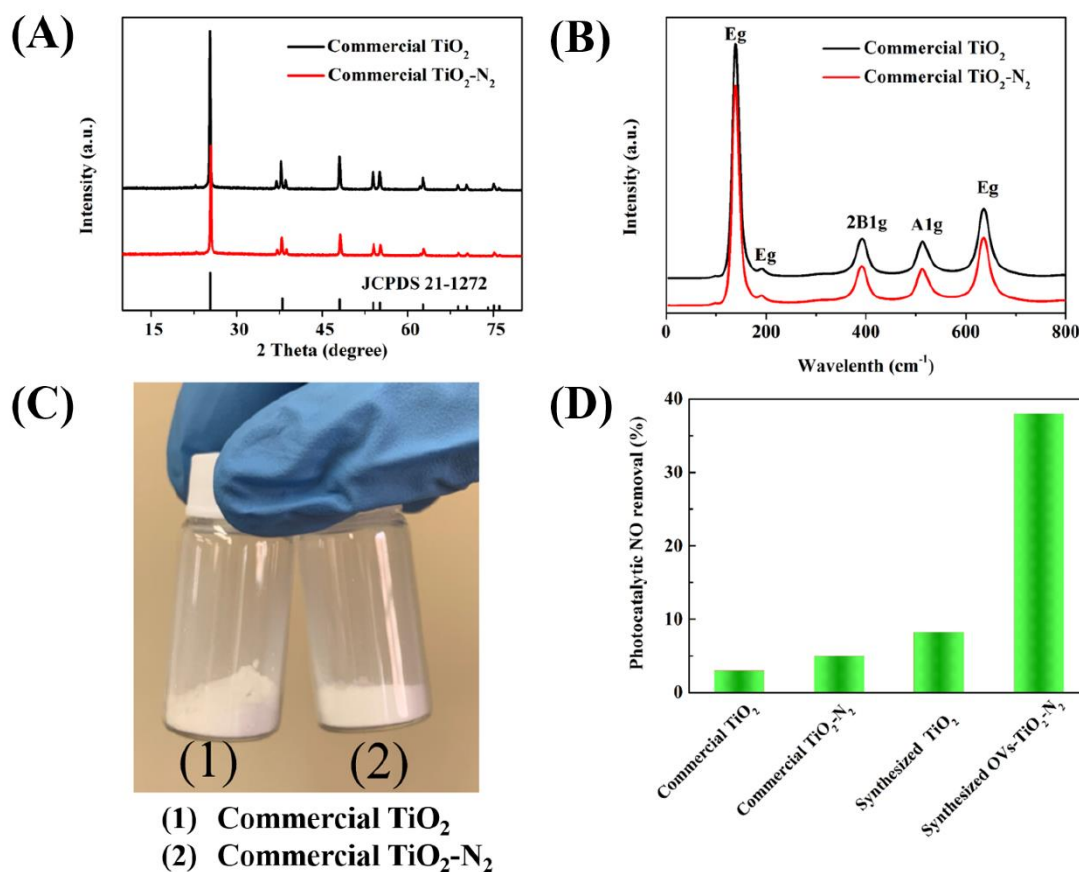
Fig. 4.2.2.9. (A)XRD patterns (B) Raman spectra (C) digital photograph of commercial TiO$_2$ and commercial TiO$_2$-N$_2$, respectively. (D) The photocatalytic performance of commercial TiO$_2$, commercial TiO$_2$-N$_2$, synthesized TiO$_2$ and synthesized OVs- TiO$_2$-N$_2$.

As expected (**Fig. 4.2.2.9**) , the OVs cannot be introduced into commercial anatase TiO$_2$. The Raman spectra of commercial TiO$_2$ treated in nitrogen atmosphere did not shift. The color of commercial TiO$_2$ treated in nitrogen atmosphere did not change. The photocatalytic performance of commercial TiO$_2$ treated in nitrogen atmosphere almost did not change. That is to say, the OVs can only be introduced carbon-doped anatase TiO$_2$ at the current condition, which demonstrated the novelty of our research work

Optical and electronic properties

UV-vis DRS spectra was measured to study the optical and electronic properties of the samples. As shown in **Fig. 4.2.2.10**a, the pristine TiO$_2$ displayed limited light edge at round 400 nm, which slightly exceeded the UV-light absorption edge (380nm) due to the intrinsic carbon-doping from the organic precursors [32], i.e., TBT and ethanol. After the calcination in N$_2$ atmosphere, the OVs-TiO$_2$-N$_2$ exhibited a distinct red shift of absorption edge in accordance with the narrowed bandgap (**Fig. 4.2.2.10**b). In addition, the OVs-TiO$_2$-N$_2$ displayed a distinct tail absorption (Urbach tail) in the visible and near infrared zone, which was regarded as the electronic states located within the bandgap (well known as mid-gap states, originating from introducing OVs into photocatalyst) [18, 19]. **Fig. 4.2.2.10**c showed the XPS spectra of the valence band and there was no significant difference in the VB of the samples, which indicated that the OVs had no influence on the VB [36]. Based on the bandgap and VB, the electronic band structures of the samples were summarized in **Fig. 4.2.2.10**d.
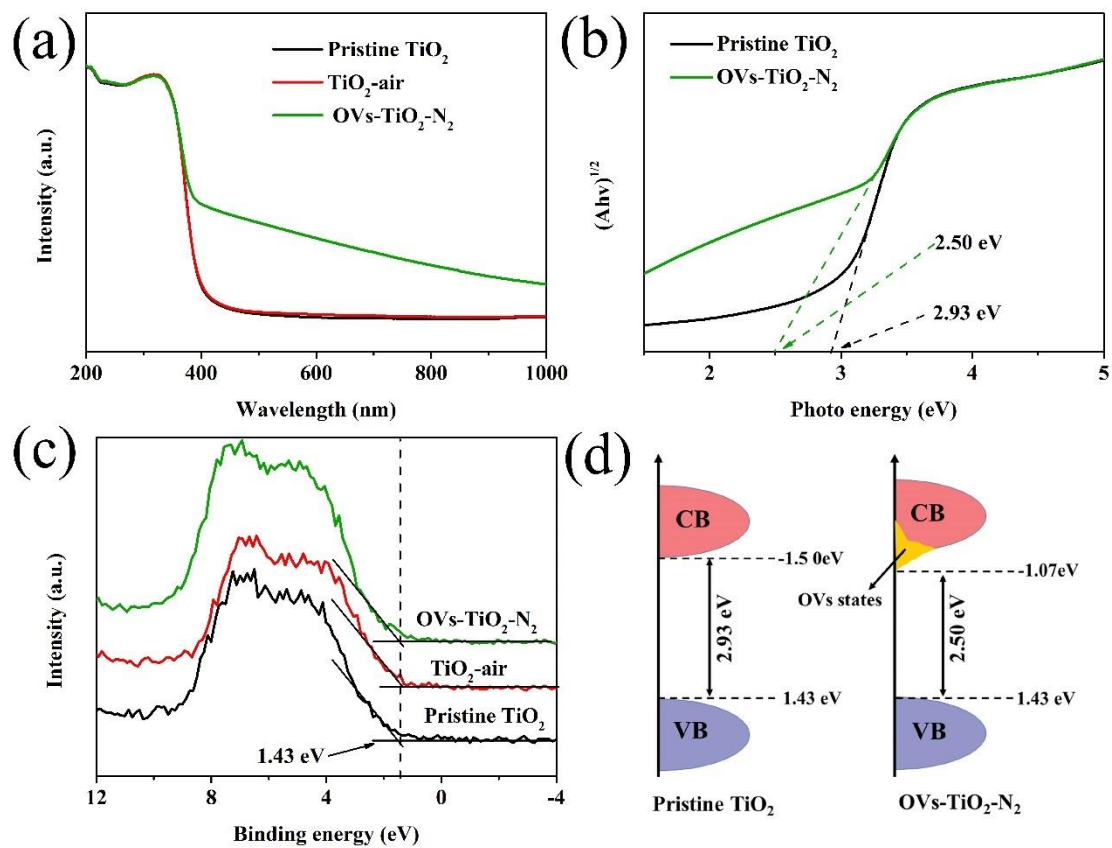
Fig. 4.2.2.10. (a)The UV-vis absorption spectra of the samples and (b) corresponding Tauc plot of pristine TiO$_2$ and OVs-TiO$_2$-N$_2$. (c) Valance band spectra of the samples. (d) Schematic electronic structure of pristine TiO$_2$ and OVs-TiO$_2$-N$_2$

Fig. 4.2.2.11. The digital photograph of the as-synthesized pristine TiO$_2$ (left), TiO$_2$-air (middle) and OVs-TiO$_2$-N$_2$ (right), respectively.

Theoretical calculation was used to study the roles of OVs in the optical property and electronic structure of the samples deeply. Compared with the perfect TiO_2, the bandgap of the OVs-TiO_2 decreased from 3.03 to 2.03 eV (**Fig. 4.2.2.12**a and **Fig. 4.2.2.12**b), which was in good agreement with the experimental results. The density of states (DOS) for the samples was examined in **Fig. 4.2.2.12**c. The valence band maximum (VBM) was mainly composed of O-*2p* orbitals, and the conduction band maximum (CBM) was mainly composed of Ti-3*d* orbitals. Two kinds of OVs-induced states were observed in the DOS of OVs-TiO_2. One state overlapped with the CB was originated from the Ti-3*d* orbitals. Another mid-gap state was derived from the hybridization of Ti-3*d* orbitals and O-2*p* orbitals, respectively [22]. The states overlapped with the CB brought about the narrowed bandgap while the mid-gap states resulted in the tail absorption (Urbach tail) [22, 36], which was in good agreement with the experimental results. It should be note that the theoretical calculation also revealed the enhanced light-harvesting capability of OVs-TiO_2 owing to crucial roles of OVs (**Fig. 4.2.2.12**d).
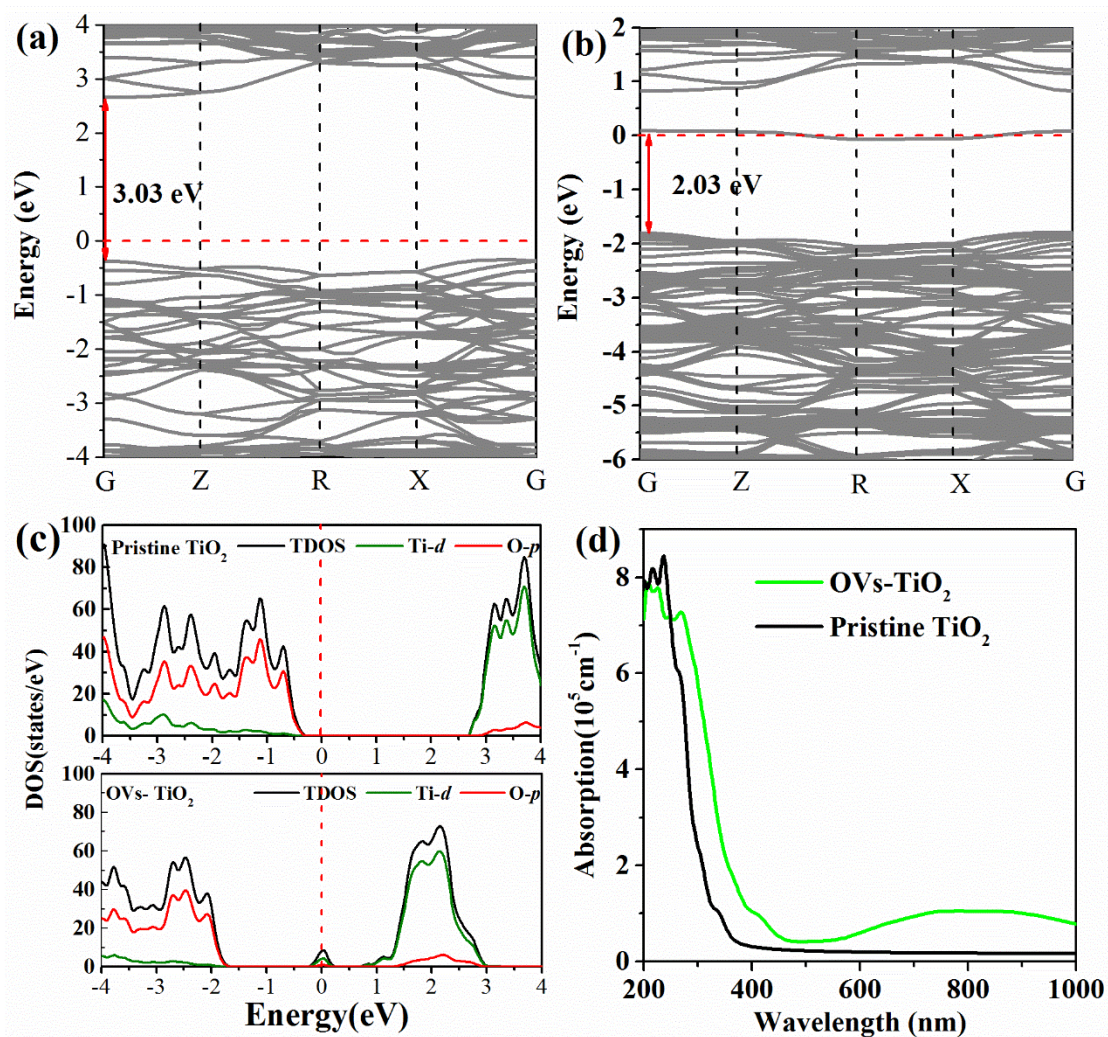
Fig. 4.2.2.12. The calculated band structure of pristine TiO_2 (a) and OVs-TiO_2 (b); (c)the DOS and (d) light absorption of the samples.

Charge carrier separation and transfer

It is universally acknowledged that the charge carrier separation and transfer played a significant role in determining the photocatalytic performance [38-41]. Therefore, the photoluminescence spectra of the samples were carried out at room temperature. Typically, the lower intensity of PL spectra indicated the lower recombination rate of photogenerated charge carrier, which would result in the higher photocatalytic performance [42]. As shown in **Fig.4.2.2.13**, the OVs-TiO_2-N_2 exhibited distinct decreased emission intensity of PL spectra in comparison with TiO_2, which was in favor of improving the photocatalytic performance.
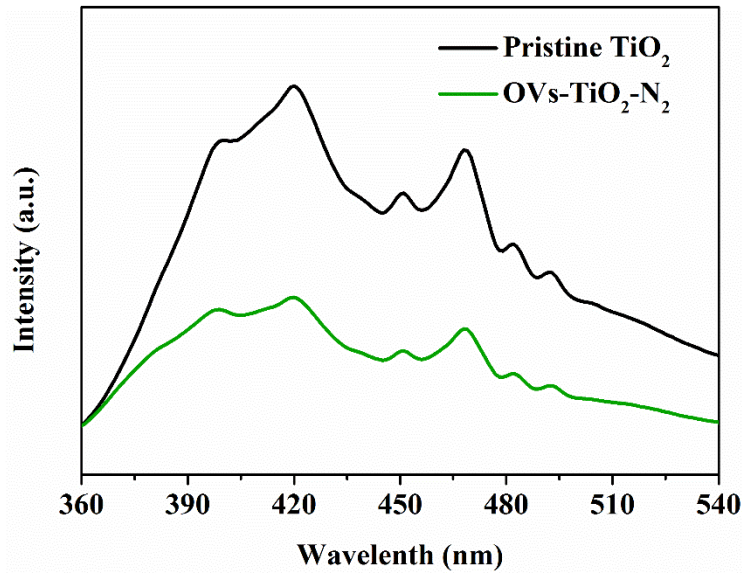
Fig.4.2.2.13. PL spectra of pristine TiO$_2$ (a) and OVs-TiO$_2$ -N$_2$ room temperature

Table4.2.2.1 Calculated effective masses of electrons and holes for TiO$_2$ and OVs-TiO$_2$ by parabolic fitting to the CBM and VBM along a specific direction in the reciprocal space. m$_0$ was the mass of free electrons.

	Direction	m_e*/ m_0	m_h^*/m_0	D
TiO$_2$	G→X	4.513	1.815	2.487
	G→Z	0.865	1.864	2.155
OVs-TiO$_2$	G→X	4.766	1.873	2.545
	G→Z	0.414	1.557	3.761

In addition, theoretical calculations were performed to investigate the charge carrier separation and transfer. The transfer rates of the photoinduced electrons and holes were inversely proportional to their effective masses according to the following equation [43, 44]:

$$v = \hbar\kappa/m^*$$ (4.2.2-7)

Where the m^* was the effective mass of electrons and holes, к was the wave vector, $\hbar$ was the reduced Planck constant, and v was transfer rate of the photogenerated electrons and holes. On the basis of the band structures, the effective masses of the photogenerated electrons (m_e^*) and holes (m_h^*) along the designated directions were calculated by fitting parabolic functions around the CBM and VBM according to the following equation[45, 46]:

$$m^* = \hbar^2 \left[\frac{\partial^2 \varepsilon(k)}{\partial k^2}\right]^{-1} \qquad (4.2.2\text{-}8)$$

where $\varepsilon(k)$ was the band edge energy as a function of wave vector к. In order to analyze the charge separation efficiency deeply, the relative effective mass (D) of the photogenerated hole to electron was defined according to the following equation (3) [45, 47]:

$$D = \left\{\frac{m_h^*}{m_e^*}, \frac{m_e^*}{m_h^*}\right\}max$$

(4.2.2-9)

It was accepted that the higher value of D meant higher separation efficiency of charge carrier. The **Table4.2.2.1** summarized the calculated effective masses of charge carriers for TiO$_2$ and OVs-TiO$_2$. Compared with the perfect TiO$_2$, the OVs-TiO$_2$ displayed smallest effective masses of the photogenerated electrons (0.414) and holes (1.557) and largest relative effective mass (3.761) along the G→Z directions, which indicated enhanced charge carrier separation efficiency. These results were consistent with experimental results, unveiling the crucial roles of OVs in improving the charge carrier separation.

Photocatalytic performance
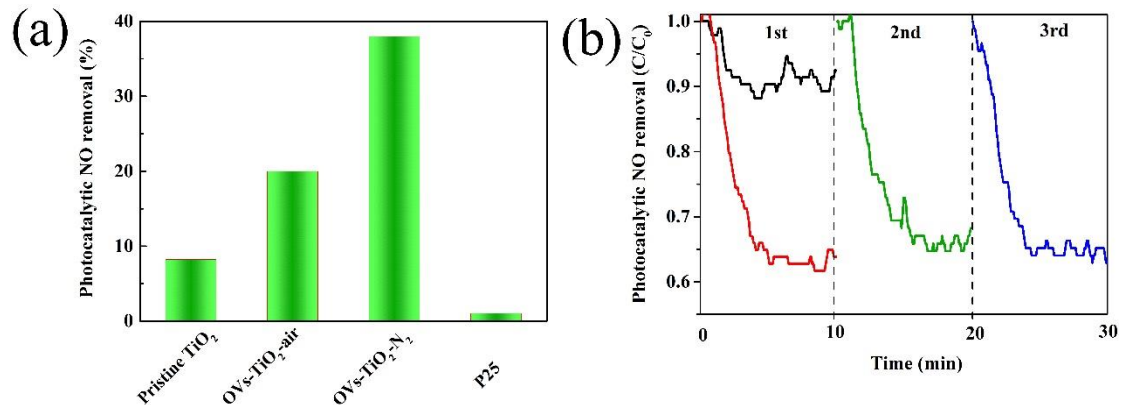
Fig.4.2.2.14. (a) Photocatalytic removal efficiency of the resultant samples under visible-light irradiation (λ>510m). (b) Cycling test for OVs-TiO$_2$ -N$_2$
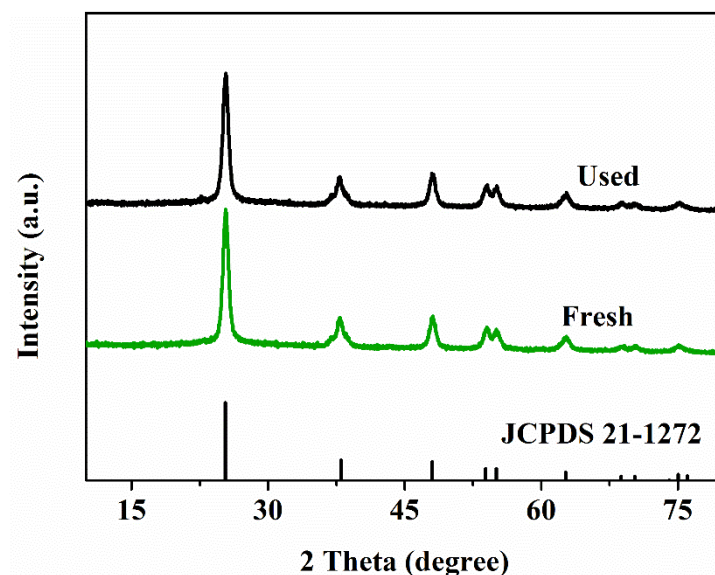
Fig.4.2.2.15. XRD patterns of OVs-TiO$_2$-325 before and after recycling test.

The photocatalytic performance of the obtained samples was evaluated by photocatalytic NO removal under visible-light irradiation (λ>510 nm). Thanks to the intrinsic carbon-doping, the pristine TiO$_2$ showed limited photocatalytic NO removal performance while the commercial P25 almost had no catalytic performance due to its too large bandgap (**Fig.4.2.2.14**a). However, the OVs-TiO$_2$-N$_2$ exhibited outstanding catalytic performance owing to the existence of intrinsic carbon-doping induced OVs. It exhibited 4.0 times higher photocatalytic activity than that of pristine TiO$_2$. In addition, the OVs-TiO$_2$-N$_2$ displayed good photocatalytic stability because there was no apparent decreased photocatalytic activity in OVs-TiO$_2$-N$_2$ after three cycles photocatalytic NO removal tests (**Fig.4.2.2.14**b). The photocatalytic stability of OVs-TiO$_2$-N$_2$ was further confirmed by the XRD results since the used and fresh OVs-TiO$_2$-N$_2$ showed similar XRD patterns (**Fig.4.2.2.15**).

Crucial roles of OVs

To study the effect of OVs on the photocatalytic NO removal process deeply, DFT calculations were performed to compare the O$_2$ and NO adsorption on the surface of

TiO$_2$ and OVs-TiO$_2$, respectively. As shown in **Fig.4.2.2.16** (a1-d1), the NO and O$_2$ molecules were difficult to be absorbed on the surface of pristine TiO$_2$ while they were easy to be absorbed on the surface of OVs-TiO$_2$. Specifically, the distances between NO and O$_2$ molecules and the surface of pristine TiO$_2$ were 1.525 and 2.417 Å, respectively (**Table 4.2.2.2**). In comparison, the distances between NO and O$_2$ molecules and the surface of OVs-TiO$_2$ both decreased to 0 Å. In addition, the adsorption energies of NO and O$_2$ were decreased from 0.836 and 1.020 eV on the surface of TiO$_2$ to -1.941 and -3.776 eV on the surface of OVs-TiO$_2$, respectively. As shown in **Table 4.2.2.2**, both the band lengths of NO and O$_2$ were lengthened from 1.165 and 1.236 Å (absorbed on the surface of TiO$_2$) to 1.301 and 1.395 Å (absorbed on the surface of OVs-TiO$_2$), respectively. Therefore, it is safe to conclude that OVs could capture the NO molecules and activate the N-O band [37], which was in favor of improving the photocatalytic NO removal performance. It is important to note that the OVs would activate the O$_2$ molecules to create reactive oxygen species (ROS)[48], which played crucial roles in photocatalytic NO removal process.

The charge density difference of O$_2$ and NO adsorption on the surface of TiO$_2$ and OVs-TiO$_2$ was showed in **Fig.4.2.2.16** (a2-d2), respectively. The light blue represented charge loss and yellow stood for the charge accumulation. According to the Bade charge analysis, there was nearly no electrons could transfer from the surface of perfect TiO$_2$ to free NO molecule and O$_2$ molecule. However, the electrons could transfer from the surface of OVs-TiO$_2$ to adsorbed NO molecule (1.008e) and O$_2$ molecule (1.045e), suggesting the chemical adsorption[49]. Therefore, OVs was beneficial for the surface adsorption and catalytic reaction, which would result in the enhanced photocatalytic activity of OVs-TiO$_2$-N$_2$.

Table 4.2.2.2. The distance between the molecules and the surface of TiO_2 and OVs-TiO_2 based on the DFT calculation. And the corresponding band length of molecules adsorbed on the surface of TiO_2 and OVs-TiO_2, respectively.

	Distance (Å)		Band length (Å)	
Molecule	NO	O_2	NO	O_2
TiO_2	1.525	2.417	1.165	1.236
OVs- TiO_2	0.0	0.0	1.301	1.395
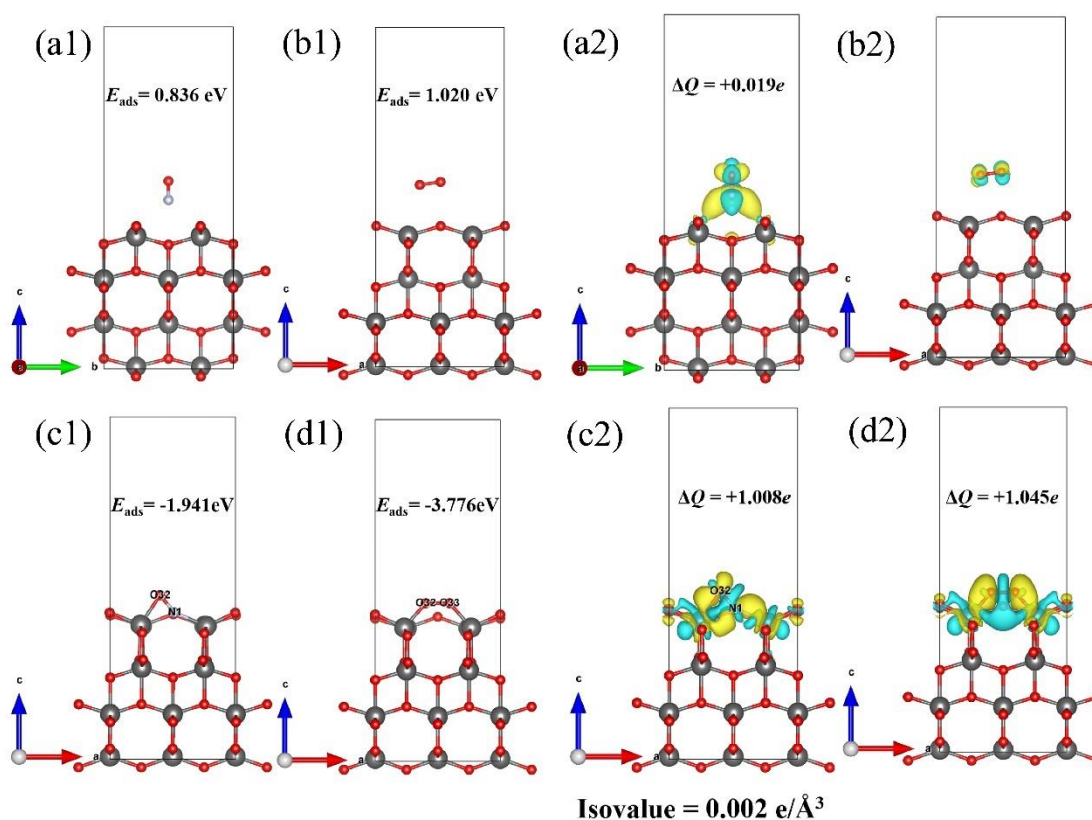
Fig.4.2.2.16. Optimized structures for NO and O_2 absorption on pristine TiO_2 (a1-b1) and OVs-TiO_2 (c1-d1). Charge density difference of optimized NO and O_2 absorbed on pristine TiO_2(a2-b2) and OVs-TiO_2 (c2-d2).

Proposed mechanism

Based on the above discussions, a possible photocatalytic schematic diagram of OVs-TiO$_2$-N$_2$ was illustrated in **Fig.4.2.2.17**. In general, the photocatalytic process involved three consecutive steps, i.e. light absorption and charge generation, charge transfer and separation, and surface catalytic reactions., the OVs could modulate the bandgap of OVs-TiO$_2$-N$_2$ to extend the range of light absorption, which was beneficial for the generation of photoinduced electron-hole pairs. Moreover, the OVs played positive roles in charge transfer and separation. On one hand, constructing OVs increased the conductivity of OVs-TiO$_2$-N$_2$ owing to the narrowed bandgap, resulting in promoting charge carrier separation efficiency. One the other hand, the surface OVs would serve as the reactive sites to trap the separated charge carrier, which was not only advantage of the charge carrier separation but also the subsequent surface catalytic reactions. It also should be note that OVs tended to accelerate the transfer rate of the photoinduced electrons and holes to enhance the charge carrier separation efficiency. Last but not least, the OVs affected the adsorption and activation of molecules (NO and O$_2$) because of the increased local electron density. Compared with pristine TiO$_2$, the OVs-TiO$_2$-N$_2$ was much easier to absorb and activate the molecules (NO and O$_2$) to participate in the surface catalytic reactions. All in all, the OVs could increase the absorption of visible-light, reduce the charge carrier recombination and enhanced the surface catalytic reactions, which brought about the significantly improved catalytic activity of OVs-TiO$_2$-N$_2$.
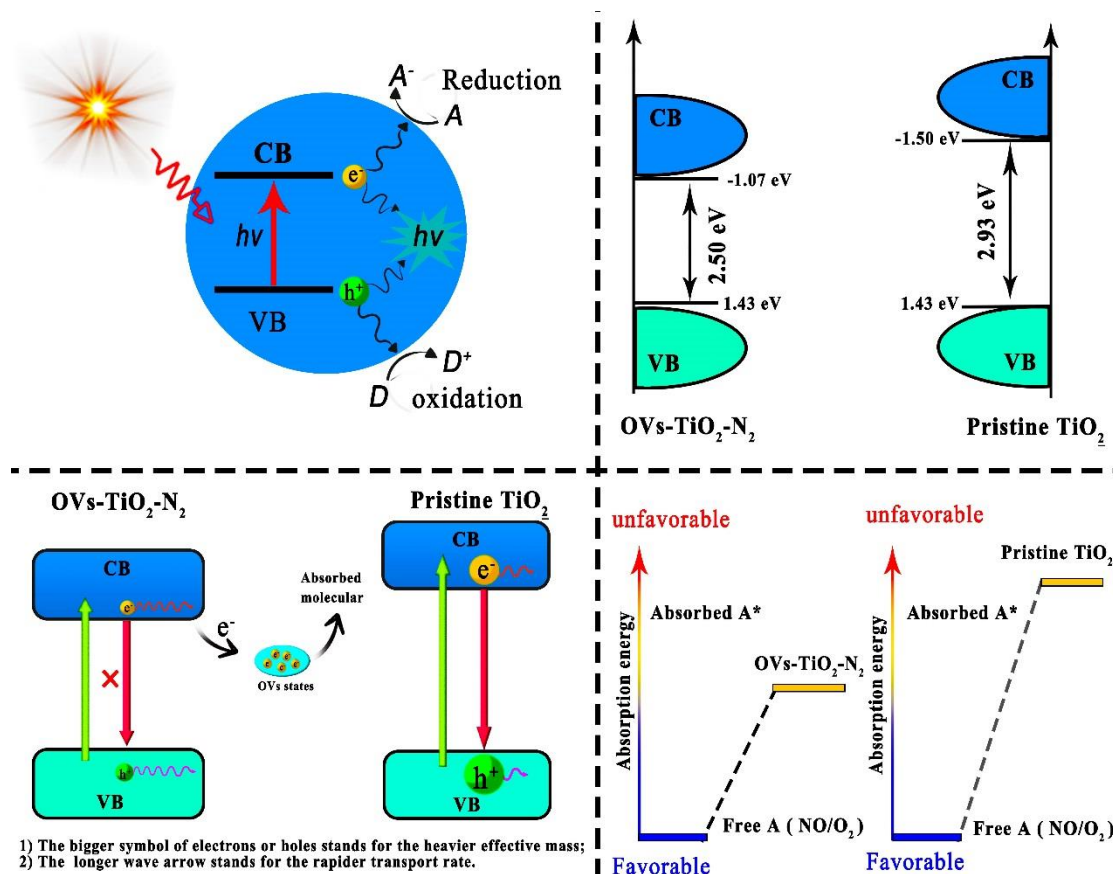
Fig.4.2.2.17. Proposed mechanism for the enhanced photocatalytic removal performance of OVs-TiO$_2$ -N$_2$

4.2.2.4. Conclusion

In summary, we successfully synthesized the OVs-TiO$_2$-N$_2$ nanocrystals via a low-temperature calcination in nitrogen atmosphere assisted solvothermal process using the TBT as precursor and the ethanol as the solvent. Because of the organic reagent of TBT and ethanol, the pristine TiO$_2$ would be natively carbon-doped without additional carbon source during the solvothermal process. The obtained pristine TiO$_2$ could be easily introduced into OVs under nitrogen atmosphere, which was not limited under the reduction atmosphere. This process was different from the conventional reduction process. Based on the DFT calculations, the facile formation of OVs was due to the intrinsic carbon-doping effect. The OVs-TiO$_2$-N$_2$ exhibited significantly improved catalytic activity, which was 4.0 times higher than that of pristine TiO$_2$. Experimental and theoretical results demonstrated that the improved the photocatalytic NO removal

performance was due to curial roles of OVs. This work provided a new idea for synthesizing OVs-TiO$_2$ nanocrystals, which had great potential in the field of photocatalysis.

4.2.2.5 References

[1] X.-L. Wang, W.-L. An, Y. Yang, Z.-Y. Hu, S. Xu, W. Liao, Y.-Z. Wang, Porous gel materials from waste thermosetting unsaturated polyester for high-efficiency wastewater treatment, Chemical Engineering Journal, **361** (2019) 21-30.

[2] X.-L. Wang, W.-L. An, F. Tian, Y. Yang, H.-X. Xu, D. Wang, X. Zhao, P.-P. Xu, S. Xu, Y.-Z. Wang, Fast microwave-assisted hydrolysis of unsaturated polyester resin into column packing for rapid purifying of dye wastewater, Journal of hazardous materials, 384 (2020) 121465.

[3] Z. Gu, Z. Cui, Z. Wang, K.S. Qin, Y. Asakura, T. Hasegawa, S. Tsukuda, K. Hongo, R. Maezono, S. Yin, Carbon vacancies and hydroxyls in graphitic carbon nitride: promoted photocatalytic NO removal activity and mechanism, Applied Catalysis B: Environmental, (2020) 119376.

[4] M. Chen, X. Li, Y. Huang, J. Yao, Y. Li, S.-c. Lee, W. Ho, T. Huang, K. Chen, Synthesis and characterization of Bi-BiPO$_4$ nanocomposites as plasmonic photocatalysts for oxidative NO removal, Applied Surface Science, 513 (2020) 145775.

[5] S. Shen, Y. Liu, D. Zhai, G. Qian, Electroplating sludge-derived spinel catalysts for NO removal via NH3 selective catalysis reduction, Applied Surface Science, 528 (2020) 146969.

[6] L. Zhao, C. Li, S. Li, X. Du, J. Zhang, Y. Huang, Simultaneous removal of Hg0 and NO in simulated flue gas on transition metal oxide M'(M'= Fe$_2$O$_3$, MnO$_2$, and WO$_3$) doping on V$_2$O$_5$/ZrO$_2$-CeO$_2$ catalysts, Applied Surface Science, 483 (2019) 260-269.

[7] Z. Gu, Y. Asakura, S. Yin, High yield post-thermal treatment of bulk graphitic carbon nitride with tunable band structure for enhanced deNO$_x$ photocatalysis, Nanotechnology, 31 (2019) 114001.

[8] D. Xu, W. Wu, P. Wang, J. Deng, T. Yan, D. Zhang, Boosting the Alkali/Heavy Metal Poisoning Resistance for NO Removal by Using Iron-Titanium Pillared Montmorillonite Catalysts, Journal of Hazardous Materials, (2020) 122947.

[9] Y. Nosaka, A.Y. Nosaka, Generation and detection of reactive oxygen species in photocatalysis, Chemical reviews, 117 (2017) 11302-11336.

[10] S. Luo, X. Liu, X. Wei, M. Fu, P. Lu, X. Li, Y. Jia, Q. Ren, Y. He, Noble-metal-free cobaloxime coupled with metal-organic frameworks NH2-MIL-125: A novel bifunctional photocatalyst for photocatalytic NO removal and H_2 evolution under visible light irradiation, Journal of Hazardous Materials, (2020) 122824.

[11] R. Hao, Z. Wang, Y. Gong, Z. Ma, Z. Qian, Y. Luo, B. Yuan, Y. Zhao, Photocatalytic removal of NO and Hg0 using microwave induced ultraviolet irradiating H_2O/O_2 mixture, Journal of hazardous materials, 383 (2020) 121135.

[12] S. Cao, J. Low, J. Yu, M. Jaroniec, Polymeric photocatalysts based on graphitic carbon nitride, Advanced Materials, 27 (2015) 2150-2176.

[13] L. Cheng, Q. Xiang, Y. Liao, H. Zhang, CdS-based photocatalysts, Energy & Environmental Science, (2018).

[14] X. Li, Z. Wang, H. Shi, D. Dai, S. Zuo, C. Yao, C. Ni, Full spectrum driven SCR removal of NO over hierarchical $CeVO_4$/attapulgite nanocomposite with high resistance to SO_2 and H_2O, Journal of Hazardous Materials, 386 (2020) 121977.

[15] D. Zu, H. Wang, S. Lin, G. Ou, H. Wei, S. Sun, H. Wu, Oxygen-deficient metal oxides: Synthesis routes and applications in energy and environment, Nano Research, (2019) 1-14.

[16] X. Sun, X. Zhang, Y. Xie, Surface Defects in Two-Dimensional Photocatalysts for Efficient Organic Synthesis, Matter, 2 (2020) 842-861.

[17] Y. Wang, X. Wang, M. Antonietti, Polymeric graphitic carbon nitride as a heterogeneous organocatalyst: from photochemistry to multipurpose catalysis to sustainable chemistry, Angewandte Chemie International Edition, 51 (2012) 68-89.

[18] S.G. Ullattil, S.B. Narendranath, S.C. Pillai, P. Periyat, Black TiO_2 nanomaterials: a review of recent advances, Chemical Engineering Journal, 343 (2018) 708-736.

[19] X. Chen, L. Liu, F. Huang, Black titanium dioxide (TiO_2) nanomaterials, Chemical Society Reviews, 44 (2015) 1861-1885.

[20] J. Nowotny, M.A. Alim, T. Bak, M.A. Idris, M. Ionescu, K. Prince, M.Z. Sahdan, K. Sopian, M.A.M. Teridi, W. Sigmund, Defect chemistry and defect engineering of TiO_2-based semiconductors for solar energy conversion, Chemical Society Reviews, 44 (2015) 8424-8442.

[21] X. Wu, S. Yin, Q. Dong, T. Sato, Blue/green/red colour emitting up-conversion phosphors coupled C-TiO$_2$ composites with UV, visible and NIR responsive photocatalytic performance, Applied Catalysis B: Environmental, 156 (2014) 257-264.

[22] Y. Huang, Y. Yu, Y. Yu, B. Zhang, Oxygen Vacancy Engineering in Photocatalysis, Solar RRL, (2020) 2000037.

[23] H. Shang, M. Li, H. Li, S. Huang, C. Mao, Z. Ai, L. Zhang, Oxygen vacancies promoted the selective photocatalytic removal of NO with blue TiO$_2$ via simultaneous molecular oxygen activation and photogenerated hole annihilation, Environmental science & technology, 53 (2019) 6444-6453.

[24] W.C. Huo, J.Y. Li, M. Liu, X.Y. Liu, Y.X. Zhang, F. Dong, Synthesis of Bi$_2$WO$_6$ with gradient oxygen vacancies for highly photocatalytic NO oxidation and mechanism study, Chemical Engineering Journal, 361 (2019) 129-138.

[25] X. Chen, L. Liu, P.Y. Yu, S.S. Mao, Increasing solar absorption for photocatalysis with black hydrogenated titanium dioxide nanocrystals, Science, 331 (2011) 746-750.

[26] S. Liu, S. Yuan, Q. Zhang, B. Xu, C. Wang, M. Zhang, T. Ohno, Fabrication and characterization of black TiO2 with different Ti3+ concentrations under atmospheric conditions, Journal of Catalysis, 366 (2018) 282-288.

[27] J.P. Perdew, K. Burke, M. Ernzerhof, Generalized gradient approximation made simple, Physical review letters, 77 (1996) 3865.

[28] G. Kresse, J. Furthmüller, Efficient iterative schemes for ab initio total-energy calculations using a plane-wave basis set, Physical review B, 54 (1996) 11169.

[29] G. Kresse, J. Furthmüller, Efficiency of ab-initio total energy calculations for metals and semiconductors using a plane-wave basis set, Computational materials science, 6 (1996) 15-50.

[30] S. Wei, R. Wu, X. Xu, J. Jian, H. Wang, Y. Sun, One-step synthetic approach for core-shelled black anatase titania with high visible light photocatalytic performance, Chemical Engineering Journal, 299 (2016) 120-125.

[31] S. Komatsuda, Y. Asakura, J.J.M. Vequizo, A. Yamakata, S. Yin, Enhanced photocatalytic NOx decomposition of visible-light responsive F-TiO$_2$/(N, C)-TiO$_2$ by charge transfer between F-TiO$_2$ and (N, C)-TiO$_2$ through their doping levels, Applied

Catalysis B: Environmental, 238 (2018) 358-364.

[32] C. Guo, X. Wu, M. Yan, Q. Dong, S. Yin, T. Sato, S. Liu, The visible-light driven photocatalytic destruction of NO_x using mesoporous TiO_2 spheres synthesized via a "water-controlled release process", Nanoscale, 5 (2013) 8184-8191.

[33] C. Di Valentin, G. Pacchioni, A. Selloni, Theory of carbon doping of titanium dioxide, Chemistry of Materials, 17 (2005) 6656-6665.

[34] L. Gu, J. -Wang, H. Cheng, Y. Zhao, L. Liu, X. Han, One-step preparation of graphene-supported anatase TiO_2 with exposed {001} facets and mechanism of enhanced photocatalytic properties, ACS Applied Materials & Interfaces, 5 (2013) 3085-3093.

[35] G. Ou, Y. Xu, B. Wen, R. Lin, B. Ge, Y. Tang, Y. Liang, C. Yang, K. Huang, D. Zu, Tuning defects in oxides at room temperature by lithium reduction, Nature communications, 9 (2018) 1-9.

[36] J. Xue, X. Zhu, Y. Zhang, W. Wang, W. Xie, J. Zhou, J. Bao, Y. Luo, X. Gao, Y. Wang, Nature of conduction band tailing in hydrogenated titanium dioxide for photocatalytic hydrogen evolution, ChemCatChem, 8 (2016) 2010-2014.

[37] G. Cheng, X. Liu, X. Song, X. Chen, W. Dai, R. Yuan, X. Fu, Visible-light-driven deep oxidation of NO over Fe doped TiO_2 catalyst: Synergic effect of Fe and oxygen vacancies, Applied Catalysis B: Environmental, (2020) 119196.

[38] Z. Gu, B. Zhang, Y. Asakura, S. Tsukuda, H. Kato, M. Kakihana, S. Yin, Alkali-assisted hydrothermal preparation of g-C_3N_4/rGO nanocomposites with highly enhanced photocatalytic NO_x removal activity, Applied Surface Science, (2020) 146213.

[39] J. Ran, T.Y. Ma, G. Gao, X.-W. Du, S.Z. Qiao, Porous P-doped graphitic carbon nitride nanosheets for synergistically enhanced visible-light photocatalytic H_2 production, Energy & Environmental Science, 8 (2015) 3708-3717.

[40] Y. Zhang, T. Mori, L. Niu, J. Ye, Non-covalent doping of graphitic carbon nitride polymer with graphene: controlled electronic structure and enhanced optoelectronic conversion, Energy & Environmental Science, 4 (2011) 4517-4521.

[41] L. Jiang, X. Yuan, G. Zeng, J. Liang, Z. Wu, H. Wang, Construction of an all-

solid-state Z-scheme photocatalyst based on graphite carbon nitride and its enhancement to catalytic activity, Environmental Science: Nano, 5 (2018) 599-615.

[42] J. Liqiang, Q. Yichun, W. Baiqi, L. Shudan, J. Baojiang, Y. Libin, F. Wei, F. Honggang, S. Jiazhong, Review of photoluminescence performance of nano-sized semiconductor materials and its relationships with photocatalytic activity, Solar Energy Materials and Solar Cells, 90 (2006) 1773-1787.

[43] J. Zhang, P. Zhou, J. Liu, J. Yu, New understanding of the difference of photocatalytic activity among anatase, rutile and brookite TiO_2, Physical Chemistry Chemical Physics, 16 (2014) 20382-20386.

[44] J. Xue, M. Fujitsuka, T. Majima, The role of nitrogen defects in graphitic carbon nitride for visible-light-driven hydrogen evolution, Physical Chemistry Chemical Physics, 21 (2019) 2318-2324.

[45] J. Zhang, S. Wageh, A. Al-Ghamdi, J. Yu, New understanding on the different photocatalytic activity of wurtzite and zinc-blende CdS, Applied Catalysis B: Environmental, 192 (2016) 101-107.

[46] W. Yu, D. Xu, T. Peng, Enhanced photocatalytic activity of gC_3N_4 for selective CO_2 reduction to CH_3OH via facile coupling of ZnO: a direct Z-scheme mechanism, Journal of Materials Chemistry A, 3 (2015) 19936-19947.

[47] J. Zhang, W. Yu, J. Liu, B. Liu, Illustration of high-active Ag_2CrO_4 photocatalyst from the first-principle calculation of electronic structures and carrier effective mass, Applied Surface Science, 358 (2015) 457-462.

[48] H. Li, J. Li, Z. Ai, F. Jia, L. Zhang, Oxygen vacancy-mediated photocatalysis of BiOCl: reactivity, selectivity, and perspectives, Angewandte Chemie International Edition, 57 (2018) 122-138.

[49] Z. Cui, C. Xiao, Y. Lv, Q. Li, R. Sa, Z. Ma, Adsorption behavior of CO, CO_2, H_2, H_2O, NO, and O_2 on pristine and defective 2D monolayer Ferromagnetic Fe_3GeTe_2, Applied Surface Science, (2020) 146894.

Chapter 5 Summary and outlook

The doctoral dissertation focuses on the modification of polymeric carbon nitride (CN) based photocatalysts for enhanced photocatalytic NO removal performance. Since the CN displays poor response to visible light, rapid charge carrier recombination, small specific surface area and few active sites, which results in deficient solar light efficiency and unsatisfactory photocatalytic performance. To solve the intrinsic drawbacks of pristine CN, effective strategies are developed to improve the photocatalytic NO removal performance. The related work presents in four chapters with the three experimental chapters.

Chapter 1 introduces the general concepts of photocatalysis, which is a green and promising technology for the environmental remediation. The key point of photocatalysis is to develop efficient and stable photocatalyts. Pristine CN suffers from low specific surface area and rapid charge carrier recombination. Therefore, much work has been to overcome the drawbacks of pristine CN. A brief review is presented to summarize the previously reported strategies for enhancing the photocatalytic performance of pristine CN. Inspired by a flood of literatures, the research objectives in the doctoral dissertation is obtained.

Chapter 2 presents the morphology control strategy to enhance the photocatalytic NO removal performance of bulk CN. Bulk CN was exfoliated into nanosheets to increase the specific surface area and active sites via facile post-thermal treatment. At the same time, the electronic structure of bulk CN was optimized during the calcination process. The specific surface area of bulk CN was increased from $13.6 \, \text{m}^2/\text{g}$ to $68.0 \, \text{m}^2/\text{g}$. The yield of CN nanosheets reached up to 67%, and its photocatalytic decomposition of NO_x activity was about 3.0 times higher than that of bulk CN. Moreover, the CN nanosheets obtained at 550°C with a higher specific surface area ($113.9 \, \text{m}^2/\text{g}$) displayed lower photocatalytic activity than that obtained at 500°C with a lower specific surface area ($68.0 \, \text{m}^2/\text{g}$), which was attributed to its lower valence band.

Chapter 3 introduces the defect engineering strategy to enhance the photocatalytic NO removal performance of pristine CN. The chapter 3 includes two works i.e., chapter

3.1 and chapter 3.2.

The chapter 3.1 presents the carbon vacancies and hydroxyls co-modified CN (CH-CN) via green hydrothermal method. The carbon vacancies and hydroxyls co-modified CH-CN displayed 2.2 times higher photocatalytic NO removal performance than that of pristine CN. Detailed experimental characterizations and density functional theory calculations revealed that the enhanced photocatalytic NO removal performance of CH-CN nanosheet was largely ascribed to the synergistic effects of carbon vacancies and hydroxyls. The carbon vacancies could narrow the bandgap of modified CH-CN nanosheet to improve the light-absorbing capability; the hydroxyls enabled to form stable covalent bonds acted as electron transport channels to facilitate the charge carrier separation.

The chapter 3.2 presents crystalline carbon nitride (CCN) via modified molten-salts method under ambient pressure, which is expected to the large-scale production of crystalline carbon nitride. The obtained crystalline carbon nitride displayed about 3.0 times higher photocatalytic NO removal performance than that of pristine carbon nitride under visible light irradiation ($\lambda > 400$ nm). Detailed experimental characterization and theoretical calculation revealed the crucial roles of crystallinity in crystalline carbon nitride for the enhanced photocatalytic NO removal performance.

Chapter 4 introduces the heterostructure construction strategy to enhance the photocatalytic NO removal performance of pristine CN. We successfully prepared g-C_3N_4/rGO nanocomposites (Chapter 4.1). When we plan to prepare CN/TiO_2 heterostructure via calcination assisted hydrothermal process. Interestingly, we prepared oxygen vacancies mediated TiO2 with excellent photocatalytic performance (Chapter 4.2.1 and Chapter 4.2.2).

The chapter 4.1 presents g-C_3N_4/rGO nanocomposites via alkali-assisted hydrothermal process. n the hydrothermal process, the NaOH not only played an important role in etching the bulk g-C_3N_4 into nanosheets to increase its specific surface area and active sites, but also promoted the reduction of GO to enhance the conductivity of rGO. The rGO sheets could act as an excellent electron acceptor and electronic conductive channels to improve the separation efficiency of photogenerated electron-

hole pairs. The resultant g-C₃N₄/rGO nanocomposites exhibited 2.7 times higher photocatalytic NO_x removal activity than that of bulk g-C₃N₄ due to the enlarged specific surface area and their enhanced separation efficiency of photogenerated carriers.

The chapter 4.2.1 presents facile approach to fabricate oxygen vacancies-mediated TiO_2 (OVs-TiO_2) nanocrystals via an intrinsic carbon-doping induced strategy. The intrinsic carbon-doped TiO_2 nanocrystals were firstly synthesized by water-controlled-releasing solvothermal (WCRS) process using ethanol, acetic acid and titanium tetraisopropoxide (TTIP) as precursors. The carbon-doped TiO_2 was calcined at 325 °C under a N_2 atmosphere to introduce the OVs. The obtained OVs-TiO_2 displayed outstanding photocatalytic NO removal performance under visible light irradiation (λ>510 nm). With the aid of DFT calculations, we revealed that the intrinsic carbon-doping was beneficial for OVs' formations in carbon-doped TiO_2. Moreover, the OVs played crucial roles in improving light absorption, facilitating charge separation, and activating surface reactions to enhance the photocatalytic NO removal performance.

The chapter 4.2.2 presents a reductant-free strategy to fabricate oxygen vacancies-mediated (OVs-mediated) TiO_2 nanocrystals. Firstly, the pristine TiO_2 was synthesized by a solvothermal process using the tetra-n-butyl titanate as precursor and ethanol as solvent. Because of the organic precursor and solvent, the obtained pristine TiO_2 was inevitably carbon-doped. Then, low-temperature calcination in nitrogen atmosphere instead of reducing gas atmosphere was carried out to introduce the OVs into the pristine TiO_2. Experimental and theoretical results revealed that the intrinsic carbon-doping was conducive to the formation of OVs. Moreover, the obtained OVs-mediated TiO_2 exhibited outstanding photocatalytic performance compared to the commercial P25, which was attributed to the crucial roles of OVs. This work not only provided a novel synthesis of OVs-mediated TiO_2, but also contributed to understanding the crucial roles of OVs.

In summary, we developed effective strategies to modified the CN-based photocatalysts for the enhanced photocatalytic NO removal performance. Considering

the good photocatalytic performance and low-cost of CN-based photocatalysts, they are promising to be used for the environmental remediation.

At the same time, it should be point out that there is much room for improvement related to the CN based photocatalysts. For example, rational design of CN/TiO$_2$ heterostructure could be developed for the enhanced photocatalytic NO removal performance. Also, as a metal-free semiconductor material, it holds the potential in other application fields, such as porous covalent organic framework for the absorption of molecules, room-temperature gas sensors and so on.

Publications

[1] **Z. Gu**, Y. Asakura, S. Yin, High yield post-thermal treatment of bulk graphitic carbon nitride with tunable band structure for enhanced deNO$_x$ photocatalysis, Nanotechnology, **31** (2019) 114001. **(Chaper 2**)

[2] **Z. Gu**, Z. Cui, Z. Wang, K.S. Qin, Y. Asakura, T. Hasegawa, S. Tsukuda, K. Hongo, R. Maezono, S. Yin, Carbon vacancies and hydroxyls in graphitic carbon nitride: Promoted photocatalytic NO removal activity and mechanism, Applied Catalysis B: Environmental, **279** (2020) 119376. **(Chaper 3.1**)

[3] **Z. Gu**, Z. Cui, Z. Wang, T. Chen, P. Sun, D. Synthesis of crystalline carbon nitride with enhanced photocatalytic NO removal performance: an experimental and DFT theoretical study, Journal of Materials Science & Technology (2021). **(Chaper 3.2**)

[4] **Z. Gu**, Z. Cui, Z. Wang, K.S. Qin, Y. Asakura, T. Hasegawa, K. Hongo, R. Maezono, S. Yin, Intrinsic carbon-doping induced synthesis of oxygen vacancies-mediated TiO$_2$ nanocrystals: Enhanced photocatalytic NO removal performance and mechanism, Journal of Catalysis, **393** (2021) 179-189. **(Chaper 4.2.1**)

[5] **Z. Gu**, B. Zhang, Y. Asakura, S. Tsukuda, H. Kato, M. Kakihana, S. Yin, Alkali-assisted hydrothermal preparation of g-C$_3$N$_4$/rGO nanocomposites with highly enhanced photocatalytic NO$_x$ removal activity, Applied Surface Science, (2020) 146213. **(Chaper 4.1.1**)

[6] **Z. Gu**, Z. Cui, Z. Wang, T. Chen, P. Sun, D. Wen, Reductant-free synthesis of oxygen vacancies-mediated TiO$_2$ nanocrystals with enhanced photocatalytic NO removal performance: an experimental and DFT study, Applied Surface Science, (2021) 148923. **(Chaper 4.2.2**)

Presentations

[1]**谷 占勇**、朝倉 裕介、殷 澍、バルクカーボンナイトライド熱処による光触媒活性の改善(A facile strategy to improve the photocatalytic activity of bulk graphitic carbon nitride via post-thermal treatment)、無機マテリアル学会 139 回学術講演会、p42-43, 2019.11.14-15 仙台

[2] **(Poster) <u>Z.GU</u>**, Y. ASAKURA, S.YIN, Facile Preparation of Graphitic Carbon Nitride/Reduced Graphene Nanocomposites with Enhanced Visible-light Photocatalytic Activity via Alkali-assisted Hydrothermal Method, The 2nd Symposium for World Leading Research Centers, - Materials Science and Spintronics-, Feb.16-18, 2019, Sendai

[3] **(Poster) <u>Z. Gu</u>**, Y. Asakura, S. Yin, Facile strategy to enhance the visible-light photocatalytic activity of graphitic carbon nitride by alkaline hydrothermal treatment and hybridizing with graphene simultaneously, 平成 30 年度 日本セラミックス協会 東北北海道支部研究発表会、郡山、2018.11.2-11.3. p63

[4] **(Poster) <u>Z.GU</u>**,Y.ASAKURA, S.YIN, Alkali-assisted hydrothermal preparation of porous graphitic carbon nitride/graphene nanocomposites with enhanced visible-light photocatalytic activity、第 18 回東北大学多元物質科学研究所研究発表会、2018 年 12 月 13 日、仙台, p27

[5] **<u>Z. GU</u>**, Y. ASAKURA, and S.YIN, Alkali-assisted Hydrothermal Preparation of Graphitic Carbon Nitride/graphene Nanocomposites with Enhanced Visible-light Photocatalytic Activity, 第 57 回セラミックス基礎科学討論会、仙台 2019.1.16-17, 1F20

[6] **<u>Z. GU</u>**, Y. ASAKURA, S.YIN, Hydrothermal Synthesis of g-C_3N_4/rGO Nanocomposites with Enhanced Visible-light Photocatalytic Activity, (1st Academic Forum on Environmental Studies), June 28, 2019, P28.

[7] **(Poster) Z. G**u, Y. Asakura and S. Yin, High yield post-thermal treatment of bulk graphitic C$_3$N$_4$ with tunable band structure for enhanced photocatalytic decomposition of NO$_x$, 化学系学協会東北大会、山形、2019.9.22, p15

[8] **Z. GU**, Y. ASAKURA, S.YIN, Intrinsic carbon-doping induced synthesis of oxygen vacancies-mediated TiO$_2$ nanocrystals: enhanced photocatalytic NO removal performance and mechanism, The 9th International Symposium on Functional Materials, Hwaseong, korea,2021.01.19.